Megacryst suite from the Salpeterkop Carbonatite Complex, Sutherland, Northern Cape, South Africa: An in-depth geochemical study

by

Chad Jordan Peel

a dissertation submitted in fulfilment of the degree of

Master of Science

Department of Geological Sciences,

University of Cape Town, South Africa

October 2019

Supervisor: Assoc. Prof. Philip Janney

Declaration

I, Chad Jordan Peel (Student Number: PLXCHA003) hereby declare that the work presented in this thesis is my own, except where otherwise stated in the text.

Signature: ..... Date: .....

Abstract

Presented here are major and trace element, stable (oxygen and hydrogen) and radiogenic (Sr-Nd-Pb) isotope analyses for a Cr-poor megacryst suite from the Salpeterkop complex, South Africa. The clinopyroxene, amphibole, phlogopite and ilmenite megacrysts all appear to be cogenetic, and based on known mineral relationships and intergrowths from xenoliths in the complex, the apparent order of mineral crystallisation is as follows: phlogopite → ilmenite → amphibole → clinopyroxene. Megacrysts of amphibole and phlogopite exhibit δD and $\delta^{18}O$ values that are aligned with these grains having crystallised from melt originating from the upper mantle. Additionally, the amphibole and phlogopite megacrysts appear to have experienced dehydration styled degassing, possibly related to their exhumation. Calculated P-T conditions have the megacrysts crystallising in the lower crust, under conditions ranging from 1 to 1.5 GPa (35 to 45 km depth) and 1000 to 1250 ℃. Calculated REE melts in equilibrium with the megacryst as well as radiogenic isotope results suggest that the Salpeterkop ultramafic lamprophyres are genetically related to the SPKC megacryst suite, however, the calculated parent melt to the megacryst appears to have mixed with a HIMU component. These findings primarily affect higher Mg-number megacrysts, suggesting that this assimilation or mixing occurred during initial stages of crystallisation. Lower Mg-number megacrysts lack the variations noted in their more primitive counterparts and present more tightly defined trends. A model of formation for the megacryst suite of the Salpeterkop complex sees grains having crystallised from an SPKC ultramafic lamprophyre-like melt originating from sublithospheric/asthenospheric conditions. During ascension the melt episodically assimilates material with a HIMU signature. The high Mg-number megacryst population crystallises from this melt at lower crustal depths. Soon after assimilation halts the megacryst parent melt homogenises (or re-homogenises), with grains to crystallise from this melt forming the low-Mg megacryst population.

Acknowledgements

- I would like to thank my supervisor, Assoc Prof Philip Janney for always taking time out of his busy schedule to assist me in any way he could. Thank you for all of the skills and knowledge passed down, and for the advice and guidance you provided over the years.

- My parents (Mr E.L. Peel and Mrs A.D. Peel), sister Kia Peel for their constant love and support throughout this project.

- Ms. Christel Tinguely (UCT) for her assistance with laser ablation and solution ICP-MS analyses and her patience, even after constantly being overloading with my samples.

- Mr. Nic Laidler (UCT) for assistance with EMPA.

- Ms. Fayrooza Rawoot (UCT) for assistance with Radiogenic analyses.

- Ms. Sherissa Roopnarain (UCT) and Ms. Bogdana Radu (UCT – Saint-Étienne) for their assistance with Stable Isotope Analysis.

- Miss Fiona Clark for her field assistance with field work.

- Mr. Vhutali Brian Gadisi, Miss Lorena Tafur, Miss Fiona Clark and Mr. Guy Solomon, my closest and most trusted friends, for always providing words of encouragement and for constantly cheering me on. Without the love and support you provided completing this thesis would have been very difficult.

- Miss Miengah Abrahams my office mate and karaoke buddy. Thank you for keeping me sane on long days and for being a healt.

- Drs Robyn Pickering, Alastair Sloan, Petrus le Roux, Assoc Prof Johann Diener and Professor Chris Harris for their council, support and assistance with various aspects of my thesis.

- Mr. David Wilson and Ms. Rene van der Merwe (UCT) for preparation of numerous thin sections and epoxy mounts.

- The Centre for Integrative Mineral and Energy Resource Analysis (CIMERA, an NRF-DST Centre of Excellence) for providing the funds that made the field and analytical work for this study possible.

Table of content

List of Figures

List of Tables

1. Introduction

The deep-seated and isolated nature of the Earth's mantle makes direct and detailed studies of its composition challenging. As a result, earth scientists are forced to rely, to a large extent, on mafic and ultramafic volcanic rocks and a limited array of deep Earth samples that are brought to surface, to aid our understanding of magma genesis and geochemical evolution of the mantle. These deep Earth materials include, but are not limited to, megacrysts and mantle xenoliths that are both most often associated with mafic alkaline volcanic rocks, such as alkali basalts and kimberlites (e.g. Gurney et al. 1979; Shaw and Eyzaguirre, 2000; Wass, 1979). These objects provide information on the geochemistry of the lithosphere, the melts that percolate through it and the nature of melt-rock interactions, making them valuable tools for studies of the composition of the upper mantle (Irving, 1974; Dawson and Smith, 1977; Braga et al. 2006).

1.1. Alkaline magmatism

Alkaline igneous rocks are those that have an overabundance of alkali metals (Na_2O + K_2O) relative to Al_2O_3 and/or SiO_2, such that their normative (and possibly modal) mineralogy includes silica-deficient minerals (i.e. feldspathoids) or alkali-bearing ferromagnesian minerals (i.e. aegirine, arfvedsonite). Alkaline igneous rocks occur in several tectonic environments, from ocean islands (i.e. Honolulu Volcanic Series, Hawaiian Islands) to continental rift (i.e. East Africa Rift system) and intraplate continental settings (i.e. Massif Central, France; Tasmanian Tertiary volcanics).

Southern Africa is well known for its wide abundance of continental intraplate alkaline rocks such as olivine melilitites, kimberlites, carbonatites and to a lesser extent, more differentiated rock types such as syenites, phonolites and trachytes. Several of these rock types are important from an economic perspective as they may host diamonds or valuable metals such as rare earth elements. The Saltpeterkop carbonatite complex is an example of an intraplate South African locality where several types of alkaline rocks can be found.

1.2. An overview of the Salpeterkop complex

The Saltpeterkop carbonatite complex (SPKC, 32°28'31.36"S, 20°50'24.96"E) in the Northern Cape province of South Africa, is a volcanic-intrusive complex of Late Cretaceous age (74-77 Ma, Duncan et al. 1978; Malarkey et al. 2010) situated 18 km east-south-east of the town of Sutherland. A 1 km diameter tuff ring composed of hydrothermally altered volcaniclastic breccia built on top of upwarped sedimentary rocks (Verwoerd, 1990). The north side of the tuff ring has been more heavily silicified than the surrounding portions, making it highly resistant to weathering (de Wet, 1975). It is this more heavily silicified portion of the tuff ring that forms the prominent peak of the complex. The peak stands at an elevation of 1766 m above sea-level and roughly 300 m above the surrounding Karoo landscape. The tuff ring itself forms a rim around the neck of shallow depression (Fig. 1.1) underlain by bedded fine-grained volcaniclastic sediments. The overall structure appears to represent a diatreme (Lorenz, 1973) and was likely produced as the result of a volatile-rich explosive eruption that led to the formation of the funnel-shaped conduit (Verwoerd, 1990; Woolsey et al. 1975). The complex is particularly interesting as it hosts a broad assortment of compositionally distinct alkaline igneous rocks ranging from differentiated carbonatites and potassic trachytes to more primitive olivine melilitite and ultramafic lamprophyres, all of which can be found scattered throughout the complex as dykes, sills, irregular intrusions and satellite pipe/diatreme features. Additionally, a handful of these satellite pipe features host mantle and lower crustal-derived nodules including megacrysts and xenoliths, which are the primary focus of this study.

1.3. Mantle-derived nodules

1.3.1. Mantle xenoliths

The term "mantle xenolith" refers to a rock of mantle origin, brought to or near the surface in a host rock of volcanic origin (Pearson et al. 2003). They often represent fragments of subcontinental lithospheric mantle that became entrained in an ascending magma (e.g. Type 1 xenoliths of Jackson and Wright, 1970), or cumulate ultramafic igneous rocks that crystallised in mantle or lower crustal magma chambers and have a mineralogy dominated by olivine, pyroxene, spinel and/or garnet (e.g. Type 2 xenoliths of Jackson and Wright, 1970).

Since ultramafic nodules are typically denser than most magmas, these fragments would tend to sink, unless the magma in which they are entrained is moving upward at significant velocity. For this reason, mantle xenoliths are nearly always associated with eruptions of rapidly moving volatile-rich low viscosity magmas. This exhumation process is typically so rapid that the xenoliths do not re-equilibrate during ascent meaning that their pre-entrainment compositions are preserved (Pearson et al. 2003). This makes xenoliths extremely valuable tools for studying the upper mantle. The compositions of xenoliths can also be used to provide constraints on numerous deep processes such as conditions of melt generation (i.e. degree, depth of melting and source mineralogy), early differentiation processes (crystallisation, immiscibility), and metasomatism/melt-rock interaction.

1.3.2. Megacrysts

The term megacrysts refers to large (> 10 mm) single crystals in igneous rocks, that are considerably larger than the typical grain size of the minerals found in that rock. Olivine, pyroxene, garnet, ilmenite, amphibole and mica are just a few of the most common mineral types that are regularly found as megacrysts (e.g. Schulze, 1987). Megacrysts have been used to understand and characterise the composition and evolution of the parent melts from which they crystallised, and their relation to the rocks that host them (Best, 1970; Irving and Frey, 1984; Gurney and Harte, 1980). They can also preserve information on pressure and temperature conditions experienced during their crystallisation. The use of thermobarometric calculations as a means of quantifying the pressure and temperature conditions experienced by these grains is, however, strongly dependent on the megacryst mineral assemblage as thermometers or barometers are based on elemental exchange between co-existing mineral (e.g. Ca-Mg exchange between clino- and orthopyoroxene; (Boyd, 1973).

Trace element and radiogenic isotope data for megacrysts have been shown to be useful tracers of processes such as fractional crystallisation and assimilation, and the effects these have on megacryst parent melt evolution, as well as mantle metasomatism, and the effects of melt and fluid-rock interaction (Bell and Moore, 2004). Hydrous megacryst phases for example, may represent crystallisation products of hydrous melts, but they can also be metasomatic in origin (Demény et al. 2005). These hydrous phases, which include amphibole and phlogopite,

contain hydroxyl groups in their mineral structure, which means that in addition to information on oxygen isotopes, it is possible to obtain data on hydrogen isotopes. Anhydrous minerals such as clinopyroxene and ilmenite differ from hydrous minerals in that they typically contain very low H concentrations, which makes it difficult to perform precise H isotopic measurements. Hydrous minerals can therefore be used to trace the origin and source of the hydrogen. Variations in the oxygen and hydrogen isotopic composition of the megacrysts could be indicative of an interaction with isotopically distinct materials (i.e. magma mixing, mantle metasomatism and crustal assimilation) or could simply reflect kinetic effects due to the structure or hydrogen content of hydrous minerals (e.g. via degassing). According to studies by several authors including King et al. (1999), amphibole megacrysts are typically H-deficient titanian pargasite or kaersutite oxy-amphiboles (nomenclature of Leake et al. 1997). Both hydrogen and oxygen isotopes are sensitive to late-stage hydrothermal alteration and/or degassing processes, which can complicate geochemical interpretations, however oxygen should be more resistant to fractionation than hydrogen in mantle derived minerals (i.e. megacrysts) (Demény et al. 2005).

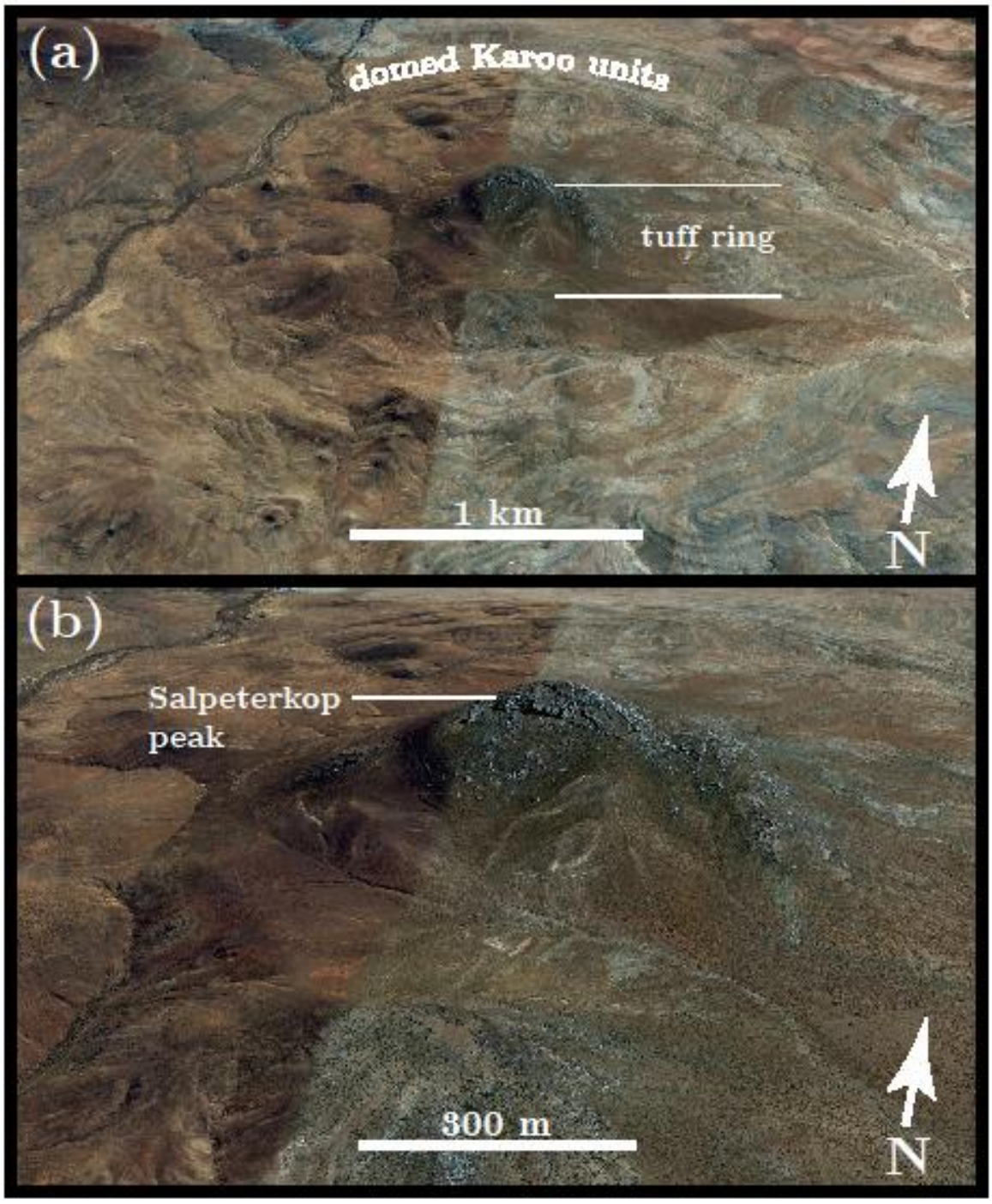

Figure 1.1: Modified Google Earth image of the Saltpeterkop central ring structure. (a) shows the tuff ring, and upwarped sedimentary units of the Beaufort Group (Karoo SG) country rock. (b) A closer image showing the main prominent peak of the complex.

1.4. Research Objectives

The purpose of this thesis is to investigate the origin of a suite of hydrous and anhydrous megacryst minerals sampled from the Saltpeterkop Complex, Northern Cape, South Africa. This investigation includes a thorough analysis of the major and trace element compositions of the megacrysts, along with their stable (hydrogen and oxygen) and radiogenic (Sr, Nd and Pb) isotope compositions. The goals of this research are:

- To constrain the major and trace element compositions of the megacrysts, using these to better understand their petrogenesis and constrain the possible source(s) of the melt(s) from which they crystallised and their possible origins;
- To comment on any compositional variations or abnormalities present within individual megacrysts or across the megacryst suite, which in turn could be used to comment on heterogeneities within the parent melt and possible causes for said heterogeneities;
- To constrain the order of crystallisation in the megacryst suite, as well as the pressures and temperatures of the megacryst crystallisation
- To determine the relation of the megacryst suite to the rock types also associated to the Salpeterkop complex, by attempting to model and constrain the major and trace element composition of melt(s) in equilibrium with the various megacryst phases;
- To compare published data on megacrysts hosted in various other alkaline igneous rock localities with those from the SPKC, to better understand megacryst petrogenesis.
- To determine if any genetic relationship exists between the xenoliths and megacrysts sampled from the same locality and how the xenoliths themselves fit in the crystallisation history of the complex.

2. Geology of the Salpeterkop Complex

The Salpeterkop complex is located near the southwestern extremity of the Proterozoic Namaqua-Natal mobile belt (NNMB), an orogenic terrain spanning several hundreds of kilometers across southern Africa (Eglington, 2006). It intrudes a sequence of sandstone, siltstone and shales belonging to the Teekloof Formation of the Beaufort Group (Karoo Supergroup). These beds which are regionally nearly flat-lying, at inclinations of between 2 and 3°, dip away from the centre of the Saltpeterkop ring structure at angles of up to 60° near the centre of the complex. The dip angles of these beds decrease to near-normal values at 3-4 km. Some authors have proposed that the updoming event experienced by these sedimentary units may have been caused by high local gas pressures or the intrusion of a shallow magma body (de Wet, 1975; Verwoerd, 1990). The Saltpeterkop complex is also associated with regional fracture systems, as documented by Newton (1987) and Chevallier (1997).

As mentioned earlier, the Saltpeterkop carbonatite complex includes numerous dykes, sills, irregular intrusions, as well as satellite diatremes and sub-volcanic pipe-like features containing a variety of intrusive and volcanic igneous rocks. These include (i) carbonatites, (ii) potassic trachytes, (iii) olivine melilitites and ultramafic lamprophyres (de Wet, 1975; Marageni, 2018). The carbonatite and potassic trachyte rocks are most abundant, whereas the olivine melilitites and ultramafic lamprophyres are the least abundant and are also the most primitive rock types associated with the complex. The latter, more primitive, rock types are believed to be the result of low-degrees of partial melting of a carbonated, likely phlogopite-bearing mantle source (Marageni, 2018). In a few localities, such as the Silver Dam breccia pipe (de Wet, 1975), a variety of xenolith and megacrysts occur. The Silver Dam breccia pipe (Fig. 2.1) is located on farm Matjesfontein, 3 km west of the Salpeterkop peak and is comprised of a 20 metres diameter satellite with an ultramafic lamprophyre host rock. The Silver Dam serves as the primary source for most of the megacrysts sampled and analysed in this study.

Figure 2.1: Photo taken of the Silver Dam breccia pipe located on farm Matjesfontein, 3 km west of the Salpeterkop. The prominent Salpeterkop peak can be seen in the background (to the east).

2.1. Western Cape olivine melilitite province

Five main mafic/ultramafic alkaline igneous rock localities of Late Cretaceous to Paleogene age form a 360 km long, roughly north south oriented linear feature extending south from the continental shelf east of Cape Agulhas, through the Western Cape near the towns of Robertson and Heidelberg, and into the southwestern most Northern Cape near the town of Sutherland (Fig. 2.2). Although these features are separated by tens to more than 100 km, they have been proposed to constitute a single age-progressive magmatic lineation (Dingle and Gentle, 1972; Duncan et al. 1978). Janney et al. (2002) termed this linear magmatic feature the "Western Cape olivine melilitite province" and demonstrated that these igneous rocks show regular geochemical variations that appear to correlate with lithospheric thickness. The localities of which the Western Cape melilitite province is comprised are: (a) alkali basalts and trachytes dredged from the Alphard Banks southeast of Cape Agulhas (Dingle and Gentle, 1972) dated at 58 ± 2.4 Ma, two main subvolcanic pipe-like features near the towns of (b) Robertson and (c) Heidelberg dated at 64 ± 1 and 63 ± 1 Ma, respectively (Duncan et al. 1978), along with a number of smaller, undated satellite pipes; (d) the Sutherland Commonage olivine melilitite dyke/sill complex, in the town of Sutherland, dated at 75 ± 3 Ma using the whole-rock K-Ar technique by Duncan et al. (1978) and also dated at 66 ± 1 Ma by the Rb-

Sr technique on groundmass phlogopite separates (K.S. Viljoen, unpublished data reported by Phillips et al. 2000); finally, (e) the Saltpeterkop complex dated at 73 ± 3 Ma by the K-Ar technique on a phlogopite macrocryst (Duncan et al. 1978). A later study by Malarkey et al. (2010) determined the age of the M5 olivine melilitite plug using high-precision Rb-Sr analysis of mineral separates and this yielded an age of 76.5 ± 3.3, within uncertainties of the age determined by Duncan et al. (1978). The southward progression of magmatism in the Western Cape melilitite province, of about 19 km/y is similar in magnitude to the estimated motion of the African plate at this time, although differing in direction by 20-30° (e.g. O'Connor and Jokat, 2015), these five alkaline magmatic features could plausibly be explained as representing products of a mantle hotspot (although one that was not entirely motionless in the mantle reference frame) as the southernmost part of the African plate passed over it.

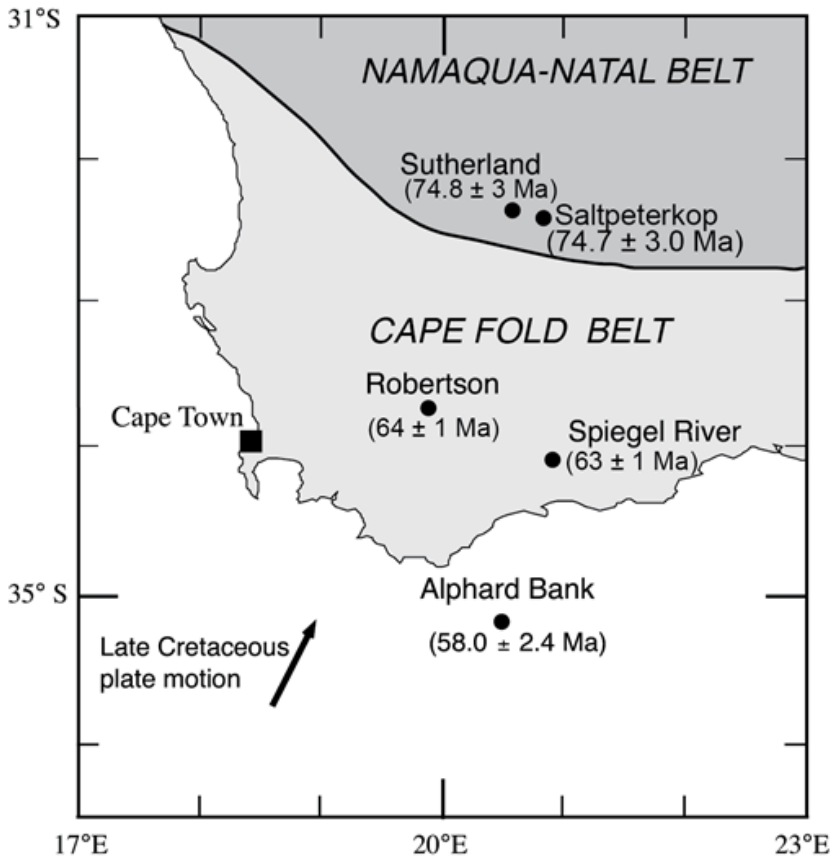

Figure 2.2: Map of the Western Cape melilitite province showing its five main dated localities. Age data from Dingle and Gentle (1972), Duncan et al. (1978) and Malarkey et al. (2010).

2.2. Rock types of the Salpeterkop Complex

Major and trace element study by Marageni (2018) revealed that the mantle beneath the complex likely experienced infiltration of hydrous, carbonated melts which resulted in metasomatism and subsequent mineralogical changes of the local lithospheric mantle (e.g., Lee and Wyllie, 2000). Heating and low-degree partial melting of this metasomatised lithospheric mantle would have generated hybrid silicate-carbonate magmas, some of which are likely responsible for the dykes and diatremes of the olivine melilitite and ultramafic lamprophyre rocks found throughout the complex (Marageni, 2018). Some of the hybrid silicate-carbonate magmas emplaced at depth experienced fractionation of dense mafic silicate minerals, leaving the melts significantly more carbonate-enriched. It is from this residual melt that the carbonatitic rocks of the complex likely crystallised.

The fourth major rock type found in the complex, the potassic trachytes, have been suggested to be the result of partial melting of continental crust that has undergone fenitisation or metasomatism. This chemical alteration of the crust was presumably caused by the interaction of the crust with a hydrous, potassic carbonatitic fluid that immiscibly separated from a carbonatite magma (Marageni, 2018). This also likely heated and lowered the solidus temperature of the crust, increasing its ability to melt.

2.3. Megacrysts of the Salpeterkop Complex

Megacrysts may be genetically related to their host rock, having crystallised from the melt parental to their igneous host rock, in which case they may essentially represent large phenocrysts, or, in contrast, they can be xenocrystic (i.e. completely unrelated to their host rock), having become entrained in a foreign magma body during its ascent to the surface. However, it is also possible for megacrysts to be related to their host magmas, but not strictly cognate, if they form as early crystallisation products of upper mantle melts that have undergone significant reaction with wallrock during ascent to the surface. The megacrysts may have been in equilibrium with the magmas prior to this extensive interaction but may not be in equilibrium with the magma that erupts at the surface. Such a process has been envisioned to occur in kimberlite megacrysts (Bell and Moore, 2004).

The study undertaken here represents the first attempt to provide a detailed description of megacrysts called from the Salpeterkop complex, in terms of their major, trace element and isotopic compositions. The megacrysts associated with Salpteterkop include monomineralic grains of clinopyroxene (mainly diopside), amphibole (mainly pargasite and kaersutite), ilmenite and mica (phlogopite). In some rare instances the megacrysts were found to contain inclusions of other minerals (i.e. calcite and/or dolomite). Additionally, polymineralic ultramafic xenoliths were recovered that are composed of varying proportions of these same phases (primarily diopside ± kaersutite ± phlogopite).

3. Overview of megacrysts

In nearly all cases, megacrysts are the products of high-pressure crystallisation of mafic alkaline melts (Irving, 1974). This view has been supported by other researchers (i.e. Green and Hibberson, 1970) based on high-pressure experimental results on alkali basaltic magmas. From their results they concluded that megacrysts of clinopyroxene, amphibole and phlogopite are near-liquidus phases of many alkaline magmas at upper mantle to lower crustal pressures. However, a genetic relationship between the megacrysts and their host rocks is not necessarily required and, in some cases,, they may have a completely different provenance, crystallising from one alkaline mafic melt (i.e. as pegmatitic veins) prior to being disrupted and incorporated in a different magma (Schulze, 1987; Shaw and Eyzaguirre, 2000).

3.1. Kimberlitic megacrysts

Kimberlites serve as the primary source of megacrysts in southern Africa. High-temperature subcalcic pyroxene and pyrope garnet are among the most commonly found phases in kimberlite megacryst suites, attesting to their deep, high-pressure and -temperature origin. Several studies (e.g. Davies et al. 2001; Merry and le Roex, 2007) have suggested that megacrysts and their host kimberlite are out of equilibrium and have a non-cognate relationship. It has been proposed that kimberlitic megacrysts have an origin related to proto-kimberlitic magmas and likely crystallise near the base of the continental lithosphere, after the megacryst parent magma interacted with the lithospheric mantle and metasomatised (Gurney and Harte, 1980). Despite this interaction, kimberlitic megacrysts often record the deep mantle signatures from which they formed, and as such, provide us with the unique opportunity to better understand the innerworkings of deep mantle processes (Kramers et al. 1981 and Davies, 2001).

3.2. Alkaline basalt megacrysts

Megacrysts have also been found associated with many other alkaline magma types, such as alkaline basalts, nephelinites, melilitites and ultramafic lamprophyres (Liotard, 1988; Schulze, 1987; Shaw and Eyzaguirre, 2000). These are easily distinguishable from kimberlitic megacrysts as they crystallise at lower temperature and pressure conditions, resulting in different suites of

minerals with different compositions to those from kimberlites. According to Schulze (1987) alkaline basalt megacrysts in particular tend to be richer in Al, Fe and Ti, and poorer in Cr. Examples of non-kimberlitic megacryst localities in southern African include (i) ultramafic lamprophyres of the Grunau/Kainab alkaline province of southern Namibia (Miller, 2008) and (ii) the Salpeterkop complex of the Western Cape melilitite province, with the latter representing the area of focus in this project. In these localities, the high temperature subcalcic clinopyroxene, and garnet phases commonly seen in the kimberlitic suite are absent and have been replaced with phases such as amphibole, possibly a consequence of the relatively shallower depth of the generation of the melilitites and lamprophyric magmas at Salpeterkop which are likely parental to the megacrysts. The Salpeterkop megacryst suite does also include both phlogopite and ilmenite megacrysts, which are also seen in kimberlites.

3.3. Examples of megacryst localities

3.3.1. Massif Central

The Massif Central, France is a megacryst bearing, continental intraplate alkaline volcanic field, that has been used in this project for comparison the SPKC megacryst suite. The Massif Central includes rocks such as basanites, alkali basalts and hawaiites (Liotard, 1988). The clinopyroxene megacrysts from Massif Central display a broad range of magnesium numbers, which were interpreted as suggesting different source melts for the megacrysts (Woodland and Jugo, 2007). Woodland and Jugo (2007) calculated the Fe/Mg ratio of the melt believed to be in equilibrium with clinopyroxene megacrysts and subsequently compared this to the basanitic lavas hosting the megacrysts. Their findings suggested that the megacrysts are non-cognate, being rather xenocrystic in nature. The geobarometer of Nimis and Ulmer (1998) applied to these samples yielded pressures of 0.27-1.3 GPa (≈ 8-39 km), suggesting that the crystallisation of clinopyroxene megacrysts began near the Moho and ceased at upper crustal depths.

3.3.2. West Eifel volcanic field

The West Eifel volcanic field, Germany, is another well-described megacryst locality. The volcanic field contains alkaline volcanic rocks such as leucitite, nephelinite and basanite, many of which host megacryst phases of clinopyroxene, phlogopite and pargasite amphibole (Mertes and Schmincke, 1985). Studies of the compositions of these megacrysts revealed the existence of three distinct groups of megacrysts (types I, II and III), each group having crystallised from a distinct magma composition (Shaw and Eyzaguirre, 2000). The first group is comprised entirely of clinopyroxene, the second of clinopyroxene, pargasite and phlogopite and the third group, again, solely of clinopyroxene. P-T estimates for the various groups reveal crystallisation pressures ranging from lithospheric mantle to crustal depths beneath the Eifel region (Shaw and Eyzaguirre, 2000). Textural and compositional characteristics shows a cognate origin of the megacrysts with their host magmas, with the megacrysts representing high-pressure crystallisation products of their respective hosts. It was established that the type II clinopyroxene and amphibole megacrysts crystallised in equilibrium.

3.4. Volatile and incompatible element behaviour in megacrysts

Incompatible elements refer to elements that do not readily substitute into the crystal structure of most mantle or major rock-forming minerals in igneous rocks because of their ionic radius, and/or charge. Some of these incompatible elements (i.e. are those with large ionic radius but small charge such as the alkali and alkaline earth elements) are easily mobilised by fluids. The main incompatible element groups are the rare earth, large iron lithophile and high field strength elements, transition metals (e.g. V and Sc) and the heavy elements (Pb, Th and U). Volatiles (which include H, H_2O, Cl and F) are also often highly incompatible in crystallising mineral phases.

3.4.1. Degassing

Volatiles play key roles in the evolution of magmatic systems, despite their low abundance within the solid Earth. Certain volatiles, primarily H_2O and CO_2, have the potential to affect the viscosity and solidus temperature of the mantle, and by extension, affect mantle

convection, partial melting and mantle differentiation. Studies performed on isotopes of oxygen and hydrogen found in various reservoirs (e.g. mantle xenoliths, megacrysts, melts, hydrosphere) can provide constraints on the evolutionary history of the Earth's mantle, as well as the behaviour and cycling of water beneath the Earth's surface (e.g. Bell and Ihinger, 2000; Schulze et al, 2001). Hydrous mineral phases, such as amphiboles and micas, in mantle-derived mafic alkaline rocks, xenoliths and megacrysts, provide an important means to trace the flux of water in the Earth's mantle (e.g. Boettcher and O'Neil, 1980). These materials, however, can be susceptible to late-stage processes such as degassing and alteration that can overprint their initial volatile contents (and H isotope ratios).

Degassing refers to the loss of volatile species, such as water (hydroxyl groups). While this term is most commonly applied to magmas, volatile-bearing minerals, including megacrysts, can also experience degassing (Demény et al. 2006). This volatile loss from minerals most often occurs in response to a decrease in pressure of the system. Degassing affects both the volatile budget and H isotopic composition of the hydrous minerals and occurs through two main processes: (1) dehydrogenation and (2) dehydration.

Dehydrogenation

Dehydrogenation refers to the loss of hydrogen (H^+) from the hydroxyl crystallographic site in hydrous minerals. A reaction between ferrous iron (Fe^{2+}) and hydroxyl groups, results in the oxidation of ferrous to ferric iron (Fe^{3+}) and the loss of H^+ to maintain charge balance.

Owing to the loss of hydrogen from the mineral being a mass-dependent process, evidence of dehydrogenation should be preserved in hydrogen isotope ratios recorded in the megacrysts (Demény et al. 2005). The dehydrogenation process is accompanied by the preferential loss of the lighter hydrogen isotope (protium - ^1H isotope), coupled to a decrease in H_2O content, as well as an increase in the Fe_2O_3/FeO^{tot} ratio (Kyser and O'Neil, 1984).

The equation below summaries the reaction via which dehydrogenation proceeds:

$$Fe^{2+} + OH^- = Fe^{3+} + O^{2-} + 1/2H_{2(g)}$$

Dehydration

Dehydration refers to a release of H_2O as water vapour from the structure of a mineral. Hydroxyl anions (OH^-) present in the mineral combine to form water molecules. The charge-neutral nature of the newly formed H_2O means that it cannot bond to anything and can be subsequently removed from the mineral. This has the effect of destabilising the mineral, leading to its eventual breakdown. Excess oxygen anions (O^{2-}) that do not contribute to the formation of water molecules remain bonded to the mineral's hydroxyl crystallographic site.

In contrast to dehydrogenation, dehydration involves the preferential loss of the heavier hydrogen isotope (deuterium - D or ^2H) (Kyser and O'Neil, 1984). Additionally, the oxidation of iron that occurs in dehydrogenation is not required for the for the removal of H_2O.

The equation below summarises the reaction by which dehydration proceeds:

$$2OH^- = O^{2-} + H_2O_{(g)}$$

3.4.2. Mantle metasomatism

Metasomatism is the process of chemical change in a rock (which is due to purely chemical changes or changes in modal mineralogy) caused by introduction of a mobile melt or fluid phase, which results in chemical, and possibly mineralogical, changes in the affected regions, relative to their pre-metasomatised states. This has the effect of changing the bulk composition of the rock undergoing metasomatism, and often causing a decrease in the solidus temperature of affected rocks, making metasomatism one of the processes that drives melting within the mantle. Metasomatism can occur through two processes, infiltration and diffusion (Yardley, 2011). Infiltration is the result of fluid pressure gradient which makes it possible for metasomatic agents (melts and/or fluids) to move from one area to another mainly along mineral grain boundaries. Solid-state diffusion is the slower process by which the compositions of mineral edges and interiors attempt to equilibrate in the presence of a gradient in chemical potential.

Metasomatism often involves volatile-rich (e.g. carbonatitic or hydrous) fluids or melts that interact with, and infiltrate, a region or rock in a pervasive manner. Under mantle

conditions, it becomes increasing difficult to distinguish between melts and volatile-rich fluids, owing to these metasomatic agents behaving in a miscible manner.

Dawson (1980) showed that mantle metasomatism results in two main effects. The first, more obvious, effect is indicated by the addition of new mineral phases or a marked change in the modal proportions of preexisting minerals in a mantle rock and is commonly referred to as "modal" metasomatism. These phases typically include, but are not limited to, clinopyroxene, amphibole and phlogopite. The second, less obvious, type of metasomatism involves the alteration of trace element abundances and isotopic characteristics of already existing phases, through melt-rock or fluid-rock interaction and equilibration and is more formally known as "cryptic" metasomatism.

4. Sampling and Analytical techniques

Samples analysed in this study were collected during two field excursions to the Salpeterkop complex during the months of June-July (2017) and April (2018). Sample preparation and analysis undertaken for this project were performed exclusively in the Department of Geological Sciences, University of Cape Town.

4.1. Sample locations

Unpublished field maps provided by Luc Chevallier were the primary guiding tools used to navigate the various sample localities of the complex. The Silver Dam breccia pipe (32° 29' 14" S, 20° 48' 19" E) located on Farm Matjiesfontein, 3 km south-west of the main peak, is the primary source of megacryst and xenoliths associated with the complex and the main source of material sampled for this investigation. Along with the Silver Dam site, three other localities across the complex were visited for additional megacryst samples. These additional localities are presented in Table 4.1.

Table 4:1: List of sample information and locations for the other megacryst localities, from the Saltpeterkop Complex, other than Silver Dam

Location	Coordinates	Type	Mount name	Megacryst phases
SPKC 14	32° 29' 40" S, 20° 50' 52" E	Dyke	SPKC phl. 1	Phlogopite
SPKC 12	32° 29' 55" S, 20° 51' 59" E	Breccia/Dyke	SPKC phl. 2-3	Phlogopite
SP-367	32° 29' 53" S, 20° 51' 01" E	Dyke	SPKC phl. 3	Phlogopite

4.2. Sample naming

A three-term naming system was implemented for the megacryst samples selected for analysis. The first term denotes the sample locality of the megacrysts. Since all were taken from the Salpeterkop complex, either SPK (Salpeterkop) or SPKC (Salpeterkop complex) was used. Samples taken from localities other than Silver Dam were mounted separately, as

described in Table 4.1. Following this, a middle term identifies the epoxy mount in which a particular megacrysts (or fragment) is mounted. Here either "M" or "min" followed by "#" was used. The "#" is a one or two-digit number. Mounts that makes use of "min" are comprised entirely of one mineral phase, with min being a place holder for the specific mineral type i.e. amph, while those with "M" (for mount) have at least two mineral phases. The third and final term "G#" is simply used to differentiate between specific grains mounted on any given epoxy mount. Examples of named mounts include SPKC amph1 G5 or SPK M6 G7.

The xenolith samples analysed in this study were cut in half and mounted as un-disaggregated rock samples, with maps of the mounted sample made to differentiate and navigate between the various grains of interest. A three-term naming system was also implemented for the xenolith epoxy mounts, with the first term being "SPK". The middle term, "XENO#" identifies the epoxy mount in which a particular xenolith sample is mounted. The final term "G#" again differentiates between specific grains mounted on any given epoxy mount and pertains to an individual grain within an un-disaggregated xenolith sample. An example of a named xenolith mount includes: SPK XENO 1 G24.

Some xenolith samples were thin sectioned in-situ within volcaniclastic breccia samples. For these, a sample prefix of "SD1" was used, as these sourced for the Silver Dam locality, followed a letter. Lastly a "G#" value was giving to each specific grain selected for analysis. An example of the naming procedure applied to the thin sections is as follows: SD1A 12 or SD1B 3. No trace element, stable isotope or radiogenic isotope data was collect for the xenolith samples, with the exception of the the clinopyroxenitic samples where trace element data was collected.

4.3. Sample Description

As mentioned earlier, megacrysts are typically mantle-derived, monomineralic nodules with dimensions exceeding 10 mm. Other mantle-derived products include mantle xenoliths, which have also been sampled from the Salpeterkop complex. These xenoliths appear to be cumulate in nature. To date, no peridotite xenoliths have been recovered from Salpeterkop. The various megacrysts and xenoliths of the Salpeterkop complex are comprised of the same

mineral phases which include: clinopyroxene, amphibole, ilmenite and phlogopite, the characteristics of which are described below. Minerals comprising the megacryst suite were sectioned and classified based on their colour, size, mineralogy, texture and chemical composition.

4.3.1. Clinopyroxene

In hand specimen the clinopyroxene megacrysts vary in colour from a dark green to green-black (Fig. 4.1). Clinopyroxene megacrysts have the largest average grain size (20 mm) as well as the largest range of grain sizes (ranging from 10 to 70 mm) of all the megacryst phases associated with the complex. The grains display an elongated prismatic crystal habit. Several of the clinopyroxene megacryst samples show numerous inclusions calcite, however no optical or chemical difference was observed between samples that contain inclusions and those that do not. Table 4.2 below summarises the collection of clinopyroxene megacrysts selected for the various analytical techniques applied in this study.

Table 4:2: Breakdown of clinopyroxene analysis

Analysis	No. of grains analysed
Major elements	139
Trace elements	139
Stable isotopes	-
Radiogenic isotopes	2

Figure 4.1: Image showing examples of the size and appearance of the clinopyroxene megacrysts sampled from Silver Dam. The largest marks of the scale bar indicate centimetres.

4.3.2. Amphibole

The amphibole megacrysts grains are dark brown to black in colour, making them easily confused with the clinopyroxene grains (Fig. 4.2). Many amphibole megacrysts do, however, exhibit characteristic 60°/120° cleavage. Sampled megacrysts of this type are, on average 20 mm, in length and never exceed 30 mm. The samples showing the best cleavage tend to be much smaller (~ 15 mm) and appear to have the least amount of alteration and/or weathering to the surface of the grain. The amphibole megacrysts have also been found to have inclusions, which include a purely Fe-oxide mineral (haematite and/or magnetite) as well as calcite. Table 4.3 below summarises the collection of amphibole megacrysts selected for the various analytical techniques applied in this study.

Table 4:3: Breakdown of amphibole analysis

Analysis	No. of grains analysed
Major elements	91
Trace elements	45
Stable isotopes	10
Radiogenic isotopes	8

Figure 4.2: Image showing examples of the size and appearance of the amphibole megacrysts sampled from Silver Dam. The largest marks of the scale bar indicate centimetres.

4.3.3. Phlogopite

Phlogopite megacrysts are subhedral and show a range in maximum dimensions from 10 to 40 mm. The phlogopite megacrysts are brown-red to orange-brown in colour. Fresh phlogopites have an even, dark colouration and are present as tight mica books up to 15 mm in thickness, whereas less fresh megacrysts show discoloured margins and often display flakiness around the rims (Fig. 4.3). Table 4.4 below summarises the collection of phlogopite megacrysts selected for the various analytical techniques applied in this study.

Table 4:4: Breakdown of phlogopite analysis

Analysis	No. of grains analysed
Major elements	37
Trace elements	37
Stable isotopes	10
Radiogenic isotopes	4

Figure 4.3: Image showing examples of the size and appearance of the phlogopite megacrysts sam pled from Silver Dam. The largest marks of the scale bar indicate centimetres.

4.3.4. Ilmenite

The ilmenite megacrysts are silver-black in colour with a dull metallic lustre on the exterior surfaces of the grains. The grains are blob-shaped and well-rounded, with dimensions that are generally less than 10 mm (Fig. 4.4). A few unusually large megacrysts have however been found, displaying dimensions on the order of up to 30 in length. Table 5 below summarises the collection of ilmenite megacrysts selected for the various analytical techniques applied in this study.

Table 4:5: Breakdown of ilmenite analysis

Analysis	No. of grains analysed
Major elements	61
Trace elements	61
Stable isotopes	-
Radiogenic isotopes	2

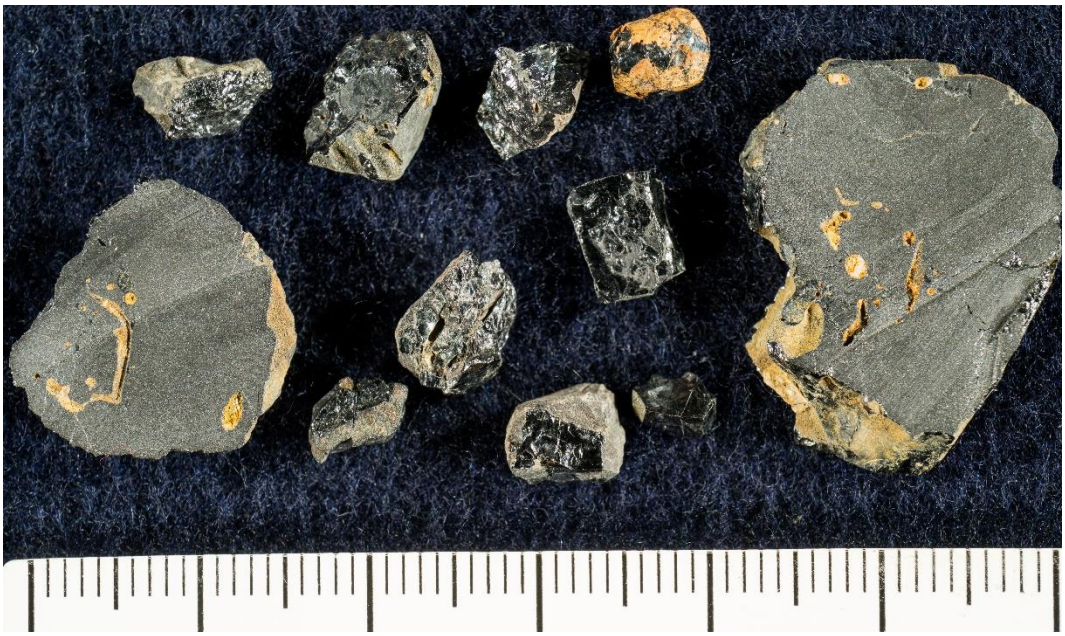

Figure 4.4: Image showing examples of the size and appearance of the ilmenite megacrysts sampled from Silver Dam. The largest marks of the scale bar indicate centimetres.

4.3.5. Xenoliths

The type 2 mafic xenoliths associated with the SPKC are comprised of the same phases that make up the megacrysts but vary in abundance and mineral combinations from xenolith to xenolith. The xenoliths range in size from 40 to 100 mm, averaging 60 mm. They tend to be well-rounded to ellipsoidal in shape, a possible result of abrasion during transport from depth to eruption at surface (Fig. 4.). Table 4.6 below summarises the minerals analysed from selected xenolith samples for major and trace elements. The xenoliths were named according to the dominant minerals present, with estimates of mineral abundance determined through point-counting.

Table 4:6: Minerals analysed in SPKC sampled xenoliths

Mineral type (major ± trace)	No. of grains (125)
Clinopyroxene	53
Amphibole	31
Ilmenite	27
Phlogopite	7

Figure 4.5: Image showing examples of the size and appearance of the xenoliths sampled from Silver Dam. The largest marks of the scale bar indicate centimetres.The top 2 samples are clinopyroxenitesand the bottom 2 MAID. The dark minerals are mainly clinopyroxene and amphibole with minor amount of phlogopite and ilmenite, while the light mineral is calcite.

Clinopyroxenite type

Xenoliths of this type are comprised almost entirely of subhedral clinopyroxene grains ($>$ 95 %) that vary in size from 0.2 to 1.0 mm (Fig. 4.5). Electron microprobe images reveal that 120° triple junctions exist between the clinopyroxene grains in the xenoliths, and that some of these grains display good cleavage. The grains lack any reaction-rim or disequilibrium

textures. Calcite occurs between the clinopyroxene grains, but calcite can also be found as inclusions in several of the clinopyroxene grains.

Clinopyroxene-amphibole-phlogopite-ilmenite type

The xenoliths of this type are typically made up of 60-80% clinopyroxene, 20-30% amphibole, 0-15% phlogopite, 0-5% ilmenite. For simplicity sake these samples are abbreviated as MAID for the mineral types that constitute them (Mica-Amphibole-Ilmenite-Diopside) (Fig. 4.5). The clinopyroxene, phlogopite and amphibole grains are subhedral in nature, while ilmenite appears anhedral (blob-like). The majority of the phlogopite grains analysed were cut perpendicular to their cleavage planes, and as such were easily identifiable, and some of these grains were found to have inclusions of clinopyroxene. A handful of the amphibole grains identified exhibited the characteristic 60°/120° cleavage.

The clinopyroxene and amphibole grains show no evidence of (i) overgrowth (based on visual appearance), (ii) veining or (iii) reaction textures, that would suggest that the grains are not primary or had experienced significant disturbance during exhumation. Some amphibole grains do however contain inclusions of clinopyroxene minerals. The ilmenite grains appear to overgrowth grain boundaries between clinopyroxene and amphibole.

Xenolith samples SD1A and SD1B were cut as thin sections (as opposed to epoxy mounts) and, as such, petrogenetic descriptions could be made of these samples. These xenolith samples are comprised entirely of clinopyroxene and amphibole grains.

SD1A

- The clinopyroxene makes up roughly 35% of the SD1A xenolith sample. These grains appear cream to green in plane polarised light (PPL) and show weak green pleochroism. In cross polarised light (XPL), 2nd order blue-pink, green, yellow-orange interference colours can be observed (Fig. 4.6a-b). Grains range in maximum dimension from 0.25 to 0.5 mm. These grains also display an equilibrated (i.e. mosaic-like) texture and show 120° triple junctions, comparable to what is observed for the clinopyroxenite xenolith samples. A tiny proportion of the grains show twinning and others rarely show exsolution lamellae.

- Amphibole accounts for approximately 60% of the xenolith sample. In PPL, grains show green to brown and colourless to dark brown colours. In XPL the grains show 1st to 2nd order pink-yellow and green-blue colours (Fig. 4.6a-b). Grains show well-defined 60°/120° cleavage and range from 0.5 to 1.5 mm. A small proportion of the amphibole grains contain inclusions of clinopyroxene.
- Opaque mineral (> 5%) – Elongated grains ranging in length from 0.1 to 0.5 mm. They are found overgrown on numerous grains of both clinopyroxene and amphibole. EMP analysis reveals that the grains are almost entirely of Fe-oxide (magnetite).

SD1B

- Clinopyroxene accounts for 80 % of the SD1B sample. Grains are tan to green in PPL, showing weak pleochroism (Fig. 4.6a). 2nd order blue-pink, green, yellow-orange interference colours can be seen in XPL (Fig. 9b). Grains vary from 0.5 to 2.0 mm in length, and those with cleavage display inclined extinction. A polyhedral (mosaic) texture was also observed, as well as 120° triple junctions between grains. Inclusions of calcite occur in many the clinopyroxene grains. These inclusions are small, anhedral and show lamellar twinning in cross-polarised light with pastel (5th to 6th order) interference colours.
- Amphibole makes up roughly 20 % of sample SD1B, with grains showing green to brown and cream to dark brown colours in PPL (Fig. 4.6c). 1st to 2nd order pink-yellow and green-blue interference colours in XPL (Fig. 4.6d). Grains show well-defined 60°/120° cleavage and are on average approximately 1.0 mm in length. Several grains were cut perpendicular to the optic axis display at least one cleavage plane.
- Opaque mineral (> 1%) occurs as round blobs overgrown on grains of clinopyroxene and amphibole, never exceeding dimensions of 0.2 mm. EMPA reveals these grains to be magnetite.

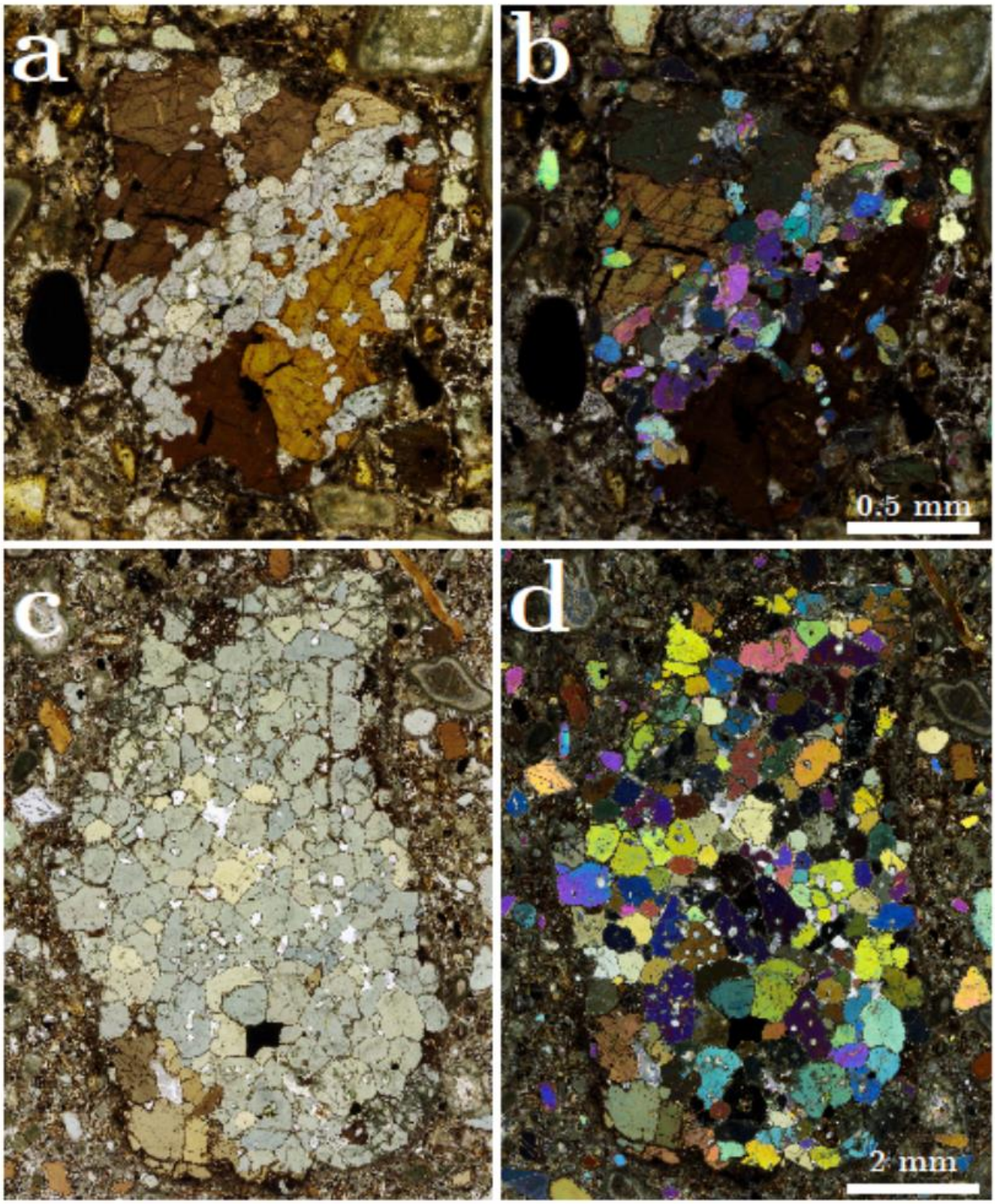

Figure 4.2: Photomicrograph of xenoliths taken from the Silver Dam locality. SD1A in PPL (a) and XPL (b) and SD1B in PPL(c) and XPL (d) show grains of clinopyroxene and amphibole and an opaque mineral, which is most likely magnetite.

5. Analytical techniques

Megacrysts were selected for analysis based on their size as well as their degree of freshness, with the largest and least altered megacrysts given priority for analysis. The freshness of the megacrysts was judged by the amount of alteration/weathering (e.g. presence of discolouration or variations in luster indicating mineral replacement) visible on the exterior of the grains, and the degree to which the grains showed clean, reflective cleavage planes or fractures on broken surfaces.

5.1. Major and Trace element analysis

The grains were broken into fragments, with one interior fragment per megacryst mounted in 25 mm diameter epoxy discs. This approach is justified because (1) the megacryst homogeneity has been tested by mounting a few larges megacrysts (cut in half) and doing transects with the EPMA and (2) because other studies of megacrysts have shown that in nearly all cases they are homogeneous in terms of major and trace element composition (e.g Hops et al., 1986; Kostrovitsky et al., 2004; Howarth, 2018). On average 20 or so mineral fragments were place on a given mount. These mounts were subsequently used for both major and trace element analyses on the megacrysts.

5.1.1. Major element analysis

The major element compositions of the grains were analysed using a JEOL Superprobe JXA-8100, at the Department of Geological Sciences, University of Cape Town (Cape Town, South Africa), using the ZAF correction method. For all megacrysts and standards analysed, the following operating conditions were used: an acceleration voltage of 15 kV, a beam current of 20 nA, a beam diameter 5 μm and counting times for the elements of 10 seconds on peak and 5 seconds on the background. The major oxides measured include: SiO_2, TiO_2, Al_2O_3, Cr_2O_3, FeO, MnO, MgO, CaO, Na_2O, K_2O, F and Cl (see Table 7 below).

Two to four spot analyses were performed on every individual megacryst fragment, with the number of spots being dependent and proportional to the size of the megacryst fragment mounted i.e. more spots were measured on larger fragments. Several natural and synthetic mineral standards were used for calibration, with repeated analyses after every 10 unknown

analyses, all to monitor and reduce the risk of instrumental drift. The standards for the analysis of the various megacryst minerals are given in Table 5.1 below.

Table 5:1: List of standards used for the major oxides

Element	Clinopyroxene	Amphibole	Mica	Ilmenite
SiO_2	CpxJJG	K-H	K-H	K-P
MgO	CpxJJG	K-H	K-H	CHRO
MnO	RHOD	RHOD	RHOD	RHOD
CaO	CpxJJG	K-H	K-H	K-P
Al_2O_3	K-P	K-H	K-H	CHRO
TiO_2	RUT	RUT	RUT	Ilm
FeO	K-P	K-H	K-H	Ilm
Cr_2O_3	CHRO	CHRO	CHRO	CHRO
Na_2O	K-H	K-H	K-H	-
K_2O	K-H	K-H	K-H	-
F	-	SrF_2	SrF_2	-
Cl	-	-	SCAP	-

- K-H: Hornblende (Kakanui) HNMH143965
- RHOD: Rhodochrosite (RHOD 320/045)
- CHRO: Stillwater Chromite 52NL11
- SrF_2: Strontium Fluoride
- RUT: Rutile (Rutile 288/133)
- CPX JJG: Clinopyroxene JJG 1424 (122/038) Thaba Putsoa websterite
- K-P: Pyrope, Kakanui, New Zealand
- Ilm: Ilmenite, Ilmen Mountains. USSR
- SCAP: Scapolite (Meionite), Brazil

5.1.2. Trace element analysis

In situ trace-element analyses using laser-ablation inductively coupled plasma mass spectrometry (LA-ICP-MS) was also performed on the mounted megacryst fragments. LA-ICP-MS provides high-sensitivity and high precision quantification of elements with a spatial resolution as small as 50 µm. The data were acquired using a Thermo-Fisher X-Series II quadrupole ICP-MS coupled with a New Wave UP213 solid-state UV laser ablation system. A beam diameter of 75µm was used to ablate the clinopyroxene, amphibole and ilmenite grains, while operating at 10 Hz. In the case of phlogopite, where grains were mounted with their cleavage oriented perpendicular to the polished mount surface, beam size was reduced to a diameter of 65µm, while keeping the other operating conditions unchanged. Helium (He) was used as the carrier gas, which was joined to an Argon (Ar) gas line downstream of the laser cell. The primary calibration standards applied are synthetic glass standards of the National Institute of Standards and Technology (NIST 610 and NIST 612), and an isotope of Si was used for internal standardisation, which were used for all minerals.

Two to four spots were analysed on each mounted megacryst grain fragment. Additionally, in-house mineral standards (San Carlos augite, San Carlos amphibole, Monastery ilmenite ROM-264 IL-52 and UINT-11 phlogopite) were analysed systematically, after every ten to twelve unknown analyses, to monitor instrumental drift. LA-ICP-MS was used to measure the concentration of the following trace elements: Sc, V, Cr, Ni, Rb, Sr, Y, Zr, Nb, Ba, Hf, Ta, Pb, Th, U, and the rare earth elements (REE; La - Lu).

A subset of megacryst samples were analysed for their Sr-Nd-Pb isotopic compositions by conventional elemental separation and analysis by multicollector ICP-MS and parent-daughter elemental compositions by solution quadrupole ICP-MS. The latter was used to calculate the initial Sr, Nd and Pb isotope compositions of the megacrysts at the time of their eruption. Amounts between 25 and 500 mg of the freshest picked megacryst fragments per sample (typically 90 mg for amphibole, 180 mg for clinopyroxene and 30 mg for phlogopite) were weighed out into teflon beakers, rinsed with ultrapure MilliQ water and subjected to a leaching procedure to remove possible secondary minerals along cleavage planes and fractures that could not be removed via careful picking. The main leaching procedure used (for amphibole and clinopyroxene) involved leaching overnight in 6 M HCl at 75 °C, rinsing in ultrapure water

then leaching for 15 minutes in 50% 6 M HCl:concentrated HF, followed by three ultrapure water rinses. The leaching procedure for phlogopite was similar, except that 2.5 M HCl was used instead of 6 M HCl due to the more open structure of phlogopite.

Following leaching and washing with ultrapure water, the samples were dried overnight at 75°C and dissolved using 4:1 concentrated hydrofluoric:concentrated nitric acid. The digested samples were dried down and concentrated nitric acid was added to convert fluorides to nitrates. This was repeated. Then the samples were dissolved in 50% ultrapure nitric acid and split such that 80% was used for elemental separation chemistry and isotope ratio measurement of Sr, Nd and Pb isotopes and the remaining 20% was used for trace element analysis by solution ICP-MS.

Accuracy and precision were monitored through the analysis of several rock and mineral standards: Basalt, Hawaiian Volcanic Observatory (BHVO-1); Icelandic Basalt (BIR-1) and the UCT in-house mid-ocean ridge basalt glass standard V5-40-56 as well as the in house standards San Carlos augite, San Carlos amphibole and Uintjiesberg phlogopite.

5.2. Isotope analysis

5.2.1. Stable isotopes

Oxygen

Oxygen isotope analysis was performed on selected amphibole and phlogopite megacrysts using the laser fluorination method described by Harris and Vogeli (2010). The method uses a 20 W New Wave CO_2 laser, mounted on a moveable stage. Ten samples and 2 standards were placed in the highly polished, pure Ni sample holder during each run. 1-2 mg of phlogopite and 2-5 mg of amphibole were loaded into the sample holder, but in most cases 1-3 mg was used. The sample holder was subsequently placed into an oven at 110 °C for at least an hour then immediately placed into the reaction chamber, to ensure no additional moisture was absorbed. The reaction chamber was subsequently evacuated. Once the vacuum was at background level, 10 kPa of BrF_5 was expanded into the sample chamber for a period of 30 seconds, before being cryogenically removed. After further pumping, a second 10 kPa batch of BrF_5 was then left in the reaction chamber overnight. All the samples and standards were reacted sequentially and for each, when the reaction had been completed, excess BrF_5,

and free Br formed by dissociation were frozen, and the remaining gases passed through a KCl trap that is maintained at about 200 ℃. This ensures the removal of any F_2 that may have been produced. The gases were then allowed to expand through a stainless-steel double-U trap immersed in liquid nitrogen, and the purified O_2 collected onto a 5 Å molecular sieves contained in glass sample bottles. All glass bottle samples were then analysed using a DeltaXP dual inlet gas source mass spectrometer, housed in the Department of Archaeology at the University of Cape Town.

A garnet megacryst (MON. GT) sampled from the Monastery kimberlite pipe (Moore, 1986) is the in-house laser silicate standard employed. Details for this standard and its composition are given in Harris et al. (2000). MON. GT has a $\delta^{18}O$ value of 5.38 ‰, calibrated using the UWG-2 garnet standard of Valley et al. (1995), measured on the current laser system. In the present study, the raw collected amphibole and phlogopite data were normalised such that the average MON. GT $\delta^{18}O$ value was 5.38 ‰. The average difference in the $\delta^{18}O$ value between duplicate analyses of MON. GT run during the duration of this study was 0.12 ‰, which corresponds to a standard deviation of ± 0.15 (2σ, n=10).

Hydrogen

For hydrogen isotope measurements, the method of Vennemann and O'Neil (1993) was followed. The amphibole and phlogopite megacrysts (the same ones used for oxygen analysis) were crushed as finely as possible, with roughly 50 mg of phlogopite and 100 mg of amphibole per sample required for analysis. The powdered samples were weighed on a digital balance and added to quartz tubes, followed by quartz grains and quartz wool to prevent loss of sample under vacuum. To ensure that no additional H_2O was absorbed by the samples, the tubes containing the samples were left in an oven overnight at ~ 110 °C. Prior to pyrolysis, the powdered samples were degassed on the vacuum line at 200 °C using a hot air gun, until no change in pressure was recorded.

The samples were then heated with a propane-oxygen torch, which melted the sample. This had the effect of liberating H_2O and CO_2, which were then collected in a liquid nitrogen trap. The CO_2 and H_2O were subsequently separated from each other using an isopropyl alcohol trap (Note: the CO_2 content was too low to be analysed). The H_2O was then frozen into a closed tube with Indiana Zn and placed in a furnace. Zinc acts as reducing agent for the

quantitative conversion of H_20 to H_2 for D/H determinations. Two water standards were used to correct the raw data. The first internal water standard (CTMP2010; δD = -7.4 ‰) was used to calibrate the data to the Standard Mean Ocean Water (SMOW) scale, and the second standard (RMW; δD = -131.4 ‰) was used to correct for scale compression. The isotopic composition of the hydrogen was then measured using the DeltaXP gas source mass spectrometer. The in-house kaolinite standard (Kao) with an accepted value of -57 ‰ (Harris et al. 1999) was also analysed. Sample data were normalised so that Kao δD = −57 ‰, though in practice, this correction is small.

The voltage measurements on the mass 2 collector were recorded in order to estimate the amount of water in each sample. Exactly 2 mg of each of the water standards was analysed and the data are reported in δ notation, where $\delta = [([R_{sample}/R_{standard}] - 1)(1000)]$, where R represents $^{18}O/^{16}O$, or D/H, relative to SMOW. This process also provided the water content of the megacrysts.

5.3. Radiogenic isotopes

As described earlier, 25 to 500 mg of optically clear megacryst fragments were hand picked and checked under a microscope, with special care taken to avoid fragments that showed signs of alteration or weathering. All trace element and Sr-Nd-Pb isotope measurements were performed on the same aliquot of dissolved sample.

5.3.1. Rb – Sr Isotopes

A modified version of the chemical separation procedure outlined by Miková and Denková, (2007) was followed and from that the Sr-isotope data was obtained using one of two NuPlasma HR multicollector inductively coupled plasma mass spectrometer (MC-ICP-MS) instruments housed in the multi-collector ICP-MS facility in the Department of Geological Sciences at the University of Cape Town. The Sr was analysed as 200 ppb Sr in 0.2% HNO_3 solutions using NIST SRM987 with a $^{87}Sr/^{86}Sr$ value of 0.710255 as a reference standard. All Sr isotope data were corrected for Rb interference using the measured ^{85}Rb signal and the natural $^{85}Rb/^{87}Rb$ ratio. The Sr isotope data were also corrected for instrumental mass fractionation using the exponential law and a $^{86}Sr/^{88}Sr$ value of 0.1194.

5.3.2. Sm – Nd Isotopes

A modified version of the chemical separation procedure outlined by Miková and Denková, (2007) was also used to obtain a Nd elemental fraction. Nd isotopes were analysed as 50 ppb Nd in 2 % HNO_3 solutions using the Nu Instruments DSN-100 desolvating nebuliser. JNdi-1 was used as Nd-isotope reference standard and all Nd isotope data were normalized to a $^{143}Nd/^{144}Nd$ value of 0.512115, after Tanaka et al. (2000). All Nd-isotope data corrected for: (1) Sm and Ce interference using the measured signals for ^{147}Sm and ^{140}Ce, and natural Sm and Ce isotope abundances; and (2) instrumental mass fractionation using the exponential law and a $^{146}Nd/^{144}Nd$ value of 07219.

5.3.3. U/Th – Pb Isotopes

The lead fractions were also analysed using the same NuPlasma MC-ICP-MS instrumentation as for Sr and Nd isotope analysis. Pb was separated from the other elements using BioRad AGx1 anion exchange resin in a HBr medium. Each Pb cut was dissolved in 2% HNO_3 and spiked with thallium (Tl) for mass-bias correction using NIST997 T1. NIST981 was used as the Pb isotope reference standard and all Pb isotope data are given relative to the following values for NIST981: $^{208}Pb/^{204}Pb = 36.7219$, $^{207}Pb/^{204}Pb = 15.4963$, and $^{206}Pb/^{204}Pb = 16.9405$ (Galer and Abouchami, 1998). On-peak background measurement corrected for any Hg interference and instrumental mass fractionation was corrected using the exponential law and an assumed $^{205}Tl/^{203}Tl$ value of 2.388 for NIST997.

6. Major element geochemistry

6.1. Clinopyroxene

Megacryst data

The general chemical formula for the clinopyroxenes megacrysts that were analysed was calculated as $(Ca_{0.9}, Mg_{0.8\text{-}0.9}, Fe_{0.2}, Ti_{<0.1}, Al_{<0.2})[(Si_{1.8\text{-}1.9}Al_{0.1\text{-}0.2})O_6]$, placing them in the diopside stability field. On the pyroxene ternary plot (Fig. 6.1), the megacrysts fall within the range $Wo_{49.6\text{-}52.9}$ $En_{31.5\text{-}35.9}$ $Fs_{12.7\text{-}18.2}$.

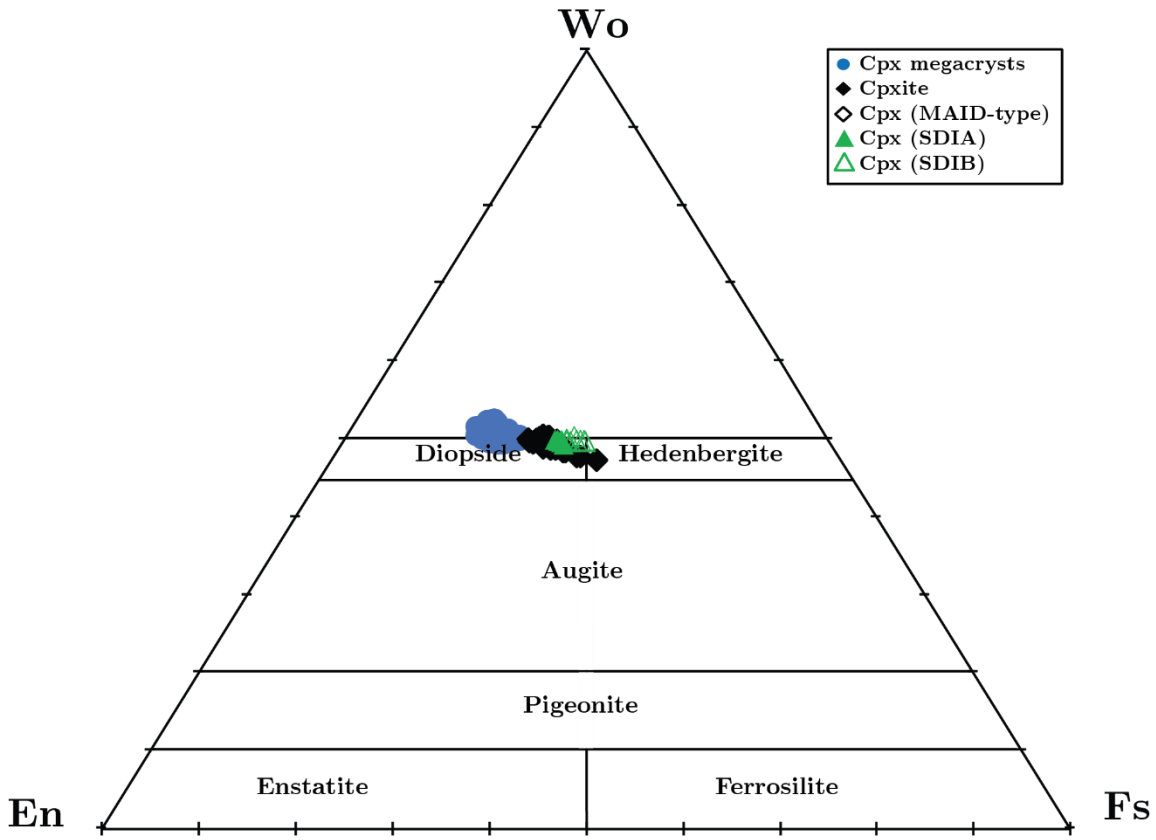

Figure 6.1: Ternary [enstatite(En)-ferrosilite(Fs)-wollastonite(Wo)] diagram used for the classification of the clinopyroxene megacrysts (blue filled circles) plotted along side clinopyroxene grains from various xenolith types associated with the complex (Morimoto et al., 1988). 2σ uncertainty for the SPKC grains are smaller than the symbols on the graph. The high Wo content (≥50%) of many clinopyroxenes is due to the presence of significant Ca-Tschermak component ($CaAl(AlSi)O_6$).

The largest clinopyroxene megacrysts, those with dimensions exceeding 50 mm, were selected to test for the presence of compositional heterogeneities in the grains, by means of core-to-rim compositional transects (Fig. 6.2). The results showed that these grains lack any

systematic chemical variations (i.e. in Mg-number) that would be indicative of compositional zoning, suggesting that these clinopyroxene grains are largely homogeneous and unzoned.

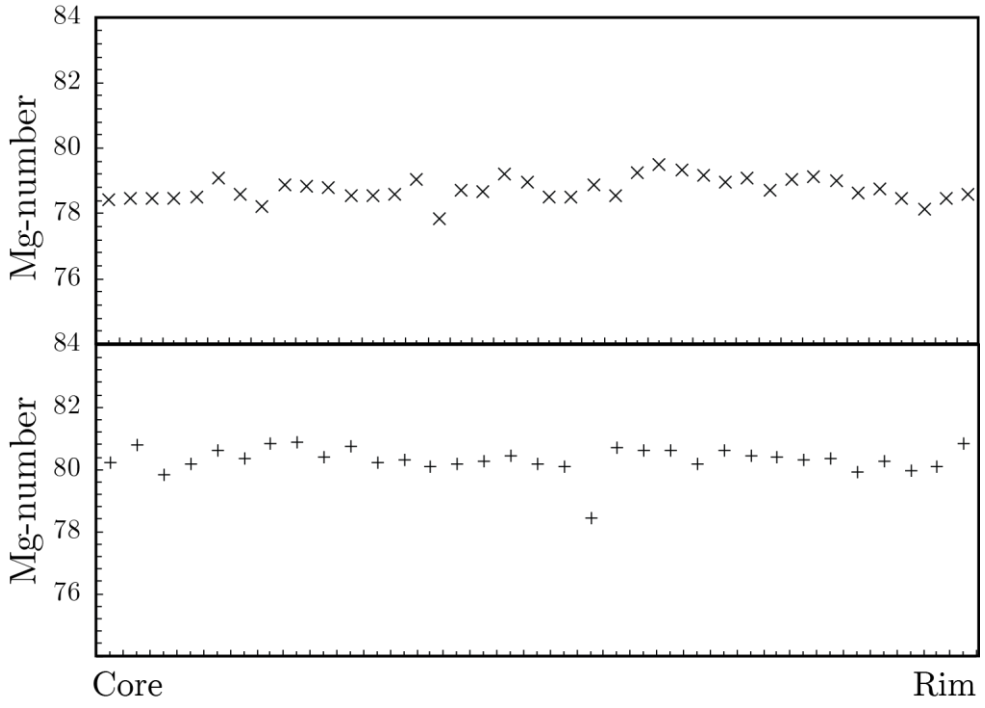

Figure 6.2: Compositional transects for 2 large clinopyroxene megacrysts(SPK cpx 1 and SPK cpx 2). These clinopyroxene megacryst transects are 29 mm long, fromcore to rim, and were used to test for compositional homogeneity within the megacrysts. 2σ uncertainty for the SPKC grains are smaller than the symbols on the graph.

As a group, the clinopyroxene megacrysts show, for most of the major oxides measured, the widest ranges in compositional variability compared to the other megacryst phases. MgO and FeO are exceptions to this and are no more heterogeneous in clinopyroxene than in other megacrysts. Na_2O (0.9 to 1.4 wt.%) is the most restricted oxide, with a range of values less than 1 wt. %, across the clinopyroxene grains analysed. CaO (20.9 to 22.6 wt. %) and TiO_2 (0.6 to 2.3 wt. %) display a range of values between 1 and 2 wt. %, FeO^{tot} (5.4 to 7.8 wt. %) and MgO (13.2 to 15.7 wt.%) between 2 and 3 wt. % and SiO_2 (47.9 to 52.4 wt. %) and Al_2O_3 (2.3 to 7.2 wt. %) showed the largest range of values across the clinopyroxene samples analysed, with values ranging from between 4 and 5 wt. %. Mg-number $(\frac{Mg}{(Mg+Fe^{2+})} \times 100)$ and Ca-number $(\frac{Ca}{(Mg+Ca)} \times 100)$ values for the clinopyroxene megacryst yielded ranges of 75.4 to 83.3 and 50.3 to 53.6 respectively.

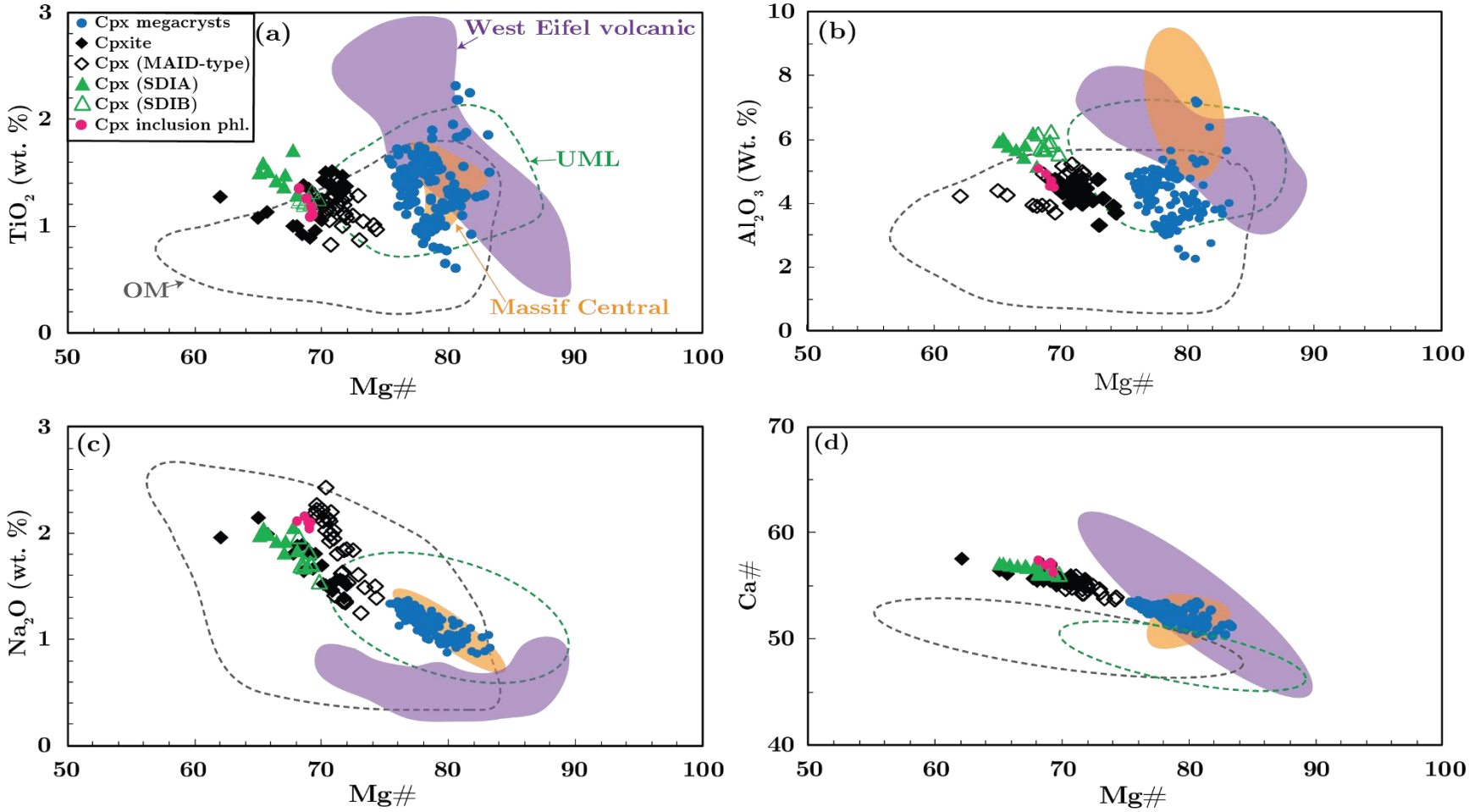

Figure 6.3: Major element variation diagrams for clinopyroxene megacrysts from the SPKC as a function of Mg-number. 2σ uncertainties for the clinopyroxene data are smaller than the symbols on the plots. Also plotted fields for clinopyroxene grains for the SPKC melilitite and lamprophyre rocks (gray and green dotted fields respectively - Marageni, 2018) and clinopyroxene megacrysts from the Massif Central and Eifel volcanic fields. Data for Massif Central, France (orange colouredfield) West Eifel volcanic field, Germany (purple colouredfield) were taken from Woodland and Jugo, (2007) and Shaw and Eyzaguirre, (2000) respectively.

Overall, TiO_2 displays virtually no correlation with Mg#. On Figure 6.3a, the data appear to form two distinct clusters, each with a weak negative correlation of TiO2 with Mg#. Clusters of data also show similar slopes. The grains with higher Al_2O_3 concentrations also have higher TiO_2 concentrations. Na_2O and Ca-number (Fig. 6.3c and d), unlike TiO_2 and Al_2O_3, form single well-defined trends displaying strong negative correlations with Mg#. Concentrations of both Cr_2O_3 and K_2O are near the detection limits of EPMA and show no trends versus Mg-number.

The clinopyroxene megacryst data from the SPKC overlap with and share compositional similarities (trends) to those from Massif Central, France (Woodland and Jugo, 2007) and West Eifel volcanic field, Germany (Shaw and Eyzaguirre, 2000). Some significant differences are notable, including: higher Al_2O_3 concentrations from both Massif Central and West Eifel samples; lower Na_2O contents as well as the much wider range of TiO_2 and Ca-number for the West Eifel samples, relative to SPKC clinopyroxene grains.

The SPKC megacrysts are compositionally comparable to clinopyroxene phenocrysts from both the olivine melilitite and ultramafic lamprophyre rocks of the SPK complex (Mabaso, 2017). In most instances, the major oxides for the megacrysts exhibit near-complete overlap with the ranges defined by the phenocrysts from each rock type, however several differences are also inmportant to note - the megacrysts grains have higher Ca-numbers as well as a steeper negative slope in the plot of Ca-number versus Mg-number; the concentrations of TiO_2, Al_2O_3 and Na_2O span smaller ranges in the megacrysts, relative to melilitite clinopyroxene phenocrysts.

Xenolith clinopyroxenes

- Clinopyroxenites

The clinopyroxene grains from the clinopyroxenites fall within the ranges $Wo_{47.5\text{-}50.7}$ $En_{25.1\text{-}29.3}$ $Fs_{20.2\text{-}27.4}$, which, as with the clinopyroxene megacrysts, places them predominantly in the diopside compositional field. A few grains fall into the hedenbergite field (Fig. 10). These grains do, however, show less variability than the clinopyroxene megacrysts: TiO_2 (0.9 to 1.5 wt. %), Na_2O (1.4 to 2.1 wt.%), MgO (11.1 to 12.5 wt.%), Al_2O_3 (3.7 to 5.2 wt. %) and CaO (20.0 to 21.6 wt. %), SiO_2 (49.0 to 51.8 wt. %) and FeO^{tot} (8.6 to 12.3 wt. %).

The calculated Mg-numbers for these clinopyroxene grains ranges from 68.9 to 81.3, while Ca-numbers fall between 50.9 and 51.1. The clinopyroxenite grains differ from the clinopyroxene megacrysts in that they are more Fe-rich and, in contrast to the megacrysts, show negative correlations of both Al_2O_3 and TiO_2 versus Mg-number. Na_2O and Ca-Number form continuous, negative trends, similar to the megacrysts. These trends can be seen in Fig. 6.3a-d.

- Clinopyroxene from Clinopyroxene-Phlogopite-Amphibole-Ilmenite (MAID-type) xenoliths

The clinopyroxene grains from the MAID xenoliths ($Wo_{48.9\text{-}50.6}$ $En_{28.3\text{-}31.0}$ $Fs_{19.0\text{-}22.3}$) also fall within the diopside compositional field (Fig. 6.1). These grains are compositionally very similar to those from the clinopyroxenites, with considerable overlap observed for most of the major oxides. The main observable difference is that these MAID-type grains have higher concentrations of Na_2O for a given Mg-number. These grains also have lower Mg-numbers relative to the clinopyroxene megacrysts - Mg-numbers for the xenolith grains range between 69.5 and 74.3 while the megacrysts have values greater than 75. Al_2O_3 and TiO_2 plotted against Mg-number display negative correlations while Na_2O and Ca-number form continuous trends with the megacryst data. All of these trends are identical to those observed in the clinopyroxenite data.

Inclusions of clinopyroxene have also been found in numerous phlogopites grains from the MAID-type xenoliths. Analysis of the inclusion clinopyroxene reveals that they are compositionally like the regular xenolith clinopyroxene grains that are not inclusions.

- Clinopyroxene from clinopyroxene-amphibole-Fe oxide xenoliths (SD1A- & SD1B)

The clinopyroxene from SD1A and SD1B xenoliths are compositionally more similar to those from the clinopyroxenites than they are to those from the MAID-type xenoliths and megacryst clinopyroxenes. Comparisons between SD1A and SD1B clinopyroxene grains and those from the clinopyroxenites shows that SD1A and SD1B clinopyroxene grains tend to be more enriched in both Al_2O_3 and TiO_2.

Plots of major oxides against Mg-number show that both SD1A and SD1B follow and continue the positive correlation trends displayed in the clinopyroxenite and MAID-type xenoliths (i.e. Fig. 6.3c-d). Clinopyroxene inclusions present in amphibole grains from sample SD1A are compositionally identical to the non-inclusion clinopyroxene grains of xenolith SD1A. Comparisons solely between clinopyroxene from SD1A and SD1B reveals that the two are compositionally near-identical, however the former have marginally higher FeO contents. In the plot of Al^{iv} versus Al^{vi} (Fig. 6.4a) clinopyroxene grains from xenolith SD1A correlate positively whereas those from xenolith SD1B show no correlation.

6.2. Amphibole

Megacryst data

The amphibole megacrysts collected from the Salpeterkop complex were characterised on the basis of their major element compositions, as outlined in Leake et al. (1997). Stoichiometry calculated from EMPA data shows that the majority of the amphibole megacrysts selected for analysis have between 5.5 and 6.5 cations per formula unit (pfu) Si and less than 0.5 pfu Ti and can therefore be classified either as pargasite of the hornblende group or Mg-hastingsite (Fig. 6.4a). Further classification (Fig. 6.4b) suggests that the grains are generally more pargasitic. However, not all of the megacrysts can be classed as pargasitor Mg-hastingsite as a small population of the megacrysts show slightly higher concentrations of titanium ($\geq$ 0.5 pfu Ti) for a given silica content (5.5 to 6.5 pfu Si), shifting these grains towards the composition of kaersutite. The more Ti-rich (kaersutitic) megacrysts are also noted

as having the higher Mg-numbers. The general chemical formula calculated for the amphibole megacrysts is as follows:

$(Na_{0.6\text{-}0.8}, K_{0.3\text{-}0.4})Ca_{1.7\text{-}1.9}(Mg_{2.7\text{-}3.3}\ Fe_{0.9\text{-}1.7}\ Al_{0.1\text{-}0.4}\ Ti_{0.4\text{-}0.5})[Si_{5.9\text{-}6.2}\ Al_{2.0}O_{22}](F+Cl_{>0.2}OH)$.

The amphibole megacrysts are generally compositionally uniform: SiO_2 (40.4 to 42.4 wt. %), Al_2O_3 (12.3 to 13.8 wt. %), CaO (10.9 to 11.9 wt. %), TiO_2 (3.2 to 4.8 wt. %), Na_2O (2.23 to 2.77 wt.%) and K_2O (1.79 to 2.20 wt. %). MgO (12.03 to 15.25 wt.%) and FeO^{tot} (7.58 to 13.45 wt. %) display the most variability of the oxides measured. Calculated Mg- and Ca-numbers for these grains range from 61.4 to 78.1 and 35.3 to 39.9 respectively. The major oxides and Ca-numbers all show more scatter at higher Mg-numbers. Al_2O_3 and TiO_2 display positive correkations with Mg-numbers (Fig. 6.6a and 6.6b respectively). The alkalis (K_2O and Na_2O) display very little variation in their concentrations, resulting in near-flat trends as a function of Mg-number. Lastly Ca-number shows a progressively steepening negative trend with decreasing Mg-numbers (Fig. 6.5e). The Salpeterkop amphibole megacrysts show significant overlap and similar trends for most of the major oxides when compared to amphibole megacrysts associated with alkali basalts (i.e. West Eiffel field volcanics, Germany; Shaw and Eyzaguirre, 2000).

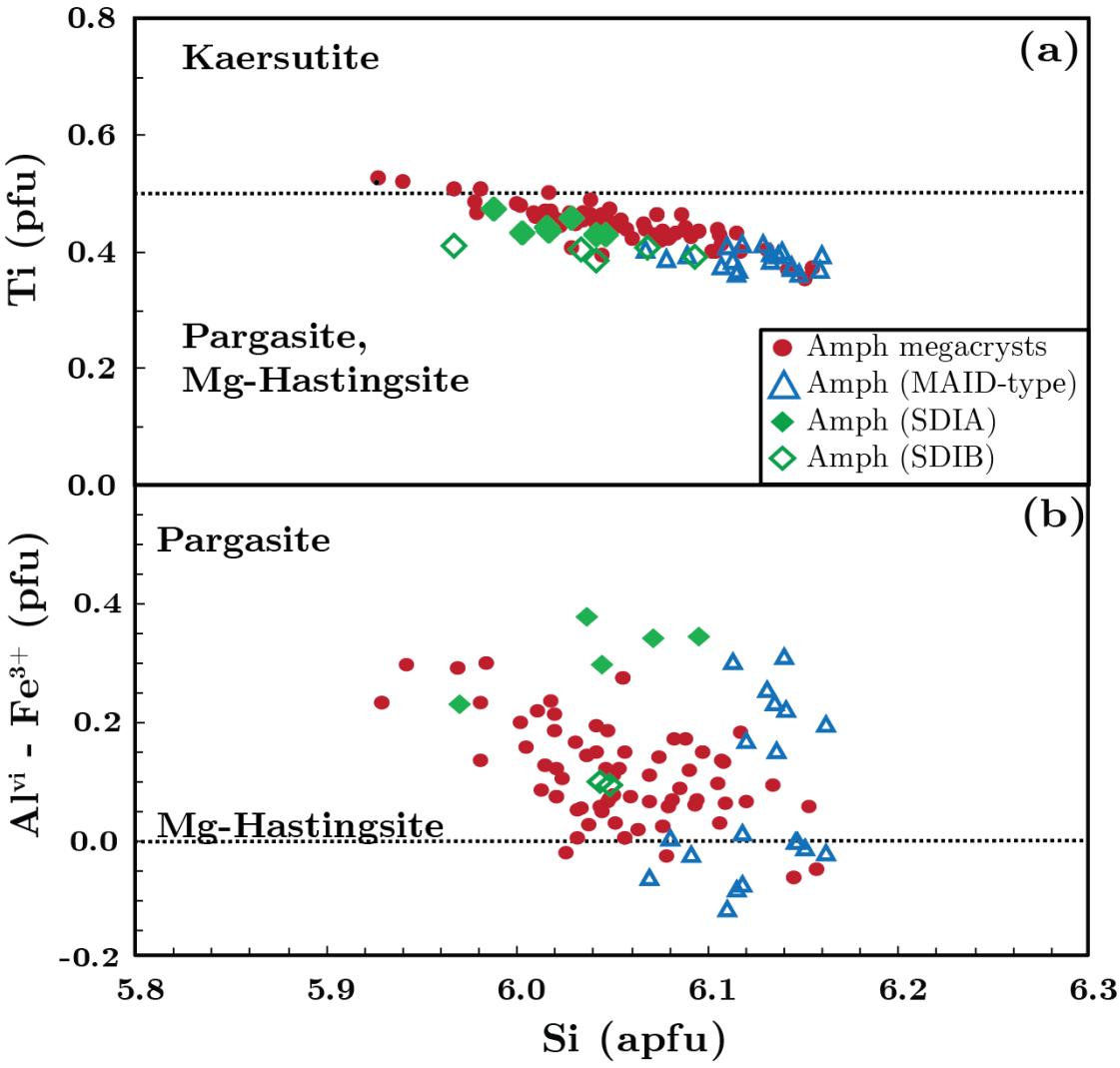

Figure 6.4: Mineral classification of amphibole megacrysts (a) Ti (pfu) versusSi (pfu) to differentiate between kaersutite and pargasite + Mg-hastingsite and (b) Al^{vi}–Fe^{3+} versus Si (pfu)to differentiate between pargasite and Mg-hastingsite, as outlined by Leake et al. (1997). Al^{vi} refers to the amountof aluminum present in the octahedral crystallographic site2σ uncertainty for the SPKC grains are smaller than the symbols on the graph.

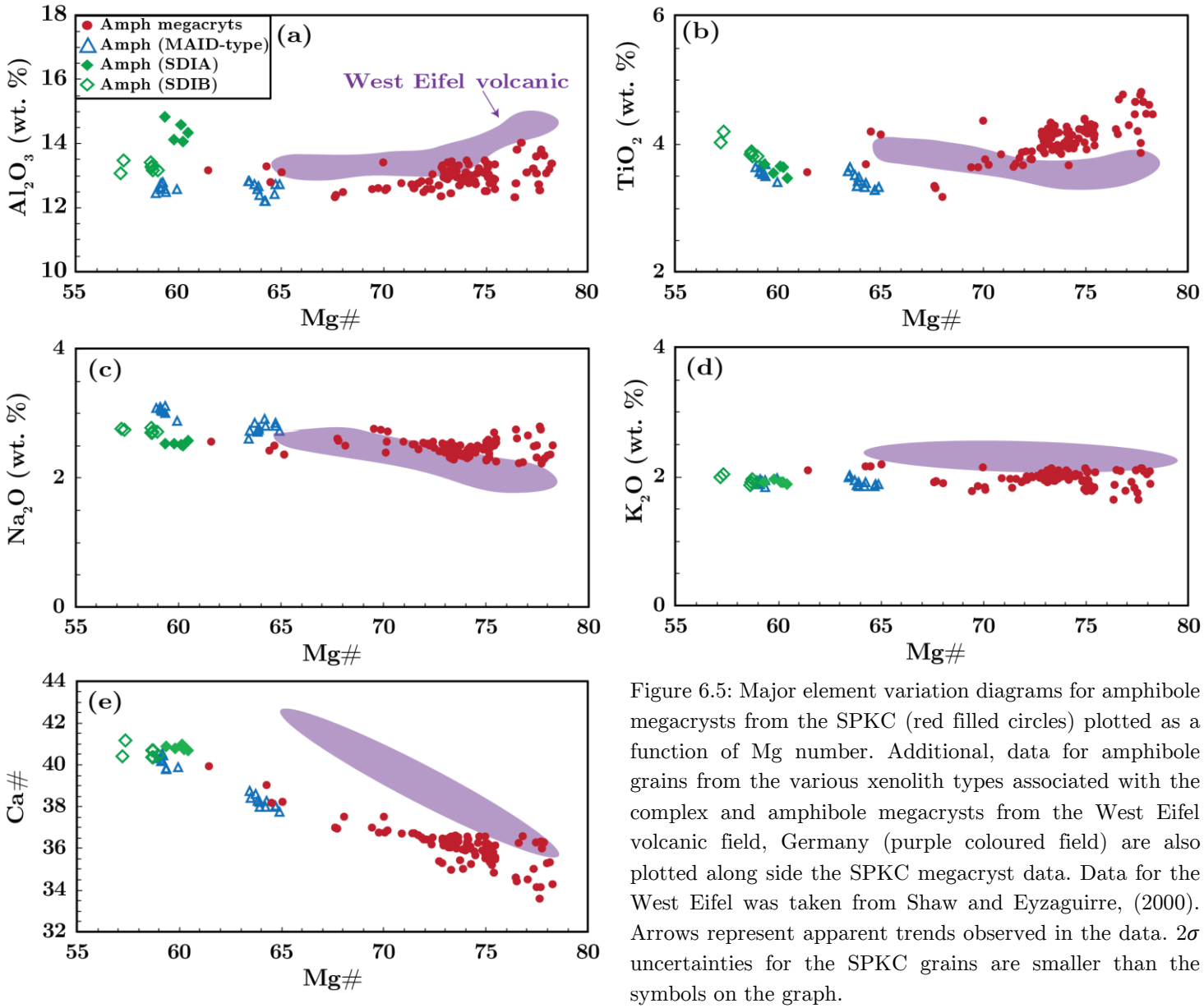

Figure 6.5: Major element variation diagrams for amphibole megacrysts from the SPKC (red filled circles) plotted as a function of Mg number. Additional, data for amphibole grains from the various xenolith types associated with the complex and amphibole megacrysts from the West Eifel volcanic field, Germany (purple coloured field) are also plotted along side the SPKC megacryst data. Data for the West Eifel was taken from Shaw and Eyzaguirre, (2000). Arrows represent apparent trends observed in the data. 2σ uncertainties for the SPKC grains are smaller than the symbols on the graph.

Xenolith amphiboles

- Amphibole from MAID-type xenoliths

The MAID amphibole grains were classified in the same manner as the amphibole megacrysts and were shown to also have a pargasitic composition ($>$ 0.41 pfu Ti and $>$ 6.2 pfu Si) similar to the amphibole megacrysts (Fig. 6.4a-b). These grains are compositionally more uniform in their MgO and FeO^{tot} contents relative to the megacrysts of the same phase. Calculated Mg- and Ca-numbers for amphibole grains from xenoliths of this type vary from 58.9 to 64.9, and 37.7 to 40.5 respectively.

These grains share many similarities with the more iron-rich amphibole megacrysts. Al_2O_3, TiO_2, K_2O and Ca-number (Fig. 6.5a-b, d-f) all display negative correlations as a function of Mg-number, comparable to the trends seen in megacryst with Mg-numbers less than 67.

- Amphibole from clinopyroxene-amphibole-Fe oxide xenoliths (SD1A- & SD1B)

The amphibole grains from both SD1A and SD1B are compositional very similar to each other as well as to grains analysed from the MAID-type xenoliths. Amphibole grains from SD1A do however have higher concentrations of Al_2O_3, lower concentrations of Na_2O, and are marginally more Mg-rich relative to the SD1B amphibole grains (6.5). Amphiboles from both xenoliths do however partially overlap and form continuous trends with the MAID-type and megacryst grains. The SD1A/B amphibole grains separately show negative correlations with Al_2O_3 and TiO_2 (Fig. 6.5a-b), which appear to match the trends displayed for the megacrysts with Mg-numbers less than 67. Virtually no correlations for K_2O, Na_2O and Ca-number versus Mg-number (Fig. 6.5c-e).

6.3. Phlogopite

Megacryst Data

The micaceous megacrysts are plotted on an annite – siderophyllite – phlogopite – eastonite quadrilateral (ASPE), which is used to show the compositional relationship between Fe/(Fe + Mg) and the total Al content of mica (Fig. 6.6). The phlogopite grains from the

Salpeterkop complex plot in the low Fe/(Fe + Mg), low Al portions of the ASPE quadrilateral, making them compositionally most closely related to the phlogopite endmember, but not pure phlogopite. The general chemical formula for analysed samples was calculated as: $K_{0.8\text{-}0.9}Na_{0.1\text{-}0.2}(Mg_{1.9\text{-}2.0},Fe_{0.4\text{-}0.5},\ Ti_{0.2\text{-}0.3},\ Al_{>0.2})[Al_{1.3\text{-}1.9}Si_{2.7\text{-}2.8}\ O_{10}](OH)_{2.0}$.

The phlogopite megacrysts analysed show very little compositional variability with respect to most of the major oxides: SiO_2 (36.7 to 38.0 wt. %), MgO (17.4 to 19.1 wt.%), Al_2O_3 (15.8 to 17.1 wt. %), K_2O (8.7 to 9.6 wt. %) and TiO_2 (4.7 to 5.9 wt. %). The FeO^{tot} (6.3 to 10.6 wt. %) is the most variable oxide recorded. Mg-numbers for these megacrysts fall between 74.9 and 84.1. The major oxides Al_2O_3, TiO_2 and K_2O all exhibit positive correlations with Mg-number (Fig. 6.7). Na_2O shows a distinctly different trend, displaying a negative correlation with Mg-numbers above values of 80 and nearly uniform values at Mg-numbers below 80. Two distinct groupings are seen in the megacryst data for all major oxides, with the division located at a Mg-number value of 80.

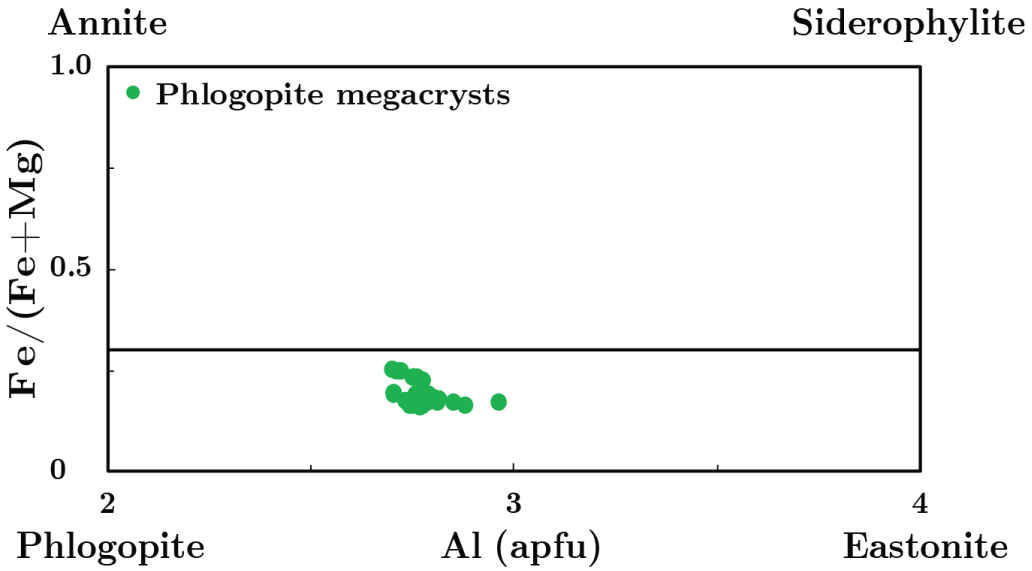

Figure 6.6: The classification of phlogopite megacrysts based on Al (pfu) as a function of Fe/(Fe+Mg) shows that these grains are compositionally more closely related to the phlogopite endmember. 2σ uncertainty for the SPKC grains are smaller than the symbols on the graph.

Comparison of the major element compositions of the SPKC phlogopite megacrysts with phlogopite grains analysed from the SPKC olivine melilitites (OM) (open circles) and ultramafic lamprophyres (Mabaso, 2017) shows that megacrysts have a greater compositional afffinity with the phlogopite grains from the UML, with a significant difference only in TiO_2 where the UML grains have a lower concentration. The SPKC phlogopite megacrysts also show compositional similarities with phlogopite megacrysts from West Eifel field volcanics, Germany (Shaw and Eyzaguirre, 2000) and Penghu Islands, Taiwan Strait (Ho et al., 2000).

Xenolith phlogopites

- Phlogopite from MAID-type xenoliths

The phlogopite grains analysed have relatively uniform major element concentrations and, as with the xenolithic clinopyroxene and amphibole megacryst grains, they plot at significantly lower Mg-numbers (61.3 to 62.5) compared to the megacrysts (74.9 to 84.1). As a function of Mg-number, Al_2O_3, TiO_2 and K_2O all show very weak negative correlations, contrasting the generally positive correlations observed for the megacrysts. Na_2O shows a near-horizontal trend in the xenoliths, which is consistent with representing an extension of the trend displayed by the lower Mg-number megacryst group.

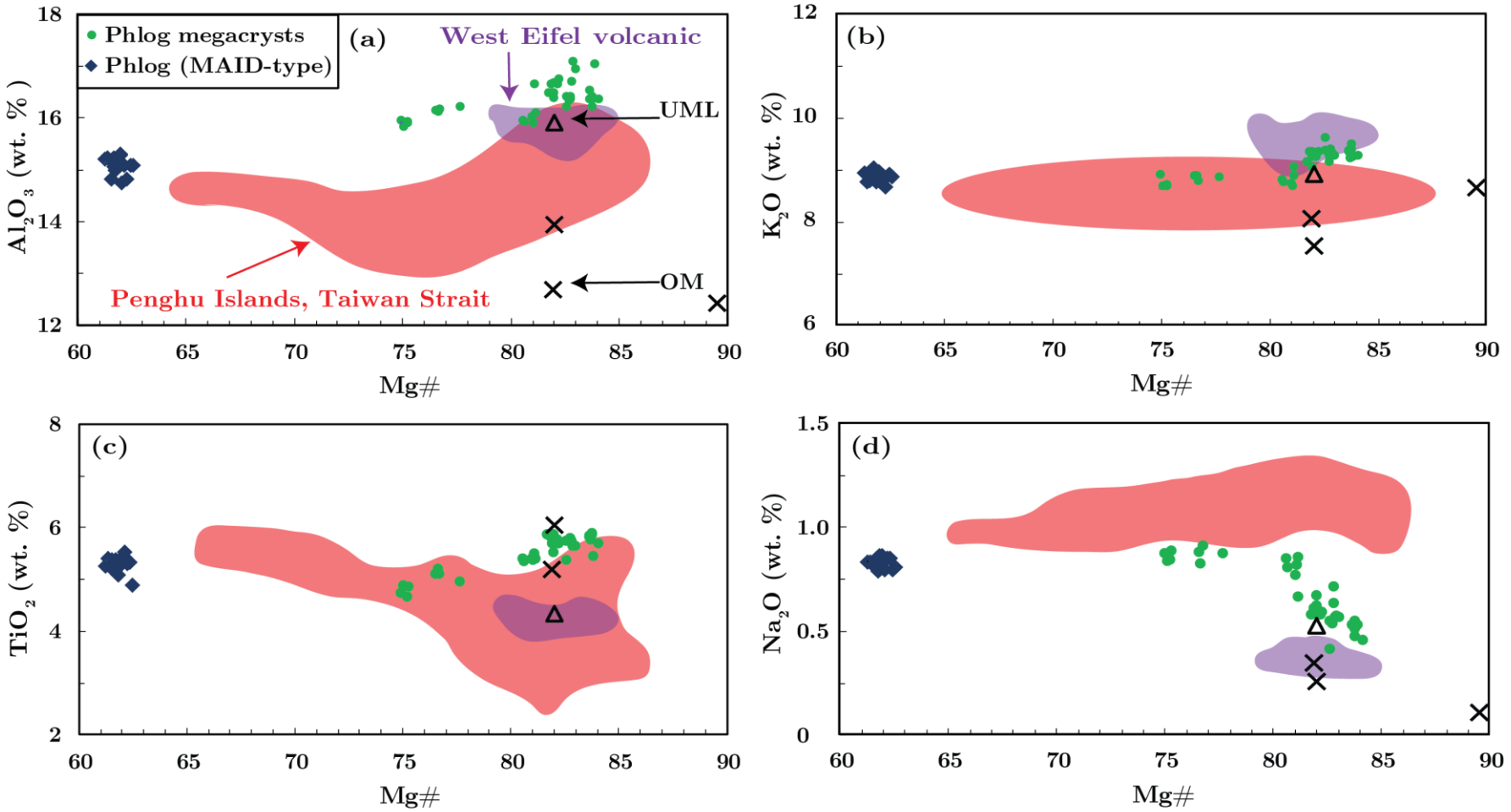

Figure 6.7: Major element variation diagrams for phlogopite megacrysts from the SPKC (green filled circles) plotted versus Mg-number. Data for (i) phlogpite grains from the MAID-type xenoliths also sampled from the complex (dark blue filled diamonds), (ii) SPKC olivine melilitites (OM) (open circles)and ultramafic lamprophyres (UML)(open triangles)(Mabaso, 2017) (iii) phologpite megacrysts from the West Eiffel volcanic field, Germany (purple coloured field) and (iv) phologpite megacrysts from the Penghu Islands, Taiwan Strait (pink coloured field) – data for these latter two megacryst localities are from Shaw and Eyzaguirre (2000) and Ho et al. (2000) respectively. 2σ uncertainties for the SPKC grains are smaller than the symbols on the graph.

6.4. Ilmenite

Megacryst data

These Fe-oxide megacrysts were classified based on three oxide mineral endmembers: ilmenite ($FeTiO_3$), haematite (Fe_2O_3) and geikelite ($MgTiO_3$). The compositions with respect to these three mineral end-members are plotted on a ternary diagram (Fig. 6.8). The ilmenite megacrysts plot closest to the ilmenite end-member, but have significant amounts of all three end-members as well as moderately variable compositions: 17.2 – 27.4 mol % geikelite and 16.9 – 27.4 mol % haematite.

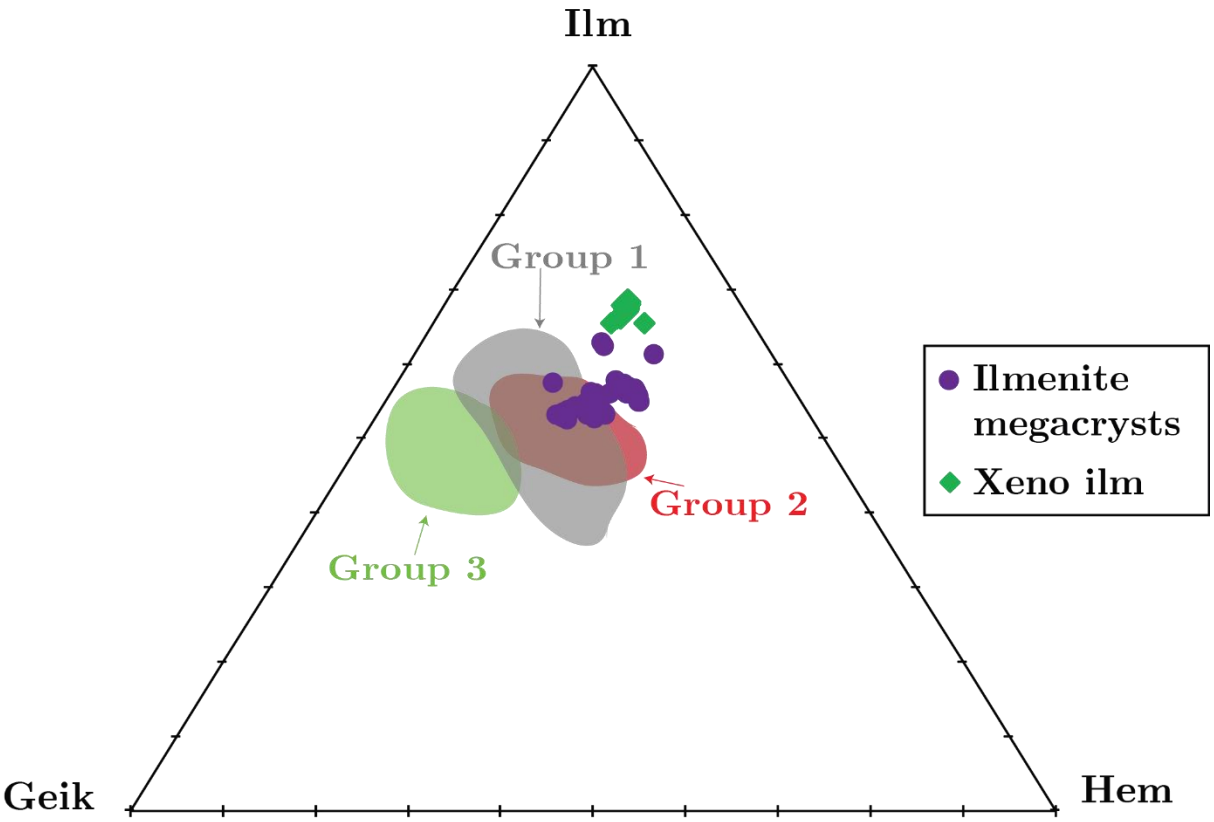

Figure 6.8: Ternary (geikelite-haematite-ilmenite) diagram used for the classification of the ilmenite megacrysts (purple filled circles) and MAID-type xenolith grains(green filled diamonds),as well as the 3 distinct ilmenite groups of the Monastery kimberlite, South Africa, as defined and described by Moore et al. (1992). These Monastery kimberlite ilmenite groups, 1 to 3, are distinguishable by the gray, red and green coloured fields respectively. 2σ uncertainty for the SPKC grains are smaller than the symbols on the graph.

Al_2O_3, MgO, TiO_2 and FeO are the only oxides present at significant concentrations in the ilmenite megacrysts. Al_2O_3 is the least abundant, showing the smaller range of values of the major oxides measures (a range of about 1 wt. %). MgO and and TiO_2 range from 4.0 to

8.4 wt. % and 45.1 to 49.6 wt. % resepctively, while FeO^{tot} ranges from 39.1 to 47.7 wt. %. The calculated Mg-number for the ilmenite megacrysts analysed range from between 17.3 to 27.5, while the Cr-number ($\frac{Cr}{(Cr+Al)} \times 100$) never exceeds 8.0, averaging ≈ 1.6.

Plots of TiO_2 and Al_2O_3 as a function of Mg-number (Fig. 6.9 a-b) show negative correlations, but not as one continuous population. A clear break in the data is visible at an Mg-number of approximately 20. SPKC ilmenite megacrysts were then compared to ilmenite grain from the Monastery, South Africa, where three distinct ilmenite groups have been observed (Moore et al. 1992). The first (Group 1) are Cr-poor ilmenites that can be explained through pure fractional crystallisation. The second (Group 2) appears to reflect a combination of a fractional crystallization trend as well as assimilation of Nb- and Cr-rich lithospheric material and lastly ilmenite grains belonging to the third and final group (Group 3), have the highest Mg-number and intermediate (but still fairly high) Cr and are believed to represent megacryst formed from parental magmas that assimilated significant bulk peridotite. The SPKC grains partially overlap the Group 1 and 2 ilmenite populations from Monastery, South Africa, which extends to both higher TiO_2 and Mg-numbers.

Xenolith ilmenites

- Ilmenite from MAID-type xenoliths

Classification of the xenolith ilmenite grains based on mineral end-members ilmenite ($FeTiO_3$), haematite (Fe_2O_3) and geikelite ($MgTiO_3$) showed that they are considerably less variable (i.e., 11.5 – 14.1 mol % geikelite and 19.2 – 27.4 mol % haematite) but compositionally like the ilmenite megacrysts (Fig. 6.8). Major oxide contents, including TiO_2 and FeO, are similar in both the MAID xenolith and megacryst grains, while MgO and Al_2O_3 are higher in the megacrysts relative to the xenolith grains. As with all of the other minerals, the xenoliths ilmenite grains have lower MgO (or Mg-number) values than the megacrysts.

In the Mg-number versus TiO_2 plot (Fig. 6.9a), the MAID xenolith ilmenite grains show a weak positive correlation, like that displayed by the megacrysts, with the lower Mg-number xenolith grains showing marginally higher concentrations of TiO_2 relative to the most differentiated (Fe-rich) megacryst samples. In the plot of Mg-number versus Al_2O_3 (Fig. 6.9b)

the xenolith ilmenite and megacryst grains align along the same general path, with an overall decrease in slope gradient apparent moving from the higher Mg-number megacrysts to the lower Mg-number xenolith grains. The megacrysts display a positive correlation of Mg-number versus Al_2O_3 while the xenoliths show a flat lying trend, indictive of a change in the source melt composition.

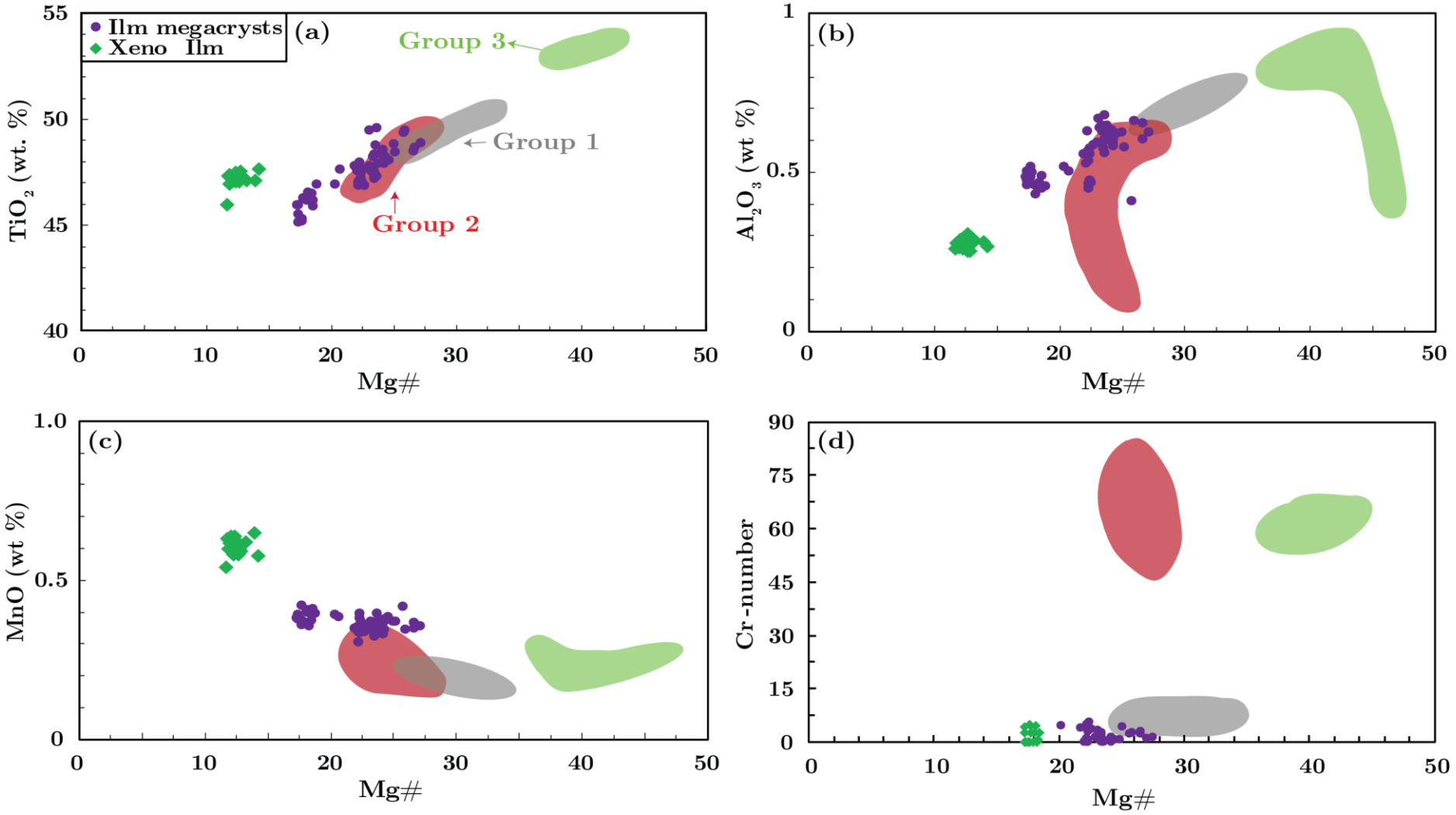

Figure 6.9: Major element variation diagrams for ilmenite megacrysts from the SPKC (purple filled circles) compared to (i) ilmenite grains from the MAID-type xenoliths (green filled diamonds) as well as (ii) the 3 distinct ilmenite groups of the Monastery kimberlite, South Africa, as defined and described by Moore et al. (1992).These Monastery kimberlite ilmenite groups, 1, 2 and 3, are distinguishable by the gray, red and green coloured fields respectively. 2σ uncertainties for the SPKC grains are smaller than the symbols on the graph.

7. Trace element geochemistry

7.1. Clinopyroxene megacrysts

The clinopyroxene megacrysts are, like most clinopyroxene megacrysts from kimberlites and alkaline basalts, moderately enriched in the high field strength and light rare earth elements, but moderately depleted in the large ion lithophile elements, i.e. Nb (0.35 to 1.9 ppm), Zr (98.8 to 406.9 ppm), Nd (12.1 to 29.7 ppm) and Y (5.5 to 14.1 ppm). The large-ion lithophile elements (LILE i.e. Sr, Fig. 7.1g) and high-field-strength elements (HFSE i.e. Zr and Hf, Fig. 7.1e and 7.1f respectively) exhibit weak negative correlations versus Mg-number, while Cr (Fig. 7.1h) shows no correlation.

The chondrite-normalised rare earth element (REE) plots for the clinpyroxene megacrysts (Fig. 7.2a) display concave-down patterns, with significantly greater enrichment visible for the LREE compared to the HREE. The greatest enrichments relative to chondrites are observed in Nd (up to 63 times). The clinopyroxene megacrysts have an average $(Nd/Yb)_N$ ratio of 9.66 ± 0.79 (1σ; n = 139). Most of the incompatible elements show primitive mantle normalised values between 0.1 and 10 (Fig. 7.2b). Ce, Nd, Zr and Hf show the highest degrees of enrichment relative to the primitive mantle, with average and maximum values for all exceeding 10 and 23, respectively. Contrasting these are Pb, K, Rb and Ba, which all show very prominent negative anomalies, with maximum values for most of these elements below 1, relative to primitive mantle. Pb is the only exception and has maximum values as high as 2.7.

The chondrite-normalised (REE) pattern for the SPKC clinopyroxene megacrysts (Fig. 7.2a) show similar trends and considerable overlap with data from other localities such as West Eifel volcanic field, Germany. These compositional similarities are also clearly visible in diagrams of various trace elements plotted as a function of Mg-number (Fig. 7.1).

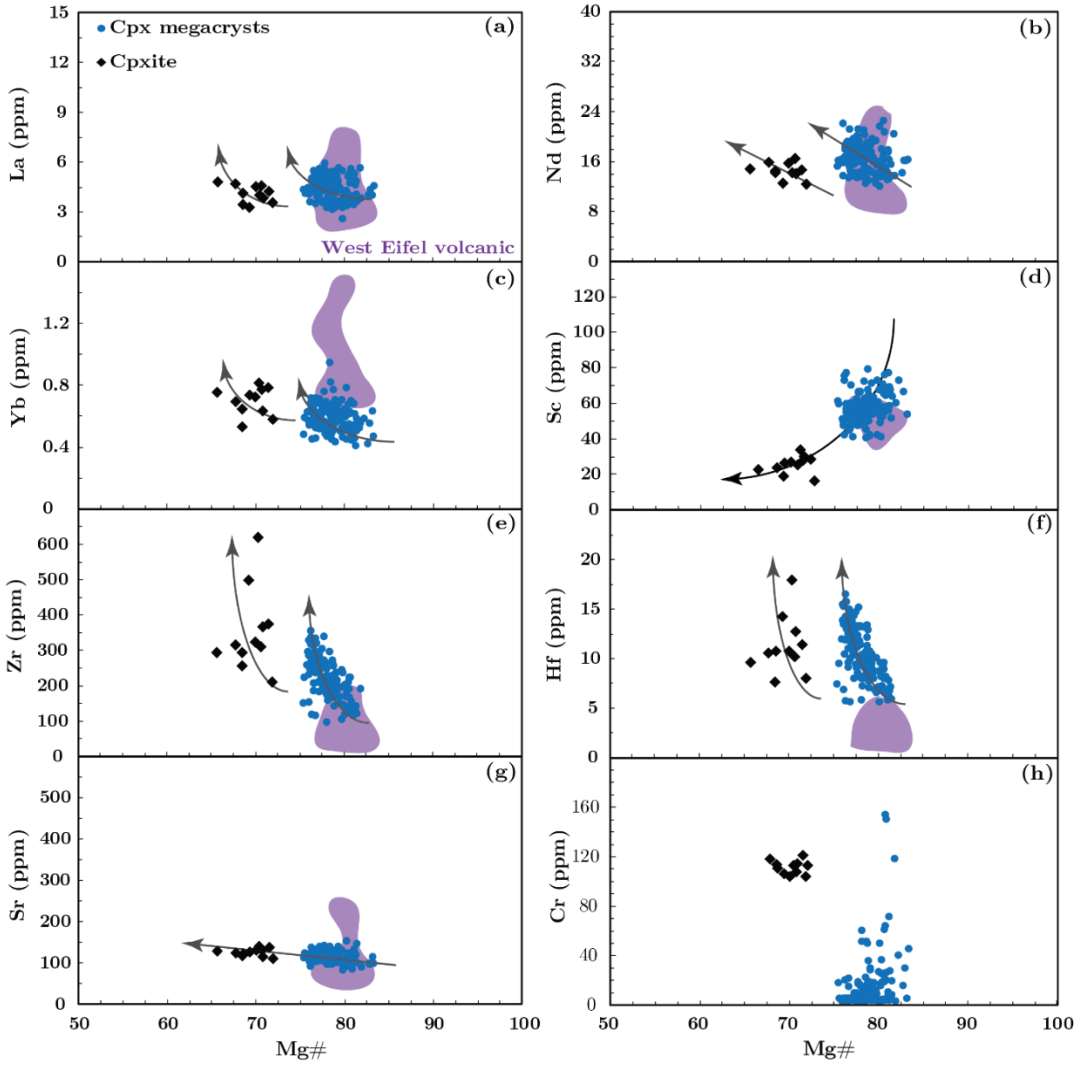

Figure 7.1: Compositional trends of trace elements (a-h) plotted as a function of Mg-number for the SPKC clinopyroxene megacrysts (blue filled circles) and clinopyroxenites (black filled diamonds). Data for West Eifel volcanic field, Germany (purple colouredfield) was taken from Shaw and Eyzaguirre, (2000). Arrows represent trends apparent in the data. 2σ uncertainties for the SPKC grains are smaller than the symbols on the graph.

The clinopyroxenite grains display concave-down REE patterns similar to those displayed by the megacrysts (Fig. 7.2a), but with considerably more uniform REE concentrations. On average, the clinopyroxenite grains have lower LREE/HREE ratios than the megacrysts, however the two still largely overlap with one another. Average and maximum $(Nd/Yb)_N$ values for these grains are 7.3 and 9.6, respectively. These similarities are present in the LREE,

REE and HFSE, where the clinopyroxenite grains continue the trends displayed by the megacryst samples.

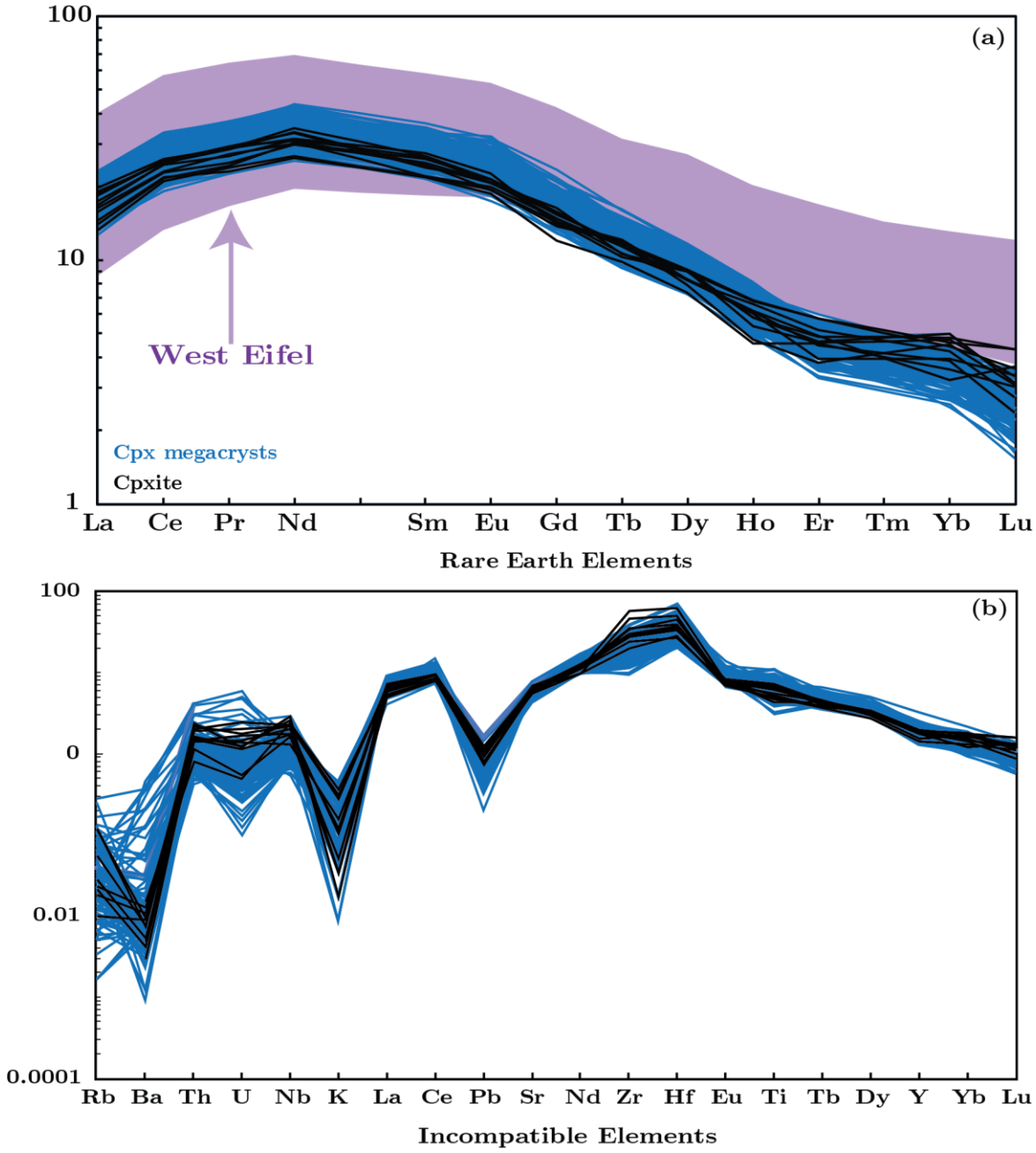

Figure 7.2: (a) Chondrite-normalised (Evensen et al. 1978) rare earth element (REE) for the SPKC clinopyroxene megacrysts (blue lines) and clinpyroxenites (black lines). Data for the West Eifel volcanic field, Germany (purple colouredfield) taken from Shaw and Eyzaguirre (2000) are also shown. (b) A primitive mantle-normalised (McDonough and Sun, 1995) incompatible element diagram for the clinopyroxene megacrysts and clinpyroxenites. Few non-REE trace elements were provided by Shaw and Eyzaguirre (2000), which is why these data are not plotted in panel (b).

7.2. Amphibole

Chondrite-normalised REE patterns for the clinopyroxene and amphibole megacrysts display nearly identical ranges in REE concentration resulting in overlapping concave-down trends with enrichment in the LREE and (Fig. 7.4a). The greatest enrichments in the amphibole megacrysts are observed in Nd (up to 49 times chondrite). The amphibole megacrysts have an average $(Nd/Yb)_N$ ratio of 13.89 ± 1.26 (1σ; n = 60). The primitive mantle-normalised incompatible element patterns for the amphibole megacrysts show that, for most elements, the amphibole megacrysts display enrichments of greater than 5 times primitive mantle. Ti, Hf, Ba, and Nb show prominent positive anomalies, with maximum enrichment values greater than 36. Pb, Th and U display distinct negative anomalies. The SPKC amphibole megacrysts share similar patterns with the average patterns for amphibole megacrysts from Kakanui, New Zealand (Fulmer et al. 2010), Massif Central, France (Woodland and Jugo, 2007) and the West Eifel volcanic field, Germany (Shaw and Eyzaguirre, 2000) in both chondrite-normalised (REE) and primitive mantle-normalised incompatible element diagrams (Fig. 7.3a-b) The SPKC amphibole megacrysts also show considerable overlap in chondrite-normalised (REE) with the clinopyroxene megacrysts.

In Figure 7.4, most of the trace elements display greater scatter at higher Mg-numbers, becoming more uniform towards the lower Mg-number grains. High-field-strength elements (HFSE i.e. Zr and Hf, Fig. 7.4e and 7.4f respectively) show the greatest scatter of all the trace elements and display apparent changes in slope direction around 75 Mg-number, resulting in parabolic trends. The other trace elements yield near-flat patterns as a function of Mg-number. There are also significantly fewer amphibole megacrysts at lower Mg-numbers relative to those above a Mg-number of 75.

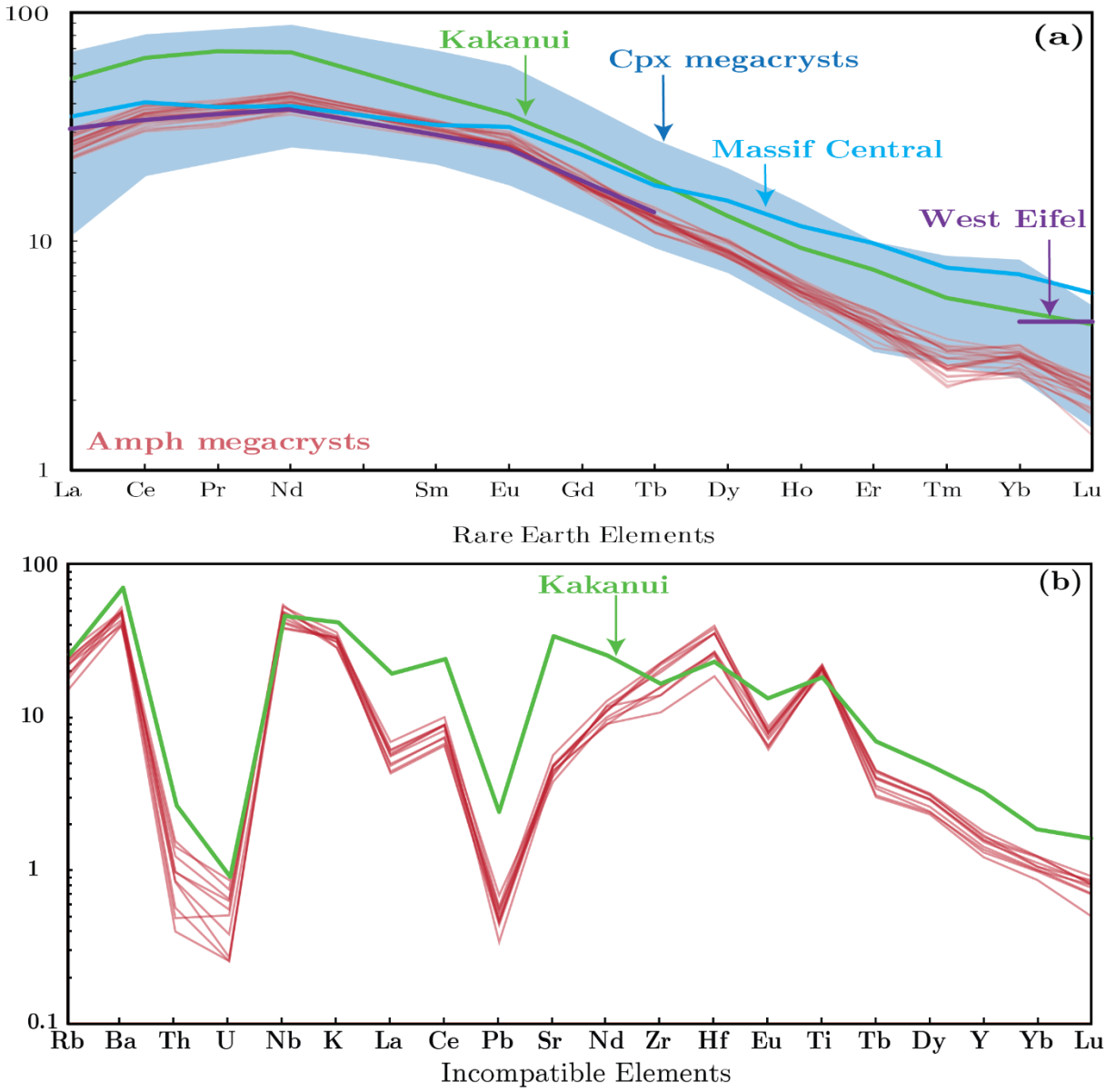

Figure 7.3: (a) A chondrite-normalised (Evensen et al. 1978) REE and (b) primitive mantle-normalised (McDonough and Sun, 1995) incompatible element diagrams for the SPKC amphibole megacrysts. Comparisons were made to average composition of amphibole megacrysts from Kakanui, New Zealand (green line; Fulmer et al. 2010), Massif Central, France (blue line; Woodland and Jugo, 2007), West Eifel volcanic field, Germany (purple line; Shaw and Eyzaguirre, 2000) and the clinopyroxene megacrysts (blue filled field). Few trace elements were provided by Shaw and Eyzaguirre (2000)andWoodland and Jugo (2007), which is why these data are not plotted in panel (a) and (b).

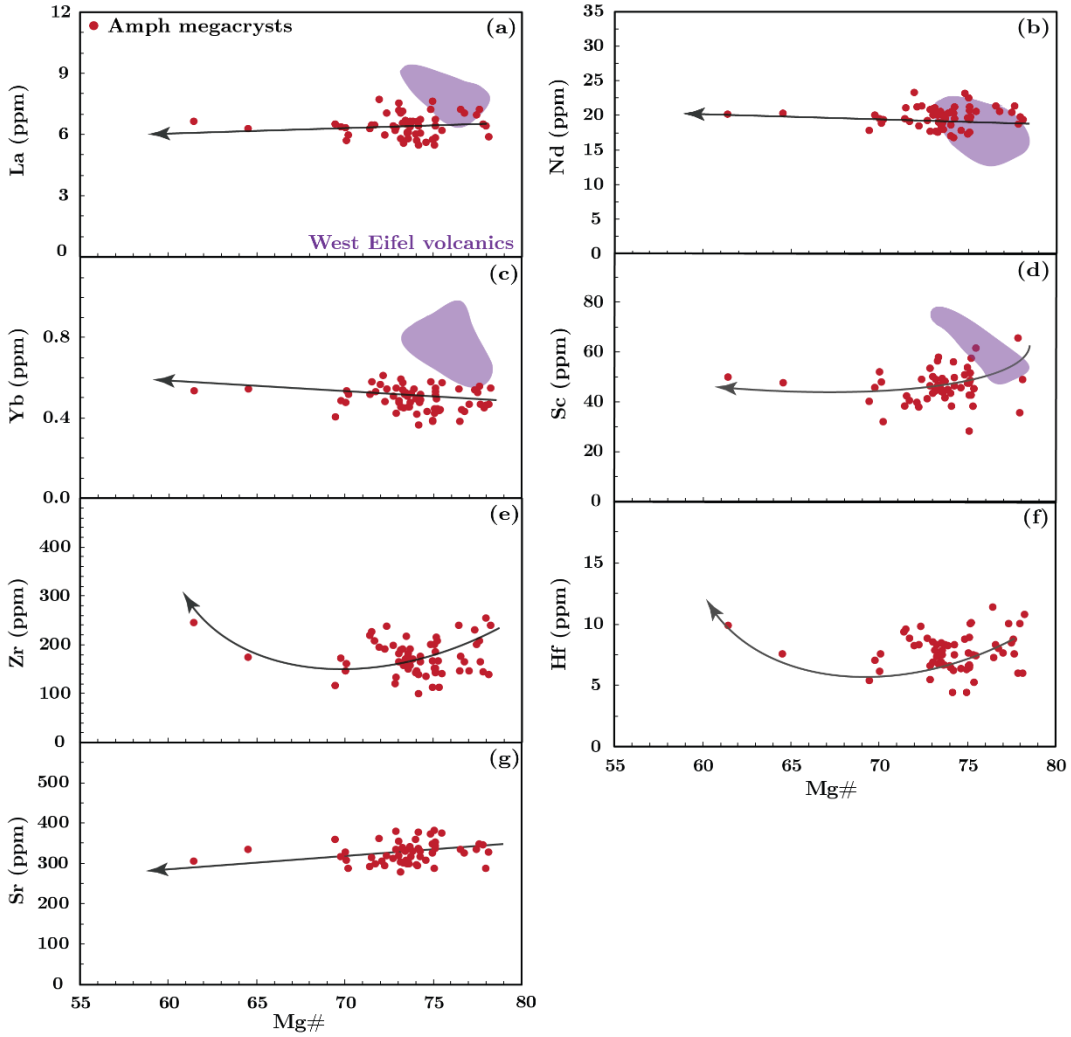

Figure 7.4: Compositional trends of trace elements (a-g) in the amphibole megacrysts, plotted as a function of Mg-number. Also shown are the fields for amphibole megacrysts from the West Eifel volcanic field, Germany (purple coloured fields; Shaw and Eyzaguirre, 2000). Arrows indicate likely magmatic evolution paths. Few amphibole megacrysts were analysed for trace elements by Fulmer et al. (2010) and Woodland and Jugo (2007), which is why this data are not plotted in panel (a) to (g). 2σ uncertainty for the SPKC grains are smaller than the symbols on the graph.

7.3. Phlogopite

The phlogopite megacrysts have low concentrations of the REE, relative to the clinopyroxene and amphibole megacrysts, with average values less than 0.1 ppm for both light and heavy REEs. The phlogopite megacrysts also show low average concentrations for various other trace elements measured including Nb (14 ppm), Zr (12 ppm), Sc (10 ppm), Ta (1 ppm) and Hf ($<$ 0.4 ppm), and in contrast to these, other elements including Cr (783 ppm), Ni (375 ppm), Rb (340 ppm), V (295 ppm), Mn (285 ppm) and Sr (126 ppm) display significantly higher concentrations. Comparisons made between phlogopite megacrysts sampled from the

various localities across the Salpeterkop complex (including the Silver Dam, SPKC 12 and SP-367-1 breccia pipes) reveals that no compositional variations are apparent, much like what was found for the major element data.

On a primitive mantle-normalised incompatible element diagram (Fig. 7.5) the phlogopite megacrysts display positive anomalies in Rb, Ba, Nb, K, Pb, Sr and Ti and these are the few trace elements with values greater than 1x primitive mantle. Rb, Ba and K display the greatest enrichments, extending to values of more than 100x primitive mantle (average values of 566, 478 and 158 respectively). Th, U and the REE are distinctly depleted, with average enrichment values less than 0.1x primitive mantle.For some of the trace elements plotted as function of Mg-number, changes in slope direction (gradient) occur around 80 Mg-number. Some trace elements (i.e Rb, Ni and V; Fig. 7.6d, f and h respectively) show positive correlations above 80 Mg-number and negative correlations below 80 Mg-number. Other trace elements (i.e. Ba and Sr; Fig. 7.6e) display negative correlations above 80 Mg-number and the converse below 80 Mg-number. Few elements do however lack these changes in slope direction seen above. Nb and Zr (Fig. 7.6a and c respectively) for instance maintain a negative correlation across 80 Mg-number but do however show an increase in slope gradient as Mg-number is varied across this point (Fig. 7.6a and 7.6c).

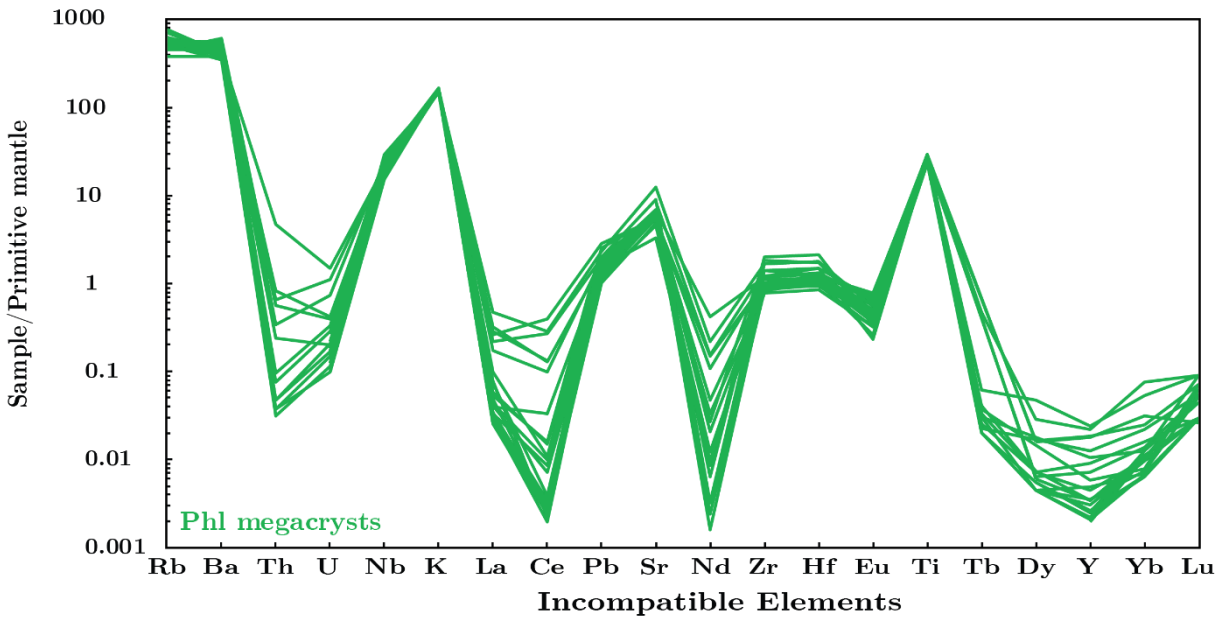

Figure 7.5: Primitive mantle-normalised (McDonough and Sun, 1995) incompatible element diagrams for the phlogopite megacryst from the Salpeterkop complex.

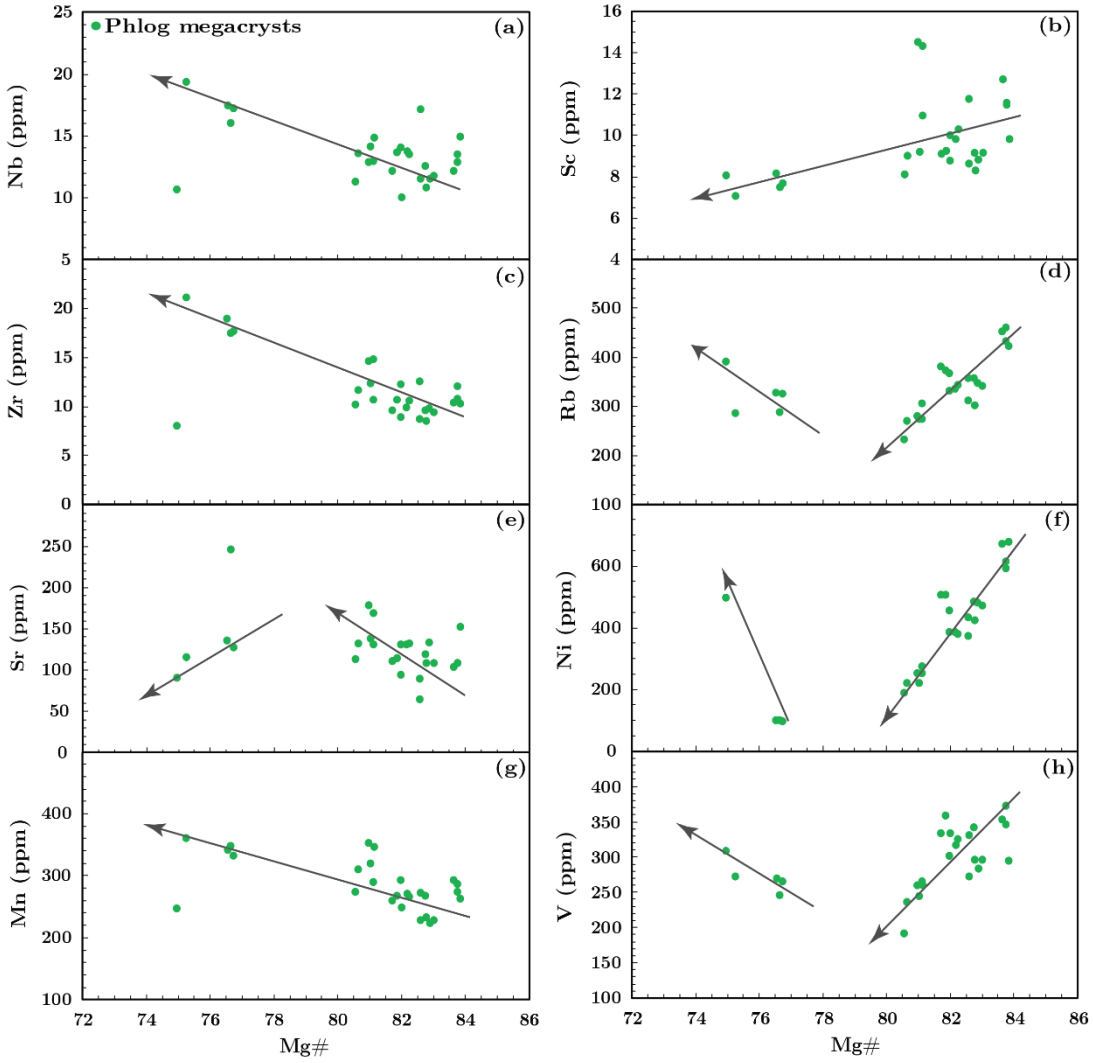

Figure 7.4: Compositional trends of trace elements (a -h) in the phlogopite megacrysts, plotted as a function of the grains Mg-number. Arrows represent apparent trends observed in the data. 2σ uncertainty for the SPKC grains are smaller than the symbols on the graph.

7.4. Ilmenite

The measured contents of HFSE in the ilmenite megacrysts range between 700 and 1500 ppm, 18 and 42 ppm and 410 and 1050 ppm for Zr, Hf and Nb respectively. Ratios of Zr/Hf fall between 28 and 58, while Nb/Zr is restricted to less than 1. The trends seen for Zr and Nb versus Mg-number (Fig. 7.7a and 7.7c respectively), display the same negative trends observed in the group 1 Monastery ilmenite megacrysts.

A weak positive correlation exists between Nb and Zr (Fig. 7.7d), similar to trends defined by the various ilmenite groups of the Monastery kimberlite. In this plot the SPKC ilmenites lie at generally lower Nb and extend to higher Zr concentrations than the Monastery ilmenite megacrysts and intergrowths. Trace elements showing compatible behaviour in the

other megacryst phases (i.e. Sc in clinopyroxene and amphibole) also show compatible behaviour in ilmenite (i.e., define positive correlations against the Mg-number). Trace elements plotted against Mg number in Figure 7.7 yield two distinct concave-up trends. Ni in the ilmenite megacrysts has an average concentration of around 90 ppm and ranges from 0 to 200 ppm. The plot of Mg# against Ni shows a U-shaped trend in the data, with the change in slope direction around a Mg-number of 20 (Fig. 7.7e). Ga ranges from 11 to 26 ppm and partially overlap with the group 1 Monastery ilmenites when plotted against Nb (Fig. 7.7f).

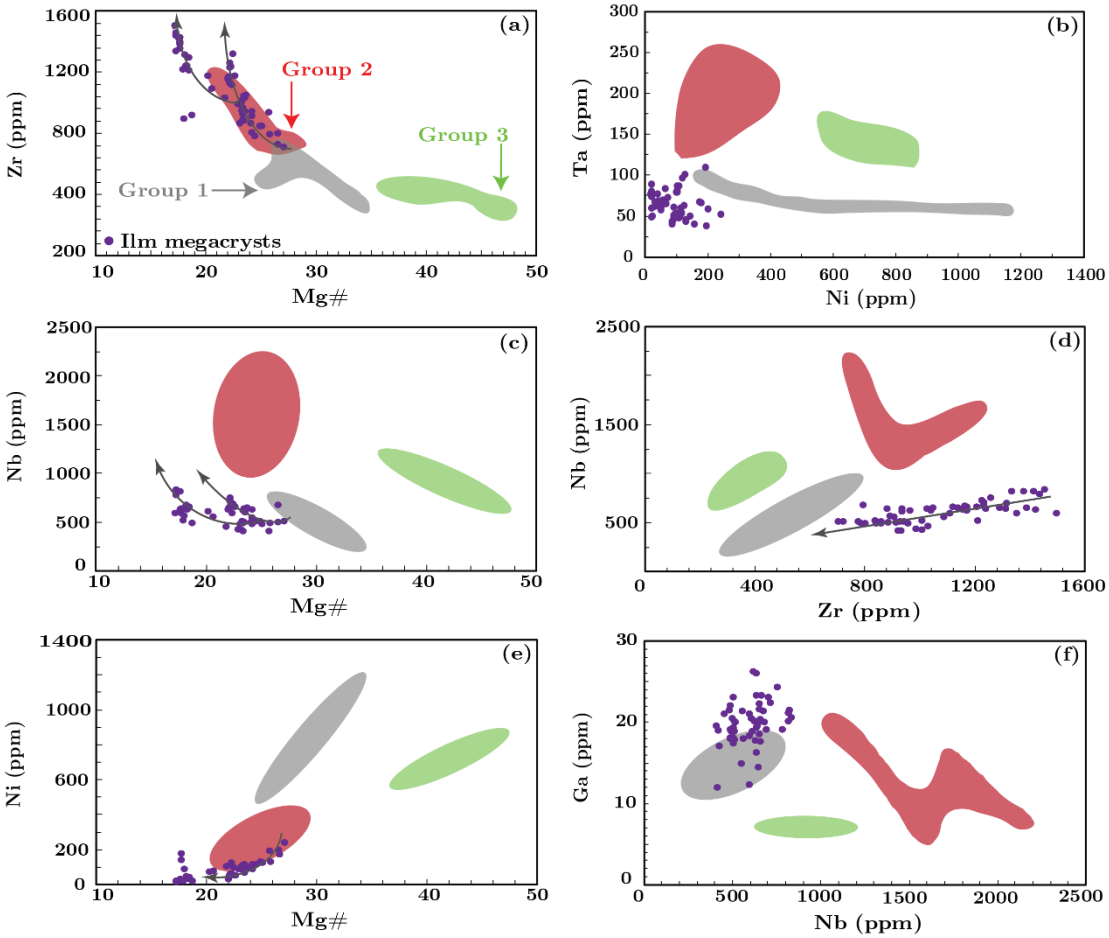

Figure 7.7: Compositional trends of trace elements (a-f) in the ilmenite megacrysts (purple filled circles), plotted as a function of Mg-number, compared to the 3 distinct ilmenite groupsof the Monastery kimberlite, South Africa (Moore et al. 1992). The group 1, 2 and 3 ilmenite megacryst groups of the Monastery kimberlite, shown as gray, red and green colouredfields respectively (data from Moore et al., 1992). Arrows represent apparent trends observed in the data. 2σ uncertainty for the SPKC grains are smaller than the symbols on the graph.

8. Stable isotopes, halogen and water content

8.1. Halogen and water contents of mica and amphibole

Amphibole

In amphibole, fluorine and chlorine occupy the same crystallographic site as the hydroxyl anion (OH^-) and, together, Cl and F make up less than 0.50 wt. % (i.e. at most 0.38 wt. % F and 0.03 wt. % Cl). Similar values are found in amphibole grains hosted in the xenolith samples. The water content for the amphibole megacrysts ranges from 0.52 to 1.29 wt. %, averaging 0.90 ± 0.27 wt. % ($1\sigma,\ n = 10$); Table 8.1. This corresponds to between 0.50 and 1.20 OH^- ions per formula unit (pfu) in the amphibole megacrysts. These values for the Salpeterkop megacrysts are comparable to the average water content (0.66 ± 0.44; $1\sigma, n = 25$) recorded in previous studies for amphibole megacrysts and xenolith grains hosted in alkali basalts from other localities (Boettcher and O'Neil, 1980; Matson et al., 1984), but are considerably lower than expected if the hydroxyl crystallographic site is filled entirely by OH^- anions (2 pfu OH^- for amphibole). Even if the halogens (F and Cl) are considered, which together make up more than 0.2 anions pfu, the hydroxyl crystallographic site is never entirely filled.

Phlogopite

As with amphibole, fluorine and chlorine can also substitute into the mineral structure of phlogopite in place of hydroxyl anions, where the combined concentrations of both elements is also below 0.50 wt. % (at most 0.35 wt. % F and 0.08 wt. % Cl respectively). The average water content for the phlogopite megacrysts is 1.55 ± 0.61 wt. % ($1\sigma, n = 10$), with a range of values from 0.72 to 2.54 wt. % OH^- (Table 8.1). This corresponds to between 0.35 and 1.20 OH^- ions pfu in the hydroxyl site of the phlogopite megacrysts. If the hydroxyl site completely filled with OH^- anions phlogopite grains would be expected to have 2 pfu OH^-, but this is not the case, even when the halogen content ($\geq$ 0.2 pfu) is considered.

Table 8:1: H_2O content (in weight %) and hydrogen and oxygen isotope compositions, for several SPKC amphibole and phlogopite megacrysts. Kaolinite samples run as a standard had an average value of -57.9 ± 0.42 wt. % (1σ,n=3).

Mineral Type	Sample name	H_2O content (wt.%)	δD (‰)	$\delta^{18}O$ (‰)
Amphibole	SPKC amph 1 G6	1.26	-34.0	5.77
	SPKC amph 1 G7	0.68	-47.8	5.66
	SPKC amph 1 G8	0.99	-53.8	5.78
	SPKC amph 1 G11	1.10	-44.9	5.84
	SPKC amph 1 G12	0.58	-32.4	5.81
	SPKC amph 1 G13	0.90	-55.3	5.84
	SPKC amph 2 G1	0.52	-74.1	5.93
	SPKC amph 2 G2	0.93	-25.7	5.95
	SPKC amph 2 G3	1.29	-44.9	5.79
	SPKC amph 2 G5	0.71	-52.5	6.02
Phlogopite	SPK phl 1 G1	0.91	-75.8	5.35
	SPK phl 1 G4	1.19	-68.7	5.48
	SPK phl 1 G5	1.46	-65.0	5.6
	SPK phl 2 G4	1.75	-54.6	5.67
	SPK phl 2 G2	2.5	-49.7	5.5
	SPKC phl 3 G6	1.6	-58.8	5.47
	SPKC phl 3 G8	2.54	-57.7	5.52
	SPKC phl 2 G3	0.72	-64.3	5.51
	SPKC phl 2 G4	1.18	-67.5	5.56
	SPKC phl 2 G6	1.69	-79.9	5.62

8.2. D/H ratio of micas and amphiboles

Amphibole

The δD values documented for the 10 selected SPKC amphibole megacrysts analysed in this study define a wide range, spanning from -74 to -26 ‰, with an average of -47 ± 14 ‰ (1σ, $n = 10$) (Fig. 8.1a). Boettcher and O'Neil (1980) calculated the δD composition of the upper mantle as being -70 ± 10 ‰, which overlaps with the more negative end of the amphibole megacryst range (Table 8.1). Amphibole megacrysts in alkali basalts from the Carpathian-Pannonian region (Demény et al. 2005) were shown to have a range of δD values from - 80 to - 50 ‰, which also partially overlaps with and is more restricted than the range for the SPKC amphibole megacrysts. On Figure 8.1a, there is a positive correlation of water content and δD values. DeLoule et al. (1991) did that illustrates extreme H isotope zoning in amphibole megacrysts, which might complicate interpretations of this data

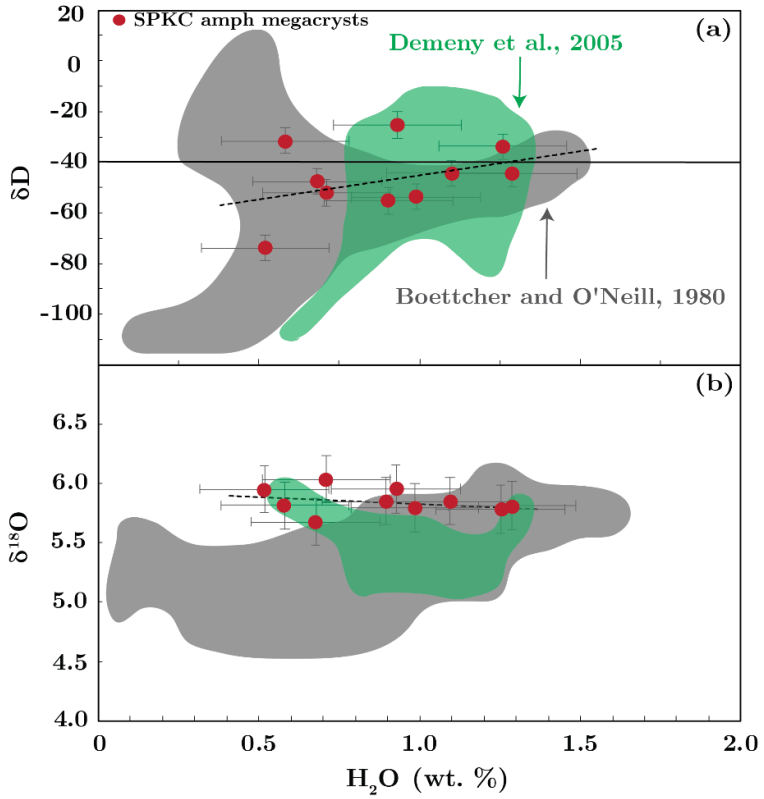

Figure 8.1: a) δD (in ‰ relative to SMOW) as a function of the water content of the amphibole megacrysts, (b) $\delta^{18}O$ (in ‰ relative to SMOW) also as a function of water content. Dotted lines show the regression lines for each plot while the error bars represent 2σ uncertainty for the SPKC amphibole megacrysts. Amphibole megacrysts data from (i)the Carpathian-Pannonian region (Demény et al., 2005; green coloured fielded) and (ii) alkali basalt and kimberlite derived amphibole grains (Boettcher and O'Neil, 1980; gray coloured fielded) were used for comparison with the SPKC amphibole.

Phlogopite

The δD values for the 10 phlogopite megacrysts show some overlap with the hydrogen isotopic compositions measured in the amphibole grains. These grains differ in that they define a narrower range of δD values (-80 to -50 ‰), and also have an overall lower average value, -64 ± 9.35 (1σ, $n = 10$), as seen in Fig. 8.2a. There is no observable isotopic difference measured in the δD values of the phlogopite megacrysts collected from the various sample localities across the Saltpeterkop complex (Table 8.1).

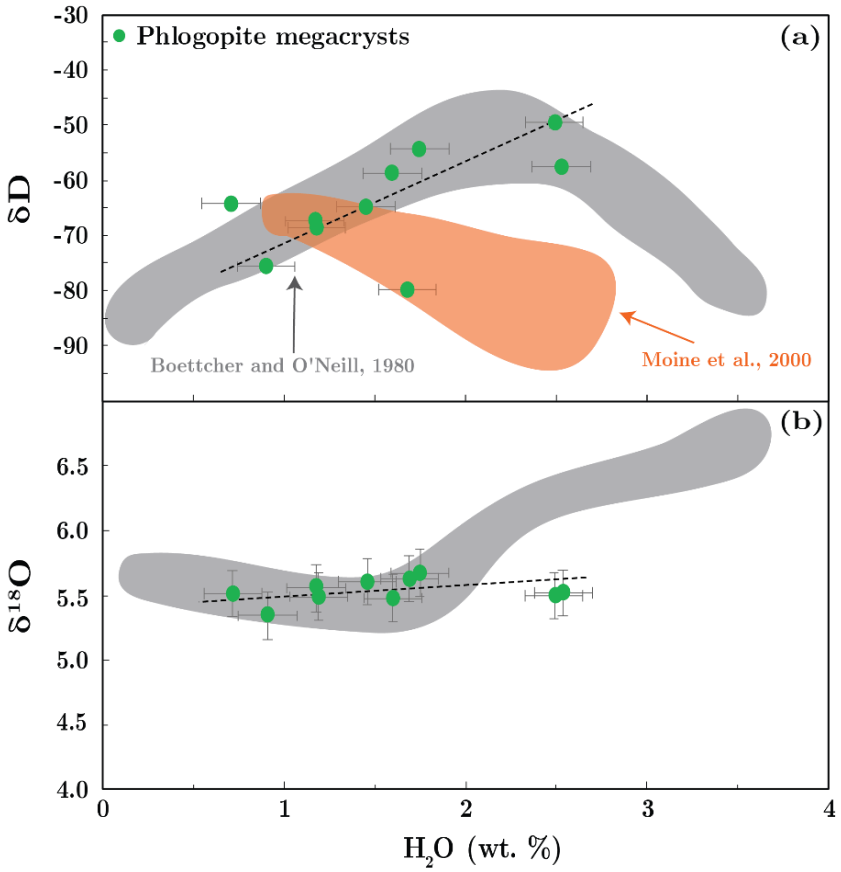

Figure 8.2: (a) δD (in ‰ relative to SMOW) as a function of the water content of the phlogopite megacrysts, (b) δ^{18}O (in ‰ relative to SMOW) also as a function of water content. Dotted lines show proposed line of best fit for each plot while the error bars represent 2σ uncertainty for the SPKC phlogopite megacrysts. (i) Phlogopite grains in xenoliths from Kerguelen Island, South Indian Ocean (Moine et al.,2000; peach coloured fielded) and (ii) alkali basalt and kimberlite derived phlogopite grains (Boettcher and O'Neil, 1980; gray coloured fielded) were used for comparison withthe SPKC phlogopite megacrysts.

Sheppard and Epstein (1970) reported that unaltered phlogopite grains derived from upper mantle to lower crustal regions have δD values of -58 ± 18 ‰, which coincides well with both the range and magnitude of the values seen for the SPKC phlogopite megacrysts. The δD values for the phlogopite megacrysts are comparable to those of δD values recorded for hydrous minerals from mantle xenoliths (−70 ± 10 ‰; Boettcher and O'Neil, 1980).

8.3. Oxygen Isotopes

Amphibole

The $\delta^{18}O$ values of the 10 amphibole megacrysts range from 5.66 to 6.02 ‰ and average 5.84 ± 0.10 ‰ (1σ); (Table 8.1). This average value is slightly higher than the $\delta^{18}O$ value for the primary mantle (5.5 ± 0.20 ‰; Chazot et al. 1997) and also higher than values reported for upper mantle-derived amphiboles hosted in alkali basalts, which have reported average $\delta^{18}O$ values of 5.26 ± 0.40 ‰ (1σ, n= 10) (Boettcher and O'Neil, 1980), 5.27 ± 0.15 ‰ (1σ, n= 8) (Dobosi et al., 1997) and 5.45 ± 0.23 ‰ (1σ, n= 15) (Demeny et al. 2005). There is no correlation between $\delta^{18}O$ and any chemical parameter (e.g. water content; Fig. 8.1b). A

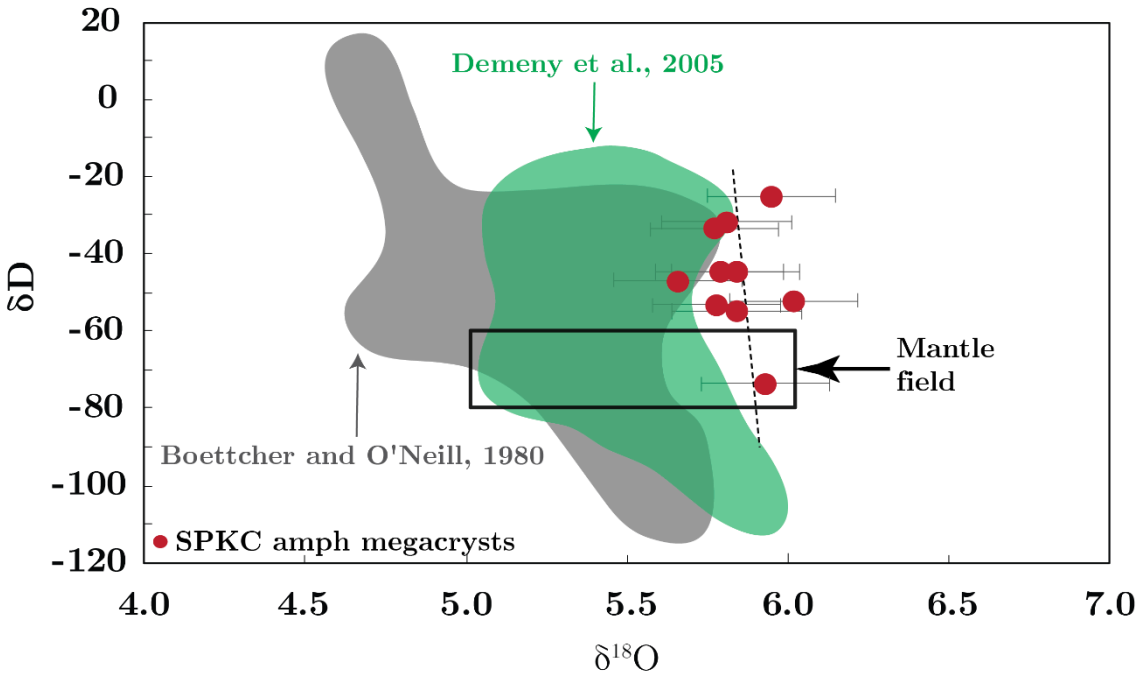

Figure 8.3: δD versus $\delta^{18}O$ (in ‰ relative to SMOW) of the amphibole megacrysts (red dots). Amphibole megacrysts data from (i) the Carpathian-Pannonian region (Demény et al., 2005; green coloured fielded) and (ii) alkali basalt and kimberlite derived amphibole grains (Boettcher and O'Neil, 1980; gray coloured fielded) were used for comparison withthe SPKC amphibole megacrysts. Error bars represent 2σ uncertainty for the SPKC amphibole megacrysts

subsequent plot drawn for the $\delta^{18}O$ against δD reveals that no observable or clear relationship exists between the two as the δD values scatters at relatively constant $\delta^{18}O$ values (Fig. 8.3).

Phlogopite

The $\delta^{18}O$ values for the phlogopite megacrysts rangess from 5.35 to 5.67 ‰, with an average value of 5.53 ± 0.09 ‰ (1σ, $n = 10$); (Table 8.1). The phlogopite $\delta^{18}O$ values are lower than those of the the amphiboles, falling closer to the accepted average mantle $\delta^{18}O$ value of 5.5 ± 0.20 ‰ (Chazot et al., 1997). Comparison of the SPKC megacrysts with kimberlitic micas reported by Boettcher and O'Neil (1980) shows that the kimberlitic grains preserve $\delta^{18}O$ values that average around 5.50 ± 0.35 ‰ (1σ, $n = 10$), nearly identical to those documented for the Salpeterkop samples. Plots of $\delta^{18}O$ as a function of (i) water content (Fig. 8.2b) and (ii) δD (Fig. 8.4), reveals that $\delta^{18}O$ values for the SPKC phlogopite megacrysts remain nearly constant with respect to these other parameters.

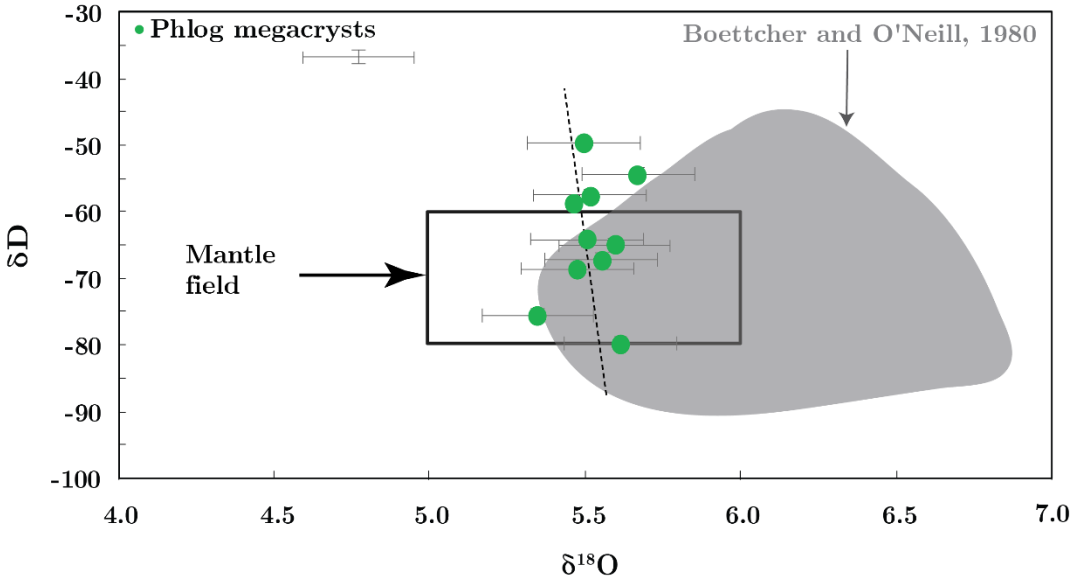

Figure 8.4: δD versus $\delta^{18}O$ (in ‰ relative to SMOW) of the phlogopite megacrysts (green dots).Alkali basalt and kimberlite derived phlogopite grains (Boettcher and O'Neil, 1980; gray coloured fielded) were used for comparison against the SPKC phlogopite megacrysts. Error bars represent 2σ uncertainty for the SPKC phlogopite megacrysts

8.4. δD and water content versus Fe^{+3}/Fe^{tot}

The low OH content in the amphibole and phlogopite megacrysts could be an indication that the minerals have experienced loss of water (hydroxyl anions) from their mineral structure (i.e. undergone degassing). Several authors (e.g. Demeny et al., 2006) have shown that the

behaviour and oxidation state of iron in hydrous minerals (i.e. the ratio of Fe^{+3}/Fe^{tot}) can correlate well against δD, and can therefore be used to provide constraints on whether the mineral had experienced degassing, as well as determining whether the style of degassing was more akin to dehydration or dehydrogenation. Thus, the ratio of Fe^{+3}/Fe^{tot} in the SPKC amphibole and phlogopite megacrysts was calculated, but since the Fe^{2+} and Fe^{3+} abundances of the megacrysts could not be determined experimentally, various models were applied to stoichiometrically approximate these values.

Amphibole

An Excel spreadsheet developed by Locock (2014) and the recalculation methods outlined by Leake et at. (1997) were both used to calculate the Fe^{+3}/Fe^{tot} ratios of the SPKC amphibole megacrysts. The Fe^{+3}/Fe^{tot} ratios for the amphibole grains determined using the model by Locock, (2013) yielded values between 0.03 and 0.08 and the calculations of Leake et at (1997) yielded values ranging from 0.08 and 0.24. While these two models provide different values for the ratio of Fe^{+3}/Fe^{tot} in the amphibole megacrysts, the overall trends observed when Fe^{+3}/Fe^{tot} plotted against both water content and δD are extremely similar. The implication of this is that, while the absolute values obtained by either or both models may not be accurate, they can still be used to document the trends and approximate behaviour of Fe^{3+}/FeO^{tot} in the amphibole megacrysts.

A weak positive correlation is observed in a plot of Fe^{3+}/FeO^{tot} against water content for the SPKC amphibole megacryst data (Fig. 8.5a). In the plot of δD against Fe^{3+}/Fe^{tot} (Fig. 8.5b), no correlation is displayed, meaning that the relationship between Fe^{3+}/FeO^{tot} and δD cannot be used to further comment and/or constrain the mode of degassing affecting these grains. In a plot of Fe^{3+}/FeO^{tot} against water content, a broadly positive correlation has been shown to exist in the amphibole megacryst data. For the plot of δD against Fe^{3+}/Fe^{tot}, too much scatter exists in the data for a correlation to be interpreted, meaning that the relationship between Fe^{3+}/FeO^{tot} and δD cannot be used to further comment and/or constrain the mode of degassing affecting these grains.

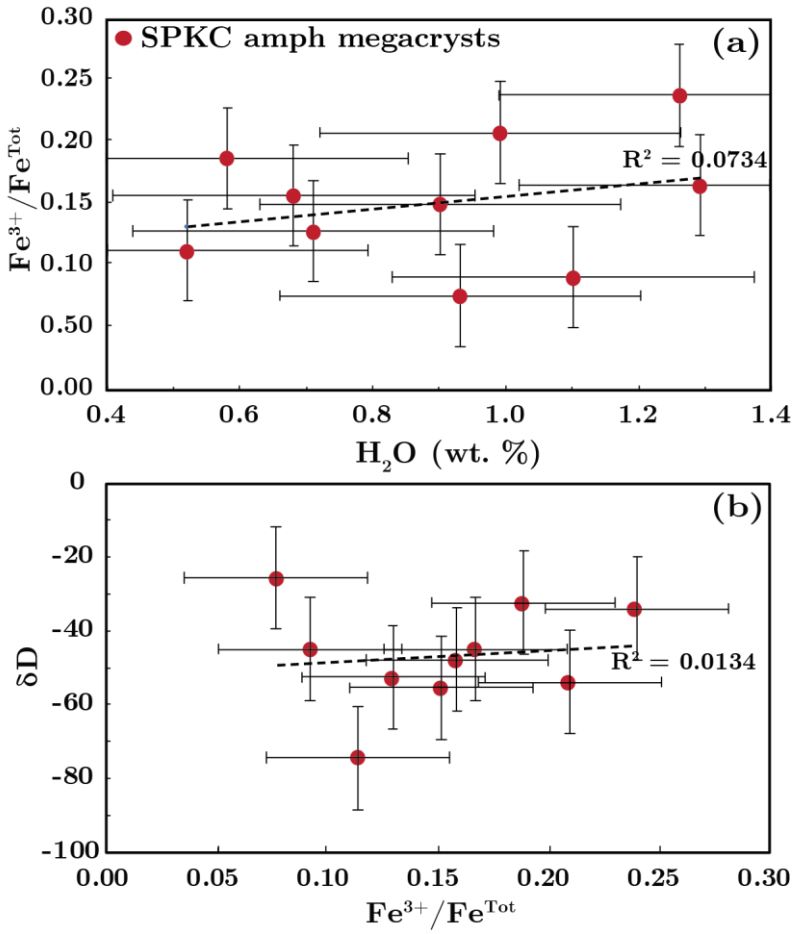

Figure 8.5: (a) A plot of Fe^{3+}/FeO^{tot} against the water content for the SPKC amphibole megacryst data. (b) δD of the SPKC amphibole megacrysts plotted against Fe3+/Fetot. The ratio of Fe^{3+}/FeO^{tot} used here was calculated using the method outlined by Leake et at. (1997)

Phlogopite

The Fe^{3+}/FeO^{tot} values for phlogopite could not be estimated, meaning that plots of Fe^{3+}/FeO^{tot} versus water content and δD (respectively) could not be constructed and that no further comments could be made on the style of degassing that affected these megacrysts.

9. Radiogenic isotopes

Radiogenic isotope data provide crucial information necessary to understand the relationship between the different megacryst minerals and between them, their parental melt and its source. Two clinopyroxene, eight amphibole, six phlogopite and two ilmenite megacrysts were selected for Sr, Nd and Pb isotopic analysis. $^{87}Sr/^{86}Sr$, $^{143}Nd/^{144}Nd$, $^{206}Pb/^{204}Pb$, $^{207}Pb/^{204}Pb$ and $^{208}Pb/^{204}Pb$) isotope ratios were determined via solution MC-ICP-MS are reported in Tables 9.1-9.3. The 2σ errors for the measured isotope ratios are 0.00001 for $^{87}Sr/^{86}Sr$; $>$ 0.0008 for $^{143}Nd/^{144}Nd$; $>$ 0.007 for $^{206}Pb/^{204}Pb$; $>$ 0.005 for $^{207}Pb/^{204}Pb$ and $>$ 0.01 for $^{208}Pb/^{204}Pb$. Initial isotope ratios were obtained for clinopyroxene, amphibole and phlogopite using the ratios of parent and daughter element concentrations (e.g., Rb/Sr, Sm/Nd, U/Pb, Th/Pb) obtained by solution ICP-MS on splits of the same samples analysed for isotope ratios (Tables 9.1-9.3).

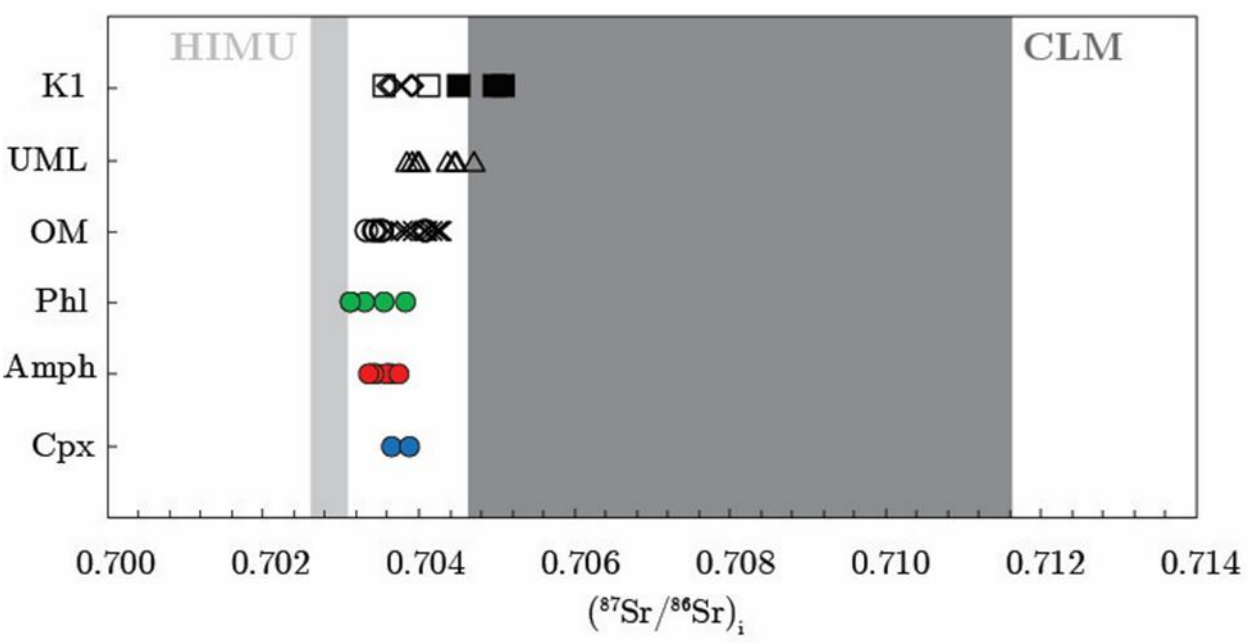

Figure 9.1: $^{87}Sr/^{86}Sr_i$ isotope ratio diagram showing the measured range in values for the clinopyroxene, amphibole and phlogopite megacrysts of the Salpeterkop Complex (2σ uncertainty for the SPKC megacrysts are smaller than the symbols on the graph); olivine melilitites (OM) of Sutherland (open circles), OM of Salpeterkop (crosses) and ultramafic lamprophyres (UML) of Salpeterkop (open triangles) (Janney et al. 2002 and unpublished); clinopyroxene (diamonds), ilmenite (coloured squares) and garnet (open squares) megacrysts from Group 1 kimberlites (K1) (Davieset al. 2001 and Nowell et al. 2004). Coloured grey fields represent HIMU ocean island basalts (OIB; light grey; Chaffey et al. 1989 and Chauvel et al. 1992) and CLM (dark grey; Hawkesworth, 1990).

9.1. Sr, Nd and Pb isotope results

Clinopyroxene and amphibole megacrysts

The initial $^{87}Sr/^{86}Sr$ and $^{143}Nd/^{144}Nd$ isotopic ratios measured falls within the ranges 0.70365 – 0.70388 and 0.51273 – 0.51277 (equivalent to eNd of +3.8 – +4.6) respectively for the SPKC clinopyroxene megacrysts and 0.70334 – 0.70373 and 0.51264 – 0.51276 (i.e., ε_{Nd} = +2.0 to +4.2) respectively for amphibole. The amphibole megacrysts generally show marginally less radiogenic ratios, compared to clinopyroxene. The initial isotopic ratios for both clinopyroxene and amphibole overlap with values of Cr-poor clinopyroxene and garnet megacrysts from on- and off-craton Group I kimberlites in southern Africa (Fig. 9.1; Davies et al., 2001 and Nowell et al., 2004). The Sutherland and Salpeterkop olivine melilitites (0.70357 – 0.70427 and 0.51263 – 0. 51275; Janney et al. 2002 and unpublished) and Salpeterkop ultramafic lamprophyres (0.70382 – 0.70470 and 0.51264 – 0. 51271; Janney et al. 2002 and unpublished) significantly overlap with both clinopyroxene and amphibole megacrysts, with the melilitites and lamprophyres extending to more radiogenic signatures for both Sr and Nb. On the $^{143}Nd/^{144}Nd$ – $^{87}Sr/^{86}Sr$ plot (Fig 9.2), both SPKC clinopyroxene and amphibole megacrysts plot within the depleted mantle quadrant and outside the fields defined for North Atlantic MORB and OIB (Dosso et al. 1991 and White and Hofmann, 1982 for North Atlantic MORB and OIB data respectively).

Initial $^{206}Pb/^{204}Pb$ ratios for clinopyroxene megacrysts (19.27 - 19.43) overlap with those for the olivine melilites from Sutherland (19.20 - 19.39) and from Salpeterkop (18.78 – 19.56; Janney et al., 2002 and unpublished). The amphibole megacrysts (19.57 - 19.97) on the other hand record values higher than both the clinopyroxene megacrysts and melilite samples from both Sutherland and Salpeterkop. The initial $^{207}Pb/^{204}Pb$ ratios for the clinopyroxene megacrysts (15.675 - 15.686) are lower than values recorded for amphibole (15.687 - 15.718). Both clinopyroxene and amphibole megacryst phases overlap with the olivine melilitite localities (15.650 - 15.689 and 15.637 - 15.691 for Sutherland and Salpeterkop respectively) and ultramafic lamprophyres (15.597 – 15.690). On the Pb-Pb isotopic diagram (Fig. 9.3), both clinopyroxene and amphibole megacrysts plot intermediate to the fields defined by North Atlantic MORB and HIMU OIB, forming a trend that aligns with clinopyroxene grains from group 1 kimberlites but at higher $^{206}Pb/^{204}Pb$ ratios (Davies et al. 2001). The SPKC

clinopyroxene and amphibole megacrysts plot closer towards HIMU OIB, relative to the melilitites and lamprophyres and the amphiboles closer towards HIMU OIB, relative to the clinopyroxene.

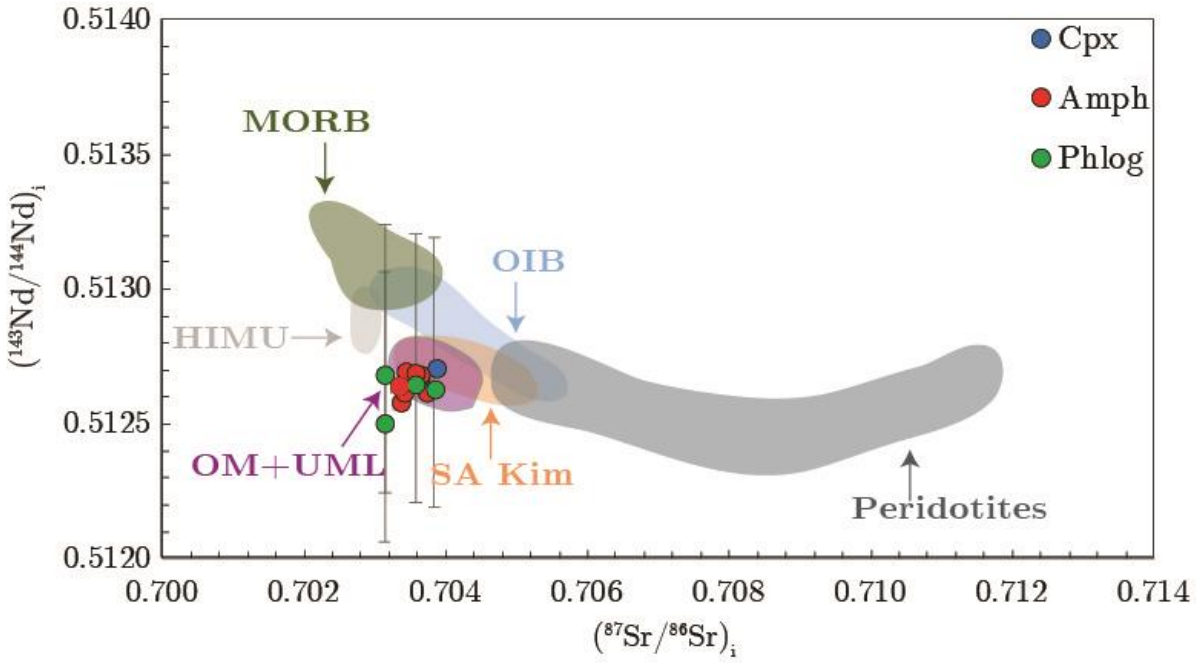

Figure 9.2: $^{87}Sr/^{86}Sr_i$ versus $^{143}Nd/^{144}Nd_i$ plot comparing the clinopyroxene, amphibole and phlogopite megacrysts of the Salpeterkop Complex with (i) OM of Sutherland and Salpeterkop and UML of Salpeterkop (purple field; Janney et al. 2002 and unpublished); (ii) Southern African kimberlites (orange field; Nowell et al. 2004); (iii) MORB (green field; Dosso et al. 1991 and White and Hofmann, 1982); (iv) OIB (blue field; White and Hofmann, 1982); (v) HIMU OIB (grey field; Chaffey et al. 1989 and Chauvel et al. 1992) and (vi) Kimberley peridotite xenoliths (whole-rock measurements, (dark grey; Hawkesworth, 1990)included for comparison. 2σ uncertainty for the SPKC clinopyroxene and amphibole megacrysts are smaller than the symbols used on the graph, while 2σ uncertainty for the phlogopite megacrysts has been plotted. The data for SPKC Phl 2 G4 was not included as it does not fall within the bounds of this plot.

Phlogopite

The initial $^{87}Sr/^{86}Sr$ and $^{143}Nd/^{144}Nd$ isotopic ratios for these samples are 0.70315 – 0.70385 (aside from one anomalous sample with a value of 0.70177) and 0.511657 – 0.512739 (i.e. eNd = -17.1 to +4.0) respectively. Two of the samples had anomalously unradiogenic Nd isotope compositions (with eNd of -17.1 and -9.8). Apart from these two samples, the other phlogopites all fall in a narrow range of eNd values from +3.0 to +4.0. The phlogopite megacrysts show significant overlap in terms of Sr and Nd isotope ratios with the Sutherland and Salpeterkop melilitites, as well as Cr-poor clinopyroxene and garnet megacrysts from Group

I kimberlites (Fig. 9.1). These grains plot within the depleted mantle quadrant and outside the fields defined for North Atlantic MORB and HIMU OIB (Fig. 9.2).

The calculated initial ratios for $^{206}Pb/^{204}Pb$ and $^{207}Pb/^{204}Pb$ range from 19.47 to 19.55 and from 15.702 to 15.703 respectively, for the phlogopite megacrysts. On the Pb-Pb isotopic diagram in Figure 9.3 these phlogopite samples plot between both North Atlantic MORB and HIMU OIB and between the clinopyroxene and amphibole megacrysts, within. The phlogopite grains do appear to have slightly elevated initial $^{207}Pb/^{204}Pb$ ratios, relative to the other megacryst phases, but are however within 2σ uncertainty.

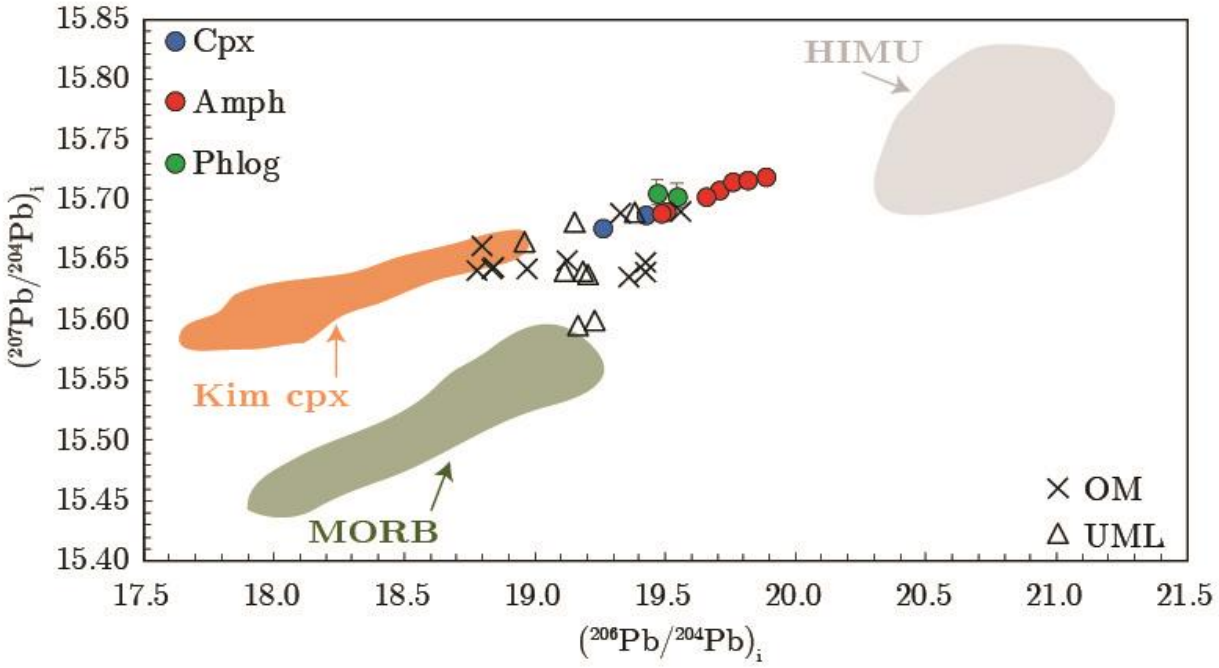

Figure 9.3: $(^{207}Pb/^{204}Pb)_i$ Versus $(^{206}Pb/^{204}Pb)_i$ plot comparing the clinopyroxene, amphibole and phlogopite megacrysts of the Salpeterkop Complex with (i) melilitites (OM) of Sutherland and Salpeterkop (crosses) and lamprophyres (open triangles) (Janney et al. 2002 and unpublished); (ii) MORB (green field; Dosso et al. 1991 and White and Hofmann, 1982), (iii) HIMU OIB (grey field; Chaffey et al. 1989 and Chauvel et al. 1992) and (iv) clinopyroxene megacrysts from Group 1 kimberlites (Gibeon Province; peach field;Davies et al. 2001). 2σ uncertainty for the SPKC clinopyroxene and amphibole megacrysts are smaller than the symbols used on the graph, while 2σ uncertainty for the phlogopite megacrysts has been plotted.

Table 9:1: Rb, Sr, and $^{87}Sr/^{86}Sr$ results for the various megacrysts of the SPKC megacryst suite

Mineral	Sample	Rb (ppm)	Sr (ppm)	$(^{87}Sr/^{86}Sr)_M$	$(^{87}Sr/^{86}Sr)_i$
Cpx	SPK M5 G3	0.0004	111.0	0.703653	0.703653
	SPK M5 G4	0.0004	105.4	0.703884	0.703884
Amph	SPKC amph 1 G6	2.339	189.2	0.703632	0.703594
	SPKC amph 1 G7	3.047	212.7	0.703420	0.703376
	SPKC amph 1 G8	3.073	193.8	0.703491	0.703442
	SPKC amph 1 G12	1.131	145.5	0.703676	0.703652
	SPKC amph 1 G11	3.433	214.5	0.703635	0.703586
	SPKC amph 1 G13	2.049	175.0	0.703770	0.703734
	SPKC amph 2 G1	1.753	293.6	0.703440	0.703421
	SPKC amph 2 G2	4.278	225.3	0.703402	0.703343
Phlog	SPK phl 1 G1	315.4	148.6	0.710394	0.703848
	SPK phl 1 G4	332.9	114.6	0.711816	0.703589
	SPK phl 1 G5	277.2	143.4	0.709111	0.703151
	SPKC phl 2 G4	341.6	149.8	0.710364	0.703332
	SPKC phl 2 G6	332.1	131.5	0.711448	0.703146
	SPKC phl 2 G3	143.2	111.9	0.707091	0.703653

The abbreviations cpx, amph, phlog and ilm denote the mineral phases clinopyroxene, amphibole, phlogopite and ilmenite respectively. $(^{87}Sr/^{86}Sr)_M$ refers to the measured Sr isotopic ratios, while $(^{87}Sr/^{86}Sr)_i$ refers to the calculated initial Sr isotopic ratios using the Duncan et al. (1978) K-Ar age of 74.7 Ma.

Table 9:7:2: Sm, Nd, and $^{143}Nd/^{144}Nd$ results for the megacrysts of the SPKC megacryst suite

Mineral	Sample	Sm (ppm)	Nd (ppm)	$(^{143}Nd/^{144}Nd)_M$	$\pm 2\sigma$ internal	$(^{143}Nd/^{144}Nd)_i$	ε_{Nd} (T)
Cpx	SPK M5 G3	1.64	7.60	0.51279	0.00001	0.51273	3.8 ± 0.3
	SPK M5 G4	1.58	7.41	0.51283	0.00001	0.51277	4.6 ± 0.2
Amph	SPKC amph 1 G6	3.19	15.00	0.51278	0.00001	0.51272	3.7 ± 0.4
	SPKC amph 1 G7	3.35	14.83	0.51270	0.00001	0.51264	2.0 ± 0.4
	SPKC amph 1 G8	3.19	14.26	0.51282	0.00001	0.51276	4.3 ± 0.2
	SPKC amph 1 G12	2.96	13.70	0.51281	0.00001	0.51274	4.1 ± 0.2
	SPKC amph 1 G11	3.81	16.43	0.51282	0.00001	0.51275	4.2 ± 0.3
	SPKC amph 1 G13	3.19	14.00	0.51274	0.00001	0.51268	2.7 ± 0.5
	SPKC amph 2 G1	6.44	25.13	0.51275	0.00001	0.51268	2.7± 0.7
	SPKC amph 2 G2	4.15	16.42	0.51277	0.00001	0.51270	3.2 ± 0.6
Phlog	SPK phl 1 G1	0.961	0.421	0.51335	0.00001	0.51269	3.0 ± 8.0
	SPK phl 1 G4	0.683	0.336	0.51330	0.00001	0.51270	3.3 ± 9.4
	SPK phl 1 G5	0.438	0.438	0.51323	0.00001	0.51274	4.0 ± 8.6
	SPKC phl 2 G4	0.739	0.457	0.51220	0.00002	0.51166	-17.1 ± 15.3
	SPKC phl 2 G6	-	-	0.51305	0.00001	-	-
	SPKC phl 2 G3	0.562	0.269	0.51264	0.00001	0.51203	-9.8 ± 12.3

The abbreviations cpx, amph and phlog denote the mineral phases clinopyroxene, amphibole and phlogopite respectively. $(^{143}Nd/^{144}Nd)_M$ refers to the measured Nd isotopic ratios, while $(^{143}Nd/^{144}Nd)_M$ refers to the calculated initial Nd isotopic ratios using the Duncan et al. (1978) K-Ar age of 74.7 Ma. Sm/Nd and $^{143}Nd/^{144}Nd$ values of 0.1960 and 0.512630 respecgtively were assumed for CHUR (Bouvier et al., 2008).

Table 9:7:3: Pb results for the various megacrysts of the SPKC megacryst suite

Mineral	Sample	Pb	Th	U	$(^{208}Pb/^{204}Pb)_M$	$\pm 2\sigma$ internal	$(^{208}Pb/^{204}Pb)_i$	$(^{207}Pb/^{204}Pb)_M$	$\pm 2\sigma$ internal	$(^{207}Pb/^{204}Pb)_i$	$(^{206}Pb/^{204}Pb)_M$	$\pm 2\sigma$ internal	$(^{206}Pb/^{204}Pb)_i$
Cpx	SPK M5 G3	0.11	0.01	0.02	39.3666	0.0041	39.3493	15.6927	0.0015	15.6860	19.5726	0.0019	19.4309
	SPK M5 G4	0.10	0.00	0.03	39.1293	0.0105	39.1238	15.6847	0.0045	15.6750	19.4714	0.0052	19.2653
Amph	SPKC amph 1 G6	0.30	0.05	0.02									
	SPKC amph 1 G7	0.26	0.06	0.02	39.5523	0.0038	39.4972	15.7211	0.0015	15.7180	20.0354	0.0019	19.9694
	SPKC amph 1 G8	0.22	0.05	0.01	39.3995	0.0042	39.3444	15.7088	0.0014	15.7067	19.8365	0.0017	19.7927
	SPKC amph 1 G12	0.18	0.04	0.01	39.4850	0.0049	39.4351	15.7156	0.0017	15.7131	19.8928	0.0020	19.8398
	SPKC amph 1 G11	0.26	0.07	0.02	39.3118	0.0034	39.2402	15.6907	0.0013	15.6883	19.6409	0.0017	19.5902
	SPKC amph 1 G13	0.28	0.05	0.01	39.2920	0.0029	39.2488	15.6892	0.0010	15.6874	19.6046	0.0013	19.5664
	SPKC amph 2 G1	0.33	0.10	0.02	39.4231	0.0042	39.3515	15.7031	0.0016	15.7005	19.7957	0.0019	19.7406
	SPKC amph 2 G2	0.22	0.04	0.01	39.4988	0.0030	39.4534	15.7175	0.0010	15.7152	19.9489	0.0011	19.8998
Phlog	SPK phl 1 G1	0.26	0.00	0.00	39.2182	0.0133	39.2139	15.7017	0.0051	15.7017	19.5499	0.0068	19.5499
	SPK phl 1 G4												
	SPK phl 1 G5												
	SPKC phl 2 G4	0.27	0.00	0.00	39.2962	0.0286	39.29316	15.7037	0.0115	15.7033	19.4810	0.0149	19.4737
	SPKC phl 2 G6					0.0041							
	SPKC phl 2 G3					0.0105							

The abbreviations cpx, amph, phlog and ilm denote the mineral phases clinopyroxene, amphibole, phlogopite and ilmenite respectively.

10. Discussion

The thesis serves as a means to establish and constrain the relationship between minerals within the megacrysts suite and cumulate xenoliths of the Salpeterkop carbonatite complex, as well as between the megacryst suite and the various igneous rocks present in the complex. Important questions of this chapter with regard to the origin and petrogenesis of the Saltpeterkop megacrysts include:

a) What is the origin and crystallisation history of the megacrysts from the Salpeterkop complex? Are the megacrysts derived from a common parent magma, a series of related magmas derived from the same source or from a variety of related sources (such as different mixtures of the same source components)?

b) Can we constrain the order of crystallisation of the megacryst phases analysed from the complex, and if so, what is this order?

c) Do the water contents and H isotope compositions of the hydrous megacrysts plausibly reflect those that they initially had upon crystallisation?

d) What similarities exist between the megacrysts and the various rock types (including particularly the olivine melilitites, ultramafic lamprophyres and carbonatites) of the complex? Can any genetic relationships be established between these rock types and the magma(s) parent to the megacrysts?

e) What constraints can be placed on the pressures and temperatures of crystallisation of the megacrysts?

10.1. Geochemical evolution of the megacrysts and mantle xenoliths

Clinopyroxene

The monomineralic nature of the SPKC clinopyroxene megacrysts coupled with their large size, homogeneity and uniform composition suggests an origin from a homogeneous body of melt. Major and trace element compositions of megacrysts display systematic differentiation trends as a function of Mg-number and Ca-number which are consistent with progressive fractional crystallisation. The negative correlation observed when Ca-number is plotted as a function of Mg-number (Fig. 6.3d) is consistent with a decrease in crystallisation temperature with increasing Fe content along the diopside-enstatite solvus.

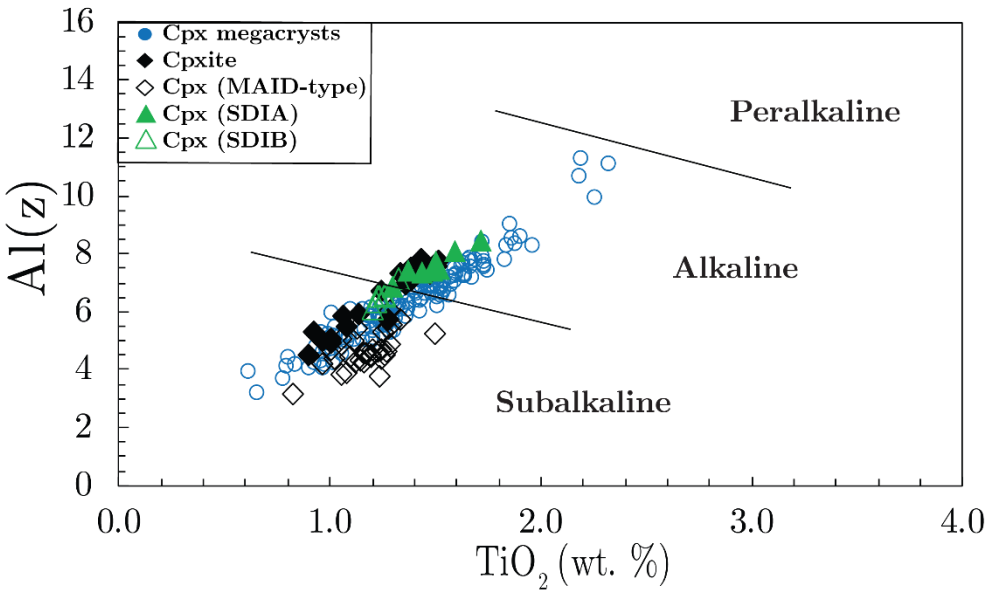

Figure 10.1: TiO_2 wt% versus. Al(z) for the SPKC clinopyroxene megacrysts and xenolith grains.Subalkaline/alkaline/peralkaline fields from Le Bas (1962). Al(z) refes to the percentage of the tetrahedral site occupied by Al.

On a plot of Al(z) (percentage of the tetrahedral site occupied by Al) versus TiO_2 (Fig. 10.1), the clinopyroxene data form a continuous array between the subalkaline and alkaline fields (Le Bas, 1962). The data appears to reflect a fractionation trend as the highest Mg-number clinopyroxene megacrysts have the highest TiO_2 and Al(z) values (Fig. 6.3a and 10.1), which suggests that the clinopyroxene megacrysts crystallised from more alkaline rather than subalkaline liquids. This argument is supported by the fact that the SPKC clinopyroxene

megacrysts have greater abundances of tetrahedral aluminum (Al^{iv}) than octahedral aluminum (Al^{vi}) (Al^{iv}/Al^{vi} ratio ranges from 1.5 to 4.3), which is characteristic of clinopyroxenes from alkalic melts (Le Bas, 1962).

TiO_2 generally correlates negatively with Mg-number in clinopyroxene, which is typical of megacrysts associated with alkali basalts (Fig. 6.3a). TiO_2 and Al_2O_3 both display significantly higher degrees of variability in the clinopyroxene megacrysts relative to the other major oxides, suggesting that Ti and Al were more variable in the parent melt. In the plots of both Al_2O_3 and TiO_2 versus Mg-number, the clinopyroxene megacryst data fall into two clusters. Each of these trends has a negative slope on the Mg# vs. TiO_2 plot, with the higher Al_2O_3 samples also higher in TiO_2 (Fig. 6.3a-b). Since these trends appear parallel, rather than converging at high Mg-number, they could possibly be the result of two separate primary magma compositions.

During closed-system magmatic fractionation, Cr and Sc typically behave compatibly in clinopyroxene. In the SPKC clinopyroxene megacrysts and clinopyroxenite xenolith grains, there is a large variation in Cr for a given Mg number (Fig. 7.1h), which may suggest open-system fractionation, but this could also be complicated by the fact that Cr_2O_3 abundances in the megacrysts are mostly near the limit of detection. Sc on the other hand exhibits the compatible behaviour expected (Fig. 7.1d). Other trace elements such as the REE, HSFE, and Sr which behave incompatibly in clinopyroxene all display the expected negative trends versus Mg-number (Fig. 7.1a-c, e-g) in the SPKC clinopyroxene megacryst and xenolith samples. These trends are consistent with the megacryst and xenolith grains having crystallised from a progressively fractionating magma. The REE patterns of the clinopyroxene megacrysts are also similar in shape and concentration to those of clinopyroxene megacrysts from other localities. These similarities suggest that the SPKC clinopyroxene megacrysts and xenolith grains share a similar alkali basaltic parent melt with these other.

The clinopyoxene megacrysts show complete overlap in Sr-Nd-Pb isotope ratio values with the Salpeterkop olivine melilitites and ultramafic lamprophyres, which may be an indication that the clinopyroxene megacrysts share some genetic relationship with either of

these rocks (Fig. 9.2 and 9.3 respectively). Studies of the Western Cape olivine melilitites, including Saltpeterkop (Janney et al., 2002) showed that the isotopic trends they display are consistent with mixing between a HIMU-type component (high $^{206}Pb/^{204}Pb$, low $^{87}Sr/^{86}Sr$, intermediate $^{143}Nd/^{144}Nd$) and a metasomatised lithospheric component (low $^{206}Pb/^{204}Pb$, high $^{87}Sr/^{86}Sr$ and low $^{143}Nd/^{144}Nd$. If the megacrysts are genetically related to either the OM or UML, then the radiogenic isotope trends seen in the clinopyroxene megacrysts suggests that their parental melt was likely also a result of mixing between a HIMU-type component such as recycled oceanic crust and carbonatite-metasomatised wall-rock material from the lithospheric mantle, as proposed by Janney et al. (2002). This mixing or more open-system behaviour may account for the lack simple linear negative correlations with Mg-number seen in the incompatible trace element data of the megacrysts.

Comparisons between the various cumulate xenolith types associated with the Salpeterkop complex and clinopyroxene megacrysts have shown that a major difference is that they each have distinct relationships of Al_2O_3 and TiO_2 with Mg number. Here the xenolithic clinopyroxene grains display trends of increasing Ti and Al with decreasing Mg-number. Several compositional similarities between the clinopyroxene xenolithic grains and the clinopyroxene megacrysts are notable, such as with Ca-number and Na_2O versus Mg-number respectively, where the xenolith grains follow and continue the trends displayed in the megacryst data, but at lower Mg-numbers. Other similarities include near-identical trends and enrichment values between the clinopyroxenite xenolith and megacryst grains in both chondrite-normalised REE and primitive mantle-normalised incompatible element plots (Fig. 7.2a-b). These similarities suggest that the SPKC clinopyroxene xenolith and megacryst grains share a common parent magma, with the megacrysts crystallising earlier in the crystallisation sequence.

The MAID-type xenolith grains differ slightly from the other xenolithic clinopyroxene grains due to the fact that they constitute a distinct high-Na_2O trend. This high-Na_2O trend could be the result of a different crystallising assemblage, one in which clinopyroxene was the dominant mineral present, and was the dominant host of Na_2O. Alternatively, the low-Na_2O trend seen in the other xenolithic clinopyroxene grains could be the result of a higher proportion of Na-compatible minerals such amphibole and/or phlogopite.

Amphibole

The amphibole megacrysts display relatively narrow ranges in several major oxides, including Al_2O_3, TiO_2, Na_2O and K_2O, (Fig. 6.5a-d) even though they extend over a wide range of Mg-numbers (61 to 78). The amphibole megacrysts show their greatest degree of major element variability at Mg-numbers greater than 67, while grains with Mg-numbers less than this exhibit more tightly defined trends. Similar patterns are observed for most of the trace elements. This scatter at higher Mg-numbers may represent initial compositional heterogeneities in the parent melt, with the decrease in scatter towards lower Mg-number a product of homogenisation of the parent melt due to increases mixing and/or melt aggregation. It is also worth noting that there are significantly fewer grains with Mg-numbers less than, compared to greater than, 67, which may reflect a potential sampling bias.

The chondrite-normalised REE patterns (Fig. 7.3a) for the amphibole grains show patterns that are similar to and have considerable overlap with those of amphibole megacrysts (i.e. Kakanui, New Zealand and Massif Central, France). The main observable differences between the SPKC amphibole megacrysts and those from other localities is that the former have greater greater variability for a given Mg number, in both LREE and HFSE, as well as lower LREE/HREE ratios, which are likely characteristics of the parent melt. The SPKC clinopyroxene megacrysts are also much more similar to the clinopyroxene megacrysts from other localities than the SPKC amphibole megacrysts are to the other amphibole localities.

A comparison between the amphibole and clinopyroxene megacrysts reveals that they have nearly identical REE patterns (Fig. 7.3). Additionally, the amphibole and clinopyroxene megacrysts also show considerable overlap in their initial $^{87}Sr/^{86}Sr$ and $^{143}Nd/^{144}Nd$ isotopic ratios. The strong chemical similarities between the two megacryst phases is consistent with a broadly co-genetic mantle origin. The amphibole megacrysts do however differ from the clinopyroxene megacrysts as well as from the SPKC OMs and UMLs in that the amphibole samples analysed have Pb isotopic values that are shifted slighly towards the HIMU mantle end-member composition (Fig. 9.3). This would suggest that during crystallisation of the amphibole megacrysts, the megacryst parent melt had a stronger influence of sublithospheric mantle sources (e.g. recycled oceanic crustal component proposed for the Sutherland UMLs; Janney et al., 2002) relative to when the clinopyroxene megacrysts were crystallising. The

xenolith amphibole grains display similar trends and often overlap with the more differentiated end of the amphibole megacryst array (i.e. those megacrysts with Mg-numbers less than 67). This suggests that the xenolithic and megacrystic amphiboles may have crystallised from the same or similar parental melts. The xenolith amphiboles are however slightly more depleted in Al_2O_3 and K_2O and slightly more enriched in Na_2O compared to the megacrysts, which could simply reflect slightly different conditions during the later stages of magmatic evolution (e.g., a different crystallising assemblage or different extents of assimilation of lithospheric wallrock).

Amphibole grains from MAID-types xenoliths also have a distinctly high-Na_2O trend, relative to amphibole from other xenolith types. This is similar to trends seen for MAID xenolithic clinopyroxene grains and may suggest that the MAID-type xenoliths potentially crystallised from a more Na-rich melt.

Phlogopite

Two distinct trends, with a sizable gap between them, can be seen in the phlogopite data at an Mg-number of around 80. From Mg-numbers of 80 to 84, the phlogopite megacrysts display strong decreases in Al_2O_3 and K_2O with decreasing Mg-number and strong enrichments in Na_2O (Fig. 6.8 a, b and d). From Mg-numbers of 78 to 74, the decreases in Al_2O_3 and K_2O with decreasing Mg-number become less and there is very little change in Na_2O content. TiO_2 shows an essentially continuous decrease at the same rate through the whole range of Mg numbers (84 to 74), which likely reflects depletion of Ti in the melt as ilmenite crystallises (Fig. 6.8c). The phlogopite megacrysts do also show compositional similarities with phlogopite megacrysts associated with alkali basalts as well as with the phlogopite grains from the SPKC ultramafic lamprophyres. As with the major element data, trace element studies performed on the phlogopite megacrysts also show changes in element behaviour about the 80 Mg-number mark. Elements including Ni, Rb and V show changes in slope from positive to negative towards lower Mg-numbers.

The phlogopite grains present in the MAID-type xenoliths have Mg-numbers that are significantly lower than those of the megacrysts, implying that they crystallised from a more fractionated melt. The xenolithic phlogopite grains are also significantly less variable in their Mg-number content relative to the phlogopite megacrysts, with Mg numbers ranging from 61 to 63. Trends of Al_2O_3, TiO_2, K_2O versus Mg-number are not apparent in this data, suggesting

crystallisation from a melt that exhibited only small changes in these oxides during differentiation, relative to the SPKC phlogopite megacrysts.

Radiogenic isotope comparisons between the phlogopite megacrysts and megacrysts of amphibole and clinopyroxene reveals these phases share considerable overlap in initial Sr and Nd isotope composition with phlogopite (Fig. 9.2). Similar findings have also been noted between the phlogopite megacrysts and the SPKC OMs and UMLs. This suggests that the phlogopite megacrysts may be co-genetic with the amphibole and clinopyroxene megacrysts, and that all these megacrysts phases are in some way genetically related to either the OM or UML rocks. On the Pb-Pb plot (Fig. 9.3), the SPKC phlogopite megacrysts are also shifted closer to the HIMU mantle end-member composition, relative to the clinopyroxene megacrysts. The phlogopite grains do however overlap with the amphibole megacrysts, within 2σ uncertainty. This suggests that during crystallisation of the phlgopite megacrysts, the parent melt had a strong influence of sublithospheric mantle sources, more so than during the crystallisation of the clinopyroxene megacrysts and similar to what was proposed above for the amphibole megacrysts.

Ilmenite

Comparisons made between the SPKC ilmenite megacryst grains and the various ilmenite megacryst groups of the Monastery kimberlite reveals that the SPKC samples are more closely related to the Group 1 and 2 grains. According to Moore et al., (1992) grains belonging to the Monastery Group 1 grains experienced a purely fractional crystallisation history, whereas those belonging to Group 2 likely experienced some wall rock assimilation and/or magma mixing in addition to fractional crystallisation.

Trace element comparisons between the SPKC grains and those of Monastery only serve to reinforce the major oxide findings, suggesting that fractional crystallisation coupled with wall rock assimilation and/or magma mixing processes were at play during the crystallisation of ilmenite megacrysts. Significant scatter of crustal rock forming elements (i.e. Co, Ni and Zn) and a lack of well-defined trends as a function of Mg-number could be an initial indication of the melt parent to the megacrysts having experienced some degree of crustal enrichment (Ni; Fig. 7.7e). Plots of Zr and Nb versus Mg-number (Fig. 7.7a and 7.7c respectively) show multiple trends which may be the result of two separate primary magma compositions. The study

performed by Moore et al. (1992) showed that the Nb content of ilmenite megacrysts can be used to show the degree of fractional crystallisation believed to have been experienced by the parent melt of the ilmenite grains. This seemingly incompatible behavior of Nb versus Mg-number in the SPKC samples is unusual as Nb should behave compatibly in ilmenite and could suggest either that ilmenite played a relatively minor role in the fractionating mineral assemblage or that Nb behaved incompatibly in the parent melt of the megacrysts. This is consistent with the weakly positive correlation seen between Nb and Zr in the SPKC ilmenite megacrysts (Fig. 7.7d). The Cr-number of the megacrysts does not correlate with Mg-number (Fig. 6.9d) and can therefore not be used as a fractionation index to either confirm or challenge the finding made using Nb. The lack of systematic trends between Cr-number and Mg-number argues that ilmenite megacrysts, like clinopyroxene, also evolved in an open-system (Bell and Moore, 2004).

Ilmenite grains are present in the MAID-type xenoliths. These grains, like the other grains hosted in the xenoliths, were found to have lower Mg-numbers in comparison to megacryst grains of the same phase, suggesting crystallisation from a less primitive melt. The xenolith grains show the same trend as the megacrysts in TiO_2, but with some enrichment observed, such that the xenolith samples have higher concentrations of TiO_2 relative to the lowest Mg-number megacrysts. In the case of Al_2O_3, depletion in the xenolith grains relative to the megacrysts has been noted. Moving from the megacryst to xenolith samples, the slope of Al_2O_3 versus Mg-number changes from being positive to near-flat lying. The parent melt of these megacrysts likely also evolved in an open system where it assimilated material that enriched it in Al_2O_3 and TiO_2. This same enrichment process may have also been responsible for the two distinct trends seen Nb and Zr for the lower Mg-number group. Since no trace element data was collected for the MAID ilmenite grains, it remains unknown if the trends seen for the megacrysts in Nb and Zr versus Mg-number continue in the xenolith samples.

Summary of compositional variations

Megacrysts of amphibole, clinopyroxene and phlogopite all show positive correlations in TiO_2 versus Mg-number which may be an initial indication that these phases were

crystallising along with ilmenite. All of the megacryst phases otherwise show geochemical trends that are consistent with progressive fractional crystallisation. The lack of purely linear trends in the trace element data for megacrysts of amphibole, clinopyroxene, ilmenite and phlogopite may, in part, be consistent with the megacryst magma crystallising under more open-system magmatic fractionation conditions. The decrease in variability in both major and trace element data, towards more Mg-poor amphibole, clinopyroxene and phlogopite megacryst grains, is suggestive of melt homogenisation and fractionation under more closed system conditions.

Comparable REE patterns and overlapping radiogenic isotope data suggests that the amphibole, clinopyroxene and phlogopite are co-genetic and are likely also genetically related to either the olivine melilities or ultramafic lamprophyres of the SPKC. Pb isotopes on the other hand suggest that the parent melt of the megacryst suite mixed with some HIMU component, exemplifying the open-system behaviour displayed by the various megacryst phases. The seemingly compatible behavior of TiO_2 versus Mg-number was observed for the amphibole, clinopyroxene and phlogopite megacrysts and could be an indication of crystallisation alongside the ilmenite megacrysts.

10.2. Megacryst relation to SPKC igneous rocks - Parental melt

Major element studies

An important question in the genesis of any megacryst suite is what is its relationship to the host igneous rocks? With regards to the Salpeterkop megacrysts and cumulate xenoliths, an initial assessment of this was performed by comparing the Fe/Mg ratio of the melts calculated to be in equilibrium with megacrysts to those of the various rock types associated with the complex, with data for these rocks supplied by Marageni (2018). Mg-number is inversely proportional to (Fe/Mg +1), meaning that lower values of Fe/Mg correspond to higher Mg-numbers. The only Fe/Mg partition coefficients that could be found are for clinopyroxene. The equation applied to determine the Fe-Mg ratio of the melt in equilibrium with clinopyroxene is as follows:

$$K_D = \left(\frac{Fe}{Mg}\right)_{cp} \left(\frac{Mg}{Fe}\right)_{melt} ;$$

where K_D is the experimentally calculated Fe-Mg partitioning between clinopyroxene and melt, and has a value of 0.275 and Fe is the total iron present in melt and mineral (Putirka et al. 2003).

The Fe/Mg ratio calculated for the SPKC rocks are from samples taken from all the various dykes and plugs around Salpeterkop. The Fe/Mg ratios for the olivine melilitite (OM) and ultramafic lamprophyre (UML) range from 0.31 to 0.58 and from 0.40 to 1.18 respectively. The ultramafic lamprophyres that host the megacrysts at the Silver Dam breccia pipe have Fe/Mg ratios that range from 0.70 to 0.75. The carbonatites and potassic trachyte have very broad compositional ranges extending to highly differentiated compositions making it implausible to relate these rock types to the clinopyroxene megacrysts. Additionally, Marageni, (2018) proposed that the trachytes likely formed due to melting of continental crust, fenitised by hydrous, potassium-rich carbonatitic fluids, which contrasts with the mantle origin inferred from the radiogenic isotopic signatures of the clinopyroxene and amphibole megacrysts, which argues against the trachytes as a possible parental melt. For melts in equilibrium with the clinopyroxene megacrysts, the calculated Fe/Mg ratios vary between 0.84 and 1.37.

The Fe/Mg ratios of the melilitites are significantly lower than those for the calculated melts in equilibrium with clinopyroxene, indicating that the clinopyroxene megacrysts crystallised from a melt more evolved than the SPKC olivine melilitites (OM). This however does not rule out OM as the parent melt to the SPKC clinopyroxene megacrysts, as the megacrysts could simply have crystallised from a more differentiated variant of the melt responsible for OM. The lamprophyres have Fe/Mg ratios that overlap substantially with the range of values for the melts calculated to be in equilibrium with clinopyroxene (Fig. 10.3).

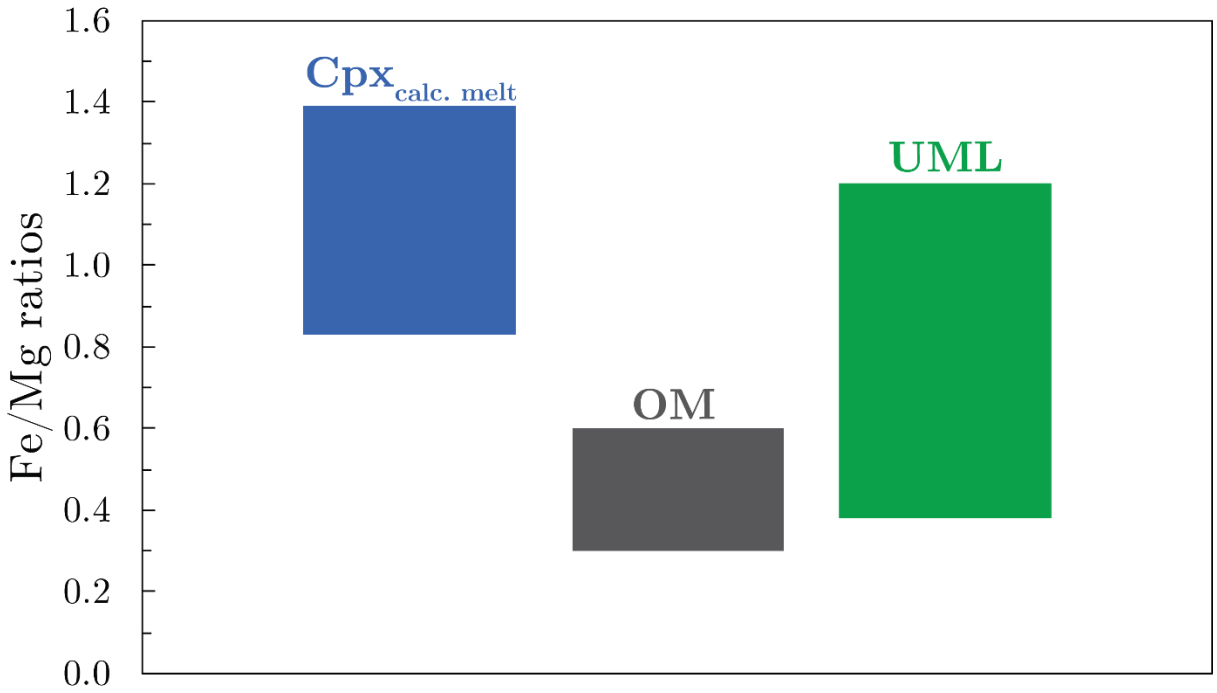

Figure 10.2: The Fe/Mg ratios forthecalculated melt in equilibruim withthe SPKC clinopyroxene megacrysts (coloured blue field), compared to the Fe/Mg ratios of the SPKC OM (coloured gray field) and UML (coloured green field).

Some of the Fe/Mg ratios of the lamprophyres are lower than the more differentiated clinopyroxene megacrysts, suggesting that these more differentiated clinopyroxene megacrysts could have crystallised from a slightly more evolved variant of the UML melt.

Modelling was undertaken of the trace element concentrations of the melt(s) in equilibrium the megacrysts in order to compare their trace element concentrations with those of the OM and UML rock types, which seem most plausibly genetically to the megacrysts. To calculate the composition of the melt in equilibrium with the megacryst minerals, one simply

needs to divide the trace element concentration in the mineral by an appropriate mineral-melt partition coefficient, as shown in the equations below.

$$K_D = \frac{C_{Mineral}}{C_{Melt}}$$

$$\therefore C_{Melt} = \frac{C_{Mineral}}{K_D};$$

where K_D is the experimentally determined partition coefficient for a specific trace element, $C_{Mineral}$ is the concentration of said trace element in the mineral and $C_{Mineral}$ the concentration in the melt (to be calculated).

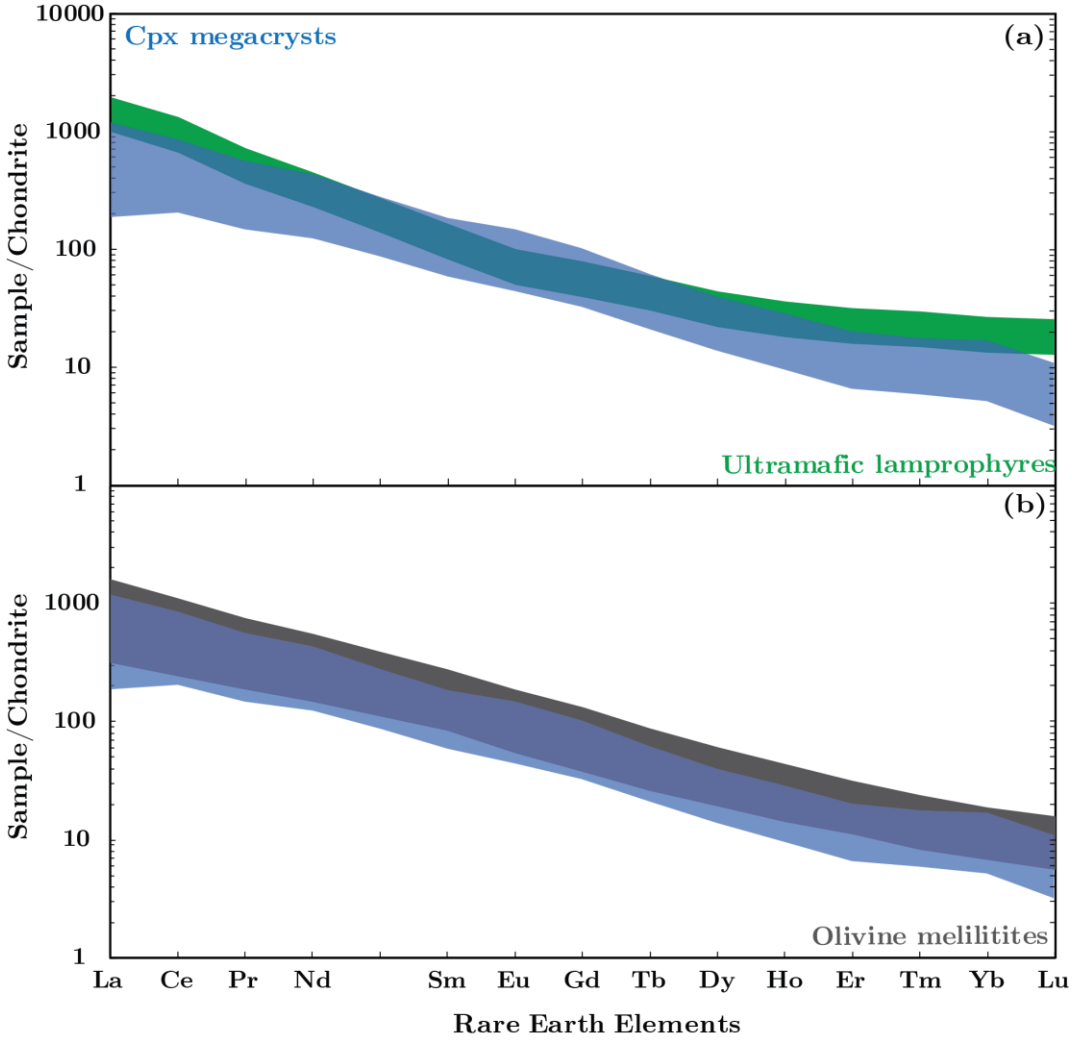

Figure 10.3: Chondrite mantle normalised REE diagrams for calculated melt in equilibrium with the clinopyroxene megacrysts (blue coloured field). Additionally, the REE compositions of the (a) lamprophyre and (b) melilitite igneous rocks (green and gray coloured fields respectively) from the SPKC (Marageni, 2018).

Trace element studies

Trace element partition coefficients are not always very well constrained as a consequence of different published values. It then becomes essential that special care be taken when deciding on what values to use. A combination of partition coefficients from Hart and Dunn (1993) and Irving and Frey (1984) were applied to the clinopyroxene megacrysts and from these a rare earth diagram was constructed to constrain the composition of the melt in equilibrium with these samples. These partition coefficients selected are both comprehensive, share resasonibly similar REE partitioning values and are relevant to clinopyroxene forming from alkali basalt parent magmas.

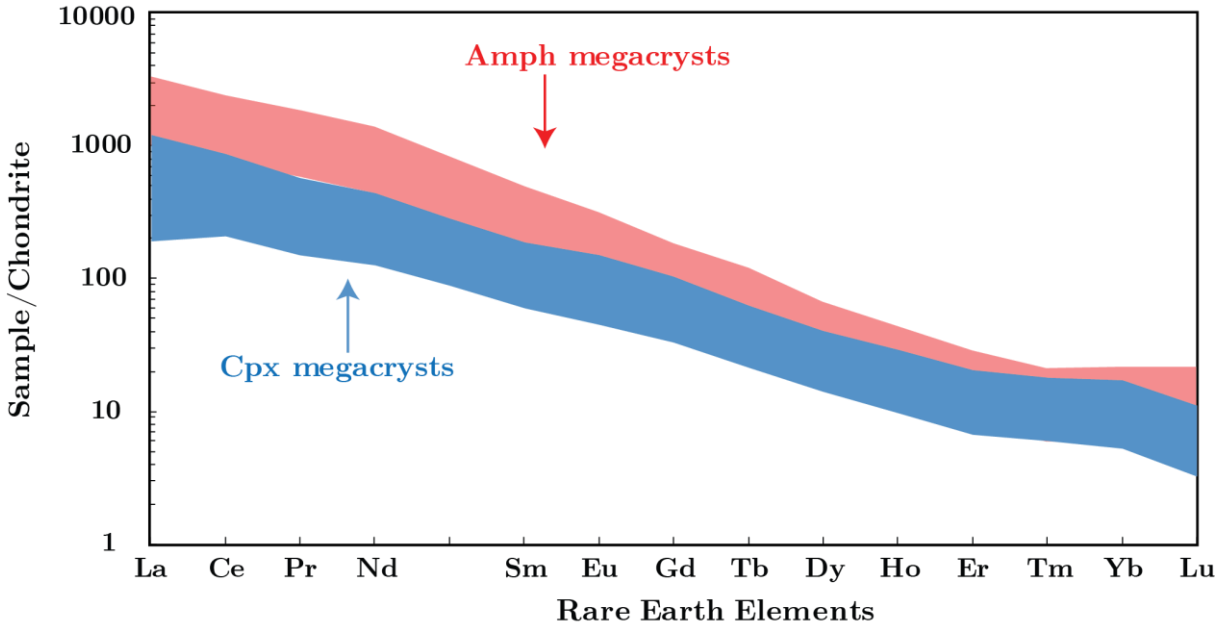

Figure 10.4: Chondrite mantle normalised REE diagram comparing the melts in equilibrium with the clinopyroxeen and amphibole megacrysts

The values of Hart and Dunn (1993) were experimentally determined for 24 trace elements in clinopyroxene grains that equilibrated at conditions of 30 kbars (kilobars) and 1380 ℃. In the case of Irving and Frey (1984), the partition coefficients were determined for several trace elements including the rare earths, from natural mineral (including clino- and orthopyroxene, amphibole and mica) samples. For the amphibole megacrysts, a combination of partition coefficients from Bottazzi et al. (1999) and Irving and Frey (1984) were used. These partition coefficients were used because both share resasonibly similar REE partitioning values and were determined for amphibole grains hosted in alkaline basalts. The values used from

Bottazzi et al. (1999) are applicable for amphiboles grains of pargasite, kaersutite, and K-richterite composition sourced from mafic alkaline magmas, with experiments performed under upper mantle conditions of up to 14 kbars and 1270 ℃.

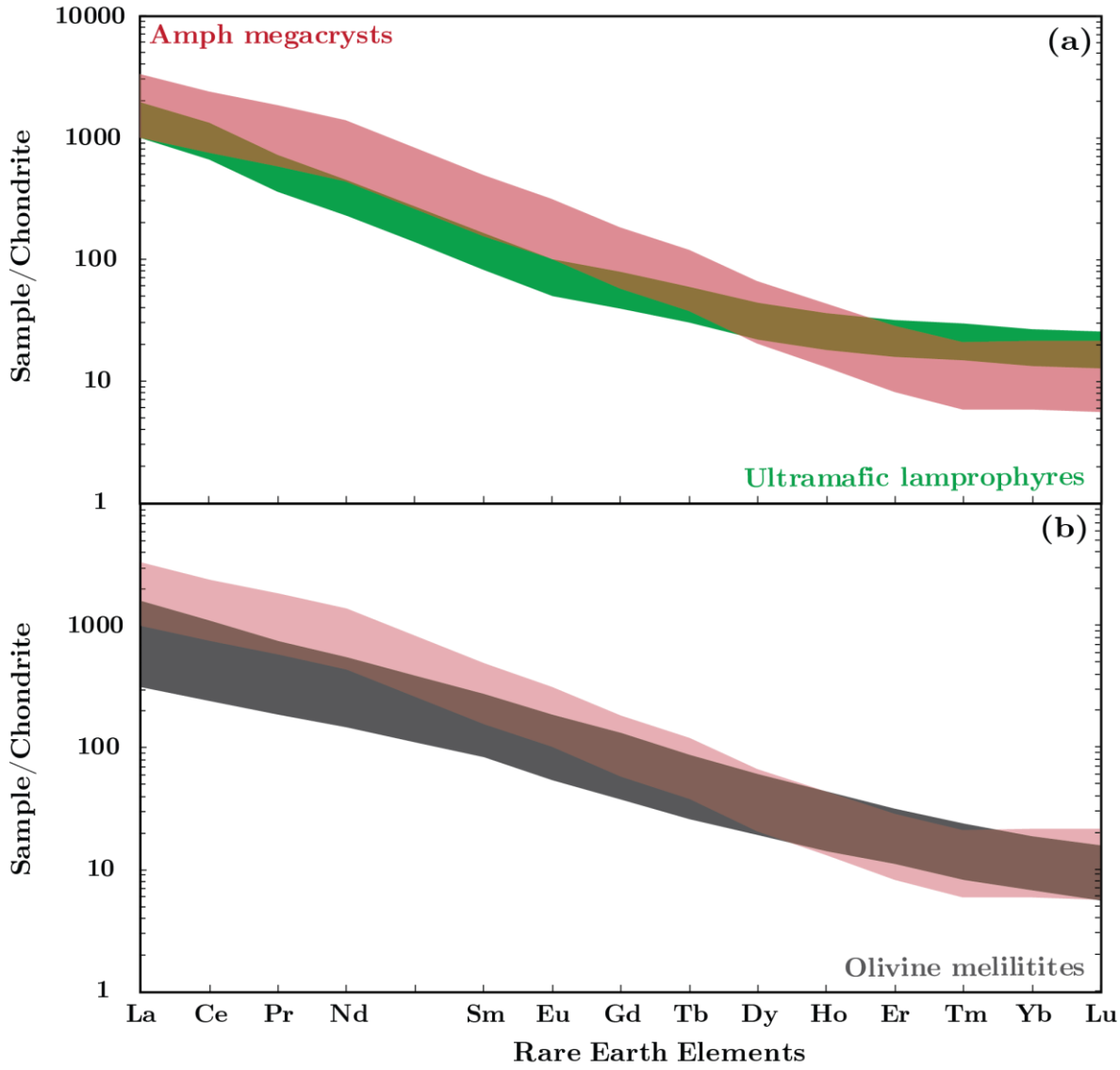

Figure 10.5: Chondrite mantle normalised REE diagrams for calculated melt in equilibrium with the amphibole megacrysts (red coloured field). Additionally, the REE compositions of the (a) lamprophyre and (b) melilitite igneous rocks (green and gray coloured fields respectively) from the SPKC (Marageni, 2018).

The rare earth patterns for the calculated melts in equilibrium with the clinopyroxene and amphibole megacrysts have been plotted in Figure 10.4, with both sharing similar slopes. The melts in equilibrium with the amphibole megacrysts have much higher LREE abundances than the clinopyroxene melts and flatten at the heaviest REEs, unlike the more HREE-depleted clinopyroxene equilibrium melts that do not (Fig. 10.4). The clinopyroxene and amphibole

megacrysts have very similar REE contents, so the differences in the calculated melt compositions has to do with the different partition coefficients for the two minerals.

The melt in equilibrium with clinopyroxene have generally linear, LREE-enriched REE patterns most similar to the OMs and largely overlapping with the UMLs except for having lower concentrations for the heaviest REE (Fig. 10.3a-b). The melts in equilibrium with amphibole do not show a particularly close correspondence to either rock type, but like the UMLs, they show a flattening of the REE patterns at the heavy REE which is not displayed by the OMs (Fig. 10.5a-b).

Isotopic studies

While these major and trace element comparisons demonstrate that the melilitites and lamprophyre are both compositionally similar to the megacryst suite, calculated initial Sr-Nd-Pb isotopic results show considerable overlap between the clinopyroxene, amphibole and phlogopite megacrysts and both the SPKC OMs and UMLs. The clinopyroxene, amphibole and phlogopite megacrysts show considerable overlap with the melilitites and lamprophyres in Sr-Nd-Pb isotope ratios, with some amphibole and phlogopite grains also show marginally less radiogenic signatures relative to both rock types. Radiogenic isotope disequilibrium, such as some clinopyroxene, amphibole phlogopite grains having less radiogenic Sr-Nd isotope ratios relative to the SPKC OMs and UMLs, suggests an open system evolution of the megacryst grains. The shift towards HIMU signatures (Fig. 9.1, Sr and 9.3, Pb) for the megacrysts relative to both the OMs and UMLs may suggest interaction with a source with stronger HIMU affinity, similar to that seen in melilitite localities located further south (Janney et al., 2002).

The radiogenic isotope as well as major element and trace element similarities between the SPKC megacrysts suite and both the SPKC OMs and UMLs makes it challenging to single out one rock type as being parent to the megacrysts. The megacryst suite of the SPKC therefore either crystallised from a differentiated version of the OMs or a melt similar in composition to the UMLs.

Summary of melt in equilibrium with the megacrysts

The major element (Fe/Mg) comparisons between the SPKC igneous rocks and the calculated melt in equilibrium with the clinopyroxene megacrysts reveals that the olivine melilitites and ultramafic lamprophyre are the only rock types associated with the complex primitive enough to yield melts capable of crystallising the megacrysts. The REE pattern of the calculated melts in equilibrium with the SPKC clinopyroxene and amphibole megacrysts overlap with both the SPKC OM and UML igenous rocks, while radiogenic isotope variations suggest that the parent melt of the megacrysts may have interacted with a HIMU component. In early chapters of this thesis, is was also shown that the SPKC clinopyroxene and phlogopite megacrysts are compositionally more like clinopyroxene and phlogopite grains from the UMLs rather than those from the OMs. These findings therefore point to the parent melt of the megacrysts being lamprophyre-like in composition, originating from sub-lithospheric mantle conditions, and having mixed or assimilated varying degrees of material with a HIMU signature.

10.3. Megacryst crystallisation order

This section aims to answer whether the SPKC megacrysts are co-genetic with each other and, if so, which megacrysts crystallized together and to what extent did their crystallization overlap?

The various megacryst phases occur as discrete fragments hosted in a volcaniclastic breccia and not in a purely magmatic rock. They are also monomineralic with few or no mineral inclusions present, making it difficult to determine how the minerals relate to each other. The xenolith samples on the otherhand appear to be texturally in equilibrium which almost certainly indicates that they are co-genetic. The xenolith grains also contain intergrowths of the same mineral phases found in megacryst form and can allow intial constraints to be placed on the crystallisation order of the minerals in the xenoliths themselves, which may then be used to potentially constrain the order of megacryst crystallision.

It is also worth noting that the xenolith minerals tend to have much lower Mg-numbers than the megacrysts, meaning that any relationship(s) present in the xenoliths may not necessarily hold true for the megacryst suites as a whole, even if the megacrysts and xenolith grains are related. As mentioned in section 10.1, the similarity in the shape of the REE and

incompatible element patterns between the clinopyroxene megacrysts and xenolithic grains strongly supports a cogenetic origin. As such, major and trace element results obtained from the xenolith grains can be compared to data from the megacrysts to better constrain mineral relations.

Xenolith-mineral relationships

Several amphiboles in sample SD1A contain clinopyroxene inclusions which show compositions indistinguishable from the (non-inclusion) clinopyroxene grains found in the same xenolith. The implication of this is that clinopyroxene started crystallising prior to amphibole, however it is entirely possible that their crystallisation overlapped to a large degree. Ilmenite is exclusively found as an overgrowth on grains of both clinopyroxene and amphibole in the MAID-type xenoliths, suggesting that the crystallisation of both clinopyroxene and amphibole took place before (and likely alongside) that of ilmenite. The MAID-type xenoliths are also host to phlogopite grains that contain inclusions of clinopyroxene. The inclusion and non-inclusion clinopyroxene grains are compositionally identical, suggesting that the clinopyroxene began crystallising before phlogopite, however some grains of clinopyroxene and phlogopite likely crystallised together. These xenolith mineral relations may be used to determine equilibrium Fe/Mg partitioning of the coexisting mineral pairs, in order to constrain the clinopyroxene-amphibole, clinopyroxene-ilmenite and clinopyroxene-phlogopite megacryst crystallisation order.

The textural relationship between ilmenite and amphibole with phlogopite in MAID xenoliths could not be established, as no direct intergrowths between ilmenite-phlogopite and amphibole-phlogopite were found in any of the xenolith types. Since the ilmenite-phlogopite and amphibole-phlogopite pairs cannot be constrained directly from existing mineral intergrowths, an effort is made to approximate these relationships from known ones e.g. using clinopyroxene-amphibole and clinopyroxene-ilmenite to approximate amphibole-ilmenite.

Table 10:1: (FeO/MgO) ratios for megacryst pairs normalised to the same value for the MAID xenoliths.

Megacryst relationships (subscripts denote Mg-number)	Min. (FeO/MgO) ratios	Max. (FeO/MgO) ratios
Cpx/Phl $_{(> 80)}$	1.14	2.35
Cpx/Phl $_{(< 80)}$	0.82	1.55
Cpx/Ilm	0.52	2.16
Cpx/Amph $_{(> 67)}$	0.62	1.72
Cpx/Amph $_{(< 67)}$	0.47	0.90
Amph $_{(67)}$/Ilm	0.48	2.09
Amph $_{(< 67)}$/Ilm	0.91	2.74
Amph $_{(> 67)}$/Phl $_{(> 80)}$	1.20	2.61
Amph $_{(< 67)}$/Phl $_{(> 80)}$	2.31	3.42
Amph $_{(> 67)}$/Phl $_{(< 80)}$	0.87	1.72
Amph $_{(< 67)}$/Phl $_{(< 80)}$	1.67	2.26

To determine these mineral relationships, the FeO/MgO ratios of two megacryst types (i.e $\frac{\text{cpx}}{\text{phl}}$) were normalised to those of the same phases from the xenoliths where their relationships are known (i.e. MAID-type xenoliths). The equation below is an example of one of the calculations performed.

$$\left(\frac{\frac{FeO}{MgO}_{cpx}}{\frac{FeO}{MgO}_{phl}}\right)_{mega} / \left(\frac{\frac{FeO}{MgO}_{cpx}}{\frac{FeO}{MgO}_{phl}}\right)_{xeno}$$

For grains co-crystallising under the same P-T-composition conditions, FeO/MgO xenolith ratios of 1 should be observed. In the example above, when ratios < 1 are observed, the megacryst type in the numerator, in this case clinopyroxene, had a lower FeO/MgO ratio and therefore a higher Mg-number i.e. crystallised from a more primitive source. If the values vary significantly from 1 it suggests that either the minerals were not in equilibrium or that their parental melt had fractioned between the crystallisation of the two phases.

Earlier in this thesis it was shown that the major and trace element data of the amphibole and phlogopite megacrysts display defining changes in behaviour at Mg-numbers of 67 and 80 respectively. Grains having Mg-numbers above and below these values were treated as separate data populations. The clinopyroxene megacrysts do not show changes in behaviour with respect to Mg-number, and as such, the grains were treated as one population. Table 10.1 shows the minimum maximum FeO/MgO ratios for a megacryst pair normalised to the same value from the MAID xenoliths minerals.

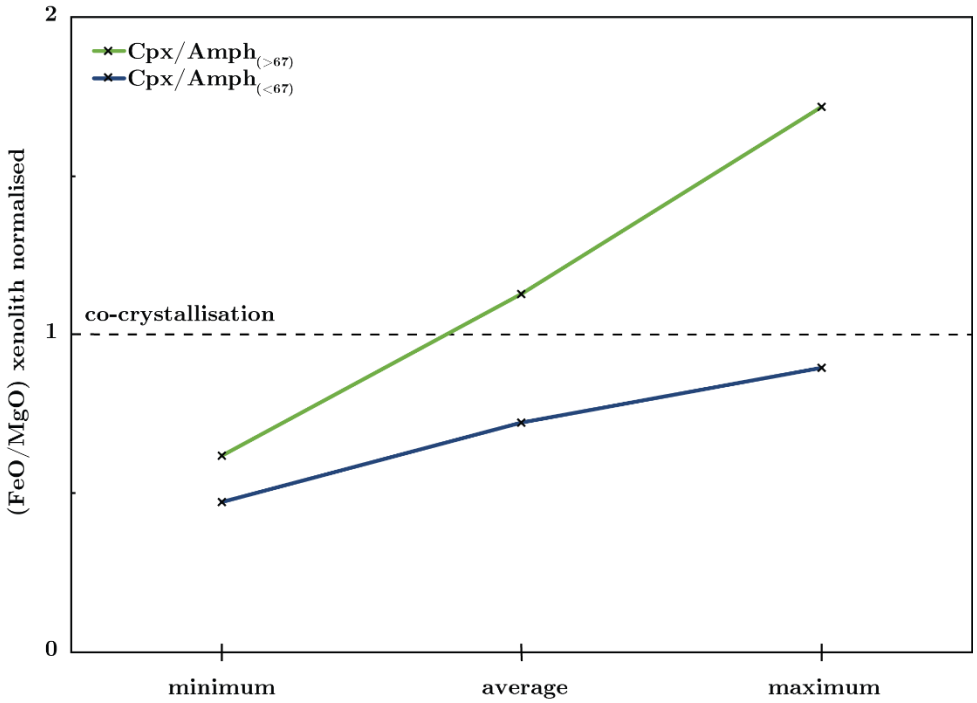

Figure 10.6: The minimum, average and maximum SD1A xenolith normalised $(FeO/MgO)_{cpx/amph}$ ratios for the clinopyroxene-amphibole megacryst pair. Dotted line represents co-crystallisation of mineral phases.

Clinopyroxene-amphibole relationship:

The study of the clinopyroxene-amphibole megacryst relationship yielded average $(FeO/MgO)_{cpx/amph}]_{meg}$ ratios (normalised to the SD1A xenolith) of 1.13 ± 0.65 (1σ; n = 7) and 0.72 ± 0.97 (1σ; n = 7) for the amphibole megacrysts above and below Mg-number = 67 respectively. $Amphibole_{(> 67)}$ megacrysts appear to have initally started crystallising prior to clinopyroxene while $amphibole_{(< 67)}$ appear to have largely crystallised after clinopyroxene (Fig. 10.6). Both average values are however within uncertainties of 1 which suggests that the clinopyroxene megacrysts could have co-crystallised, to some extent, with amphibole megacrysts above and below Mg-number 67.

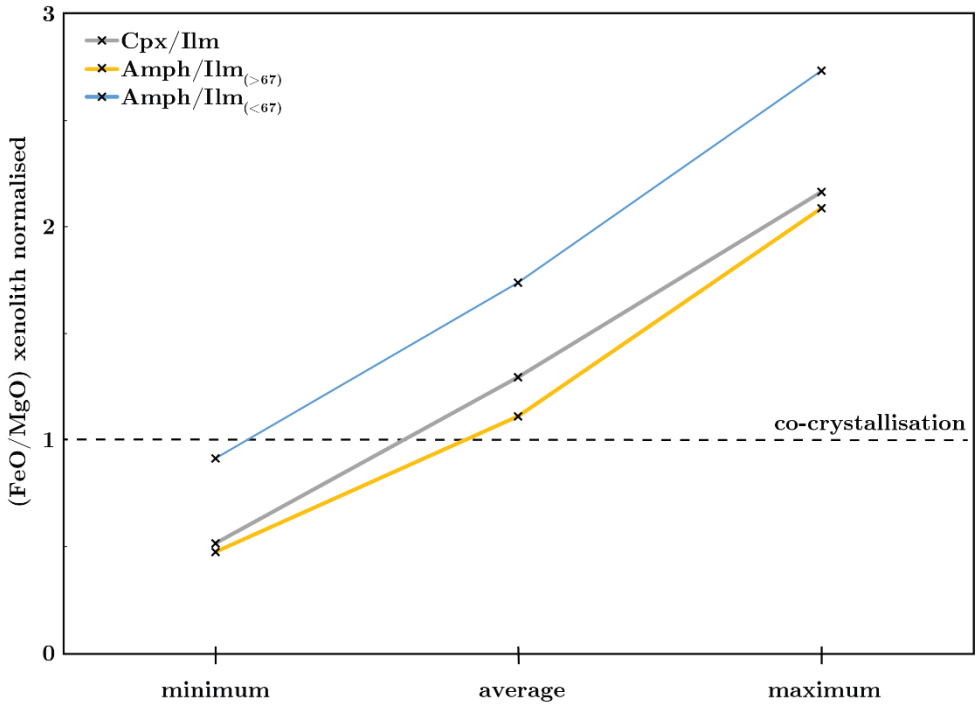

Figure 10.7: The minimum, average and maximum MAID xenolithnormalised $FeO/MgO)_{cpx/ilm}$ and ($FeO/MgO)_{amph/ilm}$ ratios for the clinopyroxene-ilmenite and amphibole-ilmenite megacrysts pairs.Dotted line represents co-crystallisation of mineral phases.

Clinopyroxene-ilmenite relationship:

The clinopyroxene-ilmenite relationship yielded an average $(FeO/MgO)_{cpx/ilm}$ ratio of 1.30 ± 0.55 (1σ; n = 20) normalised to the MAID xenoliths (Fig. 10.7). This suggests that the ilmenite megacrysts possibly began crystalling from a more primitive source than the clinopyroxene megacrysts, but that grains of ilmenite and clinopyroxene could have crystallised in equilibrium.

Amphibole-ilmenite relationship:

Using amphibole$_{>67}$ megacrysts, the average $(FeO/MgO)_{amph/ilm}$ ratio normalised to the same value for the MAID xenoliths, was calculated as being 1.11 ± 0.35 (1σ; n = 7), indicating that the ilmenite megacrysts possibly began crystalling from a more primitive source than the amphibole megacrysts, but that grains of ilmenite and amphibole could have crystallised in equilibrium. (Fig. 10.7).

For the amphibole$_{<67}$-ilmenite relationship, the average $(FeO/MgO)_{amph/ilm}$ ratio for these megacrysts, normalised to the MAID xenoliths values was found to be 1.74 ± 0.23 (1σ;

n = 7), much larger than the average amphibole$_{>67}$-ilmenite and clinopyroxene-ilmenite values. This relationship is also outside the uncertainty of 1, suggesting that any co-crystallisation between the ilmenite and amphibole$_{<67}$ megacrysts was unlikely.

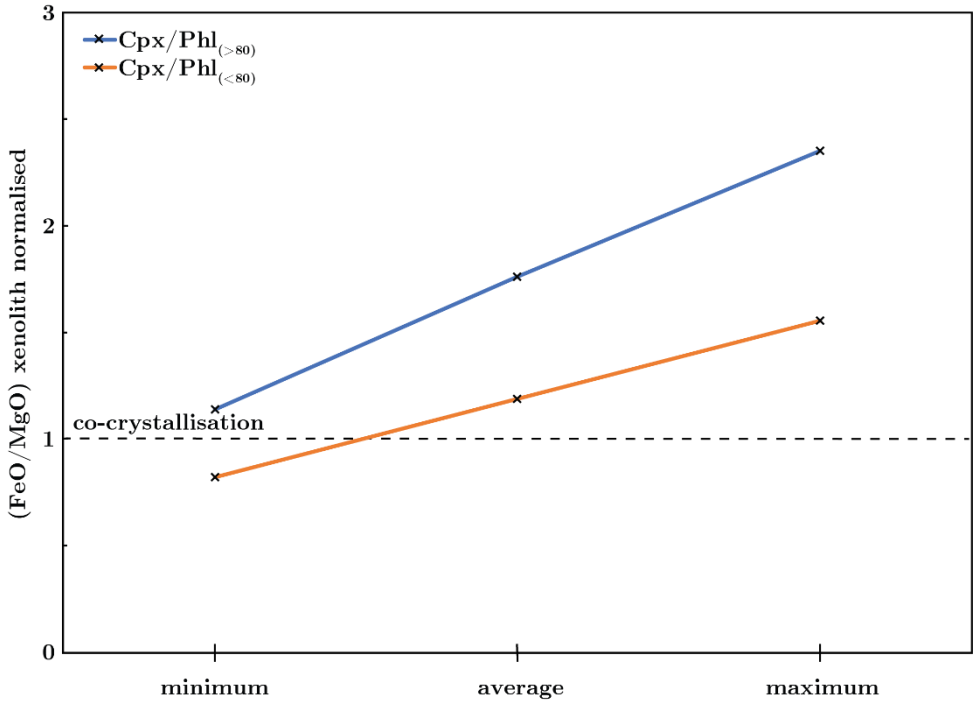

Figure 10.8: The minimum, average and maximum MAID xenolith normalised $(FeO/MgO)_{cpx/phl}$ ratios for the clinopyroxene-phlogopite megacryst pair. Dotted line represents co-crystallisation of mineral phases.

Clinopyroxene-phlogopite relationship:

The average $(FeO/MgO)_{cpx/phlogopite}$ ratio in these megacrysts normalised to the MAID xenoliths was calculated as being 1.76 ± 1.96 (1σ; n = 4) and 1.19 ± 1.81 (1σ; n = 4) using values for phlog$_{>80}$ and phlog$_{<80}$ respectively. This suggesting that the phlogopite megacrysts could have began crystallising from a more primitive melt that the clinopyoxene megacrysts, but that some grains of phlogopite and clinopyroxene could have crystallized in equilibrium. (Fig. 10.8).

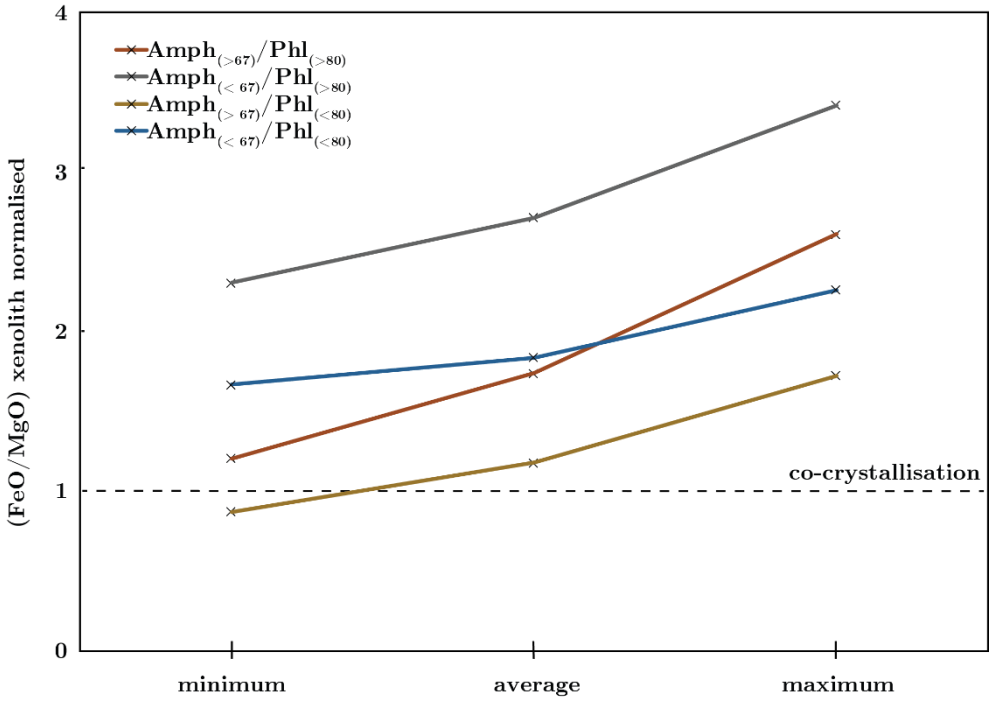

Figure 10.9: The minimum, average and maximum MAID xenolith normalised $(FeO/MgO)_{amph/phl}$ ratios for the amphibole-phlogopite megacryst pair. Dotted line represents co-crystallisation of mineral phases.

Amphibole-phlogopite relationship:

Earlier it was mentioned that the clinopyroxene and amphibole megacrysts show considerable overlap in their $(FeO/MgO)_{cpx/amph}$ ratio normalised to MAID xenoliths, more than between any other two mineral pairs. As such, the FeO/MgO ratio between clinopyroxene and phlogopite grains from MAID xenoliths were used as a proxy for that of amphibole and phlogopite megacrysts. It should again be stated that since there are no direct mineral relations or mineral intergrowth between these two phases, any interpretations made from these results have greater uncertainties than the other mineral-mineral calculations performed.

Table 10:2: (FeO/MgO) ratios for amphibole-phlogopite megacryst normalised to the same value for the MAID xenoliths.

Megacryst relationships	Average (FeO/MgO) ratios
Amph $_{(> 67)}$/Phl $_{(> 80)}$	1.74 ± 1.10 (1σ; n = 7)
Amph $_{(< 67)}$/ Phl $_{(> 80)}$	2.71 ± 0.74 (1σ; n = 7)
Amph $_{(> 67)}$/Phl $_{(< 80)}$	1.17 ± 1.02 (1σ; n = 7)
Amph $_{(< 67)}$/ Phl $_{(< 80)}$	1.72 ± 0.68 (1σ; n = 7)

The average MAID xenolith-normalised $(FeO/MgO)_{amph/phlog}$ ratios in Table 10.2 and Figure 10.9 show that phlogopite$_{>80}$ initally started crystallising before amphibole. The relationship between the amphibole$_{>67}$ and phlogopgite$_{<80}$ megacrysts is closest to 1 and does also fall within the uncertainty of 1, suggesting that these two phases, to some extent, did co-crystallise.

Phlogopite-ilmenite relationship:

No direct mineral relations or mineral intergrowth were found between phlogopite and ilmenite, making it extremely difficult to accurately determine their relation. Instead an approximation of their relationship to each other was estimated based on how each relates to the other megacryst phases. The FeO/MgO ratios for amphibole-phl$_{>80}$ and clinopyroxene-phl$_{>80}$ are larger than the FeO/MgO ratios for amphibole-ilmenite and clinopyroxene-ilmenite. This may suggest that the phl$_{>80}$ megacrysts initally begin to crystallise before ilmenite. The FeO/MgO ratios for amphibole-phl$_{<80}$ and clinopyroxene-phl$_{<80}$ are similar in magnitude to the FeO/MgO ratios for amphibole-ilmenite and clinopyroxene-ilmenite which may indicate that phl$_{>80}$ and ilmenite broadly crystallised in equilibrium.

Summary of megacryst crystallisation order

The attempts made here to constrain the order of crystallisation of the various phases that constitute the megacryst suite of the Salpeterkop complex suggest that phlogopite was the first mineral to crystallise, then grains of ilmenite, amphibole and lastly clinopyroxene joined the crystallising mineral assemblage, in that order, but the proposed order of megacryst crystallisation, including commencement and conclusion of each phase can be found below:

phlogopite$_{>80}$ $\rightarrow$ phlogopite$_{>80}$ + ilmenite $\rightarrow$ phlogopite$_{<80}$ + ilmenite $\rightarrow$ phlogopite$_{<80}$ + ilmenite + amphibole$_{>67}$ $\rightarrow$ phlogopite$_{<80}$ + ilmenite + amphibole$_{>67}$ + clinopyroxene $\rightarrow$ ilmenite + amphibole$_{>67}$ + clinopyroxene $\rightarrow$ clinopyroxene + amphibole$_{<67}$ $\rightarrow$ amphibole$_{<67}$

10.4. P-T Estimates

The chemical compositions of minerals in any system is, to varying degrees, affected by the pressure and temperature conditions experienced by that mineral during crystallisation. For a given assemblage of minerals that are known to be in equilibrium, geothermobarometric calculations can be used to estimate the pressure and/or temperature conditions under which those minerals crystallised and/or equilibrated. Many geothermometers and geobarometers are calibrated using coexisting mineral phases, e.g temperatures obtained from Ca-Mg exchange in pyroxene (diopside – enstatite; Lindsley and Andersen, 1983), Fe-Mg exchange between garnet and clinopyroxene (Krogh, 1988) or between garnet and olivine (O'Neill and Wood, 1979) and pressures obtained from Ca-Al exchange between garnet and pyroxene (Brey et al., 1986).

In the case of minerals belonging to a megacryst suite, determination of the P-T conditions is made more difficult by the fact that the megacrysts are typically monomineralic in nature, as is the case with the Salpeterkop megacryst suite. The task of finding geothermobarometers that could be applied directly to individual mineral phases was the next best option available (e.g. Nimis and Taylor, 2000 and Ryan et al., 1996) that allow one to calculate temperatures and possibly pressures without knowing the compositions of co-existing phases. They do however require that the mineral(s) of interest be in equilibrium with certain minerals (e.g., cpx with garnet and opx for Nimis and Taylor, 2000 or garnet with olivine($\pm$ chromite) for Ryan et al., 1996).

Clinopyroxene

To quantitively comment on the P-T conditions experienced by the clinopyroxene megacrysts during their crystallisation, several thermometers and barometers equations developed by Putirka (2008) were employed. Three different barometers were applied to the major element data collected to provide insight into the pressures at which these grains equilibrated. The first (1) barometeric equation was calibrated using all avaliable data from clinopyroxene-saturated experiments (experiments where clinopyroxene was a part of the crystallising assemblage). The second (2) improves on the precision of the barometer used by Nimis (1995), which uses the relationship between the clinopyroxene unit-cell and site volume to constrain the pressures of magmatic crystallisation. Barometer 2 differs from the Nimis

(1995) barometer as it was recalibrated using experiments performed from 0.001-8.0 GPa. The third (3) equation used in this study removes systematic errors associated with the equation 2 barometer, but in exchange requires knowledge or an estimation of the H_2O content of the melt in equilibrium with the clinopyroxene.

Comparisons made earlier in this thesis between the megacrysts and clinopyroxene grains from the SPKC olivine melilitites and ultramafic lamprophyres revealed that a substantial number of compositional similarities exist, sufficient to suggest that the parent melt of the megacrysts was genetically related to the either the OMs or UMLs. For this reason, the average compositions of the SPKC OMs and UMLs were independently tested as parental melt compositions for the megacrysts. The results of the pressure calculations from the 3 barometers are presented below in Table 10.3.

Table 10:3: Pressure ranges were calculated from clinpyroxene megacryst data from this study and OM and UML assumed to be in equilibrium with the average olivine melilitite or ultramafic lamprophyre compositions from Marageni (2018). Barometers used here are those developed by Putirka (2008).

Rock types	Pressure (GPa)		
	Barometer 1	Barometer 2	Barometer 3
Olivine melilitite	1.01 – 1.71	1.04 – 2.02	1.01 – 1.53
Ultramafic lamp	1.04 – 1.90	1.00 – 1.86	0.73 – 1.43

To calculate the temperatures at which these grains crystallised, two thermometers were also applied to the megacryst data. The first being a thermometer outlined by Nimis and Taylor (2000). This equation is however not ideal as the by Nimis and Taylor (2000) thermometer was developed to be applied to peridotitic clinopyroxene (i.e. xenocrystic or xenolithic, with high Cr), not magmatic clinopyroxene (which has low Cr), as is the case with the SPKC clinopyroxene megacrysts. The consequence of this being that inaccurate results may arise from the use of this thermometer. The second equation calculates the temperature at which a melt becomes saturated with clinopyroxene for any given pressure. Using the pressures calculated earlier (i.e. those shown in Table 10.3), the temperature ranges for the onset of clinopyroxene crystallisation are given in Table 10.4.

Table 10:4: Temperature estimates for the clinopyroxene megacrysts using data from this study and OM and UML assumed to be in equilibrium with the average olivine melilitite or ultramafic lamprophyre compositions from Marageni (2018). Thermometers used here are those developed by Putirka (2008).

Rock types		Temperature (℃)	
		Thermometer 1	Thermometer 2
Olivine melilitite			
	Barometer 1	1193 - 1212	1165 - 1250
	Barometer 2	1201 - 1212	1111 - 1217
	Barometer 3	1198 - 1212	1163 - 1231
Ultramafic lamp			
	Barometer 1	1147 - 1160	1178 - 1246
	Barometer 2	1147 - 1161	1156 - 1238
	Barometer 3	1154 - 1162	1135 - 1209

- Olivine Melilitite

If the mean SPKC olivine melilitite (Table 10.5) is assumed to represent the composition of the melt parental to the clinopyroxene megacrysts, barometers 1, 2 and 3 yield average pressures of 1.4 ± 0.2 GPa, 1.6 ± 0.2 GPa and 1.3 ± 0.1 Gpa respectively. The results from all three of the barometer equations overlap to some extent and indicate that the clinopyroxene megacrysts crystallised at pressures between 1 and 2 GPa, however if only the range of values for which all three barometers overlap is considered, this shrinks to between 1.0 and 1.5 GPa.

This range of values was then used to calculate the crystallisation/equilibration/formation temperatures of the clinopyroxene megacrysts. Pressures from barometer 1 yielded average temperature values of 1202 ± 3 ℃ and 1205 ± 13 ℃ for thermometers 1 and 2. When pressures from barometer 2 were used, average temperatures of 1200 ± 4 ℃ and 1188 ± 17 ℃ were achieved, and lastly for barometer 3, average temperatures of 1206 ± 3 ℃ and 1190 ± 15 ℃ respectively were recorded for

thermometers 1 and 2. Temperature readings across both thermometers shows a range of values extending from 1118 ℃ to as high as 1250 ℃, with an average value of 1184 ± 66 ℃.

Table 10:5: Mean SPKC OM and UML compositions used in the P-T estimates of the SPKC clinopyroxene megacrysts

(wt. %)	SiO_2	TiO_2	Al_2O_3	FeO^t	MnO	MgO	CaO	Na_2O	K_2O	Cr_2O_3
OM	34.18	2.76	7.65	11.76	0.21	14.19	15.53	2.84	1.99	0.10
UML	36.38	1.19	8.15	9.12	0.39	6.07	12.76	0.84	5.24	0.05

- Ultramafic Lamprophyres

When the mean ultramafic lamprophyres (Table 10.5) is assumed to be the liquid in equilibrium with the clinopyroxene megacrysts, average pressures of 1.6 ± 0.2 GPa, 1.5 ± 0.2 GPa and 1.1 ± 0.2 GPa respectively are generated for barometers 1, 2 and 3. The results from all three of the barometer equations overlap to some extent and indicate that the clinopyroxene megacrysts crystallised at pressures between 1 and 2 GPa, however if only the range of values for which all three barometers overlap is considered, this shrinks to between 1.0 and 1.4 GPa, which is slightly smaller than calculated if the parent melt is assumed to be olivine melilitite (i.e., 1.0 to 1.5 GPa).

Using these new pressure values to calculate the temperature conditions leads to average temperatures of 1151 ± 3 ℃ and 1217 ± 14 ℃ for barometer 1; 1153 ± 3 ℃ and 1207 ± 14 ℃ for barometer 2, and 1157 ± 2 ℃ and 1180.6 ± 15 ℃ for barometer 3. Temperature calculations across both thermometers shows a range of values that are less variable but very similar to those calculated using the average melilitite as the parent liquid. Calculated temperatures across both thermometers shows a range of values extending from 1135 to 1246 ℃, which averages out to 1191 ± 56 ℃.

Amphibole

Thermobarometric equations from Ridolfi and Renzulli (2012) were used as means to constrain the P-T conditions experienced by the amphibole megacrysts from the Salpeterkop complex. These equations are valid for calcic amphiboles derived from calc-alkaline and alkaline

magmas but have limitations that restrict them to grains that have experienced temperature and pressure conditions between 800 and 1130° C and 0.8 and 2.2 GPa respectively.

When applied to the data collected for the SPKC amphibole megacrysts, pressures calculated for these samples show a range of values extending from 1.0 to 1.3 GPa, with a mean value of 1.1 ± 0.1 GPa. These values are similar to those calculated for the clinopyroxene megacrysts. Calculated temperatures for the amphibole megacrysts extend from 1000 ℃ to 1074 ℃, with a mean value of 1034 ± 14 ℃. These values are on the order of 100 ℃ lower than those in the clinopyroxene megacrysts. The similarities in calculated pressures for the clinopyroxene and amphibole megacrysts could be explained by isobaric fractionation (i.e., cooling at a near-constant pressure).

Summary of Pressure-Temperature conditions during megacryst crystallisation

Thermobarometry calculations performed on clinopyroxene and amphibole megacryst compositions and assumptions parental melt compositions based on SPKC olivine melilitite and ultramafic lamprophyre compositions yielded pressures on the order of 1.0 to 1.5 GPa, which are equivalent to depths of 30-45 km. Since typical crustal thickness is 40 km, it is possible that the megacrysts crystallised around the moho or lower crust and not in the mantle as previously suggested. Temperature estimates for clinopyroxene average close to 1200 ℃ and 200 ℃ lower than this for amphibole.

10.5. Degassing

Amphibole

Stable isotope analyses performed on the amphibole megacrysts showed that their hydroxyl sites are on average less than half-filled (0.80 ± 0.24 apf; $1\sigma,\ n = 10$). These less than half-filled hydroxyl sites of the megacrysts is an initial indication that these minerals may have experienced some form of degassing or mineral breakdown, resulting in the release or removal of hydroxyl anions from the mineral structure. In addition to this, the amphibole megacrysts analysed show ranges of both D/H and $\delta^{18}O$ ratios that are wider and more enriched in deuterium and ^{18}O, relative to both the phlogopite megacrysts and more importantly the field

that defines primary mantle products (Fig. 8.3 and 8.4). The small overall variation in $\delta^{18}O$ suggests a uniform oxygen isotope composition of their parent melt.

The first concrete piece of evidence in favour of degassing is the broad correlation observed between the H_2O content of the amphibole megacrysts and their respective δD values (Fig. 8.1a). The positive nature of this trend argues that the megacrysts have been subjected to dehydration as the primary degassing process at work rather than dehydrogenation. Dehydrogenation is always accompanied by an increase in oxidation state (Fe^{3+}/Fe^{tot}) with decreasing water content, yielding a negative correlation (Demény et al. 2006). Additionally, no correlation exist between Cl, F or the ratio of F/Cl each as a function of the H_2O content of the megacrysts. This is evidence that the halogen content of the grains was not simply replacing hydroxyl groups, further supporting a degassing event.

While a dehydration reaction is charge balanced, it does generate a vacancy in a crystallographic site of amphibole, which can potentially result in the mineral becoming unstable and breaking down. This vacant space produced in the hydroxl site can, however be stabilised by the oxidation of Fe^{2+} to Fe^{3+} (Dyar et al. 1992; King et al. 1999), which can be seen in the weakly positive $Fe^{3+/}Fe^{tot}$-H_2O correlation (Fig. 8.5a). The dehydration experienced by the amphibole megacrysts likely took place through the following reaction:

$$2OH^-_{amph} = O^{2-}_{amph} + H_2O_{(released)}$$

Given that the amphibole and phlogopite megacrysts formed at depth, and not close to the surface, their degassing was modelled as a closed system process described by the following equation:

$$\delta D_{min} = \delta D^i_{min} - (1-F)1000 \ln \alpha_{H20-melt};$$

Where F is the overall remaining fraction of water in the mineral (i.e. amphibole or phlogopite) and α is the fractionation factor for water speciation (OH^- and H_2O) in the minerals (Underwood et al. 2013). The starting composition is given by the sample with the highest, H_2O contents and related δD values (i.e. 1.28 wt. % and -34‰). The model tracks how the δD composition of the mineral changes as water is lost. Amphibole-water fractionation factor of +

40‰ and + 80‰ were used in this thesis, based on earlier work done on Hydrogen isotope exchange between amphibole and H_2O (Graham et al., 1984; Suzuoki and Epstein, 1976 and Vennemann and O'neil, 1996). The modelled dehydration for the SPKC amphiboles megacrysts show that positive slopes appear to fit the data. The model curves plotted on the δD-H_2Owt% plot (Fig. 10.10a) indicate that water-amphibole fractionation factors of between + 40% and+ 80% can explain the positive slope observed in the SPKC amphiboles megacrysts.

Phlogopite

The phlogopite megacrysts were also shown to have less than half-filled (1.49 ± 0.56 apfu; $1\sigma,\ n = 10$) hydroxyl sites, suggesting that the grains may have undergone volatile-loss (dehydration or dehydrogenation) comparable to that inferred for amphibole megacrysts. The δD values recorded for these grains overlaps significantly with the range of values that define the primary mantle, suggesting that they are products of a melt derived from mantle conditions. δD plotted as a function of the water content for the phlogopite megacryst produces a broadly negative correlation, which only serves to confirm that these grains have experienced degassing related processes equivalent to what has been observed for the amphibole megacrysts.

Given the similarities in the behaviour of δD, H_2O, $\delta^{18}O$ between the amphibole and phlogopite megacrysts, the degassing modelling performed on the phlogopite megacrysts was done using the same closed-system dehydration reaction applied to be amphibole megacrysts, using fractionation values of + 40‰ and + 80‰ and a starting composition with the highest H_2O contents and related δD values (i.e. 2.54 wt. % and -58 ‰). The model curves were again plotted on a δD-H_2Owt% plot (Fig. 10.10b) and indicate that a water-phlogopite fractionation factors of between + 40‰ and + 80‰ best fits the phlogopite megacryst data.

The $\delta^{18}O$ values of phlogopite megacrysts also falls within the range defined by mantle values, further supporting their mantle origin. The pholopite megacrysts also display $\delta^{18}O$ values that are relatively uniform (5.53 ± 0.1 apfu; $1\sigma,\ n = 10$), similar to that of the amphibole megacrysts (5.84 ± 0.1 apfu; $1\sigma,\ n = 10$), which indicates a parental melt with a relatively homogenous $\delta^{18}O$ isotopic composition.

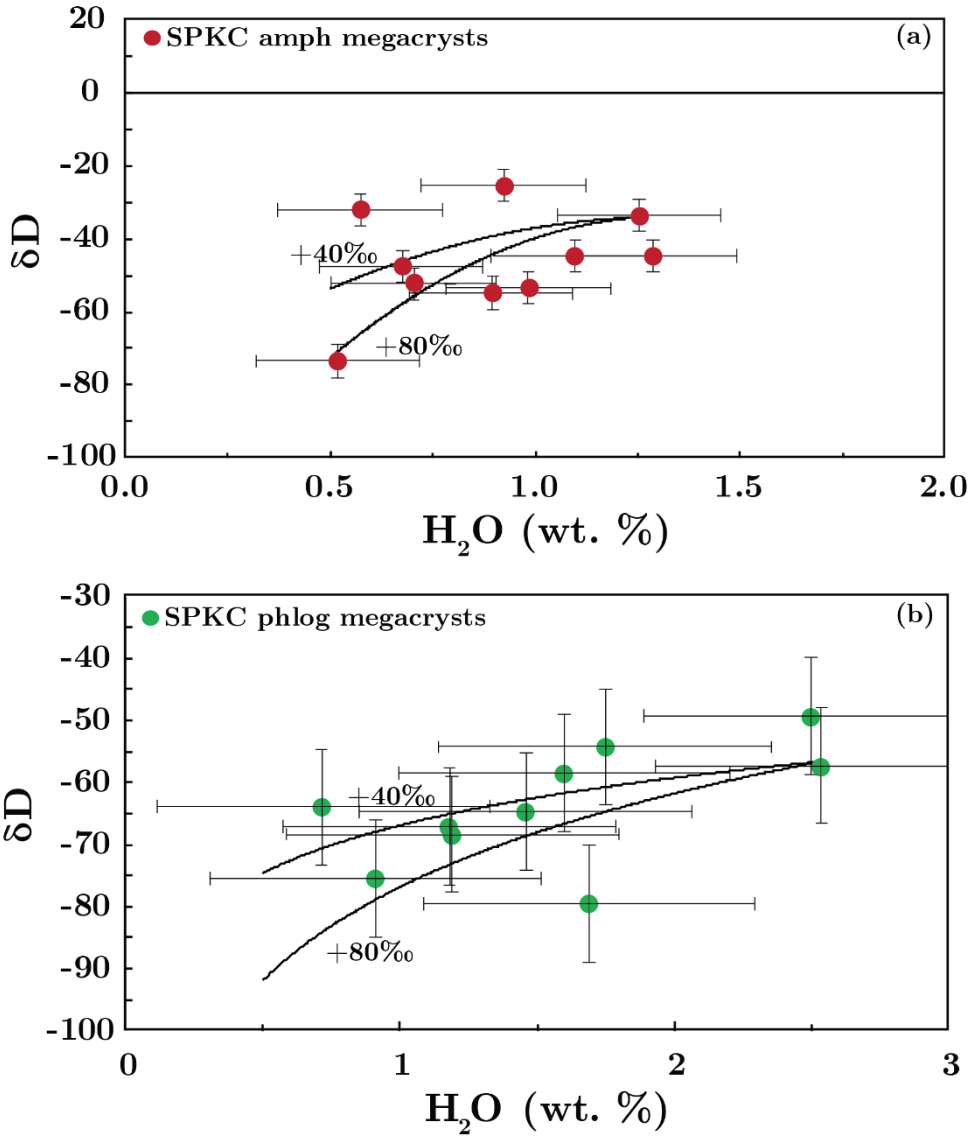

Figure 10.10: δD values versus H_2O contents (in wt%) in the (a) amphibole and (b) phlogopite megacrysts of SPKC show. The curved lines are for open-system degassing using fractionation values of +40 and +80 ‰ and were modelled after curves used by Demeny et al., 2006

Summary of stable isotope results

The amphibole and phlogopite megacrysts have H_2O contents that indicate that, on average, hydroxyl ions occupy less than half of the avaliable sites in these minerals, with the remaining hydroxyl sites not substantially filled with F^- and Cl^- ions. This combined with findings from plots of water content against δD, $\delta^{18}O$ and Fe^{3+}/Fe^{tot} respectively suggests that these grains underwent degassing, specifically dehydration. Due to the effects of degassing, the amphibole and phlogopite grains cannot be used to evaluate the primary δD characteristics of

the parental magma. Additional, the $\delta^{18}O$ and δD isotope ratios perserved for both mineral types are do not correlate against any other parameters (e.g. Mg-number).

11. Conclusion

This study explored the origins and petrogenesis of the megacryst suite from the Salpeterkop Carbonatite Complex. The major and trace element, stable and radiogenic isotopic analyses allowed for serveral conclusions to be drawn. The clinopyroxene, amphibole and phlogopite megacrysts share numerous similarities in REE and radiogenic isotopes (Sr-Nd-Pb), which suggests a co-genetic relationship between these mineral phases. FeO/MgO ratios calculated using xenolith mineral pairs suggests that phlogopite, ilmenite, amphibole and clinopyroxene entered the crystallisating assemblage in that order. Thermobaromatric equations applied to the clinopyroxene and amphibole megacrysts indicate that these samples crystallised under pressure of between 1.0 and 1.5 GPa, equivalent to 30-45 km, which is mainly in the lower crust, and temperatures of between 1000 and 1250℃.

Stable isotopes studies on the hydrous megacryst phases (amphibole and phlogopite) yield δD and $\delta^{18}O$ values that are consistent with them having crystallized from mantle-derived. There is very little variation in the δD and $\delta^{18}O$ values for both amphibole and phlogopite, which indicates that their parent melt(s) had a relatively homogenous $\delta^{18}O$ isotopic composition. The half-empty hydroxyl crystallographic site in both amphibole and phlogopite, megacrysts as well as trends in plots of δD and $\delta^{18}O$ against water content are consistent with these phases having experienced dehydration styled degassing as the minerals partially breakdown, owing to the loss of OH^- from the mineral structure.

The SPKC megacryst suite is proposed to have crystallised from a fractionating melt with a REE composition, similar to that of the carbonated SPKC ultramafic lamprophyres. Pb isotopic disequilibrium between the megacryst suite and ultramafic lamprophyre rocks of Salpeterkop does however suggest that the parent melt of the megacryst suite had a slightly greater affinity with the HIMU component, such as seen in the Robertson and Spiegel River melilitites to the south, that are also part of the Western Cape olivine melilitite province. This HIMU component could represent ancient subducted oceanic crustal material recycled via a mantle plume or other convective upwelling from the deep mantle.

12. References

Adam, J. and Green, T., 2006. Trace element partitioning between mica-and amphibole-bearing garnet lherzolite and hydrous basanitic melt: 1. Experimental results and the investigation of controls on partitioning behaviour. Contributions to Mineralogy and Petrology, 152, 1-17.

Banerjee, S., Kyser, T.K. and Mitchell, R.H., 2018. Oxygen and hydrogen isotopic composition of phlogopites and amphiboles in diamond-bearing kimberlite hosted MARID xenoliths: constraints on fluid-rock interaction and recycled crustal material in the deep continental lithospheric mantle. Chemical Geology, 479, 272-285.

Bell, D.R. and Ihinger, P.D., 2000. The isotopic composition of hydrogen in nominally anhydrous mantle minerals. Geochimica et Cosmochimica Acta, 64, 2109-2118.

Bell, D.R. and Moore, R.O. 2004. Deep chemical structure of the southern African mantle from kimberlite megacrysts. South African Journal of Geology, 107, 59–80.

Best, M.G., 1970. Kaersutite-peridotite inclusions and kindred megacrysts in basanitic lavas, Grand Canyon, Arizona. Contributions to Mineralogy and Petrology, 27, 25-44.

Bindeman, I., 2008. Oxygen isotopes in mantle and crustal magmas as revealed by single crystal analysis. Reviews in Mineralogy and Geochemistry, 69, 445-478.

Blundy, J. and Dalton, J., 2000. Experimental comparison of trace element partitioning between clinopyroxene and melt in carbonate and silicate systems, and implications for mantle metasomatism. Contributions to Mineralogy and Petrology, 139, 356-371.

Boettcher, A.L. and O'Neil, J.R., 1980. Stable isotope, chemical, and petrographic studies of high-pressure amphiboles and micas: evidence for metasomatism in the mantle source regions of alkali basalts and kimberlites. American Journal of Science, 280, 594-621.

Bottazzi, P., Tiepolo, M., Vannucci, R., Zanetti, A., Brumm, R., Foley, S.F. and Oberti, R., 1999. Distinct site preferences for heavy and light REE in amphibole and the prediction of $^{Amph/L}D_{REE}$. Contributions to Mineralogy and Petrology, 137, 36-45.

Bouvier, A., Vervoort, J.D. and Patchett, P.J., 2008. The Lu–Hf and Sm–Nd isotopic composition of CHUR: constraints from unequilibrated chondrites and implications for the bulk composition of terrestrial planets. Earth and Planetary Science Letters, 273(1-2), pp.48-57.

Boyd, F.R., 1973. A pyroxene geotherm. Geochimica et Cosmochimica Acta, 37, 2533-2546.

Braga, R., Morten, L. and Zanetti, A., 2006. Origin of a mica megacryst in an alkaline dyke from the Veneto Volcanic Province, Italy. European Journal of Mineralogy, 18, 223-231.

Brey, G.P., Nickel, K.G. and Kogarko, L., 1986. Garnet-pyroxene equilibria in the system CaO-MgO-Al_2O_3-SiO_2 (CMAS): prospects for simplified ('T-independent') lherzolite barometry and an eclogite-barometer. Contributions to Mineralogy and Petrology, 92, 448-455.

Burgess, S.R., Harte, B., 1998. Tracing lithosphere evolution through the analysis of heterogeneous G9/G10 garnets in peridotites xenoliths, I: Major element chemistry. In: Gurney, J.J., et al. (Ed.), Proceedings of the 7th IKC, VOl 1. Red Roof Design, Cape Town, p. 66–80.

Chaffey, D.J., Cliff, R.A. and Wilson, B.M., 1989. Characterization of the St Helena magma source. In: Saunders, A. D. & Norry, M.J. (eds) Magmatism in the Ocean Basins. Geological Society, London, Special Publications, 42(1), pp.257-276.

Chazot, G., Lowry, D., Menzies, M. and Mattey, D., 1997. Oxygen isotopic composition of hydrous and anhydrous mantle peridotites. Geochimica et Cosmochimica Acta, 61, 161-169.

Chevallier, L. (1997). Distribution and tectonics of South African Cretaceous kimberlites: implications for dynamics of the mantle, Russian Geology and Geophysics 38, 509-517.

Cooper, A.F. and Reid, D.L., 2000. The association of potassic trachytes and carbonatites at the Dicker Willem Complex, southwest Namibia: coexisting, immiscible, but not cogenetic magmas. Contributions to Mineralogy and Petrology, 139, 570-583.

Davies, G.R., Spriggs, A.J. and Nixon, P.H., 2001. A non-cognate origin for the Gibeon kimberlite megacryst suite, Namibia: implications for the origin of Namibian kimberlites. Journal of Petrology, 42, 159-172.

Dawson, J.B. and Smith, J.V., 1977. The MARID (mica-amphibole-rutile-ilmenite-diopside) suite of xenoliths in kimberlite. Geochimica et Cosmochimica Acta, 41, 309-323.

De Wet, J.J., 1975. Carbonatites and related rocks at Saltpetre Kop, Sutherland, Cape Province. Annals, University of Stellenbosch (Series A1) 1, 193-232.

Deloule, E., Albarede, F. and Sheppard, S.M., 1991. Hydrogen isotope heterogeneities in the mantle from ion probe analysis of amphiboles from ultramafic rocks. Earth and Planetary Science Letters, 105(4), pp.543-553.

Demény, A., Vennemann, T.W., Homonnay, Z., Milton, A., Embey-Isztin, Antal and Nagy, Géza, 2005. Origin of amphibole megacrysts in the Pliocene-Pleistocene basalts of the Carpathian-Pannonian region. Geologica Carpathica, 56, 179-189.

Demény, A., Vennemann, T.W., Harangi, S., Homonnay, Z. and Fórizs, I., 2006. H_2O-δD-Fe^{III} relations of dehydrogenation and dehydration processes in magmatic amphiboles. Rapid Communications in Mass Spectrometry, 20, 919-925.

Dingle, R.V. and Gentle, R.I., 1972. Early Tertiary volcanic rocks on the Agulhas Bank, South African continental shelf. Geological Magazine, 109, 127-136.

Dobosi, G., Downes, H., Mattey, D. and Embey-Isztin, A., 1998. Oxygen isotope ratios of phenocrysts from alkali basalts of the Pannonian basin: Evidence for an O-isotopically homogeneous upper mantle beneath a subduction-influenced area. Lithos, 42, 213-223.

Dosso, L., Hanan, B.B., Bougault, H., Schilling, J.G. and Joron, J.L., 1991. Sr-Nd-Pb geochemical morphology between 10° and 17° N on the Mid-Atlantic Ridge: a new MORB isotope signature. Earth and Planetary Science Letters, 106, 29-43.

Doucouré, C.M., de Wit, M.J. and Mushayandebvu, M.F., 1996. Effective elastic thickness of the continental lithosphere in South Africa. Journal of Geophysical Research: Solid Earth, 101, 11291-11303.

Duncan, R.A., Hargraves, R.B. and Brey, G.P., 1978. Age, palaeomagnetism and chemistry of melilite basalts in the Southern Cape, South Africa. Geological Magazine, 115, 317-327.

Eggler, D.H., McCallum, M.E. and Smith, C.B. 1979. Megacryst assemblages in kimberlite from Northern Colorado and Southern Wyoming: Petrology, geothermometry-barometry, and areal distribution. In: F.R. Boyd and H.O.A. Meyer (Eds) The Mantle Smple: Inclusions in Kimberlites and Other Volcanics. Proceedings of the 2nd International Kimberlite Conference, American Geophysical Union, 213–226.

Eglington, B.M., 2006. Evolution of the Namaqua-Natal Belt, southern Africa–A geochronological and isotope geochemical review. Journal of African Earth Sciences, 46, 93-111.

Evensen, N.M., Hamilton, P.J. and O'nions, R.K., 1978. Rare-earth abundances in chondritic meteorites. Geochimica et Cosmochimica Acta, 42, 1199-1212.

Fulmer, E.C., Nebel, O. and van Westrenen, W., 2010. High-precision high field strength element partitioning between garnet, amphibole and alkaline melt from Kakanui, New Zealand. Geochimica et Cosmochimica Acta, 74, 2741-2759.

Galer, S.J.G. and Abouchami, W., 1998. Practical application of lead triple spiking for correction of instrumental mass discrimination. Mineralogical Magazine A, 62, 491-492.

Graham, C.M., Harmon, R.S. and Sheppard, S.M., 1984. Experimental hydrogen isotope studies: hydrogen isotope exchange between amphibole and water. American Mineralogist, 69, 128-138.

Green, D.H. and Hibberson, W., 1970. The instability of plagioclase in peridotite at high pressure. Lithos, 3, 209-221.

Gurney, J.J. and Harte, B. 1980. Chemical variations in upper mantle nodules from southern African kimberlites. Philosophical Transactions of The Royal Society of London, A297, 273–293.

Gurney, J.J., Jakob, W.R.O. and Dawson, J.B., 1979. Megacrysts from the Monastery kimberlite pipe, South Africa. In B. Henry and O. Meyer (Eds), The Mantle Sample: Inclusion in Kimberlites and Other Volcanics (2), 227-243.

Hammouda, T., Chantel, J., Manthilake, G., Guignard, J. and Crichton, W., 2014. Hot mantle geotherms stabilize calcic carbonatite magmas up to the surface. Geology, 42, 911-914.

Harmon, R.S. and Hoefs, J., 1995. Oxygen isotope heterogeneity of the mantle deduced from global δ18O systematics of basalts from different geotectonic settings. Contributions to Mineralogy and Petrology, 120, 95-114.

Harris, C., Smith, H.S. and le Roex, A.P., 2000. Oxygen isotope composition of phenocrysts from Tristan da Cunha and Gough Island lavas: variation with fractional crystallization and evidence for assimilation. Contributions to Mineralogy and Petrology, 138, 164-175.

Harris, C. and Vogeli, J., 2010. Oxygen isotope composition of garnet in the Peninsula Granite, Cape Granite Suite, South Africa: constraints on melting and emplacement mechanisms. South African Journal of Geology, 113, 401-412.

Hart, S.R. and Dunn, T., 1993. Experimental cpx/melt partitioning of 24 trace elements. Contributions to Mineralogy and Petrology, 113, 1-8.

Hawkesworth, C.J., Erlank, A.J., Kempton, P.D. and Waters, F.G., 1990. Mantle metasomatism: isotope and trace-element trends in xenoliths from Kimberley, South Africa. Chemical Geology, 85, 19-34.

Ho, K.S., Chen, J.C., Smith, A.D. and Juang, W.S., 2000. Petrogenesis of two groups of pyroxenite from Tungchihsu, Penghu Islands, Taiwan Strait: implications for mantle metasomatism beneath SE China. Chemical Geology, 167, 355-372.

Hops, J.J., Gurney, J.J. and Harte, B., 1986, September. Megacrysts and deformed nodules from the Jagersfontein kimberlite pipe. In International Kimberlite Conference: Extended Abstracts (Vol. 4, pp. 256-258).

Howarth, G.H., 2018. Olivine megacryst chemistry, Monastery kimberlite: Constraints on the mineralogy of the HIMU mantle reservoir in southern Africa. Lithos, 314, pp.658-668.

Irving, A.J. and Frey, F.A., 1984. Trace element abundances in megacrysts and their host basalts: constraints on partition coefficients and megacryst genesis. Geochimica et Cosmochimica Acta, 48, 1201-1221.

Irving, A.J., 1974. Megacrysts from the Newer Basalts and other basaltic rocks of southeastern Australia. Geological Society of America Bulletin, 85, 1503-1514.

Jackson, E.D. and Wright, T.L., 1970. Xenoliths in the Honolulu volcanic series, Hawaii. Journal of Petrology, 11, 405-433.

Janney, P.E., le Roex, A.P., Carlson, R.W. and Viljoen, K.S., 2002. A chemical and multi-isotope study of the Western Cape olivine melilitite province, South Africa: implications for the sources of kimberlites and the origin of the HIMU signature in Africa. Journal of Petrology, 43, 2339-2370.

Jelsma, H.A., De Wit, M.J., Thiart, C., Dirks, P.H., Viola, G., Basson, I.J. and Anckar, E., 2004. Preferential distribution along transcontinental corridors of kimberlites and related rocks of Southern Africa. South African Journal of Geology, 107, 301-324.

Kamenetsky, V.S., Belousova, E.A., Giuliani, A., Kamenetsky, M.B., Goemann, K. and Griffin, W.L. 2014. Chemical abrasion of zircon and ilmenite megacrysts in the Monastery kimberlite: Implications for the composition of kimberlite melts. Chemical Geology, 383, 76–85.

King, P.L., Hervig, R.L., Holloway, J.R., Vennemann, T.W. and Righter, K., 1999. Oxy-substitution and dehydrogenation in mantle-derived amphibole megacrysts. Geochimica et Cosmochimica Acta, 63, 3635-3651.

Kostrovitsky, S.I., Malkovets, V.G., Verichev, E.M., Garanin, V.K. and Suvorova, L.V., 2004. Megacrysts from the Grib kimberlite pipe (Arkhangelsk province, Russia). Lithos, 77(1-4), pp.511-523.

Kramers, J.D., Smith, C.B., Lock, N.P., Harmon, R.S. and Boyd, F.R., 1981. Can kimberlites be generated from an ordinary mantle?. Nature, 291, 53.

Kyser, T.K. and O'Neil, J.R., 1984. Hydrogen isotope systematics of submarine basalts. Geochimica et Cosmochimica Acta, 48, 2123-2133.

Le Bas, M.J., 1962. The role of aluminum in igneous clinopyroxenes with relation to their parentage. American Journal of Science, 260, 267-288.

Leake, B.E., Woolley, A.R., Arps, C.E., Birch, W.D., Gilbert, M.C., Grice, J.D., Hawthorne, F.C., Kato, A., Kisch, H.J., Krivovichev, V.G. and Linthout, K., 1997. Report. Nomenclature of amphiboles: report of the subcommittee on amphiboles of the International Mineralogical Association Commission On New Minerals And Mineral Names. Mineralogical magazine, 61, 295-321.

Lee, W.J. and Wyllie, P.J., 2000. The system CaO-MgO-SiO_2-CO_2 at 1 GPa, metasomatic wehrlites, and primary carbonatite magmas. Contributions to Mineralogy and Petrology, 138, 214-228.

Lindsley, D.H. and Andersen, D.J., 1983. A two-pyroxene thermometer. Journal of Geophysical Research: Solid Earth, 88, A887-A906.

Liotard, J.M., Briot, D. and Boivin, P., 1988. Petrological and geochemical relationships between pyroxene megacrysts and associated alkali-basalts from Massif Central (France). Contributions to Mineralogy and Petrology, 98, 81-90.

Locock, A.J., 2014. An Excel spreadsheet to classify chemical analyses of amphiboles following the IMA 2012 recommendations. Computers & Geosciences, 62, 1-11.

Lorenz, V., 1973. On the formation of maars. Bulletin Volcanologique, 37, 183-204.

Mabaso, S. 2017. Mineral chemistry study of olivine melilitites at Saltpeterkop, unpublished. BSc Honours Thesis. University of Cape Town.

Malarkey, J., Pearson, D.G., Kjarsgaard, B.A., Davidson, J.P., Nowell, G.M., Ottley, C.J. and Stammer, J., 2010. From source to crust: tracing magmatic evolution in a kimberlite and a melilitite using microsample geochemistry. Earth and Planetary Science Letters, 299, 80-90.

Marageni, M., 2018. The geochemistry and petrogenesis of the Saltpeterkop carbonatite complex near Sutherland, Northern Cape, South Africa. Masters dissertation Thesis. University of Cape Town.

Martin, L.H., Schmidt, M.W., Mattsson, H.B. and Guenther, D., 2013. Element partitioning between immiscible carbonatite and silicate melts for dry and H_2O-bearing systems at 1–3 GPa. Journal of Petrology, 54, 2301-2338.

Matson, D.W., Muenow, D.W. and Garcia, M.O., 1984. Volatiles in amphiboles from xenoliths, Vulcan's Throne, Grand Canyon, Arizona, USA. Geochimica et Cosmochimica Acta, 48, 1629-1636.

Mattey, D., Lowry, D. and Macpherson, C., 1994. Oxygen isotope composition of mantle peridotite. Earth and Planetary Science Letters, 128, 231-241.

McDonough, W.F. and Sun, S.S., 1995. The composition of the Earth. Chemical geology, 120, 223-253.

Merry, M. and le Roex, A., 2007. Megacryst suites from the Lekkerfontein and Uintjiesberg kimberlites, southern Africa: evidence for a non-cognate origin. South African Journal of Geology, 110, 597-610.

Mertes, H. and Schmincke, H.U., 1985. Mafic potassic lavas of the Quaternary West Eifel volcanic field. Contributions to Mineralogy and Petrology, 89, 330-345.

Míková, J. and Denková, P., 2007. Modified chromatographic separation scheme for Sr and Nd isotope analysis in geological silicate samples. Journal of Geosciences, 52, 221-226.

Miller, R.M., 2008. The Geology of Namibia, Ministry of Mines and Energy, Geological Survey.

Mitchell, R.H., 1995. Kimberlites, Orangeites, and Related Rocks. Springer, New York, NY, 406.

Moore, R.O., Griffin, W.L., Gurney, J.J., Ryan, C.G., Cousens, D.R., Sie, S.H. and Suter, G.F., 1992. Trace element geochemistry of ilmenite megacrysts from the Monastery kimberlite, South Africa. Lithos, 29, 1-18.

Moore, R.O., 1986. A study of the kimberlites, diamonds and associated rocks and minerals from the monastery mine, South Africa. Doctoral Thesis, University of Cape Town.

Morimoto, N., 1988. Nomenclature of pyroxenes. Mineralogy and Petrology, 39(1), pp.55-76.

Newton, A.R. (1987). The fracture pattern around the Sutherland diatreme, Cape Province, from remote sensing. South African Journal of Geology 90, 99-106.

Nimis P (1995) A clinopyroxene geobarometer for basaltic systems based on crystals-structure modeling. Contrib Mineral Petrol 121, 115-125.

Nimis P, Taylor WR (2000) Single clinopyroxene thermobarometry for garnet peridotites. Part 1 Calibration and testing of a Cr-in-cpx barometer and an enstatite-in-cpx thermometer. Contrib Mineral Petrol 139, 541-554.

Nimis, P. and Ulmer, P., 1998. Clinopyroxene geobarometry of magmatic rocks Part 1: An expanded structural geobarometer for anhydrous and hydrous, basic and ultrabasic systems. Contributions to Mineralogy and Petrology, 133, 122-135.

Nowell, G.M., Pearson, D.G., Bell, D.R., Carlson, R.W., Smith, C.B., Kempton, P.D. and Noble, S.R., 2004. Hf isotope systematics of kimberlites and their megacrysts: new constraints on their source regions. Journal of Petrology, 45, 1583-1612.

O'Connor, J.M. and Jokat, W., 2015. Tracking the Tristan-Gough mantle plume using discrete chains of intraplate volcanic centers buried in the Walvis Ridge. Geology, 43, 715-718.

Pearson, D.G., Canil, D. and Shirey, S.B., 2003. Mantle samples included in volcanic rocks: xenoliths and diamonds. The Mantle and Core, Treatise on Geochemistry, Vol. 2, p. 171-275.

Phillips, D., Kiviets, G.B., Biddulph, M.G. and Madav, M.K. (2000). Cenozoic volcanism. In Partridge, T.C., Maud, R.R. (Eds.), The Cenozoic of Southern Africa, Oxford Monographs on Geology and Geophysics 40, 182-197.

Putirka, K.D., 2008. Thermometers and barometers for volcanic systems. In K. Putirka and F. Tepley (Eds), Minerals, Inclusions and Volcanic Processes, Reviews in Mineralogy and Geochemistry, Vol. 69, p. 61-120.

Reguir, E.P., Chakhmouradian, A.R., Halden, N.M., Malkovets, V.G. and Yang, P., 2009. Major-and trace-element compositional variation of phlogopite from kimberlites and carbonatites as a petrogenetic indicator. Lithos, 112, 372-384.

Ridolfi, F. and Renzulli, A., 2012. Calcic amphiboles in calc-alkaline and alkaline magmas: thermobarometric and chemometric empirical equations valid up to 1,130° C and 2.2 GPa. Contributions to Mineralogy and Petrology, 163, 877-895.

Savin, S.M. and Epstein, S., 1970. The oxygen and hydrogen isotope geochemistry of clay minerals. Geochimica et Cosmochimica Acta, 34, 25-42.

Schulze DJ. 1987. Megacrysts from alkaline volcanic rocks. In: Nixon PH (Ed.), Mantle Xenoliths, Chichester: J.Wiley & Sons, 433–452.

Schulze, D.J., Valley, J.R., Bell, D.R. and Spicuzza, M.J., 2001. Oxygen isotope variations in Cr-poor megacrysts from kimberlite. Geochimica et Cosmochimica Acta, 65, 4375-4384.

Shaw, C.S. and Eyzaguirre, J., 2000. Origin of megacrysts in the mafic alkaline lavas of the West Eifel volcanic field, Germany. Lithos, 50, 75-95.

Sheppard, S.M. and Dawson, J.B., 1975. Hydrogen, carbon and oxygen isotope studies of megacryst and matrix minerals from Lesothan and South African kimberlites. Physics and Chemistry of the Earth, Vol. 9, 747-763. Proceedings of the International Kimberlite Conference, edited by L. Ahrens, J.B. Dawson, A.R. Duncan and A.J. Erlank.

Sheppard, S.M. and Epstein, S., 1970. D/H and $^{18}O/^{16}O$ ratios of minerals of possible mantle or lower crustal origin. Earth and Planetary Science Letters, 9, 232-239.

Suzuoki, T. and Epstein, S., 1976. Hydrogen isotope fractionation between OH-bearing minerals and water. Geochimica et Cosmochimica Acta, 40, 1229-1240.

Sweeney, R.J., Green, D.H. and Sie, S.H., 1992. Trace and minor element partitioning between garnet and amphibole and carbonatitic melt. Earth and Planetary Science Letters, 113, 1-14.

Tanaka, T., Togashi, S., Kamioka, H., Amakawa, H., Kagami, H., Hamamoto, T., Yuhara, M., Orihashi, Y., Yoneda, S., Shimizu, H. and Kunimaru, T., 2000. JNdi-1: a neodymium isotopic reference in consistency with LaJolla neodymium. Chemical Geology, 168, 279-281.

Underwood, S.J., Feeley, T.C. and Clynne, M.A., 2013. Hydrogen isotope investigation of amphibole and glass in dacite magmas erupted in 1980–1986 and 2005 at Mount St. Helens, Washington. Journal of Petrology, 54, 1047-1070.

Valley, J.W., Kitchen, N., Kohn, M.J., Niendorf, C.R. and Spicuzza, M.J., 1995. UWG-2, a garnet standard for oxygen isotope ratios: strategies for high precision and accuracy with laser heating. Geochimica et Cosmochimica Acta, 59, 5223-5231.

Vennemann, T.W. and O'Neil, J.R., 1993. A simple and inexpensive method of hydrogen isotope and water analyses of minerals and rocks based on zinc reagent. Chemical Geology, 103, 227-234.

Vennemann, T.W. and O'Neil, J.R., 1996. Hydrogen isotope exchange reactions between hydrous minerals and molecular hydrogen: I. A new approach for the determination of hydrogen isotope fractionation at moderate temperatures. Geochimica et Cosmochimica Acta, 60, 2437-2451.

Verwoerd, W.J., 1990. The Salpeterkop ring structure, Cape Province, South Africa. Tectonophysics, 171, 275-285.

White, W.M. and Hofmann, A.W., 1982. Sr and Nd isotope geochemistry of oceanic basalts and mantle evolution. Nature, 296, 821.

Woodland, A.B. and Jugo, P.J., 2007. A complex magmatic system beneath the Deves volcanic field, Massif Central, France: evidence from clinopyroxene megacrysts. Contributions to Mineralogy and Petrology, 153, 719-731.

Woolsey, T.S., McCallum, M.E. and Schumm, S.A., 1975. Modeling of diatreme emplacement by fluidization. In Physics and Chemistry of the Earth, vol. 9, p. 29-42. Proceedings of the International Kimberlite Conference, edited by L. Ahrens, J.B. Dawson, A.R. Duncan and A.J. Erlank

Yardley, B., 2011. Metasomatism. In Encyclopedia of Astrobiology (p 1022-1022). Springer, Berlin, Heidelberg.

Appendices

Appendix 1: Mineral compositions for SPKC megacrysts

Table 12:1: Major and trace element data for clinopyroxene megacrysts

Sample	SPK M5 G1	SPK M5 G2	SPK M5 G3	SPK M5 G4	SPK M5 G5	SPK M5 G6	SPK M5 G7	SPK M5 G8	SPK M5 G9
SiO2	50.97	51.04	50.18	51.55	51.04	50.27	50.54	51.16	50.46
TiO2	1.28	1.25	1.59	1.15	1.23	1.56	1.57	1.23	1.60
Al2O3	4.08	4.13	4.81	3.50	4.08	4.75	4.76	4.15	4.82
Cr2O3	0.03	bd	0.02	0.02	0.02	0.0045	0.01	0.01	0.01
FeO	7.37	7.30	6.80	6.74	7.48	7.12	7.31	6.30	6.68
MnO	0.15	0.10	0.09	0.09	0.12	0.10	0.10	0.12	0.09
MgO	13.92	13.86	13.99	14.65	13.97	13.91	13.87	14.51	14.22
CaO	21.50	21.29	21.44	21.74	21.42	21.71	21.48	22.49	21.85
Na2O	1.24	1.23	1.12	1.01	1.25	1.21	1.24	0.96	1.19
K2O	0.01	0.01	0.002	0.01	0.0045	0.01	0.004	0.001	0.0035
Total	100.54	100.20	100.05	100.45	100.61	100.65	100.88	100.93	100.92
Mg#	77.10	77.16	78.55	79.46	76.90	77.66	77.17	80.41	79.12
Ca#	52.62	52.49	52.45	51.64	52.43	52.89	52.69	52.72	52.51
Sc	41	48	60	59	60	60	60	71	72
V	240	267	283	243	301	297	301	263	288
Cr	1.8	2.3	10.8	10.4	1.8	6.2	6.2	1.6	10.2
Ni	4.5	4.3	14.0	13.0	5.3	10.3	10.1	12.8	16.1
Rb	< d.l.	< d.l.	0.01	0.07	< d.l.	0.01	0.02	0.01	0.04
Sr	107	122	125	127	129	134	130	125	134
Y	6.9	7.5	9.2	8.5	9.2	9.7	9.9	10.1	10.5
Zr	212	258	219	197	322	274	274	283	239
Nb	0.74	0.77	0.92	0.64	0.95	1.05	1.03	0.76	0.87
Ba	0.03	0.03	0.06	0.07	0.09	0.06	0.08	0.45	0.10
La	3.86	4.43	5.03	4.47	4.76	5.64	5.59	5.14	5.14
Ce	14.7	16.7	19.0	17.0	18.4	21.0	20.6	20.2	19.8
Pr	2.53	2.90	3.24	2.92	3.00	3.56	3.53	3.46	3.38
Nd	13.8	16.2	18.4	16.7	18.2	20.1	19.7	18.0	18.6
Sm	3.70	4.24	4.93	4.32	4.73	5.24	5.39	5.35	5.15
Eu	1.32	1.44	1.65	1.39	1.60	1.74	1.69	1.65	1.79
Gd	3.07	3.35	3.94	3.50	3.83	4.00	4.25	4.34	4.41
Tb	0.405	0.446	0.558	0.483	0.536	0.543	0.556	0.484	0.549
Dy	2.12	2.22	2.72	2.33	2.51	2.69	2.88	2.84	2.75
Ho	0.285	0.370	0.428	0.345	0.402	0.423	0.401	0.445	0.375
Er	0.680	0.746	0.726	0.831	0.800	0.799	0.896	0.737	0.849
Tm	0.086	0.075	0.096	0.094	0.094	0.103	0.101	0.108	0.109
Yb	0.534	0.583	0.638	0.618	0.704	0.683	0.716	0.678	0.645
Lu	0.061	0.078	0.057	0.061	0.074	0.065	0.066	0.072	0.087
Hf	10.4	11.9	10.3	8.86	14.3	12.5	13.0	12.9	10.0
Ta	0.20	0.24	0.23	0.15	0.26	0.29	0.28	0.20	0.19
Pb	0.09	0.11	0.07	0.12	0.11	0.07	0.08	0.13	0.09
Th	0.07	0.07	0.08	0.06	0.08	0.09	0.11	0.18	0.08
U	0.01	0.02	0.01	0.01	0.02	0.01	0.02	0.06	0.01

Appendix 1, Table 12.1 continued

Sample	SPK M5 G10	SPK M5 G11	SPK M5 G12	SPK M5 G13	SPK M5 G14	SPK M5 G15	SPK M5 G16	SPK M5 G17	SPK M4 G1
SiO_2	50.42	50.96	50.99	51.23	50.90	50.44	50.67	51.35	50.43
TiO_2	1.64	1.28	1.43	1.31	1.23	1.49	1.53	1.20	1.41
Al_2O_3	4.91	4.23	4.26	3.95	4.07	4.75	4.72	3.95	4.36
Cr_2O_3	bd	0.02	0.003	bd	0.01	0.01	0.01	0.01	0.01
FeO	6.95	7.63	6.87	6.25	7.49	7.26	6.66	7.44	7.37
MnO	0.14	0.12	0.12	0.14	0.12	0.11	0.15	0.15	0.10
MgO	13.98	13.77	14.47	14.75	13.99	13.79	14.27	13.94	14.00
CaO	21.74	21.73	21.80	21.85	21.48	21.59	21.91	21.48	21.87
Na_2O	1.16	1.23	1.14	1.02	1.24	1.17	1.11	1.18	1.21
K_2O	0.01	0.01	0.003	0.02	0.01	0.01	0.01	0.004	0.01
Total	100.94	100.98	101.07	100.51	100.53	100.61	101.04	100.71	100.78
Mg#	78.17	76.28	78.95	80.77	76.89	77.17	79.23	76.94	77.17
Ca#	52.79	53.16	52.00	51.60	52.49	52.98	52.48	52.57	52.92
Sc	59	51	58	57	55	56	63	50	51
V	290	272	261	226	270	277	259	252	263
Cr	10.9	2.6	10.0	23.5	1.5	6.0	9.8	2.8	2.8
Ni	12.9	4.8	12.9	19.0	4.9	9.4	14.9	4.0	6.7
Rb	0.01	0.01	0.01	< d.l.	< d.l.	0.01	0.02	0.03	0.01
Sr	127	119	116	106	113	120	119	114	118
Y	8.9	8.1	8.4	7.0	8.0	8.7	8.7	7.2	7.9
Zr	216	269	205	141	288	250	201	248	238
Nb	0.93	0.93	0.81	0.60	0.87	0.94	0.65	0.70	0.89
Ba	0.06	0.15	0.07	0.02	0.12	0.07	0.03	0.01	0.03
La	5.03	4.30	4.59	3.82	4.07	5.19	4.62	3.87	4.57
Ce	18.9	16.4	17.2	13.5	15.7	18.9	17.3	14.8	17.8
Pr	3.21	2.80	3.02	2.41	2.86	3.22	3.12	2.61	2.96
Nd	18.2	16.2	17.2	14.1	16.0	18.3	17.1	14.6	16.5
Sm	4.99	4.32	4.50	3.66	4.13	4.67	4.60	3.84	4.40
Eu	1.55	1.44	1.50	1.29	1.41	1.53	1.44	1.28	1.44
Gd	3.93	3.29	3.64	2.94	3.40	3.66	3.76	2.96	3.45
Tb	0.540	0.452	0.488	0.389	0.454	0.494	0.491	0.441	0.466
Dy	2.58	2.34	2.40	2.04	2.24	2.52	2.42	2.17	2.35
Ho	0.367	0.358	0.391	0.317	0.366	0.397	0.422	0.346	0.363
Er	0.829	0.679	0.872	0.799	0.711	0.794	0.687	0.708	0.767
Tm	0.106	0.073	0.094	0.083	0.085	0.086	0.093	0.054	0.073
Yb	0.629	0.634	0.605	0.488	0.594	0.625	0.608	0.539	0.552
Lu	0.064	0.071	0.065	0.045	0.068	0.075	0.067	0.057	0.046
Hf	9.69	11.9	9.49	6.71	13.6	11.9	9.14	11.6	10.8
Ta	0.25	0.22	0.24	0.13	0.24	0.27	0.15	0.21	0.23
Pb	0.06	0.10	0.06	0.08	0.07	0.07	0.08	0.10	0.10
Th	0.08	0.08	0.09	0.07	0.09	0.10	0.08	0.07	0.08
U	0.01	0.01	0.01	0.01	0.02	0.01	0.01	0.02	0.01

Appendix 1, Table 12.1 continued

Sample	SPK M4 G4	SPK M4 G5	SPK M4 G7	SPK M4 G8	SPK M4 G9	SPK M4 G10	SPK M4 G11	SPK M4 G12	SPK M4 G13
SiO_2	49.79	50.33	50.00	50.73	50.66	50.31	50.90	47.86	50.17
TiO_2	1.65	1.50	1.45	1.10	1.15	1.47	1.26	2.19	1.43
Al_2O_3	4.87	4.55	4.47	3.65	3.80	4.57	3.74	7.11	4.43
Cr_2O_3	0.005	0.01	0.004	0.01	0.02	bd	bd	0.03	0.01
FeO	7.25	7.38	7.56	6.16	7.31	6.95	6.43	5.89	7.63
MnO	0.10	0.11	0.11	0.09	0.14	0.13	0.14	0.08	0.13
MgO	13.82	13.91	13.88	14.82	14.33	14.11	14.97	13.83	13.77
CaO	21.76	21.76	21.89	22.52	21.80	21.66	21.67	22.00	21.80
Na_2O	1.23	1.23	1.31	1.02	1.12	1.21	1.02	1.04	1.29
K_2O	0.001	0.004	0.01	0.01	0.02	-	0.005	0.01	0.001
Total	100.48	100.78	100.67	100.10	100.34	100.39	100.13	100.04	100.65
Mg#	77.24	77.05	76.59	81.08	77.73	78.34	80.56	80.72	76.28
Ca#	53.12	52.95	53.15	52.22	52.25	52.48	51.02	53.36	53.24
Sc	60	58	53	77	66	72	66	127	60
V	283	293	262	248	321	302	226	294	313
Cr	7.4	0.9	0.2	1.5	2.9	5.7	16.0	154.7	2.8
Ni	9.1	5.3	4.7	13.7	6.2	15.4	22.4	57.8	5.6
Rb	0.01	0.07	0.04	0.17	< d.l.	0.58	0.02	0.04	0.00
Sr	128	120	110	134	142	140	116	103	138
Y	8.6	9.7	8.2	9.7	10.3	14.1	8.7	10.8	9.1
Zr	297	288	261	309	340	298	168	224	357
Nb	1.15	1.13	1.20	0.79	1.09	1.20	0.64	1.46	1.22
Ba	0.11	0.31	2.28	2.43	0.05	12.21	< d.l.	0.38	0.09
La	5.09	4.87	4.47	5.30	5.93		4.70	5.58	5.00
Ce	19.1	18.8	16.9	18.4	22.5	21.3	17.2	19.7	19.8
Pr	3.21	3.31	2.95	3.15	3.81	5.97	2.95	3.28	3.28
Nd	18.7	19.0	17.2	17.8	21.2	21.1	16.3	20.7	18.0
Sm	4.68	5.13	4.70	4.78	5.61	6.69	4.30	5.59	4.85
Eu	1.60	1.86	1.51	1.49	1.86	2.10	1.36	1.83	1.58
Gd	3.78	4.00	3.66	4.05	4.41	5.12	3.53	4.75	3.81
Tb	0.525	0.545	0.503	0.524	0.584	0.658	0.470	0.601	0.516
Dy	2.41	2.74	2.58	2.81	3.22	3.40	2.37	2.97	2.60
Ho	0.388	0.435	0.395	0.431	0.482	0.520	0.360	0.460	0.442
Er	0.897	0.807	0.769	0.802	0.996	0.949	0.672	0.857	0.854
Tm	0.092	0.111	0.089	0.109	0.139	0.101	0.084	0.094	0.091
Yb	0.626	0.690	0.581	0.685	0.763	0.950	0.553	0.701	0.680
Lu	0.091	0.065	0.059	0.068	0.074	0.094	0.061	0.050	0.078
Hf	14.4	13.9	12.6	14.5	15.3	13.2	8.10	11.3	16.5
Ta	0.38	0.31	0.26	0.22	0.29	0.23	0.12	0.40	0.33
Pb	0.09	0.13	0.08	0.21	0.10	0.12	0.12	0.06	0.11
Th	0.10	0.12	0.12	0.23	0.11	0.12	0.07	0.16	0.11
U	0.02	0.02	0.02	0.05	0.01	0.05	0.02	0.02	0.02

Appendix 1, Table 12.1 continued

Sample	SPK M4 G14	SPK M4 G15	SPK M4 G16	SPK M4 G17	SPK M4 G18	SPK M4 G19	SPK M4 G20	SPK M4 G21	SPK M2 G1
SiO_2	51.33	51.24	49.29	52.06	51.21	50.82	49.63	50.52	52.39
TiO_2	1.05	1.01	1.85	0.61	1.00	1.30	1.43	1.27	0.83
Al_2O_3	3.60	3.25	5.37	2.25	3.13	3.64	4.41	3.94	3.05
Cr_2O_3	0.04	0.01	0.04	-	0.01	0.003	0.002	-	-
FeO	6.92	7.24	6.09	6.68	7.20	5.78	7.51	6.97	7.20
MnO	0.13	0.14	0.07	0.14	0.15	0.09	0.13	0.14	0.16
MgO	14.41	14.45	14.71	15.60	14.61	15.67	13.81	14.42	14.37
CaO	21.84	22.03	21.97	22.13	21.93	22.15	21.66	21.98	22.30
Na_2O	1.09	1.10	1.05	0.94	1.05	0.88	1.30	1.15	1.19
K_2O	0.01	0.00	0.01	0.02	0.003	0.003	0.001	0.003	-
Total	100.43	100.47	100.44	100.42	100.30	100.34	99.87	100.40	101.50
Mg#	78.76	78.06	81.15	80.61	78.34	82.84	76.60	78.65	78.04
Ca#	52.15	52.30	51.79	50.50	51.91	50.42	53.01	52.30	52.76
Sc	58	55	69	66	62	89	59	60	48
V	255	254	258	193	243	232	305	259	214
Cr	15.9	2.1	72.0	1.2	0.6	27.0	0.6	14.4	60.9
Ni	8.3	4.9	42.6	9.9	4.7	35.6	4.8	11.1	39.7
Rb	< d.l.	< d.l.	0.01	0.00	0.01	0.04	0.03	0.06	0.01
Sr	127	127	125	120	118	97	128	131	97
Y	8.4	8.0	8.8	8.9	8.9	8.0	10.1	8.6	5.9
Zr	202	231	142	224	226	194	312	231	99
Nb	0.69	0.68	0.65	0.89	0.58	0.93	1.10	0.72	0.51
Ba	0.09	0.05	0.04	2.96	0.05	0.09	0.04	0.06	0.06
La	4.41	4.18	4.88	5.31	3.94	4.31	5.20	4.88	3.41
Ce	16.6	16.0	17.8	16.7	15.1	16.4	19.7	17.7	15.3
Pr	2.87	2.83	3.13	2.73	2.58	2.87	3.32	3.03	2.45
Nd	16.4	16.0	17.5	17.0	15.7	16.2	19.3	17.4	13.6
Sm	4.19	4.20	4.43	4.28	4.08	4.12	5.04	4.50	3.55
Eu	1.45	1.37	1.38	1.50	1.37	1.27	1.61	1.46	1.21
Gd	3.44	3.31	3.80	3.56	3.58	3.55	4.01	3.66	2.74
Tb	0.436	0.463	0.488	0.390	0.503	0.427	0.546	0.491	0.381
Dy	2.51	2.31	2.55	2.38	2.37	2.03	2.88	2.39	1.95
Ho	0.339	0.350	0.426	0.386	0.388	0.299	0.452	0.389	0.304
Er	0.826	0.819	0.840	0.795	0.815	0.585	0.904	0.756	0.580
Tm	0.079	0.102	0.080	0.107	0.093	0.088	0.112	0.115	0.073
Yb	0.557	0.560	0.617	0.628	0.618	0.555	0.704	0.651	0.473
Lu	0.057	0.059	0.067	0.068	0.079	0.063	0.074	0.080	0.050
Hf	9.20	10.0	7.91	9.68	10.5	9.48	14.3	10.8	5.94
Ta	0.14	0.14	0.15	0.11	0.14	0.20	0.35	0.21	0.15
Pb	0.09	0.11	0.07	0.21	0.11	0.09	0.11	0.08	0.10
Th	0.07	0.06	0.08	0.24	0.05	0.10	0.10	0.06	0.06
U	0.02	0.01	0.01	0.07	0.01	0.01	0.02	0.01	0.01

Appendix 1, Table 12.1 continued

Sample	SPK M2 G2	SPK M2 G3	SPK M2 G7	SPK M2 G11	SPK M2 G14	SPK M2 G15	SPK M1 G1	SPK M1 G2	SPK M1 G3
SiO_2	52.01	52.07	49.91	49.79	51.06	49.97	51.26	50.21	50.88
TiO_2	1.01	0.80	1.86	1.59	1.16	1.63	1.16	1.43	1.31
Al_2O_3	3.11	3.44	5.65	4.82	4.07	4.82	3.69	4.52	4.10
Cr_2O_3	0.01	0.003	0.09	0.004	0.001	bd	bd	bd	0.02
FeO	6.91	6.84	5.36	7.77	6.70	7.77	6.64	7.47	6.42
MnO	0.15	0.12	0.07	0.13	0.13	0.13	0.14	0.10	0.12
MgO	14.79	14.33	14.83	13.46	14.22	13.37	14.70	13.77	14.66
CaO	22.24	22.20	21.80	21.44	22.02	21.35	21.66	21.70	21.72
Na_2O	1.01	1.11	1.04	1.33	1.03	1.34	1.02	1.17	1.04
K_2O	0.01	0.001	0.01	0.001	0.003	0.003	0.01	0.01	0.01
Total	101.23	100.92	100.60	100.33	100.40	100.37	100.27	100.38	100.28
Mg#	79.22	78.86	83.12	75.53	79.09	75.39	79.77	76.65	80.26
Ca#	51.96	52.71	51.40	53.40	52.69	53.46	51.46	53.13	51.58
Sc	54	56	54	60	59	61	42	45	52
V	261	228	275	250	182	221	182	235	216
Cr	15.5	9.9	2.5	2.4	0.8	15.5	6.3	2.0	23.0
Ni	14.3	9.3	5.2	6.9	10.6	20.9	12.0	6.3	18.7
Rb	< d.l.	0.02	0.01	< d.l.	0.02	0.03	0.01	0.05	0.02
Sr	117	118	116	124	109	114	84	108	104
Y	8.4	7.7	8.4	8.9	7.8	7.4	5.5	7.2	6.4
Zr	216	180	319	223	189	151	105	207	125
Nb	0.95	0.58	1.07	0.56	0.35	0.54	0.38	0.75	0.47
Ba	0.05	0.04	0.01	0.02	0.08	0.02	0.08	0.08	0.05
La	4.82	4.23	4.01	4.13	4.21	4.34	2.59	4.24	3.35
Ce	19.2	15.7	15.8	16.0	15.6	16.3	12.3	16.8	13.4
Pr	3.18	2.62	2.88	2.82	2.68	2.80	2.14	2.93	2.42
Nd	17.5	14.7	16.2	16.2	14.4	15.3	12.5	16.1	13.6
Sm	4.53	3.94	4.36	4.22	3.78	3.98	3.40	4.01	3.58
Eu	1.61	1.41	1.34	1.42	1.30	1.27	1.16	1.25	1.11
Gd	3.68	3.12	3.36	3.49	2.99	3.24	2.64	3.32	2.91
Tb	0.504	0.383	0.501	0.455	0.450	0.426	0.400	0.403	0.411
Dy	2.54	2.23	2.39	2.52	2.19	2.19	1.94	2.30	1.91
Ho	0.328	0.335	0.295	0.443	0.356	0.317	0.305	0.354	0.289
Er	0.860	0.614	0.716	0.767	0.728	0.677	0.655	0.778	0.718
Tm	0.087	0.085	0.097	0.108	0.075	0.087	0.077	0.070	0.062
Yb	0.651	0.577	0.636	0.592	0.566	0.483	0.470	0.541	0.455
Lu	0.058	0.062	0.084	0.072	0.057	0.065	0.065	0.080	0.046
Hf	10.5	8.62	14.7	9.59	8.01	7.47	6.66	11.1	6.96
Ta	0.26	0.13	0.30	0.12	0.06	0.12	0.12	0.21	0.13
Pb	0.13	0.08	0.09	0.09	0.13	0.10	0.09	0.13	0.07
Th	0.09	0.05	0.08	0.05	0.12	0.06	0.04	0.11	0.04
U	0.01	0.01	0.01	0.01	0.02	0.01	0.01	0.03	0.01

Appendix 1, Table 12.1 continued

Sample	SPK M1 G5	SPK M1 G7	SPK M1 G8	SPK M1 G9	SPK M1 G10	SPK M1 G11	SPK M1 G12	SPK M1 G13	SPK M1 G14
SiO_2	51.81	51.33	50.53	49.83	51.30	51.28	49.07	50.25	51.58
TiO_2	0.96	1.34	1.47	1.66	0.96	0.98	1.72	1.44	0.98
Al_2O_3	3.04	4.13	4.65	5.09	3.35	3.29	5.36	4.41	3.22
Cr_2O_3	bd	bd	0.02	0.04	0.02	bd	0.06	bd	bd
FeO	7.17	6.64	7.52	6.76	7.46	7.28	6.80	7.51	7.18
MnO	0.07	0.10	0.12	0.10	0.11	0.13	0.13	0.15	0.14
MgO	14.65	14.85	13.70	13.95	14.41	14.37	13.61	13.72	14.53
CaO	21.93	21.82	21.71	21.85	22.10	21.71	21.63	21.45	21.79
Na_2O	1.10	1.04	1.21	1.09	1.08	1.14	1.15	1.22	1.00
K_2O	0.003	0.01	0.003	0.02	0.01	0.01	0.02	0.02	0.01
Total	100.74	101.25	100.92	100.38	100.78	100.18	99.56	100.15	100.42
Mg#	78.45	79.93	76.43	78.59	77.49	77.86	78.09	76.50	78.28
Ca#	51.85	51.39	53.27	52.99	52.45	52.09	53.34	52.93	51.90
Sc	50	61	54	62	49	49	56	53	53
V	231	235	284	254	234	232	255	277	229
Cr	2.0	24.1	2.7	51.6	2.2	2.1	51.6	2.8	2.9
Ni	4.4	18.6	7.3	22.5	5.1	4.7	23.4	6.7	8.6
Rb	0.04	0.08	0.03	0.15	0.04	0.06	0.08	$<$ d.l.	0.02
Sr	128	111	127	126	113	115	118	124	111
Y	7.3	7.5	9.3	8.4	7.2	7.7	9.2	8.3	7.8
Zr	200	146	270	197	206	209	197	268	180
Nb	0.54	0.65	0.96	0.78	0.71	0.57	0.79	0.98	0.50
Ba	0.06	0.01	0.11	0.05	0.02	0.08	0.06	0.05	0.18
La	3.82	3.86	4.86	5.16	3.65	3.68	5.06	5.48	3.76
Ce	15.2	14.3	19.3	19.0	14.0	14.1	18.7	19.2	14.4
Pr	2.62	2.49	3.24	3.23	2.42	2.47	3.18	3.31	2.53
Nd	15.1	15.4	18.5	17.5	14.3	14.0	17.8	19.1	14.3
Sm	4.09	4.02	4.69	4.66	3.87	3.74	4.83	4.62	3.90
Eu	1.32	1.11	1.64	1.51	1.24	1.28	1.42	1.54	1.27
Gd	3.21	3.26	3.65	3.83	3.08	3.26	3.84	3.68	3.15
Tb	0.439	0.359	0.538	0.500	0.428	0.476	0.430	0.504	0.430
Dy	2.18	2.23	2.45	2.56	2.03	1.97	2.42	2.52	2.20
Ho	0.335	0.282	0.411	0.428	0.323	0.318	0.389	0.376	0.347
Er	0.692	0.721	0.869	0.777	0.725	0.738	0.857	0.872	0.743
Tm	0.076	0.080	0.092	0.077	0.086	0.081	0.097	0.087	0.080
Yb	0.526	0.549	0.710	0.660	0.529	0.492	0.650	0.661	0.532
Lu	0.052	0.041	0.074	0.074	0.056	0.073	0.066	0.057	0.079
Hf	9.19	7.18	13.1	8.93	9.45	9.97	9.59	12.1	8.09
Ta	0.14	0.14	0.27	0.26	0.12	0.15	0.18	0.28	0.12
Pb	0.13	0.09	0.09	0.09	0.11	0.09	0.10	0.07	0.08
Th	0.05	0.06	0.11	0.10	0.05	0.06	0.11	0.12	0.06
U	0.00	0.00	0.01	0.02	0.01	0.01	0.01	0.02	0.01

Appendix 1, Table 12.1 1 continued

Sample	SPK M1 G15	SPK M1 G16	SPK M1 G17	SPK M1 G18	SPK M1 G19	SPK M3 G1	SPK M3 G2	SPK M3 G3	SPK M3 G4
SiO_2	50.32	50.04	50.12	51.74	51.37	51.31	50.34	51.35	51.65
TiO_2	1.43	1.56	1.50	1.06	1.22	1.33	1.83	0.99	0.93
Al_2O_3	4.59	4.57	4.73	3.24	3.75	3.96	5.23	3.28	3.19
Cr_2O_3	bd	bd	bd	bd	bd	0.03	0.02	bd	bd
FeO	7.48	7.01	7.24	7.32	6.82	6.59	6.32	7.43	7.33
MnO	0.14	0.10	0.16	0.12	0.11	0.12	0.14	0.18	0.20
MgO	13.91	14.00	13.90	14.65	14.93	14.91	14.82	14.44	14.55
CaO	21.66	21.71	21.57	22.08	21.88	21.87	21.92	21.96	21.86
Na_2O	1.36	1.17	1.15	1.07	1.01	1.00	1.02	1.17	1.06
K_2O	0.01	0.01	0.03	0.005	0.01	0.01	0.01	0.02	0.01
Total	100.90	100.18	100.40	101.27	101.08	101.13	101.64	100.79	100.77
Mg#	76.81	78.04	77.38	78.09	79.59	80.11	80.69	77.59	77.94
Ca#	52.83	52.74	52.75	52.03	51.32	51.34	51.55	52.25	51.95
Sc	55	59	58	53	56	53	65	47	51
V	280	263	262	227	227	204	242	230	223
Cr	2.8	1.6	1.9	2.7	9.3	13.4	64.7	2.0	0.7
Ni	7.0	7.8	8.8	7.8	13.9	16.7	41.8	5.0	3.9
Rb	0.02	0.05	0.01	0.02	0.05	0.01	0.10	0.01	0.01
Sr	124	122	118	110	110	96	116	112	102
Y	8.7	9.0	9.0	7.6	7.5	6.7	8.0	6.9	7.5
Zr	282	224	223	176	151	120	137	197	181
Nb	1.08	0.87	0.81	0.52	0.57	0.44	0.97	0.57	0.48
Ba	0.19	0.20	0.09	0.11	0.37	0.03	1.34	0.04	0.02
La	5.18	4.78	4.68	3.82	3.63	3.35	4.84	3.53	3.25
Ce	19.5	18.1	17.2	14.2	14.0	12.2	16.7	13.8	12.7
Pr	3.32	3.20	2.92	2.50	2.50	2.18	2.75	2.38	2.30
Nd	18.6	18.0	16.9	14.3	14.1	12.1	15.2	13.4	13.5
Sm	4.93	4.70	4.46	3.85	3.95	3.45	4.03	3.58	3.75
Eu	1.46	1.62	1.38	1.21	1.26	1.07	1.28	1.21	1.26
Gd	3.83	3.77	3.73	3.21	3.15	2.86	3.44	2.99	3.11
Tb	0.533	0.491	0.500	0.428	0.450	0.389	0.464	0.390	0.439
Dy	2.57	2.56	2.59	2.17	2.10	1.89	2.13	2.10	2.14
Ho	0.397	0.450	0.402	0.352	0.357	0.323	0.375	0.294	0.306
Er	0.906	0.869	0.833	0.728	0.737	0.625	0.758	0.737	0.691
Tm	0.110	0.095	0.103	0.072	0.077	0.071	0.079	0.066	0.090
Yb	0.686	0.651	0.619	0.532	0.504	0.517	0.528	0.542	0.527
Lu	0.061	0.057	0.070	0.052	0.057	0.056	0.064	0.054	0.047
Hf	12.8	10.4	10.4	8.04	6.97	5.68	6.57	9.07	8.27
Ta	0.28	0.25	0.20	0.12	0.13	0.11	0.17	0.13	0.10
Pb	0.10	0.06	0.09	0.10	0.05	0.08	0.07	0.10	0.05
Th	0.11	0.08	0.05	0.06	0.05	0.03	0.08	0.04	0.04
U	0.01	0.01	0.01	0.01	0.01	0.01	0.01	0.01	0.01

Appendix 1, Table 12.1 continued

Sample	SPK M3 G5	SPK M3 G6	SPK M3 G7	SPK M3 G8	SPK M3 G9	SPK M3 G10	SPK M3 G12	SPK M3 G13	SPK M3 G14
SiO_2	51.87	50.49	49.57	48.42	50.12	51.46	50.55	52.44	51.48
TiO_2	1.07	1.40	1.72	2.18	1.47	1.18	1.50	0.79	1.00
Al_2O_3	3.52	4.48	4.94	7.13	4.61	3.71	4.68	2.55	4.25
Cr_2O_3	0.001	0.01	bd	0.07	bd	bd	0.004	0.004	0.04
FeO	7.21	7.68	7.09	5.81	7.73	6.56	7.27	7.12	6.53
MnO	0.11	0.08	0.10	0.08	0.04	0.17	0.07	0.14	0.14
MgO	14.51	13.64	13.85	13.75	13.64	15.02	14.02	15.32	14.42
CaO	21.83	21.85	21.66	21.83	21.50	21.86	22.05	22.12	22.58
Na_2O	1.09	1.32	1.17	1.00	1.32	1.00	1.22	0.97	0.97
K_2O	0.01	0.01	0.02	0.02	0.004	0.01	0.01	0.01	0.002
Total	101.23	100.95	100.12	100.30	100.42	100.97	101.37	101.46	101.41
Mg#	78.19	75.96	77.68	80.82	75.86	80.32	77.45	79.31	79.74
Ca#	51.97	53.54	52.95	53.32	53.13	51.15	53.08	50.94	52.97
Sc	50	50	57	96	51	58	58	61	73
V	201	272	258	244	282	214	267	173	281
Cr	5.1	2.4	15.2	151.2	0.6	16.4	7.4	1.2	1.7
Ni	7.3	5.5	14.7	51.4	5.1	21.5	10.2	11.6	13.0
Rb	0.00	0.01	0.01	0.05	0.02	0.01	0.01	< d.l.	0.01
Sr	104	122	123	87	113	108	124	101	131
Y	7.0	7.5	9.2	7.3	7.6	7.2	7.1	8.2	9.5
Zr	161	298	224	157	261	142	252	192	337
Nb	0.52	1.10	0.90	1.15	0.94	0.52	1.29	0.55	0.82
Ba	0.05	0.04	0.13	0.84	0.03	0.09	0.04	0.10	1.94
La	3.56	4.37	5.18	3.92	4.43	4.16	4.39	3.58	5.45
Ce	13.5	16.5	19.2	15.7	17.4	15.1	17.1	14.0	20.4
Pr	2.35	2.83	3.21	2.68	2.98	2.58	2.91	2.50	3.49
Nd	13.7	16.0	18.3	15.2	16.4	14.2	15.8	14.4	19.3
Sm	3.57	4.14	4.59	4.09	4.46	3.80	4.38	3.83	5.13
Eu	1.20	1.30	1.57	1.43	1.41	1.23	1.24	1.25	1.64
Gd	2.81	3.39	3.90	3.32	3.65	3.03	3.44	3.12	4.04
Tb	0.399	0.457	0.478	0.442	0.533	0.410	0.449	0.463	0.564
Dy	2.05	2.16	2.41	2.17	2.39	2.08	2.20	2.37	2.90
Ho	0.368	0.308	0.367	0.344	0.362	0.296	0.329	0.407	0.396
Er	0.717	0.767	0.845	0.783	0.682	0.678	0.689	0.773	0.868
Tm	0.082	0.081	0.088	0.080	0.109	0.080	0.098	0.093	0.089
Yb	0.543	0.578	0.640	0.516	0.627	0.511	0.612	0.607	0.709
Lu	0.055	0.058	0.060	0.047	0.058	0.060	0.074	0.079	0.065
Hf	7.31	13.9	11.2	8.23	12.1	6.87	11.9	8.57	15.8
Ta	0.10	0.27	0.26	0.29	0.28	0.11	0.23	0.10	0.40
Pb	0.07	0.11	0.10	0.11	0.11	0.08	0.09	0.08	0.18
Th	0.07	0.08	0.08	0.14	0.10	0.08	0.08	0.06	0.31
U	0.00	0.01	0.02	0.03	0.01	0.01	0.01	0.02	0.10

Appendix 1, Table 12.1 continued

Sample	SPK M3 G16	SPK M3 G17	SPK M3 G18	SPK M3 G19	SPK M6 G1	SPK M6 G2	SPK M6 G3	SPK M6 G4	SPK M6 G5
SiO_2	50.75	50.84	50.94	50.17	49.72	49.87	51.56	50.25	50.76
TiO_2	1.19	1.34	1.28	1.63	1.87	1.67	1.07	1.41	1.40
Al_2O_3	4.23	4.30	3.85	4.89	5.27	5.09	3.41	4.35	4.31
Cr_2O_3	bd	bd	0.001	bd	0.03	bd	bd	0.01	0.03
FeO	7.51	7.43	7.58	7.11	5.93	7.25	6.88	7.40	6.40
MnO	0.11	0.14	0.13	0.16	0.12	0.07	0.12	0.09	0.09
MgO	13.91	14.06	14.09	14.05	14.54	13.83	14.82	13.78	14.84
CaO	21.58	21.92	21.60	21.75	21.87	21.43	22.02	21.62	21.86
Na_2O	1.29	1.30	1.28	1.24	1.03	1.19	0.94	1.22	0.97
K_2O	0.01	0.02	0.02	0.01	0.01	bd	0.002	0.01	bd
Total	100.56	101.34	100.77	101.01	100.39	100.40	100.82	100.13	100.65
Mg#	76.73	77.12	76.80	77.88	81.36	77.24	79.31	76.82	80.51
Ca#	52.74	52.87	52.44	52.68	51.97	52.72	51.66	53.03	51.45
Sc	57	58	54	66	51	55	64	70	68
V	310	301	255	304	232	225	241	408	388
Cr	2.5	2.9	2.2	6.2	5.8	2.9	5.5	460.4	21.9
Ni	4.4	6.6	5.8	12.4	7.0	7.9	9.1	170.0	92.8
Rb	0.02	0.00	0.07	0.03	0.02	0.01	0.02	0.02	0.01
Sr	133	141	125	128	147	128	141	430	474
Y	9.8	9.5	8.6	10.0	7.3	7.7	8.9	8.6	10.3
Zr	336	286	237	256	277	185	319	117	212
Nb	1.06	0.95	0.67	1.04	0.83	0.53	1.73	0.86	1.01
Ba	0.08	0.04	0.03	0.09	0.21	0.08	5.38	0.03	0.04
La	5.03	5.32	4.07	5.47	4.83	4.15	5.66	7.00	9.27
Ce	19.4	19.4	15.7	20.4	17.7	15.9	20.7	24.1	30.7
Pr	3.32	3.42	2.65	3.47	2.92	2.73	3.45	3.87	4.82
Nd	18.6	18.6	15.2	19.4	15.6	15.6	19.7	21.1	27.3
Sm	4.98	4.92	4.26	5.12	3.87	4.08	4.91	5.26	6.23
Eu	1.64	1.67	1.29	1.76	1.23	1.32	1.60	1.77	2.24
Gd	4.23	4.06	3.30	4.24	3.06	3.24	3.91	4.09	4.93
Tb	0.540	0.464	0.429	0.604	0.418	0.432	0.554	0.519	0.612
Dy	2.78	2.66	2.28	2.85	2.07	2.23	2.66	2.48	3.15
Ho	0.430	0.433	0.355	0.418	0.361	0.332	0.400	0.375	0.456
Er	0.926	0.897	0.737	0.953	0.732	0.721	0.800	0.708	0.928
Tm	0.098	0.100	0.077	0.120	0.096	0.070	0.113	0.069	0.103
Yb	0.720	0.626	0.627	0.696	0.590	0.523	0.681	0.459	0.619
Lu	0.077	0.061	0.071	0.076	0.074	0.064	0.074	0.052	0.078
Hf	15.0	12.8	10.0	11.9	12.4	8.09	14.8	5.72	9.29
Ta	0.25	0.23	0.15	0.26	0.19	0.13	0.43	1.82	2.44
Pb	0.12	0.12	0.11	0.09	0.24	0.07	0.18	0.25	0.29
Th	0.10	0.07	0.06	0.09	0.32	0.06	0.29	0.08	0.10
U	0.02	0.01	0.01	0.01	0.48	0.01	0.11	0.01	0.01

Appendix 1, Table 12.1 continued

Sample	SPK M6 G6	SPK M6 G7	SPK M6 G8	SPK M6 G9	SPK M6 G10	SPK M6 G11	SPK M6 G13	SPK M6 G14	SPK M6 G15
SiO_2	50.69	49.86	51.15	49.95	51.05	51.26	50.03	52.11	50.66
TiO_2	1.29	1.47	0.97	1.43	1.02	1.04	1.47	0.77	1.19
Al_2O_3	4.01	4.53	3.19	4.44	3.31	3.08	4.52	2.35	3.69
Cr_2O_3	bd	bd	bd	0.02	0.03	0.01	bd	bd	bd
FeO	6.54	7.64	7.37	7.71	7.09	7.28	7.50	6.81	6.55
MnO	0.08	0.16	0.12	0.14	0.14	0.14	0.10	0.15	0.12
MgO	14.73	13.85	14.40	13.81	14.73	14.86	13.78	15.14	14.82
CaO	21.92	21.58	21.85	21.69	21.90	21.79	21.40	22.03	21.75
Na_2O	0.97	1.29	1.10	1.23	1.07	0.99	1.21	0.88	0.99
K_2O	0.01	0.01	0.01	0.01	0.003	0.003	0.01	bd	0.001
Total	100.25	100.38	100.16	100.42	100.35	100.44	100.03	100.22	99.76
Mg#	80.04	76.34	77.68	76.15	78.72	78.43	76.59	79.84	80.12
Ca#	51.71	52.86	52.20	53.04	51.68	51.34	52.76	51.14	51.37
Sc	68	77	67	73	79	63	60	56	49
V	378	281	394	368	381	319	429	202	274
Cr	50.1	464.1	16.4	17.2	50.2	0.7	12.6	0.2	0.6
Ni	107.3	85.5	97.3	99.1	93.8	4.1	58.2	6.9	4.4
Rb	0.02	0.01	0.03	0.02	0.03	0.01	0.01	0.04	0.03
Sr	477	116	476	535	467	127	454	95	110
Y	10.6	8.5	9.8	10.9	12.3	10.1	11.6	7.2	7.5
Zr	204	120	196	248	268	407	186	238	302
Nb	0.45	0.70	0.44	0.89	0.53	1.34	0.82	0.57	1.19
Ba	0.05	0.05	0.02	0.03	0.19	0.18	0.04	2.57	0.08
La	9.47	4.86	9.04	11.4	13.8	4.92	8.63	4.22	4.25
Ce	31.7	16.6	30.0	37.2	38.8	19.1	30.0	16.6	16.5
Pr	5.22	2.83	4.79	5.53	5.47	3.29	4.81	2.81	2.87
Nd	27.1	15.9	25.1	29.7	28.0	20.3	26.6	15.5	16.0
Sm	6.77	4.28	6.26	6.98	7.17	5.34	6.24	4.05	4.19
Eu	2.16	1.43	1.97	2.38	2.17	1.68	2.10	1.34	1.48
Gd	5.05	3.43	5.06	5.59	5.60	4.32	5.31	3.27	3.32
Tb	0.666	0.489	0.686	0.641	0.635	0.603	0.677	0.453	0.485
Dy	3.13	2.23	3.00	3.36	3.43	2.93	3.38	2.16	2.41
Ho	0.511	0.389	0.382	0.457	0.552	0.430	0.459	0.383	0.362
Er	1.06	0.733	0.887	0.934	0.986	0.796	1.09	0.788	0.698
Tm	0.101	0.066	0.088	0.090	0.136	0.104	0.104	0.089	0.084
Yb	0.648	0.456	0.536	0.685	0.777	0.827	0.675	0.634	0.601
Lu	0.073	0.052	0.057	0.076	0.079	0.068	0.068	0.064	0.074
Hf	8.83	5.79	8.60	10.5	11.3	19.8	9.20	12.6	15.0
Ta	2.17	0.15	2.30	2.44	2.54	0.44	2.65	0.24	0.38
Pb	0.31	0.03	0.32	0.28	0.37	0.10	0.36	0.15	0.10
Th	0.11	0.06	0.12	0.13	0.14	0.07	0.10	0.33	0.09
U	0.02	0.02	0.02	0.02	0.10	0.02	0.01	0.12	0.02

Appendix 1, Table 12.1 continued

Sample	SPK M6 G18	SPK M6 G19	SPK M6 G20	SPK-M9_G7	SPK-M9_G9	SPK-M9_G12	SPK-M9_G13	SPK-M9_G14	SPK-M9_G18
SiO_2	47.91	50.49	51.00	49.88	50.19	50.95	50.00	49.58	50.45
TiO_2	2.32	1.19	1.28	1.54	1.40	1.28	1.48	1.52	1.29
Al_2O_3	7.21	3.92	3.79	4.64	4.59	3.83	4.77	4.56	3.97
Cr_2O_3	0.04	0.01	bd	0.04	0.03	d	0.01	0.001	0.01
FeO	5.84	7.66	5.88	7.27	6.96	5.50	6.09	7.32	5.98
MnO	0.08	0.12	0.13	0.17	0.11	0.09	0.10	0.13	0.08
MgO	13.62	13.69	15.24	13.36	13.51	14.73	13.86	13.22	14.69
CaO	21.84	21.57	21.97	21.20	21.39	21.62	22.00	21.05	21.47
Na_2O	0.92	1.12	0.86	1.34	1.23	1.02	0.99	1.27	0.99
K_2O	0.01	0.02	bd	0.01	0.02	0.02	0.01	0.02	0.01
Total	99.78	99.79	100.14	99.46	99.42	99.03	99.32	98.66	98.95
Mg#	80.59	76.08	82.20	76.58	77.57	82.67	80.20	76.29	81.41
Ca#	53.55	53.13	50.90	53.30	53.24	51.35	53.32	53.40	51.25
Sc	76	76	73	46	59	67	55	57	64
V	374	391	411	264	274	224	203	282	222
Cr	61.8	435.0	40.8	2.1	1.2	13.0	14.4	2.6	17.2
Ni	97.9	168.2	117.7	5.2	5.8	26.0	23.6	5.8	24.4
Rb	0.04	0.02	0.00	0.01	0.05	< d.l.	< d.l.	0.00	0.00
Sr	373	468	431	111	121	99	155	123	101
Y	9.0	9.6	9.5	8.1	8.7	6.5	10.6	8.7	7.3
Zr	193	153	188	271	251	181	195	336	121
Nb	1.10	0.71	0.76	0.97	0.89	0.85	1.01	1.25	0.43
Ba	0.50	0.04	0.08	0.04	0.07	0.20	0.43	0.04	0.05
La	7.39	8.23	8.73	4.26	4.63	3.97	3.97	4.86	3.63
Ce	23.4	27.4	28.0	16.8	17.9	15.3	25.3	17.4	13.3
Pr	3.95	4.40	4.40	2.85	3.13	2.66	4.09	3.06	2.32
Nd	22.6	22.1	26.0	17.0	17.4	14.2	21.6	16.8	13.7
Sm	5.59	5.34	6.09	4.42	4.74	3.74	5.19	4.38	3.67
Eu	1.76	1.90	1.97	1.32	1.52	1.16	1.69	1.46	1.23
Gd	4.37	4.73	4.66	3.51	3.56	2.85	4.17	3.61	2.95
Tb	0.435	0.610	0.585	0.467	0.482	0.351	0.520	0.448	0.423
Dy	2.73	2.43	2.95	2.32	2.61	1.89	2.82	2.53	2.02
Ho	0.417	0.370	0.428	0.362	0.388	0.289	0.497	0.405	0.318
Er	0.899	0.750	0.860	0.655	0.880	0.541	1.104	0.692	0.716
Tm	0.059	0.065	0.089	0.091	0.103	0.064	0.141	0.103	0.071
Yb	0.554	0.552	0.585	0.599	0.668	0.422	0.789	0.640	0.510
Lu	0.039	0.057	0.068	0.066	0.068	0.039	0.091	0.069	0.054
Hf	9.05	6.93	8.33	12.5	11.2	8.78	8.62	15.8	6.02
Ta	2.02	1.83	2.36	0.28	0.20	0.21	0.21	0.33	0.12
Pb	0.24	0.40	0.35	0.08	0.10	0.11	0.16	0.11	0.08
Th	0.10	0.12	0.06	0.07	0.07	0.11	0.23	0.11	0.05
U	0.02	0.01	0.02	0.01	0.01	0.01	0.10	0.01	0.01

Appendix 1, Table 12.1 continued

Sample	SPK-M10_ G2	SPK-M10_ G3	SPK-M10_ G4	SPK-M10_ G5	SPK-M10_ G6	SPK-M10_ G7	SPK-M10_ G9	SPK-M10_ G11	SPK-M10_ G12
SiO_2	51.94	49.93	50.78	49.80	49.45	50.31	50.97	51.75	50.48
TiO_2	1.01	1.82	1.36	1.59	1.96	1.42	1.42	1.06	1.36
Al_2O_3	3.27	5.26	4.14	4.87	5.39	4.42	4.47	3.41	4.37
Cr_2O_3	0.001	0.01	0.02	bd	0.003	bd	0.01	bd	0.01
FeO	6.85	6.66	6.24	6.55	6.17	7.55	6.79	6.95	7.50
MnO	0.14	0.12	0.09	0.12	0.09	0.12	0.12	0.11	0.12
MgO	14.36	13.87	14.26	13.99	14.23	13.45	13.94	14.42	13.55
CaO	21.67	21.59	21.55	21.29	21.31	21.45	21.49	21.49	21.15
Na_2O	1.09	1.13	1.18	1.21	1.12	1.28	1.16	1.16	1.31
K_2O	0.02	0.02	0.02	0.01	0.03	0.02	0.01	0.02	0.02
Total	100.34	100.41	99.63	99.43	99.75	100.00	100.39	100.35	99.88
Mg#	78.88	78.76	80.27	79.20	80.43	76.04	78.52	78.70	76.28
Ca#	52.05	52.81	52.08	52.26	51.86	53.42	52.58	51.74	52.89
Sc	50	64	56	61	53	50	55	50	55
V	226	283	249	271	216	277	268	233	285
Cr	2.2	36.0	36.6	3.3	23.0	2.3	6.7	1.9	0.7
Ni	6.0	20.7	16.4	11.0	20.6	3.6	11.5	6.7	2.7
Rb	0.02	0.02	0.06	0.05	0.00	0.06	< d.l.	0.02	0.03
Sr	116	128	119	125	98	115	124	115	123
Y	7.3	9.1	7.2	9.4	6.4	7.5	7.9	7.3	9.4
Zr	194	257	175	199	135	329	214	196	319
Nb	0.63	1.18	0.65	0.84	0.75	1.06	0.81	0.56	0.92
Ba	0.87	0.09	0.08	0.04	0.05	0.04	0.10	< d.l.	0.06
La	3.72	5.21	3.83	4.92	3.63	4.22	4.49	3.87	4.92
Ce	14.5	20.2	15.1	19.0	14.4	15.9	17.2	14.7	18.8
Pr	2.51	3.33	2.58	3.28	2.50	2.84	2.99	2.63	3.22
Nd	14.8	19.0	15.1	18.9	14.1	15.8	16.6	14.4	18.7
Sm	3.76	4.78	3.96	4.87	3.71	4.21	4.46	3.99	4.98
Eu	1.25	1.55	1.37	1.59	1.21	1.40	1.40	1.28	1.64
Gd	3.13	3.83	3.12	3.94	2.84	3.26	3.45	3.06	4.02
Tb	0.428	0.540	0.453	0.541	0.400	0.476	0.451	0.481	0.540
Dy	2.09	2.54	2.17	2.72	1.98	2.28	2.32	2.11	2.69
Ho	0.330	0.408	0.324	0.397	0.302	0.382	0.321	0.363	0.411
Er	0.740	0.946	0.695	0.895	0.615	0.758	0.760	0.660	0.894
Tm	0.081	0.086	0.081	0.099	0.085	0.090	0.084	0.071	0.118
Yb	0.518	0.689	0.514	0.627	0.516	0.630	0.568	0.552	0.723
Lu	0.065	0.068	0.054	0.090	0.055	0.069	0.062	0.071	0.086
Hf	8.86	12.2	8.22	9.56	7.32	15.4	10.6	8.83	14.4
Ta	0.15	0.30	0.19	0.20	0.21	0.35	0.21	0.12	0.31
Pb	0.10	0.11	0.10	0.10	0.05	0.11	0.11	0.11	0.07
Th	0.05	0.11	0.07	0.09	0.05	0.09	0.06	0.06	0.09
U	0.01	0.02	0.01	0.02	0.01	0.01	0.01	0.01	0.02

Appendix 1, Table 12.1 1 continued

Sample	SPK-M10_G14	SPK-M10_G15	SPK-M10_G16	SPK-M10_G19	SPK-M11_G1	SPK-M11_G2	SPK-M11_G3	SPK-M11_G4	SPK-M11_G5
SiO_2	51.44	51.62	50.08	50.12	49.65	50.98	49.17	51.14	50.06
TiO_2	0.97	0.89	1.54	1.37	1.67	1.11	1.90	1.26	1.48
Al_2O_3	3.16	2.97	4.81	4.78	4.98	3.73	5.63	3.78	4.58
Cr_2O_3	bd	0.01	0.03	0.03	0.005	bd	bd	bd	0.02
FeO	6.77	7.13	6.48	7.35	7.42	7.45	6.64	6.16	7.13
MnO	0.07	0.16	0.12	0.12	0.13	0.12	0.11	0.12	0.11
MgO	14.25	14.43	14.08	13.49	13.26	13.79	13.77	14.89	13.66
CaO	21.48	21.37	21.45	21.01	21.01	21.16	21.39	21.68	21.21
Na_2O	1.13	1.09	1.17	1.35	1.34	1.27	1.16	1.03	1.24
K_2O	0.02	0.01	0.02	0.03	0.02	0.02	0.02	0.02	0.02
Total	99.29	99.69	99.77	99.63	99.50	99.62	99.79	100.08	99.52
Mg#	78.95	78.28	79.45	76.58	76.09	76.73	78.70	81.16	77.32
Ca#	52.02	51.57	52.30	52.85	53.26	52.47	52.77	51.15	52.76
Sc	42	48	58	52	42	46	68	59	54
V	201	204	254	273	249	237	256	208	284
Cr	1.7	0.6	15.1	18.8	0.3	2.0	11.2	1.6	2.9
Ni	4.9	2.4	15.6	16.7	3.7	3.1	20.6	14.0	6.6
Rb	< d.l.	0.03	< d.l.	< d.l.	0.02	0.01	0.02	0.02	0.03
Sr	103	103	116	127	92	103	103	101	119
Y	6.2	7.1	8.3	8.8	5.9	6.7	8.7	6.7	8.7
Zr	169	181	172	209	232	266	273	131	277
Nb	0.52	0.46	0.70	0.73	1.00	0.71	1.26	0.55	0.99
Ba	0.09	0.02	0.05	< d.l.	0.37	0.04	0.02	0.03	0.06
La	3.26	3.25	4.47	4.64	3.61	3.49	5.30	3.53	4.92
Ce	12.9	12.9	16.9	18.8	13.9	14.0	20.3	13.5	18.8
Pr	2.28	2.34	2.80	3.20	2.44	2.42	3.33	2.38	3.27
Nd	13.0	13.7	16.0	17.8	13.8	13.4	18.9	13.3	18.5
Sm	3.42	3.69	4.26	4.56	3.67	3.55	4.83	3.68	4.85
Eu	1.13	1.23	1.36	1.53	1.19	1.20	1.65	1.16	1.57
Gd	2.64	2.91	3.28	3.81	2.89	2.92	3.89	2.97	3.77
Tb	0.349	0.349	0.428	0.474	0.384	0.412	0.524	0.373	0.499
Dy	1.83	2.08	2.16	2.57	1.88	2.02	2.60	1.99	2.48
Ho	0.273	0.296	0.356	0.399	0.314	0.315	0.388	0.278	0.420
Er	0.552	0.733	0.785	0.818	0.663	0.622	0.929	0.610	0.772
Tm	0.069	0.079	0.080	0.104	0.081	0.070	0.090	0.076	0.099
Yb	0.438	0.547	0.582	0.640	0.547	0.526	0.647	0.459	0.627
Lu	0.065	0.062	0.063	0.082	0.052	0.051	0.088	0.056	0.067
Hf	7.80	8.22	8.08	9.69	13.5	12.8	13.5	6.37	12.8
Ta	0.12	0.09	0.15	0.23	0.32	0.21	0.39	0.12	0.28
Pb	0.09	0.06	0.06	0.11	0.09	0.10	0.09	0.09	0.07
Th	0.05	0.05	0.07	0.06	0.08	0.07	0.18	0.05	0.10
U	0.00	0.01	0.01	0.01	0.01	0.01	0.02	0.01	0.01

Appendix 1, Table 12.1 continued

Sample	SPK-M11_G6	SPK-M11_G7	SPK-M11_G8	SPK-M11_G9	SPK-M11_G10	SPK-M11_G11	SPK-M11_G12	SPK-M11_G13	SPK-M11_G14
SiO_2	50.75	49.85	49.98	49.68	51.19	51.54	51.30	51.22	49.85
TiO_2	1.22	1.63	1.49	1.52	1.05	0.96	1.19	0.95	1.32
Al_2O_3	3.93	5.01	4.54	4.70	3.33	3.00	3.50	3.11	4.38
Cr_2O_3	0.02	bd	0.01	0.01	0.01	0.02	0.01	bd	0.03
FeO	7.19	7.01	6.89	7.32	6.92	6.94	6.24	6.90	7.05
MnO	0.14	0.12	0.12	0.14	0.12	0.12	0.15	0.12	0.10
MgO	13.65	13.57	13.72	13.28	14.22	14.28	14.92	14.24	13.52
CaO	21.51	21.27	21.50	21.14	21.59	21.44	21.37	21.53	21.19
Na_2O	1.21	1.22	1.18	1.29	1.14	1.15	0.95	1.07	1.32
K_2O	0.02	0.02	0.02	0.02	0.01	0.01	0.01	0.02	0.01
Total	99.65	99.71	99.44	99.09	99.57	99.47	99.63	99.17	98.76
Mg#	77.16	77.51	78.00	76.37	78.54	78.56	80.98	78.62	77.35
Ca#	53.14	53.01	52.99	53.38	52.21	51.92	50.74	52.09	53.00
Sc	53	57	58	56	41	45	58	52	55
V	272	288	266	289	196	224	211	226	281
Cr	2.5	6.2	1.9	2.8	1.4	1.9	8.2	2.1	2.6
Ni	3.9	9.9	7.4	6.3	4.9	3.7	16.6	5.3	6.9
Rb	0.03	< d.l.	0.04	0.07	0.05	0.03	0.01	0.08	0.04
Sr	126	120	115	120	98	110	108	116	125
Y	8.3	9.0	9.5	8.9	5.7	6.7	7.6	7.6	8.9
Zr	289	306	248	333	168	204	133	204	275
Nb	0.85	1.17	0.82	1.37	0.52	0.59	0.48	0.86	1.01
Ba	0.04	0.06	0.07	0.07	0.05	0.33	0.04	0.60	0.07
La	4.76	4.65	4.72	4.90	3.12	3.42	3.50	3.95	4.90
Ce	17.6	18.2	18.5	18.2	12.8	13.3	13.6	14.4	18.9
Pr	3.10	3.14	3.24	3.06	2.19	2.37	2.54	2.49	3.31
Nd	17.0	17.8	17.8	16.7	12.5	13.6	14.4	14.2	17.9
Sm	4.48	4.89	5.07	4.67	3.30	3.49	3.79	3.89	4.59
Eu	1.48	1.43	1.51	1.40	1.01	1.22	1.25	1.26	1.37
Gd	3.61	3.91	4.02	3.61	2.72	2.80	3.14	3.16	3.92
Tb	0.455	0.563	0.533	0.436	0.354	0.417	0.454	0.392	0.435
Dy	2.43	2.61	2.66	2.54	1.92	1.96	2.15	2.17	2.59
Ho	0.351	0.406	0.424	0.368	0.305	0.323	0.349	0.343	0.371
Er	0.720	0.905	0.891	0.863	0.663	0.673	0.723	0.795	0.877
Tm	0.077	0.107	0.108	0.107	0.074	0.086	0.091	0.090	0.106
Yb	0.621	0.672	0.680	0.622	0.453	0.492	0.532	0.575	0.632
Lu	0.052	0.082	0.056	0.058	0.048	0.052	0.069	0.063	0.078
Hf	13.3	14.8	11.5	15.9	8.38	9.71	6.16	9.36	12.5
Ta	0.23	0.36	0.25	0.35	0.13	0.15	0.10	0.15	0.27
Pb	0.10	0.07	0.07	0.10	0.10	0.08	0.07	0.08	0.12
Th	0.09	0.11	0.09	0.10	0.05	0.06	0.05	0.07	0.10
U	0.02	0.02	0.01	0.01	0.01	0.01	0.01	0.02	0.01

Appendix 1, Table 12.1 continued

Sample	SPK-M11_G15	SPK-M11_G16	SPK-M11_G17	SPK-M11_G18	SPK-M12_G1	SPK-M12_G2	SPK-M12_G3	SPK-M12_G4	SPK-M12_G5
SiO_2	49.80	49.44	49.06	50.02	48.78	50.55	50.71	51.15	51.18
TiO_2	1.50	1.63	1.74	1.56	2.25	1.36	1.50	1.20	1.08
Al_2O_3	4.53	5.03	5.04	4.55	6.38	4.33	3.99	3.55	3.54
Cr_2O_3	0.004	0.02	0.01	0.03	0.01	0.01	bd	0.01	0.001
FeO	6.61	6.48	6.83	5.93	5.60	7.41	5.38	6.41	6.81
MnO	0.17	0.10	0.11	0.10	0.11	0.12	0.09	0.10	0.11
MgO	13.66	13.71	13.36	14.41	14.10	13.66	15.07	14.55	14.34
CaO	21.15	21.07	20.91	21.11	21.86	21.63	21.99	21.64	21.79
Na_2O	1.27	1.19	1.28	1.07	1.11	1.30	0.91	1.03	1.13
K_2O	0.01	0.02	0.02	0.03	0.02	0.03	0.02	0.02	0.01
Total	98.69	98.68	98.37	98.79	100.22	100.40	99.67	99.66	100.01
Mg#	78.64	79.03	77.68	81.24	81.75	76.67	83.30	80.17	78.94
Ca#	52.69	52.52	52.96	51.31	52.74	53.24	51.22	51.68	52.23
Sc	59	63	60	68	92	52	89	41	42
V	272	269	285	242	258	273	232	208	195
Cr	1.8	27.6	14.8	25.2	118.9	2.2	45.8	12.9	16.0
Ni	8.1	19.8	11.6	30.2	49.2	4.7	39.9	13.9	7.7
Rb	0.18	< d.l.	0.02	0.01	< d.l.	0.00	0.00	0.01	0.04
Sr	131	124	121	120	97	124	100	93	101
Y	9.3	9.8	9.2	8.5	8.0	7.8	7.0	5.7	5.9
Zr	226	233	274	136	233	298	192	171	144
Nb	1.93	0.84	1.12	0.57	1.65	1.01	1.09	0.61	0.56
Ba	25.81	0.03	0.08	0.05	0.12	0.04	0.10	0.03	0.78
La	5.42	5.44	5.09	4.64	5.67	4.42	4.57	3.50	3.46
Ce	19.8	20.1	18.1	16.1	21.3	16.7	16.7	15.0	13.2
Pr	3.29	3.37	3.36	2.74	3.55	2.90	2.88	2.62	2.32
Nd	18.4	19.0	16.6	16.4	20.5	16.6	16.3	14.2	13.1
Sm	4.75	4.81	4.79	4.33	5.23	4.22	4.12	3.87	3.30
Eu	1.49	1.56	1.59	1.48	1.47	1.37	1.36	1.31	1.06
Gd	3.81	4.10	3.54	3.51	3.42	3.38	3.27	2.76	2.62
Tb	0.532	0.469	0.548	0.478	0.487	0.455	0.397	0.375	0.371
Dy	2.63	2.76	2.64	2.32	2.42	2.29	2.04	2.01	1.93
Ho	0.398	0.414	0.407	0.327	0.312	0.357	0.334	0.290	0.293
Er	0.901	0.991	0.923	0.712	0.661	0.765	0.613	0.621	0.614
Tm	0.081	0.111	0.080	0.073	0.077	0.096	0.074	0.073	0.065
Yb	0.636	0.709	0.571	0.552	0.526	0.629	0.471	0.544	0.438
Lu	0.069	0.057	0.079	0.070	0.056	0.075	0.047	0.060	0.048
Hf	10.2	10.8	13.3	6.82	12.5	13.8	9.65	9.63	7.10
Ta	0.21	0.23	0.31	0.12	0.45	0.31	0.26	0.23	0.12
Pb	0.12	0.09	0.11	0.06	0.10	0.09	0.11	0.09	0.09
Th	0.12	0.08	0.06	0.08	0.20	0.05	0.11	0.07	0.06
U	0.05	0.01	0.02	0.01	0.03	0.02	0.02	0.02	0.01

Appendix 1, Table 12.1 continued

Sample	SPK-M12_G6	SPK-M12_G7	SPK-M12_G8	SPK-M12_G9	SPK-M12_G10	SPK-M12_G11	SPK-M12_G12	SPK-M12_G13	SPK-M12_G14
SiO_2	51.42	51.19	50.13	49.83	49.54	49.65	49.65	49.59	52.04
TiO_2	1.27	1.23	1.52	1.66	1.62	1.73	1.69	1.73	0.92
Al_2O_3	3.51	4.07	4.48	4.87	4.93	5.02	4.97	4.89	2.73
Cr_2O_3	0.03	0.004	0.01	0.02	0.01	0.02	0.01	0.003	0.01
FeO	6.26	7.25	7.20	6.76	6.77	7.31	6.97	7.51	6.14
MnO	0.11	0.09	0.14	0.11	0.12	0.13	0.13	0.13	0.12
MgO	14.97	13.96	13.93	14.13	13.87	13.49	13.83	13.36	15.54
CaO	22.06	21.56	21.36	21.49	21.45	21.21	21.56	21.45	21.86
Na_2O	1.01	1.29	1.22	1.14	1.20	1.33	1.23	1.35	0.89
K_2O	0.02	0.02	0.02	0.01	0.02	0.02	0.01	0.02	0.02
Total	100.64	100.66	100.03	100.01	99.52	99.90	100.05	100.03	100.26
Mg#	80.99	77.44	77.50	78.82	78.49	76.68	77.95	76.02	81.85
Ca#	51.46	52.63	52.45	52.24	52.67	53.07	52.85	53.58	50.29
Sc	56	54	62	65	57	60	57	47	60
V	201	266	272	252	258	291	273	249	191
Cr	5.2	0.7	0.6	2.0	20.0	2.8	12.6	1.6	0.6
Ni	13.2	4.3	5.6	11.4	16.9	7.7	11.3	4.0	10.3
Rb	0.01	0.02	0.01	0.04	0.00	< d.l.	< d.l.	0.02	0.05
Sr	105	122	106	108	124	118	122	104	91
Y	7.9	8.0	9.0	8.2	8.7	9.0	9.1	7.0	7.5
Zr	118	258	401	260	209	318	265	286	192
Nb	0.50	0.75	1.48	1.17	0.82	1.16	1.13	1.35	1.08
Ba	0.07	0.02	0.03	0.09	0.06	0.04	0.04	1.36	1.41
La	3.42	4.32	4.63	4.83	5.14	4.69	4.77	4.08	3.84
Ce	13.3	16.5	18.1	18.0	18.8	17.8	18.2	16.0	14.4
Pr	2.30	2.90	3.05	3.06	3.30	3.08	3.06	2.77	2.44
Nd	13.2	16.2	17.1	17.0	18.4	17.0	17.2	15.9	13.7
Sm	3.54	4.30	4.55	4.45	4.80	4.80	4.74	4.19	3.68
Eu	1.32	1.36	1.56	1.39	1.58	1.53	1.55	1.44	1.22
Gd	3.12	3.44	3.66	3.54	3.79	3.77	3.82	3.24	2.97
Tb	0.401	0.459	0.461	0.454	0.509	0.509	0.516	0.432	0.394
Dy	2.04	2.36	2.43	2.39	2.53	2.54	2.47	2.27	2.10
Ho	0.306	0.383	0.375	0.362	0.406	0.410	0.389	0.387	0.289
Er	0.613	0.782	0.786	0.723	0.808	0.782	0.884	0.706	0.744
Tm	0.086	0.097	0.104	0.083	0.060	0.086	0.079	0.081	0.082
Yb	0.492	0.609	0.660	0.578	0.599	0.685	0.652	0.639	0.555
Lu	0.057	0.079	0.069	0.070	0.066	0.089	0.075	0.066	0.067
Hf	5.86	12.2	18.8	13.0	10.3	14.9	13.3	15.5	8.82
Ta	0.10	0.21	0.48	0.31	0.21	0.35	0.33	0.43	0.15
Pb	0.07	0.09	0.13	< d.l.	0.08	0.12	0.09	0.14	0.14
Th	0.04	0.07	0.14	0.13	0.07	0.09	0.09	0.13	0.12
U	0.00	0.01	0.02	0.02	0.01	0.01	0.01	0.02	0.03

Appendix 1, Table 12.1 continued

Sample	SPK-M12_G15	SPK-M12_G16	SPK-M12_G17	SPK-M12_G18	SPK-M12_G19
SiO_2	49.73	50.34	50.40	51.14	52.23
TiO_2	1.72	1.53	1.32	1.30	0.65
Al_2O_3	4.98	4.77	4.02	3.70	2.33
Cr_2O_3	0.01	0.01	0.03	0.003	0.003
FeO	6.98	6.58	6.22	6.08	6.79
MnO	0.12	0.09	0.15	0.10	0.15
MgO	13.77	13.87	14.65	14.83	15.01
CaO	21.57	21.40	21.71	21.53	21.69
Na_2O	1.25	1.21	1.14	1.02	0.95
K_2O	0.02	0.02	0.02	0.02	0.02
Total	100.15	99.82	99.65	99.72	99.81
Mg#	77.85	78.97	80.76	81.30	79.74
Ca#	52.97	52.60	51.59	51.08	50.98
Sc	57	57	56	65	60
V	266	255	233	216	204
Cr	13.6	25.7	17.2	1.9	1.2
Ni	11.1	18.0	17.5	14.3	2.7
Rb	0.01	0.03	0.02	0.01	0.00
Sr	120	122	111	103	105
Y	8.8	8.6	7.2	7.3	7.5
Zr	266	195	142	145	246
Nb	1.17	0.83	0.60	0.52	0.46
Ba	0.09	0.05	0.21	0.05	0.02
La	4.63	4.91	3.70	4.07	3.23
Ce	17.8	18.3	13.8	14.1	13.1
Pr	3.13	3.10	2.32	2.43	2.30
Nd	17.4	17.3	13.6	13.6	13.2
Sm	4.44	4.43	3.56	3.85	3.67
Eu	1.53	1.43	1.12	1.24	1.25
Gd	3.64	3.50	2.93	3.20	2.98
Tb	0.481	0.478	0.357	0.390	0.410
Dy	2.50	2.54	1.89	2.16	2.09
Ho	0.337	0.405	0.295	0.382	0.346
Er	0.823	0.906	0.647	0.742	0.598
Tm	0.093	0.092	0.056	0.080	0.104
Yb	0.667	0.557	0.447	0.411	0.525
Lu	0.070	0.062	0.056	0.042	0.060
Hf	13.3	9.03	6.96	7.19	10.1
Ta	0.35	0.23	0.12	0.13	0.11
Pb	0.15	0.10	0.10	0.10	0.12
Th	0.07	0.10	0.05	0.05	0.06
U	0.01	0.02	0.04	0.01	0.01

Table 12:2: Major and trace element data for amphibole megacrysts

Sample	SPK amph 1 G4	SPK amph 1 G10	SPK amph 1 G11	SPK amph 1 G15	SPK amph 1 G16	SPK amph 1 G25	SPK amph 1 G26	SPK amph 1 G27	SPK amph 1 G28
SiO_2	41.90	40.91	41.53	40.84	41.67	41.62	41.10	41.92	41.85
TiO_2	3.67	3.68	4.29	4.76	4.09	3.96	4.65	3.98	3.92
Al_2O_3	12.76	13.29	13.33	13.81	13.20	12.81	13.60	12.86	12.80
Cr_2O_3	0.02	0.003	0.01	bd	0.02	0.01	0.02	1	bd
FeO	9.22	12.53	8.59	7.64	8.84	9.24	7.78	9.14	9.10
MnO	0.08	0.08	0.10	0.09	0.08	0.06	0.06	0.08	0.10
MgO	14.86	12.66	14.83	14.92	14.63	14.76	14.98	14.71	14.67
CaO	11.62	11.26	11.67	11.82	11.72	11.48	11.86	11.55	11.46
Na_2O	2.49	2.43	2.26	2.23	2.47	2.41	2.33	2.41	2.40
K_2O	1.97	2.18	2.08	2.14	2.03	2.02	2.11	2.02	1.99
F	0.21	0.19	0.20	0.20	0.09	0.14	0.15	0.16	0.07
Cl									
Total	98.71	99.13	98.80	98.36	98.81	98.44	98.57	98.77	98.33
H_2O									
Mg#	74.15	64.27	75.45	77.67	74.67	73.99	77.43	74.12	74.17
Ca#	36.00	39.02	36.15	36.30	36.57	35.88	36.29	36.10	35.97
Sc		56		62			66		
V		376		315			319		
Mn		525		551			520		
Co		45		52			45		
Ni		114		138			124		
Cu		1.3		1.0			0.6		
Zn		52		28			32		
Rb		12		12			11		
Sr		336		375			358		
Y		7		8			8		
Zr		100		141			143		
Nb		22		26			27		
Ba		253		303			297		
La		5.48		6.22			6.01		
Ce		18.9		20.9			19.7		
Pr		2.98		3.50			3.25		
Nd		16.7		20.5			18.5		
Sm		4.00		5.00			4.68		
Eu		1.32		1.70			1.52		
Gd		3.08		4.05			3.74		
Tb		0.402		0.535			0.443		
Dy		1.90		2.63			2.20		
Ho		0.288		0.377			0.344		
Er		0.556		0.801			0.698		
Tm		0.060		0.089			0.076		
Yb		0.365		0.574			0.495		

Lu	0.040	0.056	0.057
Hf	4.42	7.41	6.55
Ta	1.44	2.14	2.02
Pb	0.24	0.29	0.23
Th	0.049	0.101	0.085
U	0.010	0.017	0.016

Appendix 1, Table 12.2 continued

Sample	SPK amph 1 G29	SPK amph 2 G1	SPK amph 2 G2	SPK amph 2 G3	SPK amph 2 G6	SPK amph 2 G7	SPK amph 2 G8	SPK amph 2 G19	SPK amph 2 G20
SiO_2	41.31	41.42	41.32	41.73	41.24	41.36	41.53	41.72	41.55
TiO_2	4.66	4.23	4.24	4.29	4.19	4.14	4.32	3.35	3.31
Al_2O_3	13.61	13.41	13.43	13.32	12.80	13.10	13.19	12.32	12.39
Cr_2O_3	0.02	bd	0.03	0.02	bd	0.01	bd	0.01	0.01
FeO	7.63	9.44	9.33	8.78	12.41	12.30	9.36	11.59	11.55
MnO	0.05	0.14	0.10	0.09	0.09	0.08	0.12	0.11	0.07
MgO	15.04	14.43	14.40	14.85	12.66	12.84	14.41	13.58	13.59
CaO	11.91	11.45	11.53	11.62	10.87	11.04	11.28	11.09	11.07
Na_2O	2.30	2.32	2.29	2.33	2.51	2.37	2.30	2.61	2.59
K_2O	2.09	2.11	2.14	2.09	2.18	2.20	2.13	1.92	1.94
F	0.11	0.11	0.02	0.12	0.14	0.08	0.38	0.08	0.11
Cl									
Total	98.68	99.01	98.83	99.17	99.02	99.49	98.84	98.33	98.13
H_2O									
Mg#	77.83	73.15	73.33	75.08	64.51	65.02	73.28	67.61	67.69
Ca#	36.28	36.33	36.54	36.02	38.17	38.22	36.02	37.00	36.94
Sc	64				29				
V	332				365				
Mn	555				858				
Co	45				45				
Ni	131				2				
Cu	0.8				2.7				
Zn	31				61				
Rb	13				18				
Sr	376				352				
Y	8				7				
Zr	138				186				
Nb	28				39				
Ba	320				287				
La	6.45				6.74				
Ce	22.0				21.5				
Pr	3.58				3.52				
Nd	20.3				20.7				
Sm	4.85				4.51				
Eu	1.54				1.45				
Gd	3.60				3.43				

Tb	0.450	0.439
Dy	2.27	2.24
Ho	0.334	0.346
Er	0.664	0.665
Tm	0.071	0.074
Yb	0.478	0.511
Lu	0.051	0.060
Hf	6.22	8.91
Ta	1.89	2.20
Pb	0.28	0.27
Th	0.092	0.072
U	0.019	0.013

Appendix 1, Table 12.2 continued

Sample	SPK amph 2 G23	SPK amph 3 G4	SPK amph 3 G6	SPK amph G7	SPK amph G8	SPK amph G9	SPK amph 3 G10	SPK amph 3 G12	SPK amph 3 G16
SiO_2	40.63	41.56	41.67	41.62	41.10	41.92	41.85	41.31	41.42
TiO_2	4.80	3.87	4.09	3.96	4.65	3.98	3.92	4.66	4.23
Al_2O_3	13.75	12.83	13.20	12.81	13.60	12.86	12.80	13.61	13.41
Cr_2O_3	0.001	bd	0.02	0.01	0.02	1	bd	0.02	bd
FeO	7.65	10.07	8.84	9.24	7.78	9.14	9.10	7.63	9.44
MnO	0.07	0.10	0.08	0.06	0.06	0.08	0.10	0.05	0.14
MgO	14.98	14.45	14.63	14.76	14.98	14.71	14.67	15.04	14.43
CaO	11.71	11.55	11.72	11.48	11.86	11.55	11.46	11.91	11.45
Na_2O	2.27	2.55	2.47	2.41	2.33	2.41	2.40	2.30	2.32
K_2O	2.13	1.92	2.03	2.02	2.11	2.02	1.99	2.09	2.11
F	0.16	0.12	0.09	0.14	0.15	0.16	0.07	0.11	0.11
Cl									
Total	98.07	98.96	98.81	98.44	98.57	98.77	98.33	98.68	99.01
H_2O									
Mg#	77.71	71.87	74.67	73.99	77.43	74.12	74.17	77.83	73.15
Ca#	36.00	36.52	36.57	35.88	36.29	36.10	35.97	36.28	36.33
Sc									66
V									300
Mn									474
Co									40
Ni									114
Cu									0.7
Zn									36
Rb									11
Sr									345
Y									8
Zr									144
Nb									25
Ba									301
La									6.54

Ce	20.1
Pr	3.17
Nd	18.7
Sm	4.57
Eu	1.38
Gd	3.55
Tb	0.423
Dy	2.20
Ho	0.327
Er	0.643
Tm	0.076
Yb	0.450
Lu	0.050
Hf	5.98
Ta	1.79
Pb	0.24
Th	0.085
U	0.011

Appendix 1, Table 12.2 continued

Sample	SPK amph 3 G17	SPK amph 3 G19	SPK amph 3 G20	SPK amph 3 G22	SPK amph 3 G23	SPK amph 4 G5	SPK amph 4 G18	SPK amph 4 G19	SPKC amph 1 G1
SiO_2	41.32	41.73	41.24	41.36	41.53	41.72	41.55	40.63	41.42
TiO_2	4.24	4.29	4.19	4.14	4.32	3.35	3.31	4.80	4.47
Al_2O_3	13.43	13.32	12.80	13.10	13.19	12.32	12.39	13.75	13.06
Cr_2O_3	0.03	0.02	bd	0.01	bd	0.01	0.01	0.001	0.01
FeO	9.33	8.78	12.41	12.30	9.36	11.59	11.55	7.65	7.67
MnO	0.10	0.09	0.09	0.08	0.12	0.11	0.07	0.07	0.06
MgO	14.40	14.85	12.66	12.84	14.41	13.58	13.59	14.98	15.22
CaO	11.53	11.62	10.87	11.04	11.28	11.09	11.07	11.71	11.53
Na_2O	2.29	2.33	2.51	2.37	2.30	2.61	2.59	2.27	2.35
K_2O	2.14	2.09	2.18	2.20	2.13	1.92	1.94	2.13	2.05
F	0.02	0.12	0.14	0.08	0.38	0.08	0.11	0.16	0.18
Cl									
Total	98.83	99.17	99.02	99.49	98.84	98.33	98.13	98.07	97.96
H_2O									
Mg#	73.33	75.08	64.51	65.02	73.28	67.61	67.69	77.71	77.95
Ca#	36.54	36.02	38.17	38.22	36.02	37.00	36.94	36.00	35.26
Sc	49	59	48	48	40				
V	327	348	337	366	420				
Mn	589	582	622	694	781				
Co	38	41	46	47	37				
Ni	24	45	48	37	7				
Cu	0.6	0.7	1.1	1.0	0.2				
Zn	65	65	38	56	70				
Rb	12	14	14	14	11				

Sr	278	333	336	333	287
Y	8	10	8	8	9
Zr	190	164	143	175	361
Nb	29	23	24	28	54
Ba	205	235	212	243	209
La	5.81	6.56	5.86	6.30	7.33
Ce	18.4	20.3	19.6	21.8	24.6
Pr	3.04	3.26	3.30	3.45	3.84
Nd	17.6	19.0	19.3	20.2	21.9
Sm	4.32	4.86	4.83	4.96	5.37
Eu	1.40	1.46	1.56	1.65	1.71
Gd	3.51	3.90	3.67	3.94	4.04
Tb	0.438	0.490	0.454	0.479	0.495
Dy	2.15	2.44	2.40	2.44	2.57
Ho	0.330	0.361	0.351	0.364	0.374
Er	0.661	0.758	0.744	0.757	0.772
Tm	0.071	0.089	0.083	0.088	0.080
Yb	0.455	0.518	0.547	0.544	0.614
Lu	0.050	0.062	0.048	0.062	0.059
Hf	7.86	6.68	6.62	7.56	15.7
Ta	2.17	1.60	1.75	2.02	4.18
Pb	0.21	0.21	0.24	0.25	0.35
Th	0.056	0.061	0.060	0.065	0.127
U	0.008	0.010	0.010	0.010	0.018

Appendix 1, Table 12.2 continued

Sample	SPKC amph 1 G2	SPKC amph 1 G3	SPKC amph 1 G4	SPKC amph 1 G5	SPKC amph 1 G6	SPKC amph 1 G7	SPKC amph 1 G8	SPKC amph 1 G9	SPKC amph 1 G10
SiO_2	41.78	41.06	41.36	41.43	41.15	41.44	41.26	40.90	41.19
TiO_2	3.64	4.36	4.22	4.60	4.15	4.22	4.03	3.76	4.02
Al_2O_3	12.57	13.40	13.05	13.20	12.95	13.09	12.89	12.53	13.01
Cr_2O_3	0.02	bd	bd	0.04	0.01	bd	0.02	bd	0.004
FeO	10.87	10.40	8.72	7.62	8.81	8.84	9.50	10.54	8.98
MnO	0.13	0.11	0.08	0.06	0.08	0.06	0.07	0.12	0.05
MgO	13.86	13.62	14.79	15.25	14.93	14.75	14.52	13.86	14.53
CaO	11.31	11.38	11.55	11.60	11.47	11.48	11.37	11.19	11.41
Na_2O	2.77	2.40	2.48	2.37	2.38	2.45	2.52	2.57	2.44
K_2O	1.79	2.16	1.96	2.09	1.96	1.94	1.93	1.84	2.00
F	0.00	0.12	0.12	0.12	0.11	0.05	0.15	0.07	0.11
Cl					0.01	0.01	0.02		
Total	98.74	98.94	98.26	98.33	99.26	99.00	99.25	97.36	97.69
H_2O					1.26	0.68	0.99		
Mg#	69.43	70.00	75.13	78.10	75.10	74.82	73.14	70.07	74.25
Ca#	36.99	37.53	35.98	35.35	35.61	35.89	36.02	36.74	36.10
Sc	36	41	52		50	52	51	45	48
V	366	386	367		353	368	374	361	340

Mn	732	605	621	655	679	738	800	656
Co	42	45	45	47	49	49	42	48
Ni	9	26	46	50	51	41	9	52
Cu	0.7	1.2	1.0	1.8	1.7	1.5	0.7	1.4
Zn	66	66	65	48	54	61	56	27
Rb	10	15	15	14	15	15	10	12
Sr	288	359	328	328	352	373	303	308
Y	7	7	8	7	8	9	9	8
Zr	255	116	146	139	151	200	315	161
Nb	37	23	24	23	25	29	38	27
Ba	196	287	238	227	243	259	193	200
La	6.44	6.53	6.33	5.89	6.43	7.23	7.06	5.70
Ce	22.7	21.3	21.7	20.7	22.5	24.7	22.2	19.1
Pr	3.55	3.21	3.36	3.33	3.64	3.99	3.71	3.23
Nd	19.7	17.7	19.4	19.4	21.2	23.2	21.1	18.9
Sm	4.63	4.26	4.67	4.64	5.12	5.62	5.19	4.71
Eu	1.51	1.37	1.53	1.48	1.63	1.75	1.68	1.50
Gd	3.32	3.15	3.50	3.39	3.73	4.16	4.15	3.57
Tb	0.411	0.383	0.425	0.434	0.483	0.526	0.541	0.495
Dy	2.09	1.91	2.21	2.22	2.45	2.73	2.68	2.25
Ho	0.302	0.302	0.334	0.337	0.356	0.395	0.396	0.362
Er	0.622	0.575	0.686	0.658	0.730	0.826	0.837	0.744
Tm	0.072	0.068	0.071	0.077	0.077	0.085	0.098	0.081
Yb	0.463	0.405	0.476	0.469	0.515	0.580	0.591	0.537
Lu	0.052	0.041	0.053	0.049	0.057	0.067	0.067	0.046
Hf	10.0	5.34	6.10	5.94	6.55	8.74	13.6	7.57
Ta	2.63	1.47	1.58	1.58	1.74	2.21	3.37	2.28
Pb	0.27	0.30	0.26	0.25	0.22	0.28	0.34	0.23
Th	0.070	0.061	0.065	0.057	0.058	0.071	0.079	0.071
U	0.012	0.011	0.010	0.011	0.012	0.012	0.017	0.012

Appendix 1, Table 12.2 continued

Sample	SPKC amph 1 G11	SPKC amph 1 G12	SPKC amph 1 G13	SPKC amph 1 G14	SPKC amph 1 G15	SPKC amph 1 G16	SPKC amph 1 G17	SPKC amph 1 G18	SPKC amph 1 G19
SiO_2	41.06	41.63	41.54	41.18	41.21	41.73	41.64	40.80	41.87
TiO_2	4.17	3.63	3.99	4.17	4.29	3.76	3.88	3.55	3.66
Al_2O_3	12.94	12.60	12.91	13.30	13.21	12.57	12.57	13.15	12.48
Cr_2O_3	0.01	0.02	0.01	0.01	0.01	0.01	0.01	0.01	0.01
FeO	8.98	10.79	9.51	9.20	9.25	9.84	9.92	13.45	9.98
MnO	0.05	0.10	0.09	0.08	0.05	0.10	0.09	0.14	0.06
MgO	14.42	13.97	14.47	14.46	14.39	14.46	14.40	12.03	14.37
CaO	11.44	11.28	11.47	11.47	11.56	11.39	11.47	11.12	11.44
Na_2O	2.46	2.75	2.51	2.36	2.43	2.56	2.53	2.57	2.53
K_2O	2.00	1.86	1.97	2.11	2.09	2.01	2.02	2.11	1.94
F	0.16	0.11	0.10	0.16	0.14	0.07	0.11	0.16	0.22
Cl	0.02	0.01	0.01						

Total	98.79	99.29	99.47	98.43	98.56	98.46	98.59	99.03	98.46
H_2O	1.10	0.58	0.90						
Mg#	74.09	69.75	73.03	73.67	73.48	72.36	72.10	61.43	71.94
Ca#	36.33	36.75	36.33	36.32	36.63	36.17	36.42	39.93	36.42
Sc	50	39	46	51	49	45	49	40	50
V	344	361	335	347	329	343	364	426	368
Mn	619	731	645	600	603	667	678	866	700
Co	44	42	44	43	44	43	43	27	44
Ni	50	9	36	60	60	28	28	11	23
Cu	1.0	1.0	1.0	0.8	1.1	0.5	0.8	0.8	0.6
Zn	41	63	73	73	45	66	75	104	76
Rb	12	10	13	14	13	12	13	16	12
Sr	315	294	316	355	341	307	319	305	305
Y	8	8	8	9	8	8	9	9	9
Zr	165	287	173	165	158	218	237	330	245
Nb	27	38	26	28	27	35	35	57	36
Ba	222	201	235	287	247	227	239	286	222
La	6.08	6.67	6.38	7.20	6.38	6.54	7.03	8.31	6.64
Ce	20.3	23.1	22.9	23.6	20.7	21.7	22.9	25.5	21.7
Pr	3.33	3.69	3.46	3.70	3.38	3.41	3.65	3.92	3.50
Nd	19.4	20.6	20.0	21.0	19.6	20.1	21.3	21.2	20.2
Sm	4.75	4.87	4.57	4.95	4.80	4.83	5.38	4.87	4.97
Eu	1.54	1.52	1.47	1.60	1.52	1.51	1.58	1.47	1.52
Gd	3.71	3.46	3.40	3.98	3.60	3.66	4.06	3.76	3.95
Tb	0.482	0.462	0.444	0.516	0.446	0.474	0.511	0.477	0.507
Dy	2.30	2.30	2.26	2.46	2.38	2.38	2.63	2.46	2.54
Ho	0.353	0.338	0.318	0.357	0.358	0.358	0.384	0.385	0.378
Er	0.725	0.707	0.689	0.756	0.741	0.713	0.774	0.814	0.782
Tm	0.082	0.076	0.074	0.075	0.073	0.078	0.097	0.092	0.086
Yb	0.519	0.501	0.487	0.486	0.477	0.508	0.546	0.609	0.535
Lu	0.054	0.051	0.047	0.056	0.059	0.063	0.057	0.071	0.055
Hf	7.47	11.0	7.00	6.89	6.62	8.41	9.78	11.2	9.88
Ta	2.12	2.82	1.82	2.01	1.96	2.47	2.67	4.27	2.71
Pb	0.28	0.27	0.25	0.28	0.27	0.25	0.29	0.47	0.25
Th	0.076	0.084	0.062	0.070	0.067	0.072	0.082	0.157	0.075
U	0.011	0.014	0.010	0.013	0.010	0.013	0.010	0.023	0.011

Appendix 1, Table 12.2 continued

Sample	SPKC amph 1 G20	SPKC amph 1 G21	SPKC amph 1 G22	SPKC amph 1 G23	SPKC amph 1 G24	SPKC amph 1 G25	SPKC amph 1 G26	SPKC amph 1 G27	SPKC amph 2 G1
SiO_2	41.31	41.81	41.34	41.35	41.05	41.24	41.55	41.20	40.93
TiO_2	4.26	3.95	4.15	4.07	4.04	4.13	4.19	4.19	4.38
Al_2O_3	13.39	12.97	12.94	12.94	12.94	13.24	13.06	13.32	13.45
Cr_2O_3	0.01	0.01	0.01	0.004	0.02	0.01	bd	0.003	0.03
FeO	8.70	9.38	9.40	9.56	9.61	9.54	8.86	9.54	8.61
MnO	0.07	0.06	0.07	0.10	0.07	0.07	0.08	0.07	0.06
MgO	14.70	14.64	14.67	14.51	14.55	14.37	14.89	14.39	14.47
CaO	11.60	11.43	11.47	11.50	11.46	11.47	11.41	11.44	11.43
Na_2O	2.51	2.44	2.43	2.43	2.39	2.44	2.53	2.46	2.29
K_2O	2.08	2.01	2.06	2.06	2.04	2.06	1.95	2.03	2.14
F	0.07	0.09	0.09	0.03	0.14	0.20	0.09	0.12	0.12
Cl									0.01
Total	98.66	98.75	98.59	98.56	98.25	98.68	98.58	98.71	98.43
H_2O									0.52
Mg#	75.06	73.55	73.55	72.99	72.94	72.85	74.95	72.87	74.95
Ca#	36.22	35.97	36.00	36.31	36.16	36.48	35.53	36.39	36.23
Sc	62	43	50						47
V	353	343	363						345
Mn	611	621	626						625
Co	47	43	43						51
Ni	49	40	40						101
Cu	0.8	1.2	0.8						1.2
Zn	64	45	64						35
Rb	15	12	12						15
Sr	362	287	307						379
Y	10	7	8						8
Zr	195	153	183						133
Nb	34	27	29						26
Ba	284	211	229						266
La	7.72	5.49	6.10						6.32
Ce	26.0	18.4	20.2						21.3
Pr	3.86	2.95	3.18						3.57
Nd	23.3	17.5	18.8						20.8
Sm	5.37	4.19	4.48						5.27
Eu	1.62	1.35	1.47						1.78
Gd	4.31	3.11	3.80						3.94
Tb	0.510	0.420	0.471						0.539
Dy	2.64	2.06	2.18						2.62
Ho	0.403	0.302	0.317						0.418
Er	0.839	0.586	0.667						0.745
Tm	0.085	0.070	0.076						0.088
Yb	0.568	0.424	0.456						0.547
Lu	0.066	0.042	0.057						0.050
Hf	8.21	6.60	7.49						6.57

Ta	2.52	2.04	2.18						1.94
Pb	0.54	0.24	0.25						0.31
Th	0.248	0.056	0.064						0.082
U	0.042	0.010	0.007						0.009

Appendix 1, Table 12.2 continued

Sample	SPKC amph 2 G2	SPKC amph 2 G3	SPKC amph 2 G4	SPKC amph 2 G5	SPKC amph 2 G6	SPKC amph 2 G7	SPKC amph 2 G8	SPKC amph 2 G9	SPKC amph 2 G10
SiO_2	40.54	40.98	41.38	41.69	41.11	41.13	41.38	41.10	40.36
TiO_2	4.39	4.01	3.92	3.98	4.26	4.06	4.04	3.96	4.20
Al_2O_3	13.45	12.51	12.51	12.57	13.48	13.09	13.08	12.95	13.35
Cr_2O_3	0.02	0.01	bd	0.02	0.03	0.01	0.01	0.01	0.03
FeO	8.54	8.79	8.82	8.66	8.92	9.50	9.10	9.14	8.89
MnO	0.08	0.09	0.08	0.06	0.06	0.11	0.09	0.08	0.07
MgO	14.35	14.76	14.90	14.92	14.30	14.40	14.58	14.49	14.31
CaO	11.50	11.39	11.41	11.41	11.47	11.40	11.44	11.30	11.39
Na_2O	2.28	2.56	2.59	2.61	2.33	2.46	2.44	2.39	2.33
K_2O	2.14	1.81	1.79	1.85	2.11	1.96	2.04	2.02	2.09
F	0.07	0.06	0.09	0.04	0.06	0.15	0.04	0.15	0.09
Cl	0.01	0.01		0.01					
Total	98.29	98.25	97.45	98.52	98.11	98.19	98.22	97.53	97.06
H_2O	0.93	1.29		0.71					
Mg#	74.95	74.94	75.04	75.43	74.07	72.98	74.05	73.85	74.15
Ca#	36.55	35.70	35.53	35.48	36.58	36.28	36.07	35.93	36.41
Sc	48	54		65					
V	310	313		334					
Mn	543	573		606					
Co	41	42		43					
Ni	74	69		73					
Cu	1.0	0.8		1.0					
Zn	46	59		64					
Rb	12	9		10					
Sr	325	347		381					
Y	8	8		9					
Zr	112	167		200					
Nb	22	25		28					
Ba	246	243		255					
La	5.76	7.64		8.19					
Ce	19.3	23.8		25.1					
Pr	2.97	3.55		3.80					
Nd	17.3	19.6		22.4					
Sm	4.11	4.65		5.36					
Eu	1.34	1.46		1.60					
Gd	3.22	3.48		4.01					
Tb	0.398	0.407		0.455					

Dy	1.93	2.05	2.30
Ho	0.280	0.290	0.345
Er	0.590	0.541	0.656
Tm	0.068	0.064	0.071
Yb	0.383	0.386	0.446
Lu	0.044	0.040	0.054
Hf	4.38	6.25	7.59
Ta	1.42	1.62	1.74
Pb	0.23	0.20	0.20
Th	0.059	0.060	0.077
U	0.009	0.010	0.017

Appendix 1, Table 12.2 continued

Sample	SPKC amph 2 G11	SPKC amph 2 G12	SPKC amph 2 G13	SPKC amph 2 G14	SPKC amph 2 G15	SPKC amph 2 G16	SPKC amph 2 G17	SPKC amph 2 G18	SPKC amph 2 G19
SiO_2	41.20	41.51	41.39	41.33	41.74	41.49	41.51	41.43	41.30
TiO_2	4.09	4.21	4.15	3.83	3.94	3.17	4.01	3.89	3.84
Al_2O_3	13.13	12.74	12.87	12.75	12.81	12.48	12.72	13.03	12.94
Cr_2O_3	0.02	bd	0.03	bd	0.02	bd	0.02	bd	bd
FeO	9.42	8.59	8.71	10.26	8.90	11.28	8.95	9.65	9.38
MnO	0.10	0.07	0.09	0.11	0.08	0.11	0.07	0.09	0.08
MgO	14.25	14.73	15.02	14.03	14.56	13.48	14.68	14.22	14.26
CaO	11.23	11.41	11.54	11.30	11.32	11.25	11.32	11.38	11.30
Na_2O	2.48	2.51	2.55	2.57	2.40	2.51	2.50	2.47	2.51
K_2O	1.98	1.81	1.84	1.98	2.01	1.91	2.01	2.00	2.02
F	0.02	0.20	0.20	0.17	0.12	0.12	0.15	0.13	0.13
Cl									
Total	97.90	97.68	98.30	98.25	97.84	97.75	97.88	98.22	97.70
H_2O									
Mg#	72.93	75.34	75.43	70.88	74.44	68.03	74.50	72.39	73.02
Ca#	36.19	35.78	35.59	36.69	35.87	37.52	35.69	36.54	36.31
Sc									
V									
Mn									
Co									
Ni									
Cu									
Zn									
Rb									
Sr									
Y									
Zr									
Nb									
Ba									
La									
Ce									

Pr
Nd
Sm
Eu
Gd
Tb
Dy
Ho
Er
Tm
Yb
Lu
Hf
Ta
Pb
Th
U

Appendix 1, Table 12.2 continued

Sample	SPK M4 G2	SPK M2 G4	SPK M2 G5	SPK M2 G6	SPK M2 G8	SPK M2 G9	SPK M2 G10	SPK M2 G13	SPK M2 G16
SiO_2	41.10	41.82	41.44	41.70	41.37	40.95	41.98	40.97	41.62
TiO_2	3.83	4.45	4.17	4.07	4.20	4.21	3.85	4.29	4.18
Al_2O_3	12.64	13.34	12.72	12.86	12.82	12.29	12.50	13.30	13.02
Cr_2O_3	0.00	0.10	0.01	0.04	0.01	0.00	0.00	0.01	0.03
FeO	9.41	7.91	9.09	9.09	8.91	8.62	8.19	8.91	8.32
MnO	0.09	0.05	0.08	0.10	0.06	0.08	0.08	0.07	0.05
MgO	14.81	15.94	15.47	15.61	15.23	15.68	15.95	15.13	16.05
CaO	11.31	11.56	11.76	11.61	11.51	11.54	11.51	11.59	11.57
Na_2O	2.54	2.53	2.54	2.73	2.58	2.78	2.78	2.56	2.53
K_2O	1.98	1.90	1.97	1.79	1.89	1.66	1.66	2.09	1.84
F									
Cl									
Total	97.71	99.60	99.25	99.60	98.57	97.81	98.49	98.91	99.20
H_2O									
Mg#	73.70	78.21	75.19	75.34	75.28	76.41	77.63	75.16	77.46
Ca#	35.45	34.29	35.36	34.86	35.22	34.61	34.16	35.52	34.15
Sc		47	58	46	39	44	47	43	
V		248	216	182	185	234	205	235	
Mn									
Co									
Ni		6	14	15	4	3	6	4	
Cu									
Zn									
Rb		13	14	14	14	11	11	16	
Sr		113	82	88	90	95	97	94	

Y	8	6	6	6	7	7	7	
Zr	240	208	113	167	240	164	216	
Nb	25	32	29	32	32	36	35	
Ba	263	307	286	319	343	321	327	
La	6.65	4.47	4.02	2.89	2.79	3.75	3.20	3.66
Ce	22.8	16.9	15.1	11.2	11.0	14.7	12.3	14.9
Pr	3.66	2.84	2.56	1.90	1.89	2.49	2.13	2.53
Nd	19.4	16.0	14.9	11.4	11.2	13.9	12.5	13.9
Sm	4.74	4.14	3.44	2.96	3.08	3.68	3.32	3.69
Eu	1.71	1.34	1.16	1.01	0.95	1.22	1.11	1.22
Gd	3.61	3.47	2.86	2.39	2.49	3.13	2.84	2.88
Tb	0.445	0.445	0.354	0.309	0.337	0.432	0.398	0.393
Dy	2.30	2.15	1.76	1.62	1.63	2.12	1.96	1.94
Ho	0.334	0.339	0.273	0.246	0.253	0.345	0.304	0.286
Er	0.674	0.770	0.568	0.567	0.550	0.690	0.642	0.668
Tm	0.070	0.088	0.064	0.064	0.064	0.082	0.067	0.075
Yb	0.524	0.549	0.446	0.440	0.435	0.544	0.468	0.497
Lu	0.052	0.062	0.048	0.054	0.047	0.055	0.058	0.056
Hf	8.30	10.7	10.1	5.23	7.43	11.3	7.52	9.97
Ta	0.23	0.23	0.09	0.11	0.23	0.11	0.22	
Pb	0.09	0.10	0.07	0.07	0.07	0.08	0.07	
Th	0.068	0.124	0.032	0.045	0.077	0.039	0.078	
U	0.008	0.015	0.005	0.005	0.013	0.010	0.011	

Appendix 1, Table 12.2 continued

Sample	SPK M2 G17	SPK M2 G18	SPK M2 G19	SPK M2 G20	SPK M1 G4	SPK M1 G6	SPK M3 G11	SPK M6 G16	SPK M6 G17
SiO_2	42.09	41.34	41.07	41.51	41.67	41.58	41.77	40.81	41.24
TiO_2	4.00	4.28	4.46	4.14	4.00	4.13	3.92	3.88	3.89
Al_2O_3	12.67	13.05	13.17	12.71	12.78	12.76	12.67	12.30	12.40
Cr_2O_3	0.02	0.00	0.06	0.02	0.01	0.00	0.00	0.01	0.00
FeO	8.22	8.40	8.11	8.67	9.50	9.25	10.03	9.89	9.84
MnO	0.07	0.06	0.06	0.04	0.14	0.12	0.07	0.04	0.04
MgO	16.00	15.80	15.52	15.84	15.07	14.98	15.00	14.90	15.17
CaO	11.26	11.59	11.63	11.55	11.30	11.35	11.44	11.30	11.35
Na_2O	2.82	2.68	2.52	2.64	2.37	2.50	2.45	2.56	2.48
K_2O	1.76	1.79	1.94	1.89	2.01	1.96	2.02	2.00	1.97
F									
Cl									
Total	98.91	98.98	98.54	99.00	98.84	98.63	99.35	97.69	98.39
H_2O									
Mg#	77.61	77.02	77.32	76.49	73.86	74.25	72.71	72.85	73.30
Ca#	33.60	34.54	35.02	34.41	35.04	35.27	35.41	35.30	34.99
Sc		95	41	66					
V		236	224	184					
Mn									

Co				
Ni		50	3	28
Cu				
Zn				
Rb		9	13	12
Sr		85	97	75
Y		7	7	5
Zr		147	231	147
Nb		27	26	28
Ba		261	324	273
La	7.21	3.93	3.60	3.15
Ce	25.0	14.9	13.8	12.5
Pr	3.97	2.58	2.46	2.15
Nd	21.3	14.8	13.7	12.0
Sm	5.16	4.00	3.60	3.09
Eu	1.69	1.29	1.22	0.99
Gd	4.03	3.31	2.88	2.45
Tb	0.477	0.445	0.404	0.298
Dy	2.56	2.08	1.98	1.56
Ho	0.376	0.323	0.291	0.248
Er	0.764	0.656	0.677	0.476
Tm	0.089	0.077	0.071	0.061
Yb	0.556	0.467	0.539	0.383
Lu	0.062	0.052	0.055	0.034
Hf	8.72	7.59	10.0	7.23
Ta		0.28	0.20	0.16
Pb		0.05	0.08	0.08
Th		0.113	0.067	0.098
U		0.018	0.006	0.013

Appendix 1, Table 12.2 continued

Sample	SPK-M9_G1	SPK-M9_G2	SPK-M9_G3	SPK-M9_G4	SPK-M9_G5	SPK-M9_G8	SPK-M9_G10	SPK-M9_G11	SPK-M9_G15
SiO_2	41.50	41.34	41.06	41.30	41.30	40.97	41.22	41.19	40.84
TiO_2	3.66	4.15	4.18	3.67	3.96	4.04	3.62	3.76	3.87
Al_2O_3	12.57	13.20	13.23	12.57	12.94	13.05	12.67	12.70	13.08
Cr_2O_3	0.00	0.01	0.01	0.02	0.01	0.02	0.01	0.03	0.02
FeO	10.57	9.28	8.71	10.05	9.34	9.01	10.07	9.88	9.11
MnO	0.15	0.07	0.05	0.09	0.07	0.08	0.10	0.08	0.09
MgO	13.96	14.39	14.76	14.16	14.35	14.42	14.11	14.04	14.26
CaO	11.33	11.49	11.62	11.43	11.50	11.42	11.40	11.29	11.42
Na_2O	2.75	2.35	2.49	2.55	2.46	2.33	2.54	2.48	2.41
K_2O	1.80	2.02	1.91	1.84	1.93	2.03	1.98	1.97	1.95
F									
Cl									

Total	98.30	98.28	98.00	97.68	97.86	97.38	97.73	97.42	97.05
H_2O									
Mg#	70.18	73.42	75.12	71.50	73.23	74.04	71.40	71.69	73.59
Ca#	36.86	36.48	36.16	36.73	36.57	36.29	36.75	36.63	36.55

Appendix 1, Table 12.2 continued

Sample	SPK-M9_G16	SPK-M9_G17	SPK-M10_G1	SPK-M10_G8	SPK-M10_G10	SPK-M10_G17	SPK-M10_G18	SPK-M10_G20
SiO_2	40.68	40.65	40.90	41.56	41.16	41.68	41.11	40.25
TiO_2	3.97	3.93	4.75	4.21	4.08	3.75	4.14	4.68
Al_2O_3	12.98	12.96	13.99	13.03	13.04	12.79	13.08	13.77
Cr_2O_3	0.02	0.00	0.04	0.00	0.04	0.00	0.01	0.01
FeO	9.19	9.21	7.89	8.89	9.40	9.83	9.53	7.94
MnO	0.11	0.08	0.07	0.08	0.12	0.05	0.09	0.05
MgO	14.33	14.34	14.63	14.66	14.45	14.36	14.50	14.56
CaO	11.43	11.33	11.73	11.61	11.42	11.43	11.57	11.52
Na_2O	2.48	2.51	2.27	2.49	2.58	2.53	2.49	2.26
K_2O	1.94	1.98	2.11	2.05	1.96	1.96	1.98	2.12
F								
Cl								
Total	97.12	97.00	98.36	98.57	98.26	98.40	98.50	97.16
H_2O								
Mg#	73.54	73.50	76.76	74.59	73.26	72.23	73.03	76.56
Ca#	36.45	36.24	36.58	36.30	36.25	36.40	36.47	36.28

Table 12:3: Major and trace element data for phlogopite megacrysts

Sample	SPK phl 1 G1	SPK phl 1 G2	SPK phl 1 G3	SPK phl 1 G4	SPK phl 1 G5	SPK phl 1 G6	SPK phl 1 G8	SPK phl 1 G7	SPK phl 1 G9
SiO_2	37.38	37.39	37.23	37.01	37.01	37.31	37.32	37.21	37.49
TiO_2	5.91	5.83	5.86	5.41	5.40	5.75	5.36	5.42	5.38
Al_2O_3	16.19	16.35	16.34	16.09	16.01	16.21	15.91	15.92	15.88
Cr_2O_3	0.58	0.61	0.58	0.12	0.10	0.23	0.01	0.02	0.01
FeO	6.56	6.61	6.56	7.78	7.91	7.16	7.99	8.12	7.71
MnO	0.02	0.02	0.05	0.04	0.05	0.04	0.04	0.03	0.04
MgO	18.98	18.95	18.97	18.76	18.89	19.05	18.67	18.86	18.49
CaO	0.06	0.10	0.02	0.05	0.09	0.01	0.04	0.04	0.04
Na_2O	0.55	0.54	0.52	0.86	0.77	0.55	0.81	0.85	0.82
K_2O	9.38	9.34	9.50	8.86	8.72	9.36	8.74	8.80	8.67
F	0.23	0.19	0.25	0.28	0.20	0.23	0.22	0.15	0.17
Cl	0.08	0.05	0.05	0.05	0.04	0.04	0.05	0.05	0.05
Total	95.84	95.89	95.78	95.18	95.09	95.81	95.07	95.41	94.68
H_2O	0.91			1.19	1.46				
Mg#	83.75	83.62	83.75	81.12	80.96	82.57	80.63	80.53	81.02
Ca#	0.24	0.39	0.06	0.21	0.33	0.03	0.17	0.17	0.17
Sc	12	13	11	14	15	9	9	8	9
V	346	353	373	259	259	272	235	191	244
Mn	275	294	287	347	354	228	311	275	320
Co	71	80	72	69	73	57	68	60	69
Ni	593	673	617	253	255	375	224	190	224
Cu	3.2	5.8	3.4		3.6	1.8	1.8	2.4	2.0
Zn	21	18	23	112	21	75	45	27	52
Rb	431	451	460	275	279	311	271	232	274
Sr	109	104	109	170	179	91	133	114	138
Y	0.08	0.02	0.03	0.10	0.08	0.01	0.01	0.01	0.01
Zr	11	10	12	15	15	9	12	10	12
Nb	13	12	14	15	13	12	14	11	14
Ba	2728	2516	2753	3982	3885	2313	3033	2486	3150
La	0.210	0.112	0.170	0.182	0.064	0.027	0.022	0.028	0.020
Ce	0.213	0.163	0.670	0.223	0.018	0.012	0.006	0.017	0.004
Pr	0.028	0.022	0.029	0.047	0.002	0.009	0.007	0.012	
Nd	0.184	0.058	0.135	0.192	0.004	0.041			
Sm	0.143	0.142	0.142	0.132	0.112	0.077	0.090	0.065	0.072
Eu	0.118	0.106	0.092	0.112	0.102	0.068	0.075	0.068	0.076
Gd			0.004	0.006			0.003	0.003	
Tb	0.011	0.007	0.027	0.028		0.005	0.003	0.004	
Dy	0.011	0.007	0.010	0.032	0.011	0.004		0.003	0.003
Ho	0.003	0.006		0.067		0.003	0.002	0.001	0.003
Er	0.004	0.003	0.002		0.006	0.003	0.002	0.004	0.004
Tm	0.003	0.002			0.016		0.003		
Yb	0.014	0.006	0.003	0.024	0.011	0.003	0.005	0.005	0.004

Lu	0.002		0.005			0.002	0.004		0.002
Hf	0.345	0.356	0.299	0.348	0.419	0.304	0.326	0.286	0.365
Ta	0.82	0.84	0.87	1.08	0.86	0.82	0.93	0.77	0.95
Pb	0.25	0.28	0.43		0.30	0.17	0.27	0.26	0.28
Th	0.045	0.019	0.066	0.052		0.003		0.003	
U	0.008	0.004	0.009	0.023	0.008	0.002	0.005	0.002	0.003

Appendix 1, Table 12.3 continued

Sample	SPK phl 2 G8	SPK phl 2 G7	SPK phl 2 G6	SPK phl 2 G5	SPK phl 2 G4	SPK phl 2 G3	SPK phl 2 G2	SPK phl 2 G1	SPKC phl 3 G1
SiO_2	37.52	36.76	37.21	37.24	37.75	37.30	37.37	37.16	36.74
TiO_2	4.75	4.89	4.86	4.66	5.85	5.69	5.77	5.74	5.20
Al_2O_3	15.92	15.82	15.92	15.89	16.52	16.36	16.39	16.32	16.10
Cr_2O_3	0.01	0.01	0.02	0.01	0.61	0.59	0.60	0.63	0.02
FeO	10.59	10.30	10.18	10.31	6.53	6.27	6.47	6.82	9.63
MnO	0.06	0.04	0.05	0.07	0.04	0.02	0.02	0.04	0.08
MgO	17.77	17.40	17.37	17.57	18.74	18.51	18.67	18.53	17.73
CaO	0.03	0.08	0.07	0.06	0.06	0.04	0.04	0.06	0.01
Na_2O	0.87	0.84	0.89	0.85	0.54	0.46	0.48	0.54	0.83
K_2O	8.90	8.68	8.70	8.68	9.37	9.26	9.22	9.14	8.86
F	0.17	0.23	0.27	0.35	0.32	0.21	0.21	0.17	0.26
Cl	0.04	0.06	0.06	0.05	0.06	0.05	0.05	0.06	0.07
Total	96.56	95.01	95.46	95.57	96.23	94.67	95.19	95.13	95.42
H_2O					1.75		2.50		
Mg#	74.93	75.05	75.25	75.22	83.63	84.07	83.72	82.70	76.62
Ca#	0.14	0.34	0.28	0.23	0.23	0.14	0.15	0.26	0.05
Sc	8			7					7
V	309			272					246
Mn	248			361					349
Co	65			53					61
Ni	498								103
Cu	2.4			1.4					2.4
Zn	52			100					59
Rb	390			285					287
Sr	91			116					247
Y	0.01			0.04					0.05
Zr	8			21					18
Nb	11			19					16
Ba	2519			3033					3640
La	0.021			0.034					0.309
Ce	0.091			0.026					0.474
Pr	0.008			0.005					0.039
Nd	0.015			0.011					0.270
Sm	0.056			0.044					0.105
Eu	0.050			0.051					0.083
Gd	0.002			0.003					0.002

Tb	0.005	0.006	0.017
Dy	0.004	0.005	0.011
Ho	0.004	0.002	0.007
Er	0.002	0.004	0.006
Tm	0.001		0.003
Yb	0.003	0.007	0.010
Lu	0.002	0.002	0.004
Hf	0.239	0.591	0.501
Ta	0.72	1.29	1.18
Pb		0.37	0.34
Th	0.004	0.004	0.027
U	0.003	0.003	0.015

Appendix 1, Table 12.3 continued

Sample	SPKC phl 3 G2	SPKC phl 3 G3	SPKC phl 3 G4	SPKC phl 3 G5	SPKC phl 3 G6	SPKC phl 3 G7	SPKC phl 3 G8	SPKC phl 3 G9	SPKC phl 3 G10
SiO_2	36.84	36.82	36.97	37.07	37.15	37.31	37.15	37.33	37.21
TiO_2	5.11	4.97	5.12	5.87	5.82	5.80	5.76	5.87	5.84
Al_2O_3	16.16	16.21	16.13	16.47	16.63	16.34	16.68	16.47	16.65
Cr_2O_3	0.02	0.01	0.01	0.32	0.31	0.29	0.42	0.32	0.35
FeO	9.59	9.20	9.65	7.18	7.32	6.96	6.82	7.26	7.20
MnO	0.04	0.04	0.05	0.05	0.04	0.02	0.03	0.02	0.02
MgO	17.74	17.95	17.66	18.31	18.53	18.76	18.45	18.21	18.39
CaO	0.01	0.07	0.04	0.01	0.01	0.01	0.01	0.02	0.01
Na_2O	0.92	0.87	0.88	0.61	0.61	0.71	0.57	0.58	0.62
K_2O	8.77	8.84	8.87	9.34	9.35	9.38	9.36	9.14	9.30
F	0.19	0.17	0.22	0.24	0.19	0.20	0.32	0.17	0.18
Cl	0.05	0.05	0.05	0.06	0.06	0.05	0.05	0.05	0.05
Total	95.35	95.13	95.55	95.40	95.92	95.74	95.48	95.35	95.75
H_2O					1.60		2.54		
Mg#	76.71	77.64	76.52	81.95	81.85	82.76	82.81	81.71	81.98
Ca#	0.04	0.30	0.17	0.03	0.05	0.04	0.04	0.06	0.06
Sc	8		8		9	8		9	9
V	265		270		358	296		333	334
Mn	332		343		269	233		260	250
Co	60		61		67	61		66	60
Ni	98		101		509	425		507	456
Cu	0.9		0.8		2.0	1.9		2.0	1.6
Zn	95		100		56	42		45	66
Rb	326		327		374	303		381	367
Sr	128		136		115	109		111	95
Y	0.02		0.03		0.07	0.01		0.04	0.01
Zr	18		19		11	9		10	9
Nb	17		17		14	11		12	10
Ba	3380		3518		3300	2576		2894	2601
La	0.050		0.048		0.434	0.016		0.038	0.017

Ce	0.004	0.006	0.008	0.005	0.025	0.004
Pr	0.004	0.012	0.167	0.005	0.003	0.001
Nd	0.008	0.033	0.507	0.003	0.026	bd
Sm	0.070	0.061	0.099	0.038	0.076	0.046
Eu	0.070	0.067	0.063	0.040	0.069	0.049
Gd	0.003	bd	0.003	bd	0.003	bd
Tb	0.005	0.006	0.020	0.003	0.007	0.003
Dy	0.005	0.004	0.020	0.002		0.003
Ho	0.003	0.003	0.005	0.003	0.007	0.003
Er	0.003	0.005	0.015	0.003	0.005	0.002
Tm	0.002	0.003		0.002		0.003
Yb	0.004	0.006	0.009	0.004	0.006	0.003
Lu	0.004	0.004	0.002	0.002	0.006	0.002
Hf	0.502	0.489	0.301	0.292	0.266	0.267
Ta	1.16	1.17	0.79	0.73	0.80	0.57
Pb	0.29	0.26	0.20	0.18	0.26	0.15
Th				0.004	0.006	bd
U	0.004	0.003	0.240	0.004	0.006	0.002

Appendix 1, Table 12.3 continued

Sample	SPKC phl 2 G1	SPKC phl 2 G2	SPKC phl 2 G3	SPKC phl 2 G4	SPKC phl 2 G5	SPKC phl 2 G6	SPKC phl 2 G7	SPKC phl 2 G8	SPKC phl 2 G9
SiO_2	36.91	37.21	36.76	37.48	37.38	37.60	37.71	37.61	38.02
TiO_2	5.47	5.78	5.64	5.79	5.66	5.54	5.70	5.50	5.38
Al_2O_3	17.02	16.64	17.07	16.39	16.93	16.36	16.46	16.63	16.39
Cr_2O_3	0.84	0.16	0.85	0.26	0.43	0.12	0.16	0.10	0.13
FeO	6.35	7.23	6.81	6.93	6.79	7.31	7.34	7.76	7.11
MnO	0.04	0.05	0.03	0.03	0.04	0.04	0.03	0.05	0.06
MgO	18.50	18.70	18.48	18.64	18.60	18.65	18.70	18.70	18.92
CaO	0.01	0.01	0.01	0.01	0.00	0.01	0.01	0.01	0.00
Na_2O	0.53	0.58	0.58	0.64	0.57	0.67	0.62	0.67	0.41
K_2O	9.24	9.25	9.32	9.26	9.28	9.05	9.25	9.05	9.60
F	0.20	0.19	0.21	0.30	0.09	0.24	0.14	0.19	0.22
Cl	0.06	0.04	0.03	0.05	0.04	0.03	0.04	0.02	0.04
Total	95.07	95.74	95.68	95.66	95.75	95.53	96.10	96.20	96.18
H_2O			0.72	1.18		1.69			
Mg#	83.84	82.16	82.87	82.72	83.00	81.96	81.93	81.10	82.57
Ca#	0.03	0.02	0.02	0.05	0.01	0.04	0.05	0.03	0.01
Sc	10	10	9	9	9	10		11	12
V	295	317	283	342	296	301		265	330
Mn	263	271	224	268	229	293		290	273
Co	70	68	59	71	59	73		66	68
Ni	678	387	483	485	474	387		276	436
Cu	3.9	1.9	1.6	1.9	2.3	4.5		2.2	2.4
Zn	44	59	63	48	46	27		54	27
Rb	422	336	348	357	342	332		305	357
Sr	153	131	134	120	109	132		131	65
Y	0.02	0.01	0.02	0.01	0.01	0.09		0.02	0.01
Zr	10	10	10	10	9	12		11	13
Nb	15	14	12	13	12	14		13	17
Ba	5631	3373	3731	2961	3028	2654		3256	2829
La	0.031	0.022	0.022	0.021	0.018	0.142		0.016	0.026
Ce	0.005	0.005	0.004	0.014	0.003	0.456		0.004	0.055
Pr	0.002	0.004	bd	0.005	0.003	0.117		bd	0.010
Nd	bd	bd	0.002	0.004	bd	0.526		bd	0.012
Sm	0.129	0.093	0.055	0.058	0.048	0.126		0.065	0.042
Eu	0.119	0.085	0.065	0.068	0.056	0.098		0.074	0.036
Gd	bd	bd	0.002	bd	bd	0.047		bd	0.004
Tb	bd	0.003	0.004	bd	bd	0.217		bd	0.006
Dy	0.002	0.004	0.003	bd	bd	0.019		0.003	0.005
Ho	bd	0.002	0.002	bd	bd	0.046		0.002	bd
Er	0.004	0.002	0.003	0.002	0.002	0.008		0.003	0.004
Tm	0.002	0.002	0.003	0.006	bd	0.004		0.002	bd
Yb	0.005	0.005	0.003	0.005	0.006	0.033		0.003	0.004
Lu	bd	0.002	0.004	bd	0.003	0.006		0.002	bd
Hf	0.347	0.330	0.301	0.335	0.307	0.369		0.321	0.416

Ta	0.82	0.89	0.67	0.82	0.72	0.79	0.89	1.11
Pb		0.24	0.26	0.20	0.23	0.29	0.23	0.23
Th						0.375	bd	0.008
U	0.006	0.003	0.004	0.004	0.002	0.030	0.004	0.007

Appendix 1, Table 12.3 continued

Sample	SPKC phl 2 G10
SiO_2	37.73
TiO_2	5.69
Al_2O_3	16.73
Cr_2O_3	0.14
FeO	7.25
MnO	0.04
MgO	18.83
CaO	0.01
Na_2O	0.59
K_2O	9.34
F	0.18
Cl	0.04
Total	96.49
H_2O	
Mg#	82.23
Ca#	0.04
Sc	10
V	324
Mn	267
Co	66
Ni	381
Cu	1.6
Zn	66
Rb	342
Sr	132
Y	0.01
Zr	11
Nb	14
Ba	3337
La	0.019
Ce	0.005
Pr	bd
Nd	bd
Sm	0.054
Eu	0.061
Gd	bd
Tb	bd
Dy	0.001
Ho	0.002

Er	0.002
Tm	0.002
Yb	0.003
Lu	bd
Hf	0.319
Ta	0.86
Pb	0.22
Th	0.003
U	0.003

Table 12:4: Major and trace element data for ilmenite megacrysts

Sample	SPK M4 G6	SPK_ M6-G1	SPK_ M6-G2	SPK_ M6-G3	SPK_ M6-G4	SPK_ M6-G5	SPK_ M6-G6	SPK_ M6-G7	SPK_ M6-G8
SiO_2	0.11	0.01	0.02	0.02	0.003	0.03	0.02	0.003	
TiO_2	48.80	47.20	48.52	47.19	46.93	47.52	48.64	47.54	46.89
Al_2O_3	0.68	0.56	0.66	0.60	0.46	0.64	0.60	0.63	0.63
Cr_2O_3	0.01		0.03	0.01		0.03	0.02	0.01	
FeO	42.64	42.94	39.77	42.30	44.40	42.06	40.29	42.28	43.26
MnO	0.35	0.37	0.35	0.35	0.40	0.37	0.37	0.35	0.34
MgO	7.35	6.93	8.08	7.26	5.76	7.12	8.20	7.21	6.90
CaO	0.01	0.01	0.02	0.01	0.003	0.02	0.02	0.01	0.01
Total	99.99	98.01	97.44	97.75	97.96	97.79	98.17	98.03	98.02
%Hematite	21.75	23.74	19.97	23.66	23.36	22.46	20.85	22.93	24.53
%Geikelite	23.35	22.19	26.42	23.28	18.65	23.02	26.45	23.17	21.99
%Ilmenite	54.90	54.07	53.61	53.07	57.99	54.52	52.70	53.90	53.47
Mg#	23.48	22.33	26.57	23.41	18.77	23.16	26.61	23.30	22.11
Cr#	1.02	0.00	2.93	1.32	0.00	3.39	2.22	0.58	0.00
Sc	50	45	51	44	31	46	53	46	44
V	2093	2010	1908	1885	1662	1927	1790	1864	1835
Co	306	273	307	259	212	259	266	261	235
Ni	99	62	200	104	21	105	173	108	53
Zn	292	307	355	345	393	373	340	328	302
Ga	26	23	23	20	19	21	20	19	18
Y	0.49	0.47	0.39	0.46	0.41	0.41	0.43	0.45	0.50
Zr	1042	1166	724	887	917	860	795	944	1167
Nb	621	663	505	501	494	484	680	505	654
Hf	35	37	25	26	22	23	23	23	28
Ta	80	84	59	54	50	49	68	48	63

Sample	SPK_ M6-G9	SPK_ M6-G10	SPK_ M6-G11	SPK_ M6-G12	SPK_ M6-G13	SPK_ M6-G15	SPK_ M6-G16	SPK_ M6-G17	SPK_ M6-G18
SiO_2	0.01	0.01	0.01	0.005	0.003	0.01	0.02	0.003	bd
TiO_2	48.86	47.34	45.98	48.84	47.94	48.21	48.22	47.66	47.11
Al_2O_3	0.63	0.60	0.48	0.63	0.47	0.65	0.58	0.63	0.54
Cr_2O_3	0.01			0.01	0.04	0.01	0.01	0.01	0.01
FeO	39.82	42.35	45.90	41.35	42.73	42.66	42.01	42.68	43.33
MnO	0.36	0.37	0.39	0.37	0.34	0.34	0.34	0.36	0.38
MgO	8.31	7.35	5.39	7.72	6.87	7.29	7.52	7.28	6.96
CaO	0.02	0.01	0.01	0.02	0.01	0.02	0.01	0.01	0.001
Total	98.02	98.03	98.15	98.93	98.39	99.19	98.71	98.63	98.33

%Hematite	20.09	23.73	26.04	20.82	22.06	22.57	22.20	23.50	24.49
%Geikelite	26.94	23.47	17.19	24.79	22.14	23.20	24.03	23.17	22.11
%Ilmenite	52.97	52.79	56.77	54.39	55.80	54.24	53.77	53.33	53.40
Mg#	27.10	23.61	17.30	24.94	22.26	23.32	24.16	23.31	22.24
Cr#	0.95	0.00	0.00	0.53	5.00	1.23	0.57	0.84	0.93
Sc	54	44	33	48	44	50	51	51	45
V	1751	2062	2041	1823	2036	1907	1756	1804	2024
Co	289	280	211	268	294	250	250	243	253
Ni	242	93	21	129	125	84	104	98	58
Zn	305	324	333	303	377	317	291	297	306
Ga	18	20	20	18	24	19	17	19	20
Y	0.43	0.43	0.40	0.45	0.50	0.45	0.46	0.45	0.44
Zr	704	938	1336	841	1258	1007	860	1009	1121
Nb	511	606	817	513	753	421	504	512	660
Hf	18	23	30	20	42	27	24	27	29
Ta	52	52	73	46	101	44	53	53	65

Sample	SPK_ M6-G19	SPK_ M6-G20	SPK_ M7-G1	SPK_ M7-G2	SPK_ M7-G3	SPK_ M7-G4	SPK_ M7-G5	SPK_ M7-G6	SPK_ M7-G7
SiO_2	0.01	0.02	0.01	0.03	bd	0.01	0.01	0.01	0.01
TiO_2	46.30	46.33	47.40	47.96	48.16	47.31	47.02	48.33	47.65
Al_2O_3	0.46	0.45	0.48	0.45	0.61	0.48	0.57	0.63	0.47
Cr_2O_3	0.00	0.03	0.02	bd	bd	0.01	0.003	0.01	0.04
FeO	45.48	45.55	42.69	42.40	41.54	43.28	43.13	42.54	42.69
MnO	0.37	0.36	0.37	0.40	0.38	0.34	0.31	0.34	0.35
MgO	5.59	5.71	6.89	6.81	7.45	6.98	6.89	7.31	6.96
CaO		0.01		0.004	0.02	0.005	0.01	0.01	0.01
Total	98.21	98.46	97.86	98.05	98.16	98.41	97.94	99.18	98.18
%Hematite	25.38	25.68	22.96	21.48	21.52	24.10	24.11	22.24	22.70
%Geikelite	17.84	18.14	22.20	22.10	24.05	22.18	22.05	23.30	22.36
%Ilmenite	56.78	56.18	54.84	56.42	54.42	53.72	53.84	54.46	54.94
Mg#	17.95	18.24	22.33	22.24	24.20	22.30	22.16	23.43	22.49
Cr#	0.00	4.31	2.87	0.00	0.00	0.77	0.35	0.94	5.43
Sc	33	37	44	43	47	40	45	50	47
V	1921	1997	1917	1894	1845	1888	1961	1881	1729
Co	213	239	273	253	261	295	255	266	238
Ni	20	45	119	108	109	191	61	67	102
Zn	308	381	403	381	344	408	354	340	341
Ga	20	21	23	22	19	23	22	20	19
Y	0.39	0.46	0.44	0.37	0.37	0.44	0.50	0.42	0.51
Zr	1212	1235	1233	1226	804	1100	1139	964	1317
Nb	519	677	706	718	488	1049	652	622	693
Hf	26	28	41	36	23	33	32	28	38
Ta	50	63	97	87	50	110	69	65	87

Appendix 1, Table 12.4 continued

Sample	SPK_ M7-G8	SPK_ M7-G9	SPK_ M7-G10	SPK_ M7-G11	SPK_ M7-G12	SPK_ M7-G13	SPK_ M7-G14	SPK_ M7-G15	SPK_ M7-G16
SiO_2	bd	0.01	0.03	0.02	0.03	0.01	0.01	0.02	0.01
TiO_2	45.94	45.22	46.25	47.05	45.28	46.49	48.08	47.37	45.14
Al_2O_3	0.49	0.52	0.50	0.58	0.49	0.47	0.62	0.58	0.51
Cr_2O_3	bd	bd	0.04	bd	0.01	bd	0.01	0.02	0.04
FeO	46.04	45.87	45.56	42.75	45.82	44.93	41.16	41.88	45.57
MnO	0.38	0.36	0.42	0.37	0.37	0.40	0.39	0.33	0.38
MgO	5.40	5.50	5.50	6.92	5.52	5.67	7.51	7.20	5.38
CaO	0.01	0.01	0.01	0.01	0.01	0.01	0.02	0.01	0.01
Total	98.25	97.49	98.31	97.69	97.52	97.98	97.80	97.41	97.02
%Hematite	26.27	27.44	25.43	23.68	27.31	24.58	21.29	22.58	26.90
%Geikelite	17.16	17.50	17.57	22.24	17.55	18.24	24.38	23.31	17.25
%Ilmenite	56.57	55.06	57.00	54.08	55.14	57.18	54.33	54.10	55.84
Mg#	17.27	17.61	17.69	22.38	17.66	18.36	24.54	23.44	17.36
Cr#	0.00	0.00	4.90	0.00	0.69	0.00	0.53	2.50	4.56
Sc	36	36	35	44	35	35	45	46	36
V	1903	2022	1910	1800	2025	2017	1920	1858	1974
Co	206	204	198	224	205	246	281	252	202
Ni	19	19	30	51	19	38	114	86	18
Zn	341	329	343	291	323	419	368	337	339
Ga	21	21	20	18	21	23	20	20	21
Y	0.42	0.45	0.43	0.46	0.44	0.42	0.43	0.44	0.42
Zr	1498	1416	1422	1111	1380	1240	777	922	1456
Nb	594	815	630	594	820	635	509	410	832
Hf	35	35	33	26	34	35	23	24	39
Ta	60	81	62	58	77	77	53	41	89

Appendix 1, Table 12.4 continued

Sample	SPK_ M7-G17	SPK_ M7-G18	SPK_ M7-G19	SPK_ M7-G20	SPK_ M8-G1	SPK_ M8-G2	SPK_ M8-G3	SPK_ M8-G4	SPK_ M8-G5
SiO_2	0.01	0.003	0.01	0.01			0.03	0.02	0.004
TiO_2	45.89	47.52	46.87	47.31	48.46	47.88	48.24	48.08	49.35
Al_2O_3	0.49	0.63	0.59	0.61	0.58	0.27	0.60	0.25	0.41
Cr_2O_3	0.02	bd	0.03	0.02	0.04	bd	0.01	0.01	0.01
FeO	44.84	41.97	42.37	41.76	40.92	43.77	41.57	43.76	39.33
MnO	0.38	0.33	0.34	0.35	0.37	0.49	0.37	0.43	0.42
MgO	5.71	7.21	6.96	7.20	7.70	5.30	7.47	5.30	7.65
CaO	0.01	0.01	0.01	0.004	0.02	0.01	0.01	0.008	0.02
Total	97.35	97.67	97.18	97.26	98.08	97.72	98.30	97.84	97.20
%Hematite	25.49	22.51	23.52	22.56	20.78	19.81	21.48	19.36	16.86
%Geikelite	18.36	23.31	22.52	23.35	24.94	17.58	24.09	17.61	25.54

%Ilmenite	56.15	54.18	53.96	54.09	54.28	62.61	54.44	63.03	57.60
Mg#	18.48	23.43	22.64	23.49	25.10	17.73	24.23	17.74	25.72
Cr#	2.73	0.00	3.53	2.06	4.25	0.00	1.44	2.37	2.16
Sc	37	47	47	48	49	44	48	43	55
V	1837	1725	1864	1813	1887	1556	1783	1455	1486
Co	217	228	232	238	296	263	219	204	233
Ni	40	91	51	98	123	179	90	143	195
Zn	378	305	339	330	327	464	238	333	266
Ga	20	18	20	18	22	14	15	12	12
Y	0.46	0.44	0.46	0.43	0.49	0.16	0.50	0.18	0.53
Zr	1292	958	1174	931	844	1391	908	1353	932
Nb	650	491	658	504	487	645	550	594	414
Hf	33	25	32	25	30	36	23	23	22
Ta	69	51	68	50	63	66	49	50	38

Appendix 1, Table 12.4 continued

Sample	SPK_ M8-G6	SPK_ M8-G7	SPK_ M8-G8	SPK_ M8-G9	SPK_ M8-G10	SPK_ M8-G11	SPK_ M8-G12	SPK_ M8-G13	SPK_ M8-G14
SiO_2	0.05	0.02	0.01	0.02	0.003	0.003	0.01		0.02
TiO_2	46.19	45.52	48.76	47.90	48.34	49.51	47.90	47.77	46.92
Al_2O_3	0.45	0.46	1.36	0.62	0.56	0.66	0.65	0.56	0.52
Cr_2O_3	0.01	0.01	0.03	0.01	bd	0.03	0.002	0.04	0.04
FeO	44.39	45.58	39.12	41.91	42.20	41.14	41.89	42.80	43.71
MnO	0.41	0.38	0.35	0.35	0.35	0.34	0.35	0.35	0.39
MgO	5.66	5.36	8.35	7.51	7.28	8.06	7.32	6.71	6.24
CaO	0.004	0.001	0.03	0.004	0.02	0.02	0.01	0.02	0.01
Total	97.15	97.33	98.00	98.32	98.75	99.76	98.13	98.24	97.84
%Hematite	24.32	26.25	19.30	22.59	21.71	20.28	22.06	22.02	23.60
%Geikelite	18.39	17.20	27.39	24.06	23.37	25.73	23.59	21.69	20.13
%Ilmenite	57.29	56.56	53.31	53.35	54.92	53.99	54.35	56.29	56.27
Mg#	18.51	17.30	27.54	24.20	23.50	25.87	23.72	21.82	20.27
Cr#	1.17	1.64	1.44	1.28	0.00	2.56	0.21	4.03	4.51
Sc	36	36	56	50	49	53	53	46	41
V	1771	1962	1723	1905	1999	1899	2003	1822	1726
Co	195	192	261	236	273	271	283	246	216
Ni	32	18	157	113	116	128	101	102	73
Zn	320	322	288	252	321	260	363	376	347
Ga	18	19	17	16	20	18	22	21	19
Y	0.43	0.43	0.43	0.42	0.41	0.44	0.45	0.41	0.49
Zr	1209	1435	741	936	882	789	1048	1029	1173
Nb	661	783	421	634	640	492	652	457	616
Hf	28	34	19	25	24	20	35	28	30
Ta	64	77	40	59	55	43	81	51	73

Appendix 1, Table 12.4 continued

Sample	SPK_M8-G16	SPK_M8-G17	SPK_M8-G18	SPK_M8-G19	SPK_M8-G20
SiO_2	0.02	bd	0.002	bd	0.01
TiO_2	46.19	46.57	47.58	47.80	45.60
Al_2O_3	0.43	0.46	0.53	0.60	0.26
Cr_2O_3	bd	bd	bd	0.01	0.00
FeO	45.40	45.09	42.97	42.62	47.72
MnO	0.40	0.41	0.35	0.35	0.42
MgO	5.61	5.61	6.83	7.13	3.97
CaO	0.01	0.01	0.02	0.02	bd
Total	98.07	98.14	98.28	98.53	97.97
%Hematite	25.57	24.52	22.89	22.81	25.72
%Geikelite	17.93	18.01	21.93	22.83	12.81
%Ilmenite	56.50	57.47	55.18	54.36	61.47
Mg#	18.04	18.13	22.05	22.96	12.90
Cr#	0.00	0.00	0.00	1.28	0.64
Sc	51	35	35	46	49
V	1841	1858	1776	1714	1960
Co	247	200	197	217	238
Ni	89	30	32	87	54
Zn	256	326	320	299	343
Ga	18	19	18	17	20
Y	0.49	0.40	0.41	0.46	0.44
Zr	892	1312	1157	986	997
Nb	564	639	631	428	679
Hf	26	31	30	25	29
Ta	61	67	67	45	69

Appendix 1,

Table 12:5 Major and trace element data for clinopyroxene xenolith grains

Sample	SPK Cpxite G1 C	SPK Cpxite G1 C	SPK Cpxite G1 R	SPK Cpxite G2 C	SPK Cpxite G3 C	SPK Cpxite G3 R	SPK Cpxite G4 C	SPK Cpxite G4 R	SPK Cpxite G5 C
SiO_2	49.42	49.39	49.77	49.29	49.17	49.92	49.15	48.96	50.04
TiO_2	1.33	1.37	1.24	1.38	1.38	1.06	1.51	1.51	0.92
Al_2O_3	4.93	4.72	4.69	5.00	4.91	4.40	5.24	4.90	3.93
Cr_2O_3	bd	bd	0.02	0.02	0.004	bd	0.02	0.01	0.004
FeO	8.72	8.62	9.41	8.97	9.73	9.18	8.91	9.20	9.77
MnO	0.16	0.11	0.16	0.16	0.12	0.10	0.18	0.10	0.12
MgO	12.44	12.39	11.93	12.14	11.91	12.03	12.14	12.26	11.92
CaO	21.49	21.57	21.33	21.48	21.20	20.99	21.35	21.04	20.69
Na_2O	1.39	1.52	1.67	1.51	1.64	1.70	1.46	1.51	1.90
K_2O	0.01	0.01	0.002	0.001	0.02	0.02	0.003	0.02	bd
Total	99.89	99.70	100.22	99.95	100.09	99.40	99.96	99.51	99.29
Mg#	71.76	71.93	69.31	70.67	68.55	69.99	70.80	70.37	68.48
Ca#	55.42	55.60	56.25	56.01	56.14	55.66	55.86	55.25	55.52
Sc		16.40	27.06	27.89	26.18	25.35	30.18	33.76	19.10
V		230.73	281.87	301.97	304.40	308.37	301.13	269.33	317.27
Cr		14.14	23.11	16.20	17.81	20.74	14.05	24.49	22.89
Ni		4.54	4.82	4.27	5.28	4.95	3.46	4.95	4.76
Rb		< d.l.	0.01	0.07	< d.l.	0.01	0.01	< d.l.	0.02
Sr		110.27	126.30	131.70	122.23	130.67	115.00	139.97	118.70
Y		6.14	6.71	8.39	7.68	7.98	8.18	8.36	7.76
Zr		209.90	500.05	311.30	295.35	323.20	367.57	620.70	256.15
Nb		0.88	1.73	1.94	1.50	1.46	1.13	1.58	1.08
Ba		0.02	0.06	0.05	0.03	0.07	0.08	0.10	0.04
La		3.55	3.25	4.56	4.08	4.49	3.84	3.99	3.42
Ce		13.8	13.3	16.2	15.8	16.1	14.5	14.7	13.8
Pr		2.21	2.31	2.75	2.81	2.80	2.41	2.61	2.35
Nd		12.4	12.6	16.5	14.6	15.7	14.1	14.2	14.3
Sm		3.34	3.36	4.08	3.75	3.66	3.82	3.96	3.38
Eu		1.08	1.12	1.23	1.12	1.24	1.21	1.24	1.15
Gd		2.44	2.78	3.20	2.88	3.12	3.00	2.91	3.00
Tb		0.368	0.445	0.426	0.454	0.435	0.424	0.383	0.397
Dy		1.85	2.00	2.29	2.11	2.26	2.09	2.27	2.12
Ho		0.256	0.267	0.303	0.349	0.382	0.348	0.327	0.339
Er		0.748	0.625	0.752	0.807	0.947	0.733	0.763	0.645
Tm		0.066	0.098	0.108	0.082	0.100	0.096	0.089	0.089
Yb		0.585	0.740	0.777	0.532	0.725	0.634	0.820	0.648
Lu		0.076	0.078	0.084	0.092	0.090	0.060	0.079	0.085
Hf		8.07	14.3	10.2	10.8	10.8	12.8	18.0	7.67
Ta		0.25	0.53	0.40	0.34	0.35	0.38	0.55	0.24
Pb		0.15	0.14	0.19	0.15	0.17	0.12	0.16	0.11
Th		0.12	0.13	0.19	0.16	0.15	0.12	0.07	0.09
U		0.03	0.03	0.03	0.05	0.04	0.02	0.01	0.01

Appendix 1, Table 12.5 continued

Sample	SPK Cpxite G5 R	SPK Cpxite G6 C	SPK Cpxite G6 R	SPK Cpxite G7 C	SPK Cpxite G7 R	SPK Cpxite G8 C	SPK Cpxite G8 R	SPK Cpxite G9 C	SPK Cpxite G9 R
SiO_2	49.39	50.32	49.50	49.40	50.66	49.47	50.46	49.26	49.94
TiO_2	1.38	1.00	1.14	1.36	1.01	1.34	0.89	1.43	1.08
Al_2O_3	4.86	3.95	4.26	4.77	3.90	4.78	3.92	5.18	4.39
Cr_2O_3	0.01	0.02	bd	0.01	bd	bd	bd	bd	0.02
FeO	8.77	9.95	10.58	9.56	10.00	9.04	9.40	9.34	10.65
MnO	0.17	0.13	0.14	0.14	0.15	0.14	0.14	0.13	0.15
MgO	12.34	11.73	11.37	11.98	11.95	12.46	11.81	12.31	11.12
CaO	21.08	20.51	20.23	20.78	20.74	21.38	20.52	21.19	20.03
Na_2O	1.57	1.80	1.99	1.81	1.88	1.55	1.82	1.53	2.14
K_2O	0.01	0.002	0.01	0.02	bd	bd	0.02	0.02	0.01
Total	99.56	99.42	99.22	99.81	100.29	100.15	98.98	100.39	99.53
Mg#	71.48	67.73	65.68	69.05	68.04	71.06	69.10	70.12	65.03
Ca#	55.13	55.71	56.14	55.52	55.52	55.24	55.56	55.31	56.44
Sc		28.62	23.75	22.83					
V		340.70	341.23	333.10					
Cr		23.71	30.95	28.11					
Ni		4.56	5.22	4.98					
Rb		0.03	0.07	0.01					
Sr		138.20	124.10	128.27					
Y		8.33	8.17	8.60					
Zr		375.40	316.40	293.75					
Nb		1.35	1.47	1.18					
Ba		0.05	0.06	0.03					
La		4.25	4.65	4.81					
Ce		15.6	15.9	16.4					
Pr		2.57	2.74	2.75					
Nd		14.7	15.8	14.9					
Sm		4.04	3.74	4.19					
Eu		1.19	1.20	1.31					
Gd		3.30	3.13	2.83					
Tb		0.393	0.433	0.441					
Dy		2.32	2.09	2.31					
Ho		0.326	0.371	0.387					
Er		0.801	0.852	0.946					
Tm		0.103	0.119	0.113					
Yb		0.787	0.695	0.757					
Lu		0.108	0.069	0.108					
Hf		11.4	10.6	9.6					
Ta		0.32	0.38	0.36					
Pb		0.17	0.11	0.11					
Th		0.11	0.18	0.12					
U		0.03	0.04	0.03					

Appendix 1, Table 12.5 continued

Sample	SPK Cpxite G10 C	SPK Cpxite G10 R	SPK Cpxite G11 C	SPK Cpxite G11 R	SPK XENO 1 G15	SPK XENO 1 G16	SPK XENO 1 G17	SPK XENO 1 G18	SPK XENO 1 G19
SiO_2	49.13	50.32	51.79	49.16	50.80	50.97	50.74	50.92	50.93
TiO_2	1.38	0.96	1.27	1.47	1.22	1.12	1.17	1.16	1.16
Al_2O_3	4.60	3.70	4.21	4.98	4.72	4.44	4.48	4.33	4.48
Cr_2O_3	bd	bd	0.01	0.02	0.01	bd	0.02	bd	0.01
FeO	9.07	9.50	12.26	8.63	8.83	8.71	8.66	8.55	8.74
MnO	0.12	0.18	0.16	0.13	0.17	0.12	0.12	0.13	0.15
MgO	12.38	12.19	11.25	12.26	11.33	11.60	11.63	11.70	11.64
CaO	21.22	20.76	21.26	21.18	19.94	20.05	20.09	20.23	20.28
Na_2O	1.47	1.81	1.96	1.56	2.27	2.16	2.14	2.02	2.02
K_2O	0.01	0.01	0.01	bd	0.01	0.02	0.01	0.01	0.01
Total	99.38	99.43	104.18	99.39	99.30	99.18	99.06	99.06	99.43
Mg#	70.84	69.55	62.04	71.68	69.56	70.35	70.52	70.90	70.36
Ca#	55.22	55.06	57.62	55.40	55.86	55.42	55.41	55.43	55.62

Appendix 1, Table 12.5 continued

Sample	SPK XENO 1 G20	SPK XENO 1 G21	SPK XENO 1 G22	SPK XENO 2 G20	SPK XENO 2 G21	SPK XENO 2 G22	SPK XENO 2 G23	SPK XENO 2 G24	SPK XENO 2 G25
SiO_2	49.48	49.81	50.36	50.84	51.02	50.93	50.96	51.36	51.44
TiO_2	1.28	1.13	1.49	1.27	1.25	1.29	1.05	0.96	1.02
Al_2O_3	4.74	4.30	4.61	4.47	4.60	4.75	4.14	3.71	3.89
Cr_2O_3	0.002	bd	bd	0.01	bd	bd	0.02	bd	0.02
FeO	8.60	8.46	8.52	8.59	8.80	8.24	8.34	7.99	8.06
MnO	0.14	0.15	0.16	0.13	0.14	0.13	0.13	0.12	0.14
MgO	11.83	12.10	11.71	12.41	12.42	12.46	12.89	12.97	13.00
CaO	20.89	21.05	20.24	20.89	20.48	20.89	20.92	21.08	20.93
Na_2O	1.41	1.35	1.95	1.54	1.62	1.61	1.49	1.39	1.50
K_2O	0.01	0.01	0.01	0.01	0.02	0.02	0.01	0.01	0.00
Total	98.38	98.35	99.05	100.17	100.36	100.31	99.95	99.60	99.99
Mg#	71.03	71.81	70.98	72.01	71.54	72.90	73.34	74.29	74.17
Ca#	55.94	55.59	55.43	54.76	54.25	54.68	53.86	53.90	53.67

Appendix 1, Table 12.5 continued

Sample	SPK XENO 2 G26	SPK XENO 2 G27	SPK XENO 3 G6	SPK XENO 3 G7	SPK XENO 3 G8	SPK XENO 3 G9	SPK XENO 3 G10	SPK XENO 3 G12	SPK XENO 3 G13

SiO_2	50.28	50.91	51.22	51.13	51.15	51.67	50.66	51.09	51.03
TiO_2	1.33	1.20	1.24	1.10	1.14	0.82	1.19	1.19	1.28
Al_2O_3	4.73	4.33	4.44	4.09	4.51	4.02	4.34	4.12	4.74
Cr_2O_3	0.001	0.01	0.001		0.004	0.01		0.001	0.02
FeO	8.61	8.59	8.87	8.28	9.01	8.68	8.81	8.63	9.01
MnO	0.16	0.15	0.13	0.13	0.16	0.16	0.13	0.12	0.17
MgO	12.20	12.23	11.63	12.23	11.57	11.79	11.59	12.02	11.55
CaO	20.48	20.19	20.12	20.78	19.87	19.88	20.10	20.60	20.11
Na_2O	1.63	1.84	2.23	1.84	2.22	2.20	2.11	1.81	2.19
K_2O	0.01	0.01	0.00	0.01	0.01	0.01	0.01	0.01	0.01
Total	99.43	99.47	99.87	99.61	99.63	99.22	98.94	99.59	100.11
Mg#	71.61	71.73	70.02	72.45	69.59	70.76	70.10	71.26	69.54
Ca#	54.70	54.28	55.44	55.00	55.27	54.81	55.50	55.22	55.60

Appendix 1, Table 12.5 continued

Sample	SPK XENO 4 G25	SPK XENO 4 G26	SPK XENO 4 G27	SPK XENO 4 G28	SPK XENO 4 G29	SPK XENO 4 G30-1	SPK XENO 4 G31	SPK XENO 4 G32	SPK XENO 4 G33
SiO_2	51.36	50.69	51.18	50.92	51.67	51.36	51.01	51.11	51.75
TiO_2	1.06	1.24	1.08	1.26	1.23	1.26	1.11	1.00	0.87
Al_2O_3	4.28	4.62	4.24	4.69	4.42	4.50	4.15	3.99	3.33
Cr_2O_3	0.005	0.003	bd	bd	0.01	0.01	0.01	0.01	0.01
FeO	8.66	8.56	8.25	8.85	8.76	8.77	8.71	8.72	8.47
MnO	0.15	0.12	0.13	0.15	0.16	0.11	0.15	0.13	0.16
MgO	11.69	11.63	11.91	11.42	11.62	11.85	12.46	12.38	12.89
CaO	20.06	20.13	20.24	19.84	19.52	20.51	21.23	21.31	21.38
Na_2O	2.12	1.99	1.85	2.16	2.43	1.92	1.36	1.35	1.24
K_2O	0.01	0.01	0.01	0.01	0.01	0.01	bd	0.01	0.01
Total	99.38	98.98	98.88	99.29	99.82	100.31	100.20	100.03	100.09
Mg#	70.63	70.76	71.99	69.66	70.27	70.64	71.83	71.65	73.05
Ca#	55.24	55.46	55.01	55.55	54.71	55.46	55.06	55.33	54.41

Appendix 1, Table 12.5 continued

Sample	SDIA G7	SDIA G8	SDIA G9	SDIA G10	SDIA G11	SDIA G12	SDIA G13	SDIA G14	SDIB G10
SiO_2	50.14	50.43	50.42	50.30	50.78	50.42	50.13	50.45	48.54
TiO_2	1.32	1.24	1.22	1.26	1.20	1.26	1.26	1.22	1.71
Al_2O_3	6.24	6.16	5.68	5.73	5.69	5.81	5.53	5.93	6.22
Cr_2O_3	bd	0.02	0.01	0.04	0.01	0.02	0.03	0.02	0.02
FeO	9.08	9.35	9.33	9.39	9.31	9.18	9.02	9.08	9.41
MnO	0.18	0.18	0.18	0.21	0.19	0.21	0.16	0.20	0.17
MgO	11.48	11.26	11.46	11.40	11.45	11.48	11.70	11.41	11.12
CaO	20.64	20.09	20.89	20.68	20.62	20.65	20.82	20.39	20.30

Na_2O	1.71	1.97	1.69	1.70	1.72	1.83	1.55	1.71	2.06
K_2O	0.01	0.02	0.00	0.01	0.01	0.00	0.01	0.01	0.00
Total	100.81	100.72	100.90	100.70	100.99	100.85	100.21	100.42	99.54
Mg#	69.25	68.20	68.62	68.38	68.67	69.01	69.78	69.11	67.80
Ca#	56.40	56.22	56.73	56.62	56.43	56.41	56.15	56.24	56.77

Appendix 1, Table 12.5 continued

Sample	SDIB G16	SDIB G14	SDIB G15	SDIB G13	SDIB G17	SDIB G12	SDIB G11
SiO_2	48.89	49.26	49.04	49.05	49.16	48.98	49.22
TiO_2	1.59	1.52	1.50	1.49	1.43	1.37	1.30
Al_2O_3	6.05	5.81	5.95	5.81	5.69	5.46	5.15
Cr_2O_3	0.05	0.05	0.07	0.03	0.07	0.03	0.04
FeO	10.27	10.14	10.37	9.66	9.95	9.83	9.58
MnO	0.16	0.10	0.14	0.15	0.16	0.15	0.19
MgO	10.90	10.97	10.85	11.09	11.07	11.25	11.47
CaO	20.20	20.27	20.14	20.24	20.30	20.66	20.45
Na_2O	2.04	1.99	1.98	1.93	1.93	1.82	1.84
K_2O	0.01	0.01	0.01	0.01	0.01	0.00	0.01
Total	100.17	100.10	100.06	99.46	99.77	99.54	99.23
Mg#	65.39	65.85	65.09	67.14	66.47	67.09	68.07
Ca#	57.15	57.06	57.18	56.77	56.87	56.92	56.20

Appendix 1

Table 12:6: Major element data for amphibole xenolith grains

Sample	SPK XENO 1 G13	SPK XENO 1 G14	SPK XENO 1 G15	SPK XENO 2 G1	SPK XENO 2 G7	SPK XENO 2 G9	SPK XENO 2 G9	SPK XENO 2 G10	SPK XENO 2 G11
SiO_2	40.54	40.93	40.96	41.59	41.17	41.41	41.49	41.59	41.56
TiO_2	3.63	3.49	3.41	3.35	3.63	3.57	3.28	3.33	3.41
Al_2O_3	12.46	12.47	12.58	12.57	12.81	12.83	12.72	12.73	12.65
Cr_2O_3	0.01	0.02	0.01	0.01	0.02	0.01	0.001	0.01	0.01
FeO	13.79	13.77	13.76	12.80	13.00	12.99	12.55	12.57	13.00
MnO	0.14	0.11	0.13	0.13	0.11	0.14	0.10	0.10	0.10
MgO	11.11	11.29	11.56	12.69	12.69	12.65	12.93	13.06	12.93
CaO	10.42	10.38	10.65	10.93	11.00	11.12	11.03	11.00	11.01
Na_2O	3.09	3.00	2.88	2.73	2.73	2.60	2.86	2.74	2.77
K_2O	1.90	1.85	1.98	1.88	2.03	2.00	1.89	1.89	1.87
F	0.08	0.08	0.15	0.21	0.12	0.18	0.02	0.15	0.26
Total	97.14	97.36	97.99	98.78	99.26	99.43	98.86	99.10	99.46
Mg#	58.91	59.37	59.94	63.84	63.48	63.41	64.72	64.91	63.91
Ca#	40.31	39.80	39.86	38.25	38.41	38.74	38.03	37.74	37.99

Appendix 1, Table 12.6 continued

Sample	SPK XENO 2 G12-1	SPK XENO 2 G13	SPK XENO 2 G14-1	SPK XENO 2 G15	SPK XENO 2 G16	SPK XENO 4 G20	SPK XENO 4 G21	SPK XENO 4 G22	SPK XENO 4 G23
SiO_2	41.76	41.26	41.36	41.58	41.79	40.73	41.07	41.04	41.12
TiO_2	3.28	3.51	3.47	3.39	3.32	3.65	3.52	3.69	3.56
Al_2O_3	12.41	12.73	12.39	12.20	12.21	12.75	12.79	12.57	12.63
Cr_2O_3	0.00	0.02	bd	0.005	0.02	0.01	0.01	0.002	bd
FeO	12.65	12.91	12.92	12.75	12.82	13.74	13.76	13.98	13.98
MnO	0.08	0.11	0.11	0.13	0.14	0.15	0.13	0.12	0.13
MgO	13.02	12.74	12.86	12.88	12.91	11.17	11.22	11.46	11.34
CaO	11.09	11.13	11.05	11.09	10.99	10.58	10.59	10.55	10.60
Na_2O	2.81	2.86	2.74	2.82	2.91	3.07	3.03	3.12	3.11
K_2O	1.86	1.95	1.93	1.93	1.86	1.97	1.94	1.96	1.93
F	0.05	0.08	0.10	0.08	0.19	0.14	0.19	0.15	0.25
Total	98.97	99.27	98.89	98.82	99.09	97.89	98.16	98.57	98.54
Mg#	64.71	63.72	63.92	64.26	64.20	59.15	59.22	59.35	59.10
Ca#	37.99	38.59	38.20	38.25	37.99	40.52	40.43	39.83	40.19

Appendix 1, Table 12.6 continued

Sample	SPK XENO 4 G24-2	SDIA G1	SDIA G2	SDIA G3	SDIA G4	SDIA G5	SDIB G6	SDIB G5	SDIB G4
SiO_2	41.13	40.15	40.74	40.91	41.35	41.06	39.71	39.95	39.78
TiO_2	3.57	3.68	3.64	3.46	3.54	3.65	4.19	4.02	3.88
Al_2O_3	12.58	14.81	14.06	14.34	14.10	14.58	13.46	13.05	13.25
Cr_2O_3	0.03	0.02	0.01	bd	0.003	0.02	0.02	0.03	0.04
FeO	13.95	13.41	13.04	13.21	13.37	13.21	14.16	14.48	13.86
MnO	0.13	0.14	0.16	0.15	0.18	0.16	0.14	0.17	0.13
MgO	11.34	10.99	11.10	11.34	11.16	11.20	10.69	10.86	11.07
CaO	10.60	10.56	10.59	10.80	10.69	10.80	10.39	10.23	10.42
Na_2O	3.05	2.54	2.51	2.59	2.53	2.52	2.74	2.77	2.70
K_2O	1.90	1.93	1.92	1.90	1.98	1.93	2.05	2.00	1.97
F	0.13	0.18	0.27	0.07	0.17	0.26	0.01	0.09	0.07
Total	98.34	98.33	97.92	98.73	99.00	99.27	97.55	97.61	97.15
Mg#	59.15	59.34	60.24	60.44	59.78	60.13	57.34	57.19	58.72
Ca#	40.21	40.88	40.71	40.67	40.78	40.98	41.16	40.39	40.37

Appendix 1, Table 12.6 continued

Sample	SDIB G2	SDIB G3	SDIB G1	SDIB G7
SiO_2	40.04	39.93	40.35	40.35
TiO_2	3.87	3.84	3.81	3.81
Al_2O_3	13.28	13.40	13.15	13.16
Cr_2O_3	0.04	0.06	0.05	0.03
FeO	14.04	13.95	14.04	13.94
MnO	0.14	0.12	0.12	0.14
MgO	11.19	11.12	11.22	11.25
CaO	10.53	10.60	10.70	10.63
Na_2O	2.70	2.78	2.72	2.72
K_2O	1.93	1.87	1.90	1.92
F	0.02	0.07	0.05	0.00
Total	97.76	97.71	98.09	97.94
Mg#	58.68	58.65	58.73	58.97
Ca#	40.36	40.68	40.69	40.46

Appendix 1

Table 12:7: Major element data for phlogopite xenolith grains

Sample	SPK XENO 1 G1	SPK XENO 1 G2	SPK XENO 1 G3	SPK XENO 1 G4	SPK XENO 1 G5	SPK XENO 1 G6	SPK XENO 1 G7	SPK XENO 1 G9	SPK XENO 1 G10
SiO_2	36.70	36.46	36.33	36.70	36.86	37.34	36.64	37.30	36.61
TiO_2	5.30	5.42	5.36	5.25	5.40	5.38	5.16	4.88	5.34
Al_2O_3	15.30	15.27	15.06	15.21	15.23	14.80	15.21	15.08	15.08
Cr_2O_3	bd	0.01	bd	0.02	0.01	0.01	0.005		0.001
FeO	15.28	15.39	15.62	15.81	15.60	15.71	15.60	15.12	15.10
MnO	0.07	0.09	0.12	0.12	0.12	0.11	0.09	0.12	0.14
MgO	13.94	14.06	14.11	14.03	13.91	14.11	14.07	14.16	14.07
CaO	bd	bd	bd	bd	0.08	bd	0.01	bd	bd
Na_2O	0.83	0.86	0.83	0.83	0.84	0.81	0.85	0.81	0.79
K_2O	8.89	8.96	9.03	8.93	8.76	8.79	9.00	8.87	8.91
F	0.11	0.13	0.25	0.18	0.22	0.23	0.19	0.34	0.13
Cl	0.05	0.05	0.03	0.04	0.06	0.05	0.03	0.05	0.04
Total	96.42	96.64	96.63	97.02	96.98	97.23	96.76	96.57	96.15
Mg#	61.92	61.93	61.67	61.25	61.36	61.53	61.64	62.51	62.39

Appendix 1, Table 12.7 continued

Sample	SPK XENO 1 G11	SPK XENO 4 G1	SPK XENO 4 G2	SPK XENO 4 G3	SPK XENO 4 G4
SiO_2	36.53	37.62	37.05	37.32	37.60
TiO_2	5.32	5.39	5.31	5.10	5.52
Al_2O_3	14.80	14.98	14.74	15.09	15.07
Cr_2O_3	bd	0.01	bd	0.001	0.00
FeO	14.93	15.48	15.01	15.36	15.41
MnO	0.12	0.08	0.07	0.10	0.09
MgO	13.82	14.01	13.77	13.96	14.20
CaO	bd	bd	bd	bd	bd
Na_2O	0.85	0.79	0.80	0.87	0.85
K_2O	8.67	8.90	8.76	8.77	8.88
F	0.04	0.12	0.19	0.08	0.18
Cl	0.04	0.04	0.04	0.05	0.04
Total	95.09	97.36	95.65	96.64	97.77
Mg#	62.25	61.72	62.03	61.80	62.13

Appendix 1,

Table 12:8: Major element data for ilmenite xenolith grains

Sample	SPK XENO 1 G23	SPK XENO 1 G24	SPK XENO 1 G25	SPK XENO 1 G26	SPK XENO 1 G27	SPK XENO 1 G28	SPK XENO 1 G29	SPK XENO 1 G30	SPK XENO 3 G14
SiO_2	0.00	0.00	0.00	0.01	0.00	0.00	0.00	0.00	0.00
TiO_2	47.06	47.20	47.33	47.20	47.07	47.13	47.07	46.93	45.94
Al_2O_3	0.28	0.27	0.25	0.26	0.28	0.26	0.28	0.28	0.26
Cr_2O_3	0.00	0.00	0.00	0.00	0.00	0.00	0.00	0.01	0.00
FeO	45.93	45.92	45.39	45.91	45.34	45.73	44.98	45.67	46.84
MnO	0.62	0.64	0.61	0.63	0.62	0.61	0.65	0.60	0.54
MgO	3.52	3.54	3.75	3.59	3.89	3.72	4.07	3.45	3.46
CaO	0.01	0.00	0.01	0.04	0.03	0.01	0.07	0.00	0.05
Total	97.42	97.56	97.34	97.64	97.24	97.46	97.12	96.93	97.09
Mg#	12.01	12.07	12.82	12.21	13.24	12.65	13.88	11.85	11.63

Appendix 1, Table 12.8 continued

Sample	SPK XENO 3 G15	SPK XENO 3 G16	SPK XENO 3 G17	SPK XENO 3 G18	SPK XENO 3 G19	SPK XENO 3 G20	SPK XENO 3 G21	SPK XENO 3 G22	SPK XENO 4 G34
SiO_2		0.01		0.01					
TiO_2	47.19	47.18	47.36	47.52	47.36	47.15	47.24	47.43	47.29
Al_2O_3	0.26	0.25	0.28	0.28	0.28	0.29	0.28	0.30	0.28
Cr_2O_3	0.001	bd	bd	bd	bd	bd	bd	bd	bd
FeO	46.15	45.95	45.81	45.93	46.09	46.09	45.91	46.10	46.25
MnO	0.62	0.62	0.60	0.61	0.63	0.60	0.60	0.64	0.63
MgO	3.52	3.72	3.73	3.77	3.49	3.54	3.76	3.64	3.45
CaO	bd	0.02	0.01	0.01	bd	bd	bd	bd	bd
Total	97.73	97.74	97.79	98.13	97.84	97.66	97.80	98.11	97.90
Mg#	11.94	12.61	12.66	12.75	11.88	12.03	12.71	12.33	11.72

Appendix 1, Table 12.8 continued

Sample	SPK XENO 4 G35	SPK XENO 4 G36	SPK XENO 4 G37	SPK XENO 4 G38	SPK XENO 4 G39	SPK XENO 4 G40	SPK XENO 4 G41	SPK XENO 4 G42	SPK XENO 4 G43
SiO_2									
TiO_2	47.31	47.66	47.46	47.34	47.40	47.31	47.09	47.02	47.02
Al_2O_3	0.27	0.27	0.26	0.31	0.26	0.28	0.29	0.27	0.27
Cr_2O_3	0.002	0.002	bd	0.003	0.01	bd	bd	bd	bd
FeO	45.70	45.26	45.89	45.86	45.93	46.07	46.05	45.92	45.78
MnO	0.59	0.58	0.62	0.60	0.61	0.58	0.60	0.60	0.58

MgO	3.76	4.22	3.63	3.72	3.68	3.60	3.57	3.62	3.73
CaO	bd	bd	bd	bd	bd	bd	bd	bd	bd
Total	97.64	97.99	97.87	97.83	97.89	97.85	97.61	97.43	97.38
Mg#	12.79	14.24	12.35	12.62	12.49	12.23	12.14	12.32	12.66